Calibration of the DUNE Far Detector Using Cosmic-ray Muon Events

Praveen Kumar

Supervisor: Prof. Vitaly Kudryavtsev

Department of Physics and Astronomy

The University of Sheffield

This thesis is submitted for the degree of
Doctor of Philosophy

July 2024

Abstract

The Deep Underground Neutrino Experiment (DUNE) aims to set new limits on parameters associated with neutrino oscillations, neutrino astrophysics, and beyond the Standard Model (SM) searches such as nucleon decay. DUNE will quantify the magnitude of CP violation in the lepton sector, and determine the neutrino mass ordering. These benefit highly from the large target mass and excellent imaging, tracking, and particle identification capabilities of Liquid Argon Time Projection Chambers (LArTPCs). Detector calibration is essential to make precise physics measurements. For instance, accurate energy reconstruction is necessary for measuring many of the aforementioned quantities with the precision required for discovering new physics and fully exploiting the capabilities of the detector. Cosmic muons are a freely available natural source of calorimetric data and can be used for calibrating various detector parameters. This thesis provides an analysis of simulated cosmic-ray muon events generated with the Muon Simulation Underground (MUSUN) generator in the DUNE horizontal drift (HD) far detector (FD). The study focuses on analysing the energy and angular distribution of various classes of muon events, as well as characterising the different particles produced by cosmic muon interactions. The analysis of $\pi^0 \to 2\gamma$ events within the cosmic-ray muon sample is presented in this thesis with a detailed study of reconstructing electromagnetic showers. The π^0 mass is reconstructed within the DUNE FD, yielding a value of (136 ± 7) MeV/c^2. Additionally, the thesis introduces methods for dE/dx calibration using simulated and reconstructed muon tracks. A calibration constant $C_{\text{cal}} = (5.469 \pm 0.003) \times 10^{-3}\text{ADC} \times \text{tick/e}$ is obtained through a model-dependent calibration process, where 1 tick corresponds to 500 ns of sampling time of an ADC. Furthermore, a calibration technique is presented, demonstrating precise translation from dQ/dx to dE/dx. This calibration method is applied to stopping muons, charged pions, and protons in the DUNE FD, addressing the measurement of energy loss in the detector volume. These are important calibrations of the DUNE FD and will contribute to achieving the exciting physics goals of the experiment.

Declaration

I hereby declare that, unless explicitly referenced to the work of others, the content of this thesis is original and has not been presented in its entirety or partially for the attainment of any other degree or qualification, either in this university or elsewhere. This thesis represents my independent work, and in cases of collaboration, appropriate acknowledgement has been provided. Contributions from other individuals have been identified, and sources for figures and tables generated by others have been duly credited.

Praveen Kumar
July 2024

Author's contributions

The author's contributions to this thesis are diverse and include several critical aspects of the research conducted for the DUNE experiment. Chapter 6 presents muon production for the DUNE far detector. The author generated and simulated cosmic-ray muon events for the DUNE horizontal drift far detector. Two different reconstruction algorithms were employed in the production of cosmic muon events. The analysis presented in this chapter is the author's own work. In Chapter 7, the author presents a detailed analysis of neutral pions. All the work presented in this chapter represents an individual contribution by the author. The author introduces two distinct methods of energy calibration of the DUNE FD in Chapter 8. The first method is based on the modified box model, originally developed by the ArgoNeuT experiment and implemented for the first time by the author in the DUNE experiment. The method implementation and analysis carried out are the author's own work. The second analysis introduces a different approach to energy calibration, being model-independent and implemented for the first time in DUNE. The methods and work presented in this chapter are the author's own work. All the work mentioned above has been presented to the DUNE collaboration.

Acknowledgements

I express my heartfelt gratitude to my supervisor, Prof. Vitaly Kudryavtsev, for providing me with the opportunity to work under his supervision. Your unwavering guidance and support have been indispensable throughout my PhD journey. Working with you has been an enriching and truly rewarding experience. I appreciate the valuable lessons I have learned from you, both academically and professionally. Your example has set a standard for the perfection of work in a professional setting.

I would like to thank Dr Viktor Pec for his invaluable help at the beginning of my PhD, providing guidance for the first one and a half years. His assistance in understanding the coding of LArSoft, computing skills, and patiently answering my numerous questions was instrumental. I would also like to thank Dr Rhiannon Jones, who supported me throughout the rest of my PhD, addressing every query. Additionally, I appreciate Dr Rhiannon Jones's effort in reading the PhD chapters. Thanks to Dr Michael Mooney for his advice during my PhD work and Leigh Whitehead for consistently answering my questions and assisting with LArSoft skills. I extend my thank to the DUNE UK collaboration for their useful suggestions and engaging discussions during meetings. Additionally, I appreciate the insightful discussions with Dr Tom Junk.

I would like to acknowledge the individuals in the Particle Physics and Particle Astrophysics group at the University of Sheffield. Thanks to individuals like Andrew, Anthony, Dom, Ed, Harry, and others for engaging in socials and useful discussions about PhD and in general. Also, thanks to Dr Elena Korolkova and Mitch for their assistance and troubleshooting of any problems related to the Sheffield machine and cluster. Pardon me if I have missed any names. I would like to thank Andrew for including me in the university football team for the Bubble Chamber Cup at Oxford. Playing with the team was a fantastic experience.

My sincere thanks to my mathematics teacher, Prof. K. C. Sinha, whose teaching skills inspired me. I thoroughly enjoyed learning mathematics, which played a significant role in my passion for learning, teaching, and advancing in academia. His teaching methodology, which I adopted, enabled me to earn and self-fund my education during my college days.

My special thanks to Dr William Durham, Dr Matt Mears, and Dr Mark Quinn for their support during my time as a Graduate Teaching Assistant (GTA) at the University of Sheffield. Their guidance helped me develop teaching skills and achieve the Fellowship of the Higher Education Academy (FHEA).

I would like to express my sincere appreciation to Dr Apurv Chauhan and Dr Surbhi Sehgal for their advice and help since my college days.

My heartfelt gratitude to my wife, Dr Poonam, whose unwavering support during my PhD has been invaluable. Thank you for being a source of strength and encouragement in this journey.

Finally, I extend my heartfelt gratitude to my parents and family, with special mention of my brother, for their help and support.

Table of contents

Abstract **v**

Declaration **vii**

Author's contribution **ix**

Acknowledgements **xii**

List of figures **xvii**

List of tables **xxiii**

Nomenclature **xxv**

1 Introduction **1**

2 Neutrinos **5**

2.1 Introduction and discovery of the neutrinos 5
2.2 Neutrinos in the Standard Model 8
2.3 Neutrino interactions 11
  2.3.1 Introduction to neutrino interactions 11
  2.3.2 Neutral current interactions 12
  2.3.3 Charge current interactions 14
2.4 Neutrino oscillations 16
  2.4.1 Neutrino oscillations in vacuum 16
  2.4.2 Neutrino oscillations in matter 22
  2.4.3 CP violation in neutrino oscillations 24
  2.4.4 Neutrino mass hierarchy 25
2.5 Experimental measurements of neutrino oscillation parameters . . . 27
2.6 Current and future neutrino experiments 29

3 Liquid Argon Time Projection Chambers 31

3.1 Detector medium and operating principle 32

3.2 Particle interactions in LArTPC 33

3.2.1 Track formation: muons, protons and charged pions 34

3.2.2 Shower formation: electrons and photons 37

3.3 Ionisation signals: formation and implications 40

3.3.1 Charge production 40

3.3.2 Ionisation charge drift 42

3.3.3 Ionisation charge detection: signal formation 44

3.4 Scintillation light signal 47

3.4.1 Production 47

3.4.2 Transmission 48

3.4.3 Detection 48

4 Deep Underground Neutrino Experiment 51

4.1 Experimental design 52

4.2 Neutrino beam 52

4.3 Near detector 54

4.4 Far detector 56

4.4.1 Overview of the far detector 56

4.4.2 Single-phase horizontal drift 58

4.4.3 Anode plane assembly 60

4.4.4 Cathode planes and high voltage 62

4.4.5 Field cage 62

4.5 Physics goals of DUNE 63

4.5.1 Neutrino oscillation physics at DUNE 63

4.5.2 Proton decay searches at DUNE 67

4.5.3 Low energy physics searches at DUNE 69

4.5.4 Beyond the standard model physics 71

5 Simulation and reconstruction of the DUNE FD 73

5.1 Monte Carlo simulation 74

5.1.1 Particle generation 74

5.1.2 Particle propagation 74

5.2 Detector simulation: charge and light 75

5.3 Event reconstruction in the DUNE FD 76

5.3.1 Signal processing and hit finding 76

5.3.2 Pandora overview 77
5.3.3 Pandora reconstruction chains 78
5.4 Energy reconstruction 79

6 Muon production 81
6.1 Muon production in the atmosphere 82
6.2 Cosmic-ray muons at the Earth's surface 82
6.3 Muon distributions underground 85
6.3.1 Cosmic-ray muon in underground experiments 85
6.3.2 Muon propagation through matter 85
6.4 Simulation of muons in the DUNE FD using MUSUN 88
6.4.1 Muon generator MUSUN 88
6.4.2 Generating muons 88
6.5 Muon distributions at the DUNE FD 90
6.6 Cosmic muon events in different reconstructions 96
6.6.1 Cosmic and neutrino oriented reconstruction methods 96
6.6.2 Event display 98
6.7 Summary 99

7 Neutral pion analysis 101
7.1 The neutral pion 102
7.1.1 Neutral pion kinematics 103
7.1.2 Neutral pion in the DUNE FD 104
7.2 Analysis framework 106
7.3 Monte Carlo simulation studies 108
7.4 Reconstruction studies 111
7.4.1 Completeness and purity 111
7.4.2 Reconstructed showers 115
7.4.3 Reconstructed shower energy 118
7.4.4 Reconstructed opening angle 121
7.5 Reconstructed π^0 mass 125
7.6 Summary 127

8 Energy calibration of the DUNE FD using stopping particles 129
8.1 dE/dx calibration using stopping muons 130
8.1.1 Introduction 130
8.1.2 Event selection 130
8.1.3 Reconstructed track selections 131

8.2 Analysis methods 134
  8.2.1 Model dependent: modified box model 134
  8.2.2 Model independent: absolute energy scale 140
8.3 dE/dx reconstruction of stopping charged pions 147
  8.3.1 Event selection 147
  8.3.2 Analysis method 148
8.4 dE/dx reconstruction of stopping protons 153
  8.4.1 Event selection 153
  8.4.2 Analysis method 154
8.5 Comparision of dE/dx reconstruction of stopping particles 159
8.6 Comparision of dQ/dx reconstruction of stopping particles 162
8.7 Summary 164

9 Conclusion **167**

References **171**

Appendix A Neutrinos **185**
A.1 Neutrinos oscillation probability 185

List of figures

2.1 Neutrino interactions in matter . . . 11
2.2 Neutrino and antineutrino cross sections as a function of energy . . 12
2.3 Neutrino mass hierarchy . . . 26
2.4 Global fit for δ_{CP} . . . 28

3.1 Operating principle of a LArTPC . . . 33
3.2 Event display of a cosmic muon . . . 34
3.3 Mean energy loss of muons, pions, and protons . . . 36
3.4 Energy loss of electrons in LAr . . . 38
3.5 Cross sections of photon interaction in LAr . . . 38
3.6 The development of EM showers . . . 39
3.7 Event display of shower formation in pion charge exchange . . . 40
3.8 Recombination factor as a function of the electric field . . . 42
3.9 Electric field lines and signal formation of a LArTPC . . . 45

4.1 Schematic of the DUNE experiment . . . 52
4.2 Schematic of neutrino beam . . . 53
4.3 Neutrino fluxes at DUNE FD . . . 54
4.4 Schematic of the near detector . . . 56
4.5 Schematic of the far detector . . . 57
4.6 Schematic of a 10 kt DUNE FD SP module . . . 59
4.7 Anode plane assembly . . . 60
4.8 Anode plane assembly built in the Daresbury laboratory . . . 61
4.9 X-ARAPUCA photon detector module . . . 62
4.10 Appearance probability for ν_e and $\bar{\nu}_e$ . . . 64
4.11 DUNE sensitivity for CP violation as a function of true δ_{CP} . . . 65
4.12 DUNE sensitivity for the neutrino mass ordering as a function of true δ_{CP} . . . 66

4.13 DUNE sensitivity for the neutrino CP violation as a function of exposure 67
4.14 Summary of nucleon decay experimental limits 69
4.15 Low energy physics targets and their energy ranges 70

5.1 Deconvolution of raw signal 77
5.2 Reconstructed hits on a wire 77

6.1 Vertical muon energy spectra at sea level 84
6.2 Underground depth dependence of the muon intensity 87
6.3 Muon generation around DUNE FD 10 kt module using MUSUN . 89
6.4 Energy distribution of muons in and around DUNE FD 91
6.5 Correlation between surface profile and azimuthal angle at DUNE FD 92
6.6 Angular distributions of muons at the DUNE FD 93
6.7 Path length of muons inside DUNE FD 94
6.8 Energy loss of muons in DUNE FD 95
6.9 dE/dx of muons in DUNE FD 95
6.10 Reconstructed tracks in the LArTPCs 97
6.11 Reconstructed showers in the LArTPCs 97
6.12 Event display of a cosmic muon event in DUNE FD 98

7.1 π^0 decay kinematics 104
7.2 Schematic of an electromagnetic shower 105
7.3 Pandora event display of a cosmic muon producing a π^0 106
7.4 Analysis layout 107
7.5 Location of π^0 in the DUNE FD 109
7.6 Zenith distribution and multiplicity of π^0 109
7.7 Energy distribution of π^0 and their daughter photons 110
7.8 Opening angle of photons from $\pi^0 \to 2\gamma$ and π^0 mass distribution . 111
7.9 An event display explaining completeness and purity 113
7.10 Completeness and purity of reconstructed photons 114
7.11 Completeness and purity of leading and subleading reconstructed photons 114
7.12 Completeness and purity of leading and subleading reconstructed photons as a function of hits 115
7.13 Reconstructed showers distribution 117
7.14 Distribution of reconstructed shower multiplicity 117
7.15 Reconstructed shower energy distribution 118

7.16 True and reconstructed shower energy of leading and subleading photons . . . 119
7.17 True and reconstructed shower energy . . . 120
7.18 Relative difference between true and reconstructed photon energy . 120
7.19 Relative energy difference of leading and subleading photons vs. number of hits . . . 121
7.20 Angle between photons and their associated showers . . . 122
7.21 Angle between photons and their associated showers vs. hits . . . 123
7.22 Opening angle between showers and photons from $\pi^0 \to 2\gamma$ . . . 123
7.23 Absolute and relative difference of opening angles . . . 124
7.24 Relative difference between reconstructed and true angle vs. hits . 125
7.25 Reconstructed mass of π^0 . . . 126

8.1 Definition of track direction angles . . . 132
8.2 Average dQ/dx distribution as a function of θ_{xz} and θ_{yz} . . . 132
8.3 Reconstructed track multiplicity of stopping muons . . . 133
8.4 Theoretical most probable dE/dx vs. kinetic energy and residual range of stopping muons . . . 134
8.5 dE/dx distribution of a residual range bin of stopping muons . . . 136
8.6 χ^2 vs. calibration constant for stopping muons . . . 137
8.7 $\chi^2 - \chi^2_{\text{min}}$ vs. calibration constant for stopping muons . . . 137
8.8 Theoretical and reconstructed dE/dx vs. kinetic energy of stopping muons . . . 138
8.9 Theoretical and reconstructed dE/dx vs. residual range of stopping muons . . . 139
8.10 The reconstructed and theoretical dE/dx vs. residual range of stopping muons with colour plot . . . 139
8.11 The colour plot of reconstructed dQ/dx vs. residual range of stopping muon tracks . . . 140
8.12 dQ/dx distribution of a residual range bin for stopping muons . . . 141
8.13 Ratio of dE/dx to dQ/dx as a function of residual range for stopping muons . . . 142
8.14 The reconstructed dE/dx vs. kinetic energy of stopping muons and compared with the theoretical prediction . . . 143
8.15 The reconstructed dE/dx vs. residual range of stopping muons and compared with the theoretical values . . . 144

8.16 The reconstructed and theoretical most probable dE/dx vs. residual range for stopping muons with colour plot 144
8.17 The reconstructed and theoretical MPV of dE/dx vs. kinetic energy of stopping muons including low kinetic energies 145
8.18 The reconstructed and theoretical MPV of dE/dx vs. residual range of stopping muons including low residual ranges 146
8.19 The reconstructed and theoretical dE/dx vs. residual range of stopping muons with colour plot including low residual ranges 146
8.20 Average dQ/dx distribution as a function of θ_{xz} and θ_{yz} for pion tracks 148
8.21 Colour plot of reconstructed dQ/dx vs. residual range of pion tracks 149
8.22 dQ/dx distribution of stopping pions for a residual range bin 149
8.23 Ratio of dE/dx to dQ/dx as a function of residual range for stopping pions 150
8.24 Comparison between theoretical and reconstructed dE/dx vs. kinetic energy of stopping pions 151
8.25 Comparison between theoretical and reconstructed dE/dx vs. residual range of stopping pions 152
8.26 Reconstructed dE/dx vs. residual range of stopping pions with colour plot 152
8.27 Average dQ/dx distribution as a function of θ_{xz} and θ_{yz} for proton tracks 154
8.28 Colour plot of reconstructed dQ/dx vs. residual range of stopping proton tracks 155
8.29 dQ/dx distribution of a residual range bin of stopping proton 156
8.30 Ratio of dE/dx to dQ/dx as a function of residual range for stopping protons 156
8.31 Reconstructed and theoretical dE/dx vs. kinetic energy of stopping protons 158
8.32 Reconstructed and theoretical dE/dx vs. residual range of stopping protons 158
8.33 Reconstructed dE/dx vs. residual range of stopping protons with colour plot 159
8.34 Reconstructed dE/dx as a function of kinetic energy of muons, pions, and protons. 160
8.35 Reconstructed dE/dx as a function of residual range of muons, pions and protons 161
8.36 Reconstructed dE/dx as a function of p/m of muons, pions and protons 162

8.37 Reconstructed dQ/dx as a function of kinetic energy of muons, pions, and protons 163
8.38 Reconstructed dQ/dx as a function of residual range of muons, pions and protons 163
8.39 Reconstructed dQ/dx as a function of p/m of muons, pions and protons 164

List of tables

2.1 Neutrino oscillation parameter values 29

4.1 Key parameters for a 10 kt SP HD FD module 58
4.2 Bias voltages for the wire planes of an APA 61

6.1 Stopping power and critical energy of muon 87
6.2 Event statistics of the generated muon sample for the DUNE FD . . 90
6.3 Event statistics of generated muon sample in two reconstruction methods 96

7.1 Event statistics of generated muon sample used in the π^0 study . . 108
7.2 Extended version of event statistics with reconstructed showers . . . 116
7.3 The cuts applied on different quantities 126

8.1 Value of the parameters of the fit function for stopping muons . . . 142
8.2 Value of the parameters of the fit function for stopping pions 151
8.3 Value of the parameters of the fit function for stopping protons . . . 157

Nomenclature

ADC	Analogue to Digital Converter
APA	Anode Plane Assembly
BDM	Boosted Dark Matter
BSM	Beyond the Standard Model
CC	Charged Current
CMBR	Cosmic Microwave Background Radiation
CNO	Carbon Nitrogen Oxygen
COH	Coherent
CP	Charge Parity
CPA	Cathode Plane Assembly
CPV	Charge-Parity Violation
CRC	Cosmic Reconstruction Chain
CRY	Cosmic RaY shower library
DAQ	Data Acquisition
DIS	Deep Inelastic Scattering
DM	Dark Matter
DUNE	Deep Underground Neutrino Experiment

ECAL	Electromagnetic Calorimeter
EM	Electromagnetic
FC	Field Cage
FD	Far Detector
Fermilab	Fermi National Accelerator Laboratory
FNAL	Fermi National Accelerator Laboratory
G4	Geant4
GUT	Grand Unified Theory
HD	Horizontal Drift
HPgTPC	High-Pressure gaseous Argon TPC
HV	High Voltage
IO	Inverted Ordering
KamLAND	Kamioka Liquid Scintillator Anti-neutrino Detector
LAr	Liquid Argon
LArTPC	Liquid Argon Time Projection Chamber
LBNF	Long Baseline Neutrino Facility
LDM	Light-mass Dark Matter
LVD	Large Volume Detector
MBM	Modified Box Model
MC	Monte Carlo
MCS	Multiple Coulomb Scattering
MIP	Minimum Ionising Particle
MPD	Multi-Purpose Detector
MSW	Mikheyev-Smirnov-Wolfenstein

MUSIC	MUon SImulation Code
MUSUN	MUon Simulation UNderground
NC	Neutral Current
ND-GAr	Near Detector Gaseous Argon
ND-LAr	Near Detector Liquid Argon
ND	Near Detector
NO	Normal Ordering
NRC	Neutrino Reconstruction Chain
PD	Photon Detector
PDG	Particle Data Group
PDS	Photon Detection System
PFParticle	Particle Flow Particle
PMNS	Pontecorvo-Maki-Nakagawa-Sakata
PMT	PhotoMultiplier Tube
POT	Protons on Target
QE	Quantum Efficiency
QE	Quasi Elastic
RES	Resonant
SAND	System for on-Axis Neutrino Detection
SBND	Short Baseline Near Detector
SCE	Space Charge Effect
SiPM	Silicon Photomultipliers
SM	Standard Model
SNB	Supernova Neutrino Burst

SNO	Sudbury Neutrino Observatory
SP	Single Phase
SSM	Standard Solar Model
SURF	Sanford Underground Research Facility
TPC	Time Projection Chamber
VUV	Vaccum Ultra-Violet
w. e.	water equivalent: x (m w. e.) = depth (or distance in metre) $\times \rho$ (g/cm^3). Density of water = 997 kg/m^3 $\sim$ 1g/cm^3
WCD	Water Cherenkov Detector
WIMPs	Weakly Interacting Massive Particles

Chapter 1

Introduction

Neutrino physics, a fascinating and challenging field of study, offers unparalleled insights into the fundamental aspects of the universe. The Deep Underground Neutrino Experiment (DUNE) [1, 2, 3, 4] facilitates in-depth studies, designed to unravel the mysteries surrounding neutrinos. This covers long-baseline neutrino physics, exploring phenomena such as neutrino oscillations, CP violation, neutrino mass ordering, and studies related to supernova neutrinos. Moreover, DUNE will probe other beyond the standard model (BSM) physics, including the search for nucleon decay.

The work included in this thesis is presented as follows. Chapter 2 presents the theoretical background of the neutrino physics. Commencing with a historical perspective on the discovery of neutrinos, the chapter unfolds the role of neutrinos within the Standard Model, providing a fundamental understanding of neutrino oscillations. Subsequent sections explore neutrino interactions, including both neutral and charge current interactions. A detailed derivation is carried out on the phenomenon of neutrino oscillations, discussing oscillations in both vacuum and matter, CP violation, and the concept of neutrino mass hierarchy. Concluding with an exploration of experimental measurements of neutrino oscillation parameters, this chapter sets the stage for the experimental focus on DUNE.

In DUNE, a critical aspect of conducting neutrino oscillation studies is to thoroughly understand the detector's response to particles produced in neutrino interactions. Precise energy reconstruction is important for accurately measuring CP violation and fully utilizing the detector's capabilities. Accurate dE/dx reconstruction for particle tracks is crucial for determining the total energy of particles and for particle identification. Stopping particles such as muons, pions, and protons are invaluable as a calibration source for LArTPCs due to their well-understood energy loss in liquid argon.

Chapter 3 introduces Liquid Argon Time Projection Chambers (LArTPCs), focusing on their use of liquid argon as a detection medium and the operating principles. The chapter discusses particle interactions, track formation (muons, protons, charged pions), and shower formation (electrons, photons). Emphasising ionisation signals, it covers the formation, implications, charge production, ionisation charge drift, and detection. The role of scintillation light signals in production, transmission, and detection is also discussed.

In Chapter 4, attention is directed towards the DUNE experiment. The chapter offers a brief overview of the experimental design, the neutrino beam, and the roles of both near and far detectors. Special emphasis is placed on the single-phase horizontal drift and anode plane assembly within the DUNE far detector (FD). The description presented in this chapter exclusively focuses on the DUNE FD. At the end of this chapter, the physics goals of DUNE are discussed, with a specific focus on neutrino oscillation and proton decay searches.

In Chapter 5, the discussion revolves around the simulation and reconstruction of events in the DUNE FD. Starting with Monte Carlo simulations, particle generation, and propagation, the chapter explores event reconstruction methods using Pandora, a reconstruction framework for the analysis of the data from the DUNE FD. Additionally, brief discussions are presented on two reconstruction algorithms: the cosmic reconstruction chain (CRC) and the neutrino reconstruction chain (NRC). The simulated events using these reconstruction chains are used in the analysis presented in the subsequent chapters on the reconstruction of neutral pion and energy calibration.

Chapter 6 presents a detailed study of cosmic-ray muons in the DUNE FD, commencing with an overview of cosmic-ray muons produced in the Earth's atmosphere and further discusses the cosmic-ray muons at the Earth's surface. Cosmic muons are produced and simulated in the DUNE FD using the MUSUN generator. The analysis focuses on angular and energy distributions of generated muons and those entering the DUNE FD. The study also presents the energy deposition in the liquid argon by muons, along with the analysis of different particles produced in the liquid argon. The event display of cosmic muons is showcased through CRC and NRC, demonstrating the effectiveness of particle reconstruction in the DUNE FD.

Chapter 7 presents the neutral pion analysis for the DUNE FD, delving into the complexities of reconstructing showers produced by neutral pions originating from cosmic-ray muons. The chapter covers Monte Carlo simulations, reconstruction studies, and a detailed analysis of invariant mass reconstruction of neutral pion, contributing to the effectiveness of shower reconstruction. The neutral pion is then successfully reconstructed in the DUNE FD, allowing for electromagnetic shower energy calibration.

In Chapter 8, the focus turns to calibrating the DUNE FD using cosmic-ray muons. The chapter outlines the two developed calibration methods for stopping muons, charged pions, and protons, providing an accurate conversion of charge to energy. Moreover, the validation of these procedures is performed through comparisons with theoretical predictions, ensuring the precision and reliability of the calibration process.

In Chapter 9 of this thesis, a summary of the research findings is provided, focusing on three main areas important to the DUNE experiment: cosmic-ray muons, neutral pion analysis, and energy calibration for the DUNE FD. The chapter presents key results from the generation and simulation of cosmic-ray muons, including analysis of their angular and energy distributions, evaluation of various reconstruction algorithms, and production statistics of different particles in the DUNE FD. Moreover, it discusses the implications of neutral pion analysis, particularly regarding the reconstructed mass of neutral pions and its significance for DUNE's sensitivity to shower energy and, consequently, neutral pion reconstruction. Furthermore, the chapter highlights the results of two energy calibration methods, emphasizing their precision, reliability, and critical role in calibrating LArTPC detectors essential to the success of the DUNE experiment. Overall, these findings underscore the importance of this study in advancing the goals and capabilities of the DUNE experiment.

Chapter 2

Neutrinos

This chapter provides a concise exploration of neutrinos, starting with the introduction and discovery of neutrinos. Section 2.2 briefly overviews neutrinos within the standard model. Section 2.3 discusses various types of neutrino interactions, exploring the underlying mechanisms. Section 2.4 focuses on neutrino oscillations, covering the theoretical formulation in a vacuum and briefly discussing the impact of matter on neutrino oscillations. A brief discussion on CP violation and the neutrino mass hierarchy is also included in this section. Section 2.5 discusses the measurement of oscillation parameters in various experiments. Finally, Section 2.6 briefly discusses the current and future neutrino experiments.

2.1 Introduction and discovery of the neutrinos

Neutrinos are the most abundant massive fundamental particles in the universe. Despite their abundance, they are among the least understood particles within the standard model (SM). Within the SM, neutrinos are among the most intriguing particles, as they display flavour oscillations, which constitute one of the earliest observed phenomena that extend beyond the standard model [5]. Neutrinos are characterised by their remarkably low interaction probabilities, allowing them to effortlessly traverse vast amounts of matter without being stopped. This property offers potential insights into the origin of the universe. Neutrinos interact via the weak force or gravity, posing a significant challenge for their detection and study, given their electrically neutral nature. Neutrino presence is everywhere, with approximately 100 trillion neutrinos passing through the human body every second [6]. Natural sources of neutrinos include stars (including the Sun), supernovae, the Earth's atmosphere, and radioactive decay. By studying neutrinos, we have the potential to answer one of the most significant open questions: 'Why is the matter more than antimatter in the observable universe?' and, most fundamentally, to understand our existence [1, 2].

The existence of neutrinos was first indicated by observing a continuous spectrum of electrons in β-decay of radioactive elements by J. Chadwick [7, 8] in 1914. This unexpected observation contradicted the principle of energy conservation [9]. A sharp peak of electron energy was expected in two-body decay. Therefore, this result was initially met with scepticism, with some suggesting it could be due to experimental or theoretical artefacts [10]. However, after a thirteen-year wait, in 1927, Ellis and Wooster [11] conducted an experiment on Radium E (now known as ^{210}Bi), providing direct evidence that the electron spectrum was continuous. In 1930, Wolfgang Pauli proposed the existence of a third particle emitted alongside the electron in β-decay [8] and initially named it a 'neutron'. Later, it was renamed 'neutrino' by E. Fermi. Pauli's proposal resolved the issue of the continuous spectrum and preserved the conservation law.

In 1934, Enrico Fermi [12] proposed a theory of β-decay, assuming β-decay is a process where neutrons decay into electrons, protons and neutrinos. Fermi also assumed that the nucleus is composed of protons and neutrons only with 1/2 spin each. At the time of Pauli's proposal of the neutrino, the nucleus was believed to be composed of protons and electrons only. Neutron was discovered in 1932 by Chadwick [13]. This theory resolved the problem of the continuous energy spectrum of electrons, preserved the conservation laws and correctly explained the nuclear structure.

After 22 years since Fermi's theory, in 1956, the neutrino was experimentally observed by Reines and Cowan in their famous experiment at the Savannah River Plant in South Carolina, USA [14]. The experiment measured the positron and neutron produced in the interaction of an antineutrino with a proton in the inverse β-decay process:

$$\bar{\nu}_e + p \rightarrow n + e^+. \tag{2.1}$$

The nuclear reactor served as the source of antineutrinos. By comparing the rate of neutrino events to the detection rate when the reactor was shut down, Reines and Cowan were able to identify a significant excess of events, ultimately leading to their groundbreaking discovery.

In the late 1950s, Davis and Harmer conducted an experimental test to address whether neutrinos and antineutrinos are identical particles [6]. Based on the findings of Reines and Cowan, the cross-reaction

$$\nu_e + n \rightarrow p + e^- \tag{2.2}$$

must occur at the same rate as the process described in Equation 2.1. Davis looked for similar reactions using antineutrinos

$$\bar{\nu}_e + n \rightarrow p + e^-. \tag{2.3}$$

However, this does not occur, concluding that neutrinos and antineutrinos are distinct particles.

In 1962, Lederman, Schwartz, Steinberger and their collaborators [15] conducted an experiment using antineutrinos from π^- decay and observed the interaction

$$\bar{\nu}_\mu + p \rightarrow \mu^+ + n, \tag{2.4}$$

but not a single interaction

$$\bar{\nu}_\mu + p \rightarrow e^+ + n, \tag{2.5}$$

was observed, which confirmed the evidence of a second type of neutrino, "muon neutrino" [6].

In 2000, the Direct Observation of the Nu Tau (DONUT) experiment conducted at Fermilab detected the final type of neutrino, known as the tau neutrino [16]. This observation was achieved by detecting tau leptons generated through a neutrino beam, as anticipated since the discovery of the tau lepton.

In 1968, Ray Davis *et. al.* [17] led an experiment to detect electron neutrinos produced by the Sun (solar neutrinos). This experiment took place deep underground at the Homestake Gold Mine in South Dakota to remove backgrounds from cosmic rays. The detector measured only about one-third of solar neutrinos predicted by the standard solar model (SSM) [18, 19], this is known as the solar neutrino problem. To address the issue, Bruno Pontecorvo suggested that the electron neutrinos originating from the Sun might transform during their journey, changing into a distinct type of neutrino, such as muon neutrinos, to which Davis's experiment was not sensitive [20]. Several experiments have been conducted to detect solar neutrinos following the Homestake experiment, as mentioned in Section 2.5. In 2002, the Sudbury Neutrino Observatory (SNO) provided key insights and confirmed solar neutrino oscillations [21]. Unlike Davis' experiment, SNO had the capability to detect all three types of neutrinos.

Atmospheric neutrinos originate from the decay processes of muons and charged pions generated through collisions involving primary cosmic-ray protons in the Earth's atmosphere. The Super-Kamiokande (Super-K) experiment [22] conducted research on atmospheric neutrinos following the Kamiokande experiment [23] and similarly observed evidence of oscillations in 1998. Other notable experiments on atmospheric neutrino oscillations are mentioned in Section 2.5. The Super-K examined the neutrino flux from various angles and noted that neutrinos arriving directly from above followed the expected flavour ratio of 2:1 for muon and electron neutrinos. However, those coming from the opposite side of the Earth did not exhibit this pattern. These observations strongly suggest that neutrinos travelling longer distances had a higher tendency to transform into another flavour, confirming the phenomenon of neutrino oscillation.

2.2 Neutrinos in the Standard Model

The Standard Model (SM) of particle physics [24, 25, 26] is based on the framework of quantum field theory [27] and explains the strong, electromagnetic and weak interactions of elementary particles. The neutrinos in the SM are described by the electroweak (EW) theory (unification of electromagnetic and weak interaction) based on gauge $SU(2) \times U(1)$ symmetry. The weak interactions are mediated by the $SU(2)$ gauge bosons, which include the charged $W^{\pm}$ and the neutral Z^0. The electromagnetic interaction is mediated by photons described by $U(1)$.

Fermions, such as neutrinos, which have half-integer spin, are governed by the $SU(2) \times U(1)$ theory. They are characterised by four component fields ψ (spinors) that satisfy the Dirac equation. The four distinct components of ψ describe the particle and antiparticle. These particles and antiparticles can have two spin projections $\boldsymbol{S} = \pm 1/2$. The Dirac spinor ψ can be expressed in terms of a two-component spinor [27]:

$$\psi = \begin{pmatrix} \psi_L \\ \psi_R \end{pmatrix} \tag{2.6}$$

The two-component objects ψ_R and ψ_L are called right-handed and left-handed Weyl spinors. The ψ_L and ψ_R are chosen using γ^5 matrix[1]

$$\psi_L = P_L \psi, \quad \psi_R = P_R \psi, \tag{2.7}$$

---

[1] The γ^5 matrix used in this chapter is a preferred choice for the study of relativistic particles such as neutrinos. Other representations of γ^5 matrices exist that satisfy the anticommutation relation $\{\gamma^\mu, \gamma^\nu\} = 2g^{\mu\nu}$ [28].

where $P_L = \frac{(1-\gamma^5)}{2}$ and $P_R = \frac{(1+\gamma^5)}{2}$ are projection operators and γ^5 is

$$\gamma^5 = \begin{pmatrix} I & 0 \\ 0 & -I \end{pmatrix}, \tag{2.8}$$

and I is a 2 × 2 unity matrix.

In the standard model, the neutrino fields have only left-handed components [28, 29, 30]. The left-handed charged lepton (l_L) and neutrino fields (ν_{lL}) are doublets of the $SU(2)$ group

$$\psi_{lL} = \begin{pmatrix} \nu_{lL} \\ l_L \end{pmatrix}, \tag{2.9}$$

where $l = e, \mu, \tau$. The right-handed components of charged lepton fields are singlets of the group. The neutrino fields enter the SM Lagrangian for charge and neutral current interactions. The standard weak interactions of neutrinos result from the interaction between leptons and the W and Z vector bosons, which are defined by the interaction component of the standard model Lagrangian. These interactions are called the charged current (CC) and neutral current (NC) interaction Lagrangians

$$\mathcal{L}^l_{\mathrm{CC}} = -\frac{g}{2\sqrt{2}} j^\rho_{\mathrm{CC}} W_\rho + \text{h.c.}, \tag{2.10}$$

$$\mathcal{L}^l_{\mathrm{NC}} = -\frac{g}{2\cos\theta_W} j^\rho_{\mathrm{NC}} Z_\rho, \tag{2.11}$$

where θ_W is the Weinberg angle given as $\tan\theta_W = g/g^{'}$, g and $g^{'}$ are the coupling constants (strength of the electroweak interactions) associated with the group $SU(2)$ and $U(1)$ respectively [28]. The Weinberg angle is the fundamental parameter of the electroweak theory and mixes the gauge fields of $SU(2)$ and $U(1)$ and also called mixing angle. W_ρ and Z_ρ are the fields of the $W^\pm$ and Z^0 vector bosons. The notation 'h.c.' denotes the Hermitian conjugate. The leptonic charge current j^ρ_{CC} and neutrino neutral current j^ρ_{NC} are given by

$$j^\rho_{\mathrm{CC}} = 2 \sum_{l=e,\mu,\tau} \bar{\nu}_{lL} \gamma^\rho l_L, \tag{2.12}$$

$$j^\rho_{\mathrm{NC}} = \sum_{l=e,\mu,\tau} \bar{\nu}_{lL} \gamma^\rho \nu_{lL}, \tag{2.13}$$

where γ^ρ ($\rho = 0, 1, 2, 3$) is gamma matrices [28]. The various types of neutrino CC and NC interactions are discussed in Section 2.3.

In the SM, neutrinos are considered massless [30]. This characteristic is a consequence of the fact that, within the SM framework, neutrinos are described solely by the left-handed chiral fields ν_{eL}, $\nu_{\mu L}$, $\nu_{\tau L}$. The corresponding right-handed fields ν_{eR}, $\nu_{\mu R}$, and $\nu_{\tau R}$ do not exist in the SM. Neutrino mass is included in the SM with the Dirac mass term generated by the Higgs mechanism, assuming right-handed singlet neutrino fields also enter into the SM. In this case, the neutrino mass term in the Lagrangian takes the form:

$$\mathcal{L}^{\mathrm{D}} = -\sum_{l,l'} \bar{\nu}_{lR} M^{D}_{ll'} \nu_{l'L} + \text{h.c.}, \tag{2.14}$$

where $l', l = e, \mu, \tau$ and M^D is a complex 3×3 matrix. M^D can be diagonalised [29] by unitary transformation

$$M^D = V \hat{m}\, U^{\dagger}, \tag{2.15}$$

where V and U are 3×3 unitary matrices. $\hat{m}$ is a diagonal matrix with positive eigenvalues expressed as $\hat{m_{kj}} = m_k \delta_{kj}$, where $k, j = 1, 2, 3$ are matrix indices. Thus, the Dirac mass term takes the form

$$\mathcal{L}^{\mathrm{D}} = -\sum_{k=1}^{3} m_k \bar{\nu}_k \nu_k \tag{2.16}$$

with ν_{lL} and ν_{lR} mentioned in Equation 2.14 are

$$\nu_{lL} = -\sum_{k=1}^{3} U_{lk} \nu_{kL}, \tag{2.17}$$

$$\nu_{lR} = -\sum_{k=1}^{3} V_{lk} \nu_{kR}, \tag{2.18}$$

where $l = e, \mu, \tau$.
Hence, considering the Dirac mass term (Equation 2.14), the three neutrino flavour fields $\nu_{lL}(l = e, \mu, \tau)$ are constructed as linear combinations of the left-handed components ν_{kL} (Equation 2.17) of three fields of neutrinos (neutrino mass states) with masses $m_k(k = 1, 2, 3)$. The unitary mixing matrix U in Equation 2.17 mixes flavour states and mass states of neutrinos. The matrix U is called the Pontecorvo-Maki-Nakagawa-Sakata (PMNS) mixing matrix, leading to neutrino oscillations. Neutrino oscillations are discussed in detail in Section 2.4.

The presence of a Dirac mass term (Equation 2.14) for the neutrino suggests the existence of a right-handed neutrino. In the standard weak interaction, right-handed fields of neutrinos (Equation 2.18) are not observed. As a result, these right-handed singlets are considered sterile or, in other words, serve the purpose of providing mass to the neutrinos without engaging in electroweak interactions.

Alternatively, a neutrino can be described as a Majorana neutrino. A Majorana fermion is considered to have identical particle and antiparticle states. In simpler terms, charge conjugation has no impact on a Majorana fermion field. This chapter does not discuss the theory related to Majorana neutrino; a detailed discussion can be found in [31, 28].

2.3 Neutrino interactions

2.3.1 Introduction to neutrino interactions

Neutrinos interact with other particles through the weak force mediated by the $W^{\pm}$ boson or Z^0 boson. Neutrino interactions mediated by a charged W and neutral Z are called charge current (CC) and neutral current (NC) interactions, respectively. Example Feynman diagrams of these interactions are shown in Figure 2.1. Neutrino interactions are identified by detecting secondary particles produced in neutrino interactions.

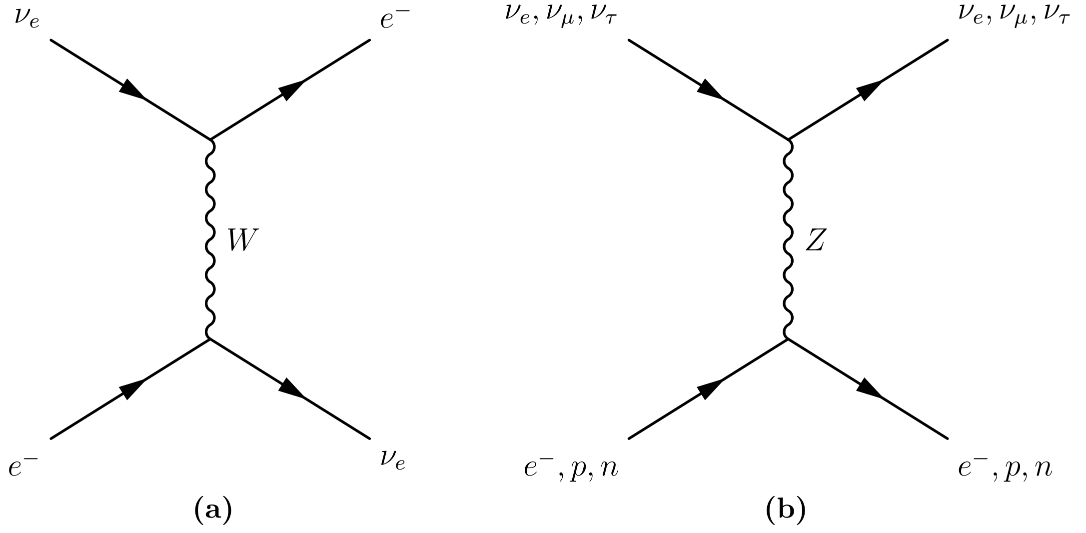

Figure 2.1. Example Feynman diagrams of neutrino interactions in matter: a) charged current (CC) interaction for ν_e mediated by a W boson, b) neutral current (NC) interaction for three flavours of neutrinos mediated by a neutral Z boson [28].

In long-baseline oscillation experiments, neutrino energies range from approximately 0.1 to 10 GeV [32], and various neutrino interaction channels become relevant. Charged current channels are of particular significance because they involve charged leptons in the final state, essential for flavour tagging. These are discussed in Section 2.3.3. Consequently, CC interactions allow for a reasonably accurate estimation of neutrino energy. On the other hand, neutral current channels do not leave behind any flavour information and typically result in missing energy, as neutrino exits the detector without detection. Therefore, NC interactions can introduce backgrounds in oscillation measurements, necessitating careful event selection strategies to mitigate them. However, it is worth noting that NC events can serve other experimental purposes, such as particles like pions for calibrating detectors.

These two interactions, CC and NC, are subdivided into elastic, quasielastic (QE), resonant (RES), deep inelastic (DIS), and coherent (COH), etc., scattering according to the nature of the interactions and energy of neutrino as shown in Figure 2.2. A concise description of each of these interaction types is provided in the following discussion.

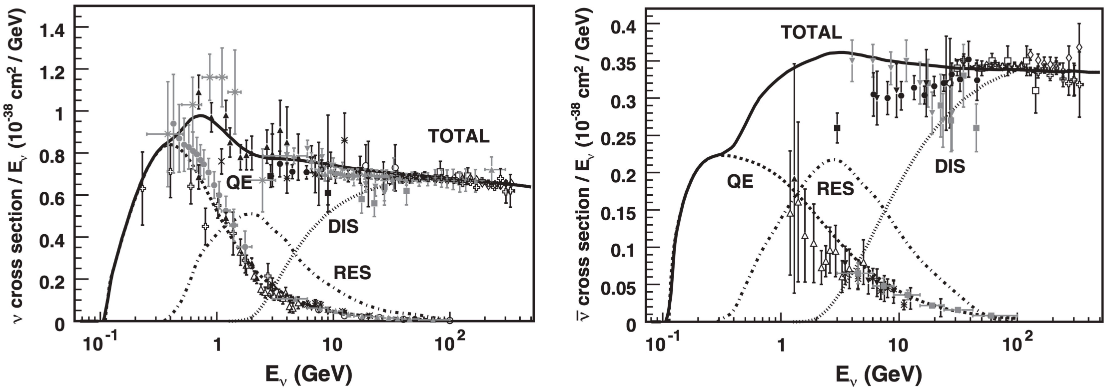

(a) (b)

Figure 2.2. The total and individual cross sections of different types of charged-current interactions for an isoscalar target: a) neutrinos and b) antineutrinos. The plots show normalised cross sections as a function of neutrino energy. In the figure, various processes are indicated: quasielastic (QE) scattering, represented by dashed lines; resonant scattering (RES), shown with dotted-dashed lines; and deep inelastic scattering (DIS), denoted by dotted lines. The figure is taken from Ref. [33].

2.3.2 Neutral current interactions

In a neutral current interaction, the final state (anti)neutrino remains the same as the incoming (anti)neutrino interacting with the target nucleus [34]:

$$\nu_l(\bar{\nu}_l) + A \rightarrow \nu_l(\bar{\nu}_l) + X, \tag{2.19}$$

where $l = e, \mu, \tau$, A is the nucleus, and X is the hadronic final state. The NC interaction is further classified as [28, 33]:

1. **Elastic scattering:** Neutrinos and antineutrinos can undergo elastic scattering with both protons and neutrons within the target material

   $$\nu_l(\bar{\nu}_l) + N \rightarrow \nu_l(\bar{\nu}_l) + N, \tag{2.20}$$

   where $N = p, n$.

   Low-energy neutrinos and antineutrinos also interact with electrons elastically

   $$\nu_l(\bar{\nu}_l) + e^- \rightarrow \nu_l(\bar{\nu}_l) + e^-. \tag{2.21}$$

   This type of neutrino interaction has no threshold because the final state is identical to the initial state. The primary effect redistributes the total energy and momentum between the two participating particles in this process. These interactions are the most straightforward to model, and, as a result, they are often employed to investigate fundamental form factors and nuclear models.

2. **Resonant scattering (RES):** At high energy ($>$ ~1 GeV), the neutrino has more energy to transfer to the target, and thus nucleons get excited to a baryon resonance (N^*), for example, a Δ baryon. These resonance states subsequently undergo a decay process, primarily leading to the emission of a pion. However, the specific outcomes can vary, depending upon the type of resonance involved, and may include kaons or multiple pions. The resonant single pion production is given as [33, 35]:

   $$\begin{aligned} \nu_\mu(\bar{\nu}_\mu) + N \rightarrow \nu_\mu(\bar{\nu}_\mu) + &N^*, \\ &N^* \rightarrow \pi + N^{'}, \end{aligned} \tag{2.22}$$

   where $N, N^{'} = n, p$. A few examples of neutral current nuclear resonance are:

   $$\nu_\mu + p \rightarrow \nu_\mu + p + \pi^0, \quad \bar{\nu}_\mu + p \rightarrow \bar{\nu}_\mu + p + \pi^0. \tag{2.23}$$

   $$\nu_\mu + p \rightarrow \nu_\mu + n + \pi^+, \quad \bar{\nu}_\mu + p \rightarrow \bar{\nu}_\mu + n + \pi^+. \tag{2.24}$$

3. **Coherent scattering:** In addition to resonance production, at low four-momentum transfers, there exists the possibility that the neutrino interacts not only with an individual nucleon but interacts coherently with the entire nucleus, transferring negligible energy to the target nucleus (A) and produces a single pion in the final state. This phenomenon is known as coherent

scattering (COH). Most of the single pion coherent scattering is measured at energy >∼2 GeV. Examples of NC coherent pion production are [33]:

$$\nu_\mu + A \rightarrow \nu_\mu + A + \pi^0, \tag{2.25}$$

$$\bar{\nu}_\mu + A \rightarrow \bar{\nu}_\mu + A + \pi^0. \tag{2.26}$$

4. **Deep inelastic scattering:** At high energy (>∼ 20 GeV), (anti)neutrinos can also interact with nucleons through the process called NC deep inelastic scattering (DIS). In this process, (anti)neutrinos can probe the individual quark constituents within the nucleon. During this process, the (anti)neutrino interacts with a quark in the nucleon by exchanging a Z^0 boson, resulting in a (anti)neutrino and hadron(s). Quarks quickly recombine, resulting in a hadronic shower [28, 33]:

$$\nu_l(\bar{\nu}_l) + N \rightarrow \nu_l(\bar{\nu}_l) + X, \tag{2.27}$$

where $l = e, \mu, \tau$, $N = p, n$, and X is set of hadrons.

2.3.3 Charge current interactions

In a charged current interaction, the incoming (anti)neutrino interacts with the target nucleus and transforms into a charged partner lepton [34]:

$$\nu_l(\bar{\nu}_l) + A \rightarrow l^-(l^+) + X, \tag{2.28}$$

where $l = e, \mu, \tau$, A is the nucleus, and X is hadronic system.

The CC interaction is further classified as [28, 33, 34]:

1. **Quasielastic scattering:** At momentum transfer above ∼500 MeV, neutrinos and antineutrinos interact with nucleons via a process called quasielastic (QE) charge current interaction. In this process, a neutrino or antineutrino scatters off a nucleon and has lepton and a single nucleon in the final state

$$\begin{aligned} \nu_l + n &\rightarrow p + l^-, \\ \bar{\nu}_l + p &\rightarrow n + l^+, \end{aligned} \tag{2.29}$$

where $l = e, \mu, \tau$.

The neutrinos interact mainly through the QE process for energy $E_\nu <\sim 2$ GeV. As a result, they serve as a source of signal events in neutrino oscillation experiments that operate within this energy range. The dominant CCQE interactions are:

$$\begin{aligned} \nu_\mu + n &\to p + \mu^-, \\ \bar{\nu}_\mu + p &\to n + \mu^+. \end{aligned} \tag{2.30}$$

Muon neutrinos with energy above the muon production threshold can interact with electrons through CCQE interaction and produce a muon in the final state

$$\nu_\mu + e^- \to \nu_e + \mu^-. \tag{2.31}$$

This process is also known as inverse muon decay.

2. **Resonant scattering (RES):** The process of charge current resonant scattering is similar to NC resonant scattering. The difference is that the neutrino transforms into the charged partner lepton. At energy greater than ~ 1 GeV, the charge current resonant single pion production is measured. The process can be described as [33, 35]:

$$\begin{aligned} \nu_\mu(\bar{\nu}_\mu) + N \to \mu^-(\mu^+) \ \ + \ \ & N^* \\ & N^* \to \pi + N^{'}, \end{aligned} \tag{2.32}$$

where $N^{'}, N = n, p$. A few examples of charge current nuclear resonance are:

$$\nu_\mu + p \to \mu^- + p + \pi^+ \quad \bar{\nu}_\mu + n \to \mu^+ + n + \pi^- \tag{2.33}$$

$$\nu_\mu + n \to \mu^- + p + \pi^0 \quad \bar{\nu}_\mu + p \to \mu^+ + n + \pi^0 \tag{2.34}$$

3. **Coherent scattering:** In addition to resonance production, charge current coherent pion production is also possible at low 4-momentum transfer. The coherent scattering is mostly observed at an energy greater than ~2 GeV. The mechanism is similar to the NC coherent scattering, except that a charged partner lepton is produced in the final state. Examples of CC coherent pion production are [33]:

$$\nu_\mu + A \to \mu^- + A + \pi^+ \tag{2.35}$$

$$\bar{\nu}_\mu + A \to \mu^+ + A + \pi^- \tag{2.36}$$

4. **Deep inelastic scattering:** At high energies (>∼ 20 GeV), where the neutrino energy significantly exceeds the nucleon mass, CC neutrino-nucleon interactions are primarily governed by deep inelastic scattering (DIS) processes. This process can be described as follows [28, 33]:

$$\begin{aligned} \nu_l + N &\rightarrow l^- + X, \\ \bar{\nu}_l + N &\rightarrow l^+ + X, \end{aligned} \tag{2.37}$$

   where $l = e, \mu, \tau,\ N = p, n$ and X is set of hadrons. The deep inelastic scattering processes are particularly significant at high energies for studying neutrino interactions with nucleons. They provide valuable insights into the internal structure of nucleons and the dynamics of strong interactions in high-energy neutrino experiments.

2.4 Neutrino oscillations

Neutrino oscillation is the phenomenon of neutrino changing flavour while travelling through vacuum or matter. Neutrino oscillation was proposed by B. Pontecorvo in 1957-58 [36, 37] and developed by Maki, Nakagawa, and Sakata in 1962 [38]. The evidence of neutrino mixing was observed in the experiment by the Super-K [22] and SNO [39, 40] experiments, for which Takaaki Kajita (Super-Kamiokande) and Arthur McDonald (SNO) received the Nobel Prize in 2015 for the discovery of neutrino oscillations. When neutrinos are produced, they have defined flavour eigenstates, the eigenstates of the weak interaction. When they propagate, flavour states form a linear superposition of the states with definite momenta known as mass eigenstates. Neutrino oscillations are the consequence of differences in neutrino flavour and mass eigenstates. The flavour and mass eigenstates are related by mixing matrix U, as stated in Equation 2.17.

2.4.1 Neutrino oscillations in vacuum

The neutrino flavour states $(\nu_e, \nu_\mu, \nu_\tau)$ and mass states (ν_1, ν_2, ν_3) are related as

$$\begin{pmatrix} \nu_e \\ \nu_\mu \\ \nu_\tau \end{pmatrix} = U \begin{pmatrix} \nu_1 \\ \nu_2 \\ \nu_3 \end{pmatrix}, \tag{2.38}$$

where

$$U = \begin{pmatrix} U_{e1} & U_{e2} & U_{e3} \\ U_{\mu 1} & U_{\mu 2} & U_{\mu 3} \\ U_{\tau 1} & U_{\tau 2} & U_{\tau 3} \end{pmatrix}. \tag{2.39}$$

The matrix U is a 3×3 matrix that satisfies the unitary condition: $UU^\dagger = I$, where I is an identity matrix of order 3. The U is parameterised using three mixing angles $(\theta_{12}, \theta_{13}, \theta_{23})$ and one phase δ, given as [28, 29]

$$U = R_{23}(\theta_{23}) \mathit{\Gamma}_\delta R_{13}(\theta_{13}) \mathit{\Gamma}_\delta^\dagger R_{12}(\theta_{12}) \tag{2.40}$$

where

$$\begin{aligned} R_{23}(\theta_{23}) &= \begin{pmatrix} 1 & 0 & 0 \\ 0 & \cos\theta_{23} & \sin\theta_{23} \\ 0 & -\sin\theta_{23} & \cos\theta_{23} \end{pmatrix}, \\ R_{13}(\theta_{13}, \delta) = \mathit{\Gamma}_\delta R_{13} \mathit{\Gamma}_\delta^\dagger &= \begin{pmatrix} \cos\theta_{13} & 0 & \sin\theta_{13} e^{-i\delta} \\ 0 & 1 & 0 \\ -\sin\theta_{13} e^{i\delta} & 0 & \cos\theta_{13} \end{pmatrix}, \\ R_{12}(\theta_{12}) &= \begin{pmatrix} \cos\theta_{12} & \sin\theta_{12} & 0 \\ -\sin\theta_{12} & \cos\theta_{12} & 0 \\ 0 & 0 & 1 \end{pmatrix}, \\ \mathit{\Gamma}_\delta &= \mathrm{diag}(e^{-i\delta}, 1, 1). \end{aligned} \tag{2.41}$$

R_{12}, R_{13}, R_{23} are 3-dimensional rotational matrices. $\mathit{\Gamma}_\delta$ is related to CP-violation. The rotation matrices are defined in such a way that mixing angles are real and defined in the interval $[0, \pi/2]$. The CP-violating phase may vary in the range $\delta \in [0, 2\pi]$. The matrix (R_{12}) that incorporates θ_{12} is commonly known as the solar mixing matrix, with its parameters primarily established through solar neutrino experiments. Similarly, the matrix (R_{23}) encompassing θ_{23} is denoted as the atmospheric mixing matrix. The reactor matrix (R_{13}) comprises θ_{13} and the phase δ_{CP}.

The PMNS matrix can be expressed in terms of rotational matrix elements as

$$U = \begin{pmatrix} c_{12}c_{13} & s_{12}c_{13} & s_{13}e^{-i\delta} \\ -s_{12}c_{23} - c_{12}s_{23}s_{13}e^{i\delta} & c_{12}c_{23} - s_{12}s_{23}s_{13}e^{i\delta} & s_{23}c_{13} \\ s_{12}s_{23} - c_{12}c_{23}s_{13}e^{i\delta} & -c_{12}s_{23} - c_{12}c_{23}s_{13}e^{i\delta} & c_{23}c_{13} \end{pmatrix} \tag{2.42}$$

where $c_{ij} = \cos\theta_{ij}$ and $s_{ij} = \sin\theta_{ij}$. This is the parameterisation given by Particle Data Group [41]. In the case of Majorana neutrino, in which neutrinos are their own antiparticles, the matrix U of Equation 2.42 will contain two additional phases and need to be multiplied to the right by an additional diagonal matrix

$$U_{\text{Majorana}} = U \times \text{diag}(1, e^{\phi_1}, e^{\phi_2}). \tag{2.43}$$

A neutrino created in charge-current weak interaction with flavour α and momentum $\vec{p}$ is described by flavour state $|\nu_\alpha\rangle$. A pure flavour state can be written as a superposition of mass eigenstates $|\nu_k\rangle$,

$$|\nu_\alpha\rangle = \sum_{k=1}^{3} U^*_{\alpha k}|\nu_k\rangle, \tag{2.44}$$

where $|\nu_\alpha\rangle$ with $\alpha = e, \mu, \tau$ are the three known active neutrino flavour states and $|\nu_k\rangle$ with $k = 1, 2, 3$ are the neutrino mass states. The flavour and mass states satisfy orthonormality conditions:

$$\begin{aligned} \langle\nu_\alpha|\nu_\beta\rangle &= \delta_{\alpha\beta}, \\ \langle\nu_k|\nu_j\rangle &= \delta_{kj}. \end{aligned} \tag{2.45}$$

The Kronecker delta, δ_{ij}, is defined as:

$$\delta_{ij} = \begin{cases} 1, & \text{if } i = j, \\ 0, & \text{if } i \neq j. \end{cases} \tag{2.46}$$

The mass states of neutrino $|\nu_k\rangle$ are eigenstate of the Hamiltonian $\hat{H}$,

$$\hat{H}|\nu_k\rangle = E_k|\nu_k\rangle, \tag{2.47}$$

The energy eigenvalue of the above equation is given by

$$E_k = \sqrt{|\vec{p}|^2 + m_k^2} \tag{2.48}$$

Here, $\vec{p}$ and m_k are the momentum and mass of the neutrino state, respectively. This chapter uses natural units ($c = \hbar = 1$).

The time-dependent Schrodinger equation for massive neutrino state $|\nu_k\rangle$

$$i\frac{\mathrm{d}}{\mathrm{d}t}|\nu_k(t)\rangle = \hat{H}|\nu_k(t)\rangle \quad \text{(in natural unit, } \hbar = 1) \tag{2.49}$$

leads to the fact that the quantum state $|\nu_k\rangle$ evolves with time as:

$$|\nu_k(t)\rangle = e^{-iE_k t}|\nu_k\rangle. \tag{2.50}$$

Using 2.44 and 2.50, the time evolution of flavour state $|\nu_\alpha\rangle$ can be written as

$$|\nu_\alpha(t)\rangle = \sum_{k=1}^{3} U^*_{\alpha k} e^{-iE_k t}|\nu_k\rangle. \tag{2.51}$$

At time $t = 0$, a neutrino is created with a definite pure flavour α such that

$$|\nu_\alpha(t = 0)\rangle = \sum_{k=1}^{3} U^*_{\alpha k}|\nu_k\rangle = |\nu_\alpha\rangle \quad \text{(from Equation 2.44)} \tag{2.52}$$

The unitarity condition satisfies the conditions

$$\begin{aligned} &U^\dagger U = I, \\ &\sum_\alpha U^*_{\alpha k} U_{\alpha j} = \delta_{jk} \end{aligned} \tag{2.53}$$

and

$$\begin{aligned} &U U^\dagger = I, \\ &\sum_k U_{\alpha k} U^*_{\beta k} = \delta_{\alpha\beta}. \end{aligned} \tag{2.54}$$

A derivation of unitary conditions is carried out in Appendix A.1. The massive neutrino states $|\nu_k\rangle$ can be written in terms of flavour states $|\nu_\alpha\rangle$ using Equation 2.44, 2.53 and 2.46 as:

$$|\nu_k\rangle = \sum_{\alpha=1}^{3} U_{\alpha k}|\nu_\alpha\rangle. \tag{2.55}$$

The time-evolved flavour state $|\nu_\alpha\rangle$ in Equation 2.51 can be expressed in terms of flavour state using Equation 2.55

$$|\nu_\alpha(t)\rangle = \sum_{\beta=e,\mu,\tau} \left(\sum_{k=1}^{3} U^*_{\alpha k} e^{-iE_k t} U_{\beta k} \right) |\nu_\beta\rangle. \tag{2.56}$$

In Equation 2.56, $|\nu_\alpha(t)\rangle$ which is the superposition of massive neutrino state, and is a pure flavour state at $t = 0$ as mentioned in Equation 2.52, becomes a superposition of different flavour states at time t.

Thus, the amplitude of flavour change $\nu_\alpha \to \nu_\beta$ is given as

$$A_{\nu_\alpha \to \nu_\beta}(t) \equiv \langle \nu_\beta | \nu_\alpha(t) \rangle = \sum_{k=1}^{3} U^*_{\alpha k} e^{-iE_k t} U_{\beta k} \tag{2.57}$$

The probability of observing a flavour state $|\nu_\beta\rangle$ at time t evolving from a flavour state $|\nu_\alpha\rangle$ at $t = 0$ is determined as

$$\begin{aligned} P_{\nu_\alpha \to \nu_\beta}(t) &= \left| A_{\nu_\alpha \to \nu_\beta}(t) \right|^2 = \left| \langle \nu_\beta | \nu_\alpha(t) \rangle \right|^2 \\ &= \left(\langle \nu_\beta | \nu_\alpha(t) \rangle \right) \left(\langle \nu_\beta | \nu_\alpha(t) \rangle \right)^* \\ &= \left(\sum_k U^*_{\alpha k} e^{-iE_k t} U_{\beta k} \right) \left(\sum_j U^*_{\alpha j} e^{-iE_j t} U_{\beta j} \right)^* \\ &= \sum_{k,j} U^*_{\alpha k} U_{\beta k} U_{\alpha j} U^*_{\beta j} e^{-i(E_k - E_j)t}. \end{aligned} \tag{2.58}$$

In the case of ultrarelativistic neutrinos ($m_k/p \ll 1$), Equation 2.48 can be approximated as

$$E_k \simeq E + \frac{m_k^2}{2E}, \tag{2.59}$$

where

$$E = |\vec{p}| \tag{2.60}$$

is the neutrino energy, ignoring the mass term. Hence, the difference in energy eigenvalue of k and j mass state can be approximated as

$$E_k - E_j \simeq \frac{\Delta m^2_{kj}}{2E}, \tag{2.61}$$

where $\Delta m^2_{kj} \equiv m_k^2 - m_j^2$. The probability in Equation 2.58 can be written as

$$P_{\nu_\alpha \to \nu_\beta}(t) = \sum_{k,j} U^*_{\alpha k} U_{\beta k} U_{\alpha j} U^*_{\beta j} \exp\left(-i \frac{\Delta m^2_{kj} t}{2E} \right). \tag{2.62}$$

The above equation uses natural units where $c = \hbar = 1$. In neutrino oscillation experiments such as DUNE [1], the length or baseline L is measured between the source and the detector instead of the propagation time t. The propagation time can be approximated as $t = L$ (in natural units, $c = 1$), considering the ultrarelativistic neutrino travels nearly equal to the speed of light. Hence, Equation 2.62 can be expressed as

$$P_{\nu_\alpha \to \nu_\beta}(t) = \sum_{k,j} U^*_{\alpha k} U_{\beta k} U_{\alpha j} U^*_{\beta j} \ \exp\left(-i \frac{\Delta m^2_{kj} L}{2E}\right). \tag{2.63}$$

The phase of the neutrino oscillations, which depend on the experimental parameters L and E is defined as

$$\varPhi_{kj} = -\frac{\Delta m^2_{kj} L}{2E}. \tag{2.64}$$

The squared mass difference Δm^2_{kj} is a physical constant.

Equation 2.63 can be expressed in terms of real and imaginary parts. A derivation for the expression of oscillation probability is carried out in Appendix A.1. A simplified expression of oscillation probability can be written as

$$\begin{aligned} P_{\nu_\alpha \to \nu_\beta}(L,E) = \delta_{\alpha\beta} &- 4 \sum_{k>j} \mathcal{R}e\left[U^*_{\alpha k} U_{\beta k} U_{\alpha j} U^*_{\beta j}\right] \sin^2\left(\frac{\Delta m^2_{kj} L}{4E}\right) \\ &+ 2 \sum_{k>j} \mathcal{I}m\left[U^*_{\alpha k} U_{\beta k} U_{\alpha j} U^*_{\beta j}\right] \sin\left(\frac{\Delta m^2_{kj} L}{2E}\right). \end{aligned} \tag{2.65}$$

A similar expression for the oscillation probability of antineutrinos can be deduced starting with the equation

$$|\bar{\nu}_\alpha\rangle = \sum_{k=1}^{3} U_{\alpha k} |\bar{\nu}_k\rangle, \tag{2.66}$$

where $|\nu_\alpha\rangle$ with $\alpha = e, \mu, \tau$. For the antineutrino case, the probability of $\bar{\nu}_\alpha \to \bar{\nu}_\beta$ oscillation follows similar steps as that of $\nu_\alpha \to \nu_\beta$. The only difference is the flavour antineutrino state in Equation 2.66, the elements of the mixing matrix are complex conjugate with respect to the flavour state used in Equation 2.44. The antineutrino oscillation probability can be written as

$$\begin{aligned} P_{\bar{\nu}_\alpha \to \bar{\nu}_\beta}(L,E) = \delta_{\alpha\beta} &- 4 \sum_{k>j} \mathcal{R}e\left[U^*_{\alpha k} U_{\beta k} U_{\alpha j} U^*_{\beta j}\right] \sin^2\left(\frac{\Delta m^2_{kj} L}{4E}\right) \\ &- 2 \sum_{k>j} \mathcal{I}m\left[U^*_{\alpha k} U_{\beta k} U_{\alpha j} U^*_{\beta j}\right] \sin\left(\frac{\Delta m^2_{kj} L}{2E}\right). \end{aligned} \tag{2.67}$$

It can be noted that the only change is to the sign of the imaginary part of the corresponding neutrino oscillation probability. Thus, Equation 2.65 and Equation 2.67

together can be expressed as

$$\begin{aligned} P_{\nu_\alpha\to\nu_\beta(\bar{\nu}_\alpha\to\bar{\nu}_\beta)}(L,E) = \delta_{\alpha\beta} - 4\sum_{k>j}\mathcal{R}e\left[U^*_{\alpha k}U_{\beta k}U_{\alpha j}U^*_{\beta j}\right]\sin^2\left(\frac{\Delta m^2_{kj}L}{4E}\right) \\ +\ (-)\ 2\sum_{k>j}\mathcal{I}m\left[U^*_{\alpha k}U_{\beta k}U_{\alpha j}U^*_{\beta j}\right]\sin\left(\frac{\Delta m^2_{kj}L}{2E}\right). \end{aligned} \tag{2.68}$$

The oscillation probability of neutrinos and antineutrinos in Equation 2.68 depends on the same kinematic properties. The oscillation length is the same for neutrinos and antineutrinos. For the antineutrino, the mixing matrix is a complex conjugate of the elements of the neutrino mixing matrix. The different sign of the last term is responsible for getting different oscillation probability values for the case of neutrino and antineutrino. The difference arises due to the imaginary part of the quartic product of the elements of the mixing matrix.

2.4.2 Neutrino oscillations in matter

Neutrinos interact with electrons, protons and neutrons while propagating through matter such as Earth. Neutrinos of any flavor can interact with matter through neutral current interactions, whereas only ν_e can specifically interact with electrons through charge current interactions, as illustrated by their respective Feynman diagrams in Figure 2.1. The imbalance among neutrino flavours can be explained by introducing an effective potential due to the presence of matter. The charge current potential for electron neutrinos interacting with electrons is given by [28]

$$V_{\mathrm{CC}} = \sqrt{2}G_{\mathrm{F}}N_e, \tag{2.69}$$

where G_{F} is the Fermi constant, and N_e is the electron density of the medium. The effective potential of neutral current is contributed only by neutrons since the neutral current potential of electrons and protons cancel each other. The effective potential of neutral current is given by

$$V_{\mathrm{NC}} = -\frac{1}{2}\sqrt{2}G_{\mathrm{F}}N_n, \tag{2.70}$$

where N_n is the neutron density of the medium. The presence of matter modifies the effective Hamiltonian, which describes the flavour evolution of neutrinos. The effective Hamiltonian $\hat{H}$ in Equation 2.47 is modified as

$$\hat{H} = \hat{H}_0 + \hat{H}_1, \tag{2.71}$$

with

$$\begin{aligned} \hat{H}_0|\nu_k\rangle &= E_k|\nu_k\rangle, \\ \hat{H}_1|\nu_k\rangle &= V_\alpha|\nu_\alpha\rangle, \end{aligned} \tag{2.72}$$

where V_α is the effective potential of flavour neutrinos due to the presence of matter. A complete description and derivation of neutrino oscillation in matter is discussed in [28]. The final expression for oscillation probability for $\nu_\mu \rightarrow \nu_e$, considering constant matter density, can be given as [42]

$$\begin{aligned} P_{\nu_\mu\rightarrow\nu_e(\bar{\nu}_\mu\rightarrow\bar{\nu}_e)} = \; & \sin^2\theta_{23}\sin^2 2\theta_{13}\frac{\sin^2(\Delta_{31}-aL)}{(\Delta_{31}-aL)^2}\Delta_{31}^2 \\ & + \sin 2\theta_{23}\sin 2\theta_{13}\sin 2\theta_{12}\frac{\sin(\Delta_{31}-aL)}{(\Delta_{31}-aL)} \\ & \times \Delta_{31}\frac{\sin(aL)}{(aL)}\Delta_{21}\cos(\Delta_{31}+(-)\;\delta_{\mathrm{CP}}) \\ & + \cos^2\theta_{23}\sin^2 2\theta_{12}\frac{\sin^2(aL)}{(aL)^2}\Delta_{21}^2, \end{aligned} \tag{2.73}$$

where

$$\begin{aligned} a &= +(-)G_{\mathrm{F}}N_{\mathrm{e}}/\sqrt{2}, \\ \Delta_{kj} &= \frac{\Delta m_{kj}^2 L}{4E}, \\ \Delta m_{kj} &= m_k^2 - m_j^2. \end{aligned} \tag{2.74}$$

The terms a and δ_{CP} are positive for $\nu_\mu \rightarrow \nu_e$ oscillation, and negative for $\bar{\nu}_\mu \rightarrow \bar{\nu}_e$ oscillation. The asymmetry between neutrino and antineutrino oscillations is caused by CP violation (δ_{CP}) as well as due to matter effects (a). As indicated by Equation 2.73, the matter effects introduce sensitivity to the sign of Δ_{31}, a parameter that defines the neutrino mass ordering. The matter effect asymmetry occurs because of the presence of electrons and the absence of positrons in the Earth [43]. In the energy range of a few GeV, the asymmetry resulting from the matter effect increases with increasing baseline, as neutrino traverse more matter. Therefore, an experiment with a longer baseline becomes more sensitive to the mass hierarchy. With a baseline longer than ∼1200 km, the asymmetry arising between matter and CP violation effects can be distinguished [44]. Therefore, the DUNE experiment [1, 2] with a baseline ∼1300 km will be able to unambiguously determine the mass ordering and δ_{CP} [45].

2.4.3 CP violation in neutrino oscillations

The operation of charge conjugation $\hat{C}$ transforms particles to their antiparticles and vice versa. A right-handed antineutrino changes to a right-handed neutrino under charge conjugation operation. Since only left-handed neutrinos participate in the weak interaction, C-symmetry is thus violated in the weak interaction. The parity operator $\hat{P}$ transforms a particle in a state $(t, \mathbf{x})$ to the state $(t, -\mathbf{x})$. Hence, a (right)left-handness changes to (left)right-handness under parity operation. Thus CP transformation transforms neutrinos into antineutrinos and reverses the helicity

$$\nu_\alpha \xleftrightarrow{\text{CP}} \bar{\nu}_\alpha. \tag{2.75}$$

Hence CP operation on $\nu_\alpha \to \nu_\beta$ is

$$\nu_\alpha \to \nu_\beta \xleftrightarrow{\text{CP}} \bar{\nu}_\alpha \to \bar{\nu}_\beta. \tag{2.76}$$

The oscillation probability of neutrino $\nu_\alpha \to \nu_\beta$ in Equation 2.65 is different from the oscillation probability of $\bar{\nu}_\alpha \to \bar{\nu}_\beta$ in Equation 2.67 and Equation 2.73 for vacuum and matter cases respectively, which manifests the CP violation in neutrino oscillation. The observable quantities in real experiments for the detection of CP violation could be

$$\Delta P^{\text{CP}}_{\alpha\beta} = P_{\nu_\alpha \to \nu_\beta} - P_{\bar{\nu}_\alpha \to \bar{\nu}_\beta} \neq 0. \tag{2.77}$$

To measure CP violation, the difference of oscillation probabilities of neutrino and antineutrino modes can be calculated, which is given by [42],

$$\begin{aligned} \Delta P^{\text{CP}}_{\alpha\beta} &= P_{\nu_\alpha \to \nu_\beta} - P_{\bar{\nu}_\alpha \to \bar{\nu}_\beta} \\ &= -16 \ J_{\alpha\beta} \sin\Delta_{12} \sin\Delta_{23} \sin\Delta_{31} \end{aligned} \tag{2.78}$$

where

$$J_{\alpha\beta} \equiv \mathcal{I}m \left(U_{\alpha 1} U^*_{\alpha 2} U^*_{\beta 1} U_{\beta 2} \right) = \pm J, \tag{2.79}$$

$$J = s_{12} c_{12} s_{23} c_{23} s_{13} c^2_{13} \sin\delta_{\text{CP}} = J^{\max} \sin\delta_{\text{CP}}. \tag{2.80}$$

where $c_{ij} \equiv \cos\theta_{ij}$ and $s_{ij} \equiv \sin\theta_{ij}$. J is called Jarlskog invariant [46] and contains all known neutrino mixing matrix parameterisations. In the case of CP violation, $J \neq 0$, thus, it serves as an experiment-independent quantity to quantify CP violation. The value of $J^{\max}$ is 0.03359 ± 0.0006 (± 0.0019) at 1σ (3σ) [47] after combining the mixing angles. From the expression in Equation 2.80, it is clear that there is no CP violation for three generations of neutrino mixing in a vacuum if $\delta_{\mathrm{CP}} = 0$ or π.

In long baseline experiments such as DUNE [2], in which the neutrino beam passes through the Earth, the matter effect comes into play and modifies the measurements of CP violation. Equation 2.73, which varies oscillation probability with the value of δ_{CP} in matter, suggests that it is possible to experimentally determine the value of δ_{CP} at a fixed baseline. This can be achieved by only analysing the observed shape of $\nu_\mu \to \nu_e$ or $\bar{\nu}_\mu \to \bar{\nu}_e$ appearance signal across an energy range that spans at least one complete oscillation interval, fitting it to Equation 2.73. A measurement indicating a value for δ_{CP} other than 0 or π, under the assumption of three-flavour neutrinos, would signify the presence of CP violation.

2.4.4 Neutrino mass hierarchy

Neutrino oscillation probabilities depend on the difference of the squared neutrino masses, as shown in Equations 2.68 and 2.73 for vacuum and matter, respectively. The experimental measurements of neutrino oscillations do not impose constraints on the absolute neutrino masses of neutrinos. However, upper limits of neutrino masses have been measured in neutrino experiments. Recent cosmological measurements suggest a tighter limit on neutrino masses as $\sum_{i=1}^{3} m_{\nu_i} < 0.12$ eV [48]. The current direct detection limit from the Karlsruhe Tritium Neutrino Experiment (KATRIN) is $m_\nu < 1.1$ eV [49]. Solar and atmospheric neutrino experiments have determined the value of Δm^2_{12} and Δm^2_{32}, respectively and termed them as $\Delta m^2_{12} \equiv \Delta m^2_{\mathrm{SOL}}$ and $\Delta m^2_{32} \equiv \Delta m^2_{\mathrm{ATM}}$. The measurement of oscillation probability in the solar neutrino oscillation experiment allowed us to determine that $\Delta m^2_{21} > 0$ [41]. The recent experiment determined that Δm^2_{32} or, equivalently Δm^2_{31} is the order of $\mathcal{O}(10^{-3})$ eV^2, whose sign is currently unknown. Two possible hierarchies of neutrino mass are:

1. Normal mass hierarchy (NH) or normal mass ordering (NO), ($m_1 < m_2 < m_3$):

$$\begin{aligned} m_1 &= m_0, \\ m_2 &= m_0 + \sqrt{\Delta m^2_{\mathrm{SOL}}}, \\ m_3 &= m_0 + \sqrt{\Delta m^2_{\mathrm{SOL}}} + \sqrt{\Delta m^2_{\mathrm{ATM}}}. \end{aligned} \tag{2.81}$$

2. Inverted mass hierarchy (IH) or inverted mass ordering (IO), ($m_3 < m_1 < m_2$):

$$\begin{aligned} m_3 &= m_0, \\ m_1 &= m_0 + \sqrt{\Delta m^2_{\mathrm{ATM}}}, \\ m_2 &= m_0 + \sqrt{\Delta m^2_{\mathrm{SOL}}} + \sqrt{\Delta m^2_{\mathrm{ATM}}}. \end{aligned} \tag{2.82}$$

where m_0 is the unknown minimal mass.
The current best-fit values for these parameters are [50]

$$\begin{aligned} \Delta m^2_{21} &= 7.50 \times 10^{-5}\ \mathrm{eV}^2, \\ |\Delta m^2_{31}|\ (\mathrm{NO}) &= 2.55 \times 10^{-3}\ \mathrm{eV}^2, \\ |\Delta m^2_{31}|\ (\mathrm{IO}) &= 2.45 \times 10^{-3}\ \mathrm{eV}^2. \end{aligned} \tag{2.83}$$

The normal and inverted mass hierarchies are shown in Figure 2.3. The coloured bands represent the probability that a particular neutrino mass eigenstate is a combination of flavour eigenstates $(\nu_e, \nu_\mu, \nu_\tau)$.

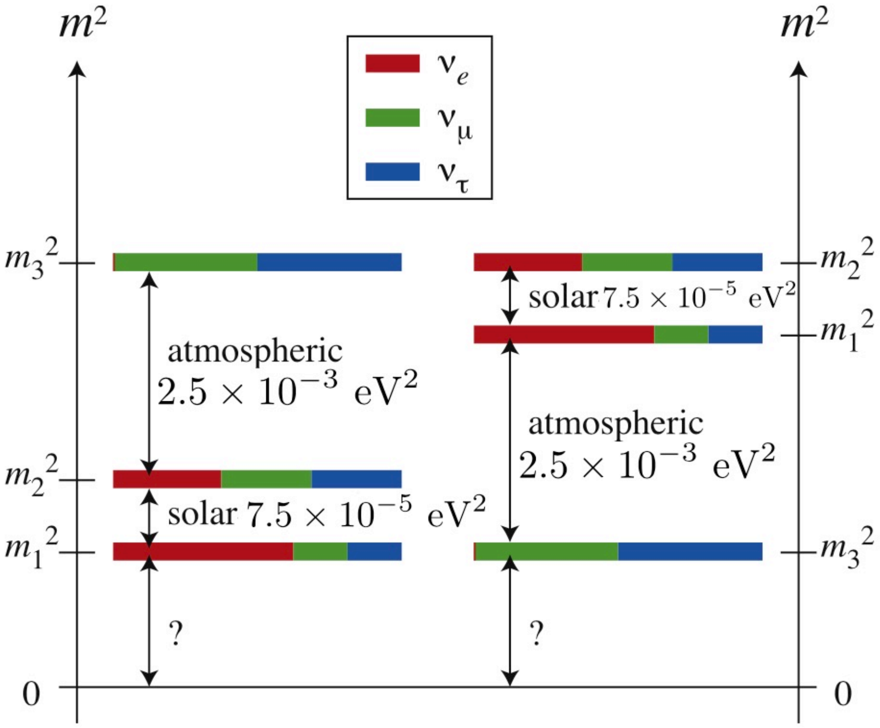

Figure 2.3. An illustration of the two possible neutrino mass hierarchies, referred to as the normal (left) or inverted (right) mass ordering. The colours in the figure represent the flavour composition of neutrino mass states ν_i with mass m_i. The value of the lightest neutrino mass is unknown. The figure is taken from Ref. [51].

2.5 Experimental measurements of neutrino oscillation parameters

In the context of three neutrinos, the probability of a neutrino oscillating between different flavours is governed by six parameters: Δm^2_{21}, $|\Delta m^2_{31}|$, θ_{12}, θ_{13}, θ_{23}, and $\delta_{\rm CP}$. These parameters collectively define the oscillation behaviour of neutrinos. Numerous experiments have been conducted to measure these parameters. Global fit analyses, such as [50], combine the results from various experiments to provide the best estimates of these parameters.

Solar neutrino oscillation experiments primarily provide sensitivity to θ_{12} and Δm^2_{12}. The results from experiments such as SAGE [52], GALLEX/GNO [53], Homestake [54], Borexino [55, 56], Kamiokande [57], Super-Kamiokande [58, 59, 60], SNO [61] are combined with KamLAND results [62, 63, 64]. This combination of experiments allows for the precise determination of parameters Δm^2_{21} and θ_{12}. Besides KamLAND, there are several other reactor neutrino oscillation experiments, such as RENO [65] and Daya Bay [66], which are quite close to the nuclear power plants, unlike KamLAND. These experiments provide greater sensitivity to θ_{13} and also contribute to determining $|\Delta m^2_{31}|$.

The oscillation parameters, θ_{23} and Δm^2_{23}, are established through atmospheric neutrino oscillation experiments that measure neutrinos produced in the atmosphere. In particular, both Super-Kamiokande [67] following the Kamiokande [23] and the DeepCore detector within the IceCube experiment [68, 69] play pivotal roles in recent analyses concerning these parameters.

Long baseline neutrino experiments such as T2K [70], K2K [71], MINOS [72], and NOνA [73] typically possess sensitivity to a range of oscillation parameters and provide essential contributions to the measurement of $|\Delta m^2_{31}|$, θ_{23} and θ_{13}. As neutrinos pass through the Earth, the baseline of these experiments also introduces matter effects as discussed in Section 2.4.2. Furthermore, these experiments can explore matter-antimatter asymmetry by comparing oscillation measurements between neutrino and anti-neutrino modes, and thus $\delta_{\rm CP}$ can be quantified. Data from the NOνA and T2K experiments provide constraints on $\delta_{\rm CP}$. Figure 2.4 shows the $\Delta\chi^2$ measurements for the $\delta_{\rm CP}$ obtained from the analysis of the data from these two experiments. This includes combining all long-baseline data (black) and the global fit (green), including data from the Super-Kamiokande experiment.

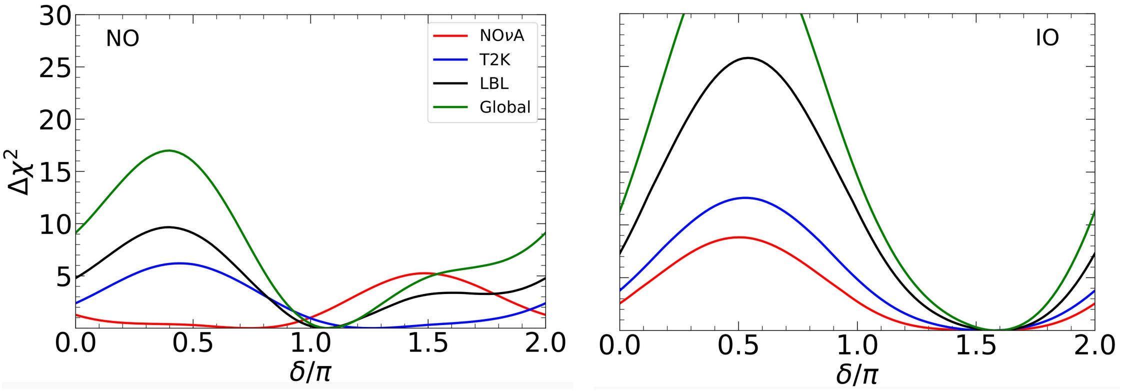

(a) **(b)**

Figure 2.4. $\Delta\chi^2$ profile for δ_{CP} measurement based on the analysis of NOνA (red) and T2K (blue) experiments, including all long-baseline data (black) and from the global fit (green): a) normal ordering, b) inverted ordering. The figure is taken from Ref. [50].

For normal neutrino mass ordering, as shown in Figure 2.4a, there exists a tension in the determination of δ_{CP} based on data from the T2K and NOνA experiments. However, this tension is not observed for inverted ordering, as shown in Figure 2.4b, where NOνA demonstrates greater sensitivity to δ_{CP} and has better agreement with the measurements from T2K.

The global combination of data provides the best-fit value for the CP phase at $\delta_{\mathrm{CP}} = 1.08\pi(1.58\pi)$ for normal ordering (inverted ordering). The value $\delta_{\mathrm{CP}} = 0$, which conserves CP, is disfavored, with $\Delta\chi^2 = 9.1(11.3)$ in normal ordering (inverted ordering), while the other CP-conserving value, $\delta_{\mathrm{CP}} = \pi$, is favoured with $\Delta\chi^2 = 0.4$ in normal ordering but is excluded with $\Delta\chi^2 = 14.6$ in inverted ordering.

The preference for normal mass ordering over inverted mass ordering is indicated by a lower $\Delta\chi^2$ for $\Delta m^2_{31} > 0$ compared to $\Delta m^2_{31} < 0$. The data combining all the long-baseline accelerator experiments, favoured inverted mass ordering (IO) with $\Delta\chi^2 = 2.4$. This outcome arises as a consequence of the tension observed in the measurement of δ_{CP} by NOνA and T2K experiments. In a combined analysis that incorporates data from both accelerator and reactor experiments, normal mass ordering (NO) is favoured with $\Delta\chi^2 = 1.4$. This enhanced support for normal mass ordering is primarily attributed to the difference observed in the measurements of $|\Delta m^2_{31}|$ between accelerator and reactor experiments. The precise determination of δ_{CP} and the mass hierarchy remains an ongoing challenge in neutrino physics. Future neutrino experiments, such as DUNE [2], are designed to address these open questions and are expected to provide more precise measurements of these parameters. To conclude, a summary of the best-fit values [50] for the oscillation parameters and their main contributors from the different classes of experiments are reported in Table 2.1.

Table 2.1. Neutrino oscillation parameter values are best estimated from the global data fit. NO and IO denote normal ordering and inverted ordering, respectively. The uncertainty represents 1σ value [50].

Parameter	Main contributor	Best fit values	
		NO	IO
Δm^2_{21} [10^{-5} eV^2]	KamLAND	$7.50^{+0.22}_{-0.20}$	$7.50^{+0.22}_{-0.20}$
$\lvert\Delta m^2_{31}\rvert$ [10^{-3} eV^2]	LBL + ATM + REAC	$2.55^{+0.02}_{-0.03}$	$2.45^{+0.02}_{-0.03}$
θ_{12} [degree]	SOL	34.3 ± 1.0	34.3 ± 1.0
θ_{23} [degree]	LBL + ATM	49.26 ± 0.79	$49.46^{+0.60}_{-0.97}$
θ_{13} [degree]	REAC	$8.53^{+0.13}_{-0.12}$	$8.58^{+0.12}_{-0.14}$
$\delta_{\rm CP}$ [degree]	LBL	194^{+24}_{-22}	284^{+26}_{-28}

2.6 Current and future neutrino experiments

Currently, there are two operational accelerator-based, long-baseline neutrino oscillation experiments: T2K (Tokai to Kamioka) [74] in Japan and NOνA [75] in the United States. These experiments have been collecting data since 2009 and 2014, respectively. Both experiments observe the disappearance of $\nu_\mu(\bar{\nu}_\mu)$ and the appearance of $\nu_e(\bar{\nu}_e)$ with baselines of 295 km and 810 km for T2K and NOνA, respectively. T2K data exhibit a pronounced asymmetry in $\nu_\mu \to \nu_e$ compared to $\bar{\nu}_\mu \to \bar{\nu}_e$, thus indicating a preference for CP-violating values of $\delta_{\rm CP}$, whereas NOνA lacks this asymmetry, leading to a slight tension between the experiments [76]. The NOνA and T2K collaborations are engaged in joint analyses of their oscillation data to leverage their complementary designs (e.g., differing balances of matter-induced and potential CP violation induced oscillation asymmetries) and to address joint systematic uncertainties. Fermilab and J-PARC/Kamioka [77] have planned to host next-generation neutrino experiments aimed at addressing unresolved questions in neutrino oscillations. The current generation of long-baseline oscillation experiments is limited by statistical considerations; therefore, next-generation experiments will need to substantially increase the baseline and the size of detector and enhance constraints on systematic uncertainties.

DUNE [2] is the next phase in Fermilab's program, while T2HK [77] builds upon the successful Super-K and T2K experiments. DUNE and T2HK are the long baseline experiment with baseline 1300 km and 295 km, respectively. T2HK will utilize a beam from J-PARC and established water Cherenkov detector (WCD) technology to rapidly collect the statistical data required for precise measurements. DUNE is configured as a precision experiment, employing LArTPCs to enable precise imaging of all final-state particles. The baseline length of T2HK is too short for the matter effect so T2HK has poor sensitivity to the mass hierarchy. Therefore, the sign degeneracy of mass ordering can pose a significant challenge in determining δ_{CP} at T2HK. On the other hand, the baseline length of DUNE is comparable to the typical length which is estimated by the matter effect, so DUNE is expected to be sensitive to the mass hierarchy. DUNE and T2HK, especially when combined, provide a valuable opportunity to explore physics beyond the standard model.

Chapter 3

Liquid Argon Time Projection Chambers

The Liquid Argon Time Projection Chamber (LArTPC) is currently a popular and rapidly developing detector technology for neutrino and dark matter experiments. The LArTPC is an evolved version of Charpak's Multi-Wire Proportional Chamber (MWPC) [78], which was further developed by Nygren in the late 1970s [79]. Originally, TPCs were typically filled with noble gases, with argon being the preferred choice in most cases. In 1977, Carlo Rubbia [80] proposed using liquefied argon as the target medium in TPCs. DUNE is a future experiment currently under construction, which utilises this technology for the study of neutrino oscillations and astroparticle physics due to its good spatial and energy resolution, as well as excellent particle identification capability. The dark matter experiments such as DarkSide-20k [81], employ dual-phase LArTPCs to detect dark matter candidates, particularly WIMPs. LArTPC is sensitive to both the scintillation light and the ionisation electrons produced by WIMP interactions in the liquid argon. Understanding the detector's effects is crucial for achieving the physics goals of experiments.

In this chapter, a brief introduction to the LArTPC detector technology is presented, encompassing in-depth explanations of the specific LArTPC detectors pertinent to the research outlined in this thesis. The first section discusses the general description and operating principles of LArTPCs. Section 3.2 provides an overview of how particles deposit energy in the detector in the context of track and shower formation. Section 3.3 covers the production, propagation, and detection of the ionisation signal, and finally, Section 3.4 discusses the production, transmission and detection of the scintillation signal.

3.1 Detector medium and operating principle

Efficient particle detection by a TPC relies on several key properties of the active medium. These properties include ionisation and scintillation yields, electron-ion pair recombination, interaction length of electromagnetic (EM) and hadronic interactions, density, transparency to its own scintillation light, and the boiling point [82]. These factors play a crucial role in determining the overall performance and capabilities of the TPC detector in accurately detecting and reconstructing particle interactions. Liquid argon (LAr) possesses distinctive characteristics that make it an excellent choice for neutrino detectors [80]. With a relatively high density of 1.41 g/cm^3, it enhances the probability of neutrino interactions within the detector. Moreover, due to its chemical inertness, argon remains unreactive and enables the migration of ionisation charges generated by interacting particles across distances spanning multiple meters. Furthermore, argon possesses a 'high light yield' and exhibits transparency to its own scintillation light, ensuring accurate timing measurement of a prompt signal. Argon becomes liquid at approximately 87 K, making it suitable for large-scale cooling using easily available liquid nitrogen. The aforementioned properties of liquid argon, its abundance in the atmosphere, and its cost-effectiveness make liquid argon an outstanding option for neutrino detectors on a large scale.

An illustration of the basic operation of the LArTPC detector is shown in Figure 3.1. Interacting neutrinos produce secondary charged and neutral particles in liquid argon. The charged particles ionise and excite the argon atoms, and as a result, ionisation electrons are produced. The ionisation electrons then drift by an applied uniform electric field towards the wires of the anode planes on a few millisecond timescale and produce an electric signal. Argon atoms in the excited states emit scintillation photons during the de-excitation process, which are subsequently captured by photon sensors like photomultiplier tubes (PMTs). These detectors are typically positioned behind the wire planes, where the scintillation light signal travels at a faster speed and is detected more rapidly compared to the drifted ionisation charge. Therefore, it allows the triggering of the detector readout system, determining the interaction time in the TPC (t_0) and facilitates comparisons with the arrival time of electrons at the anode. The anode plane comprises three parallel planes of conducting wires, each wire positioned at varying angles to one another. This arrangement enables precise 2D localisation of ionisation by capturing charge induction signals from all three sense wires. Typically, the wires intersect at a single point in all three planes, facilitating accurate measurement. By incorporating timing information and creating two-dimensional representations of the ionisation charge movement in space, the system achieves a three-dimensional high-resolution image of neutrino interactions. The collected charge also provides information on the energy deposited by the charged particle (referred to as calorimetry information). The number of electrons on each wire corresponds to the particle's energy loss for a given distance travelled, known as dE/dx. Further elaboration on this topic will be provided in the subsequent sections.

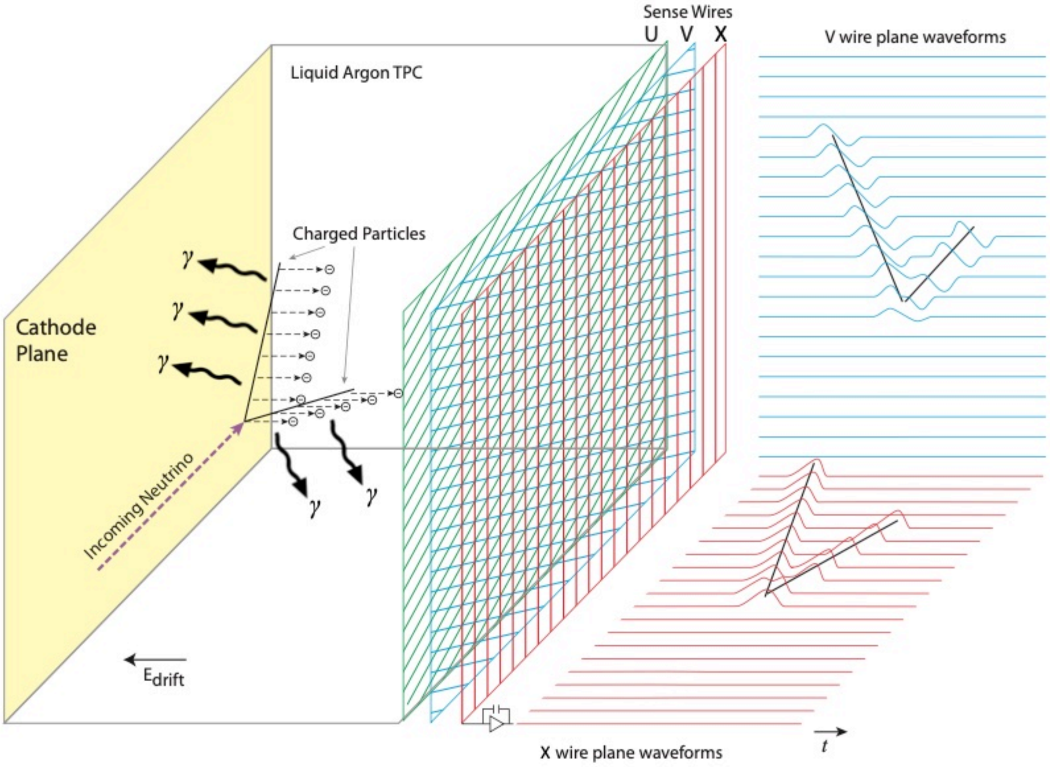

Figure 3.1. The basic operating principles of a LArTPC [2] detector, showing how charged particles cause ionisation of the liquid argon and generate electron-ion pairs. Ionisation electrons are guided towards the anode wire readout by a continuous electric field. Signal induction and collection occur on the wire planes, which are oriented at different angles to one another and offer distinct viewpoints of the event. The figure is taken from Ref. [2].

3.2 Particle interactions in LArTPC

As charged particles move through the LArTPC, they produce tracks and showers of ionisation electrons that move towards the anode wires. Although neutrinos and other neutral particles cannot be directly detected, their presence can be indirectly observed by identifying secondary charged particles that are generated when they interact with liquid argon.

3.2.1 Track formation: muons, protons and charged pions

Charged particles such as muons and pions (charged pions, unless otherwise stated) produce tracks of ionisation electrons in the LArTPC. An example of an event display of a cosmic muon interaction in the LArTPC, producing track-like energy deposition, is shown in Figure 3.2.

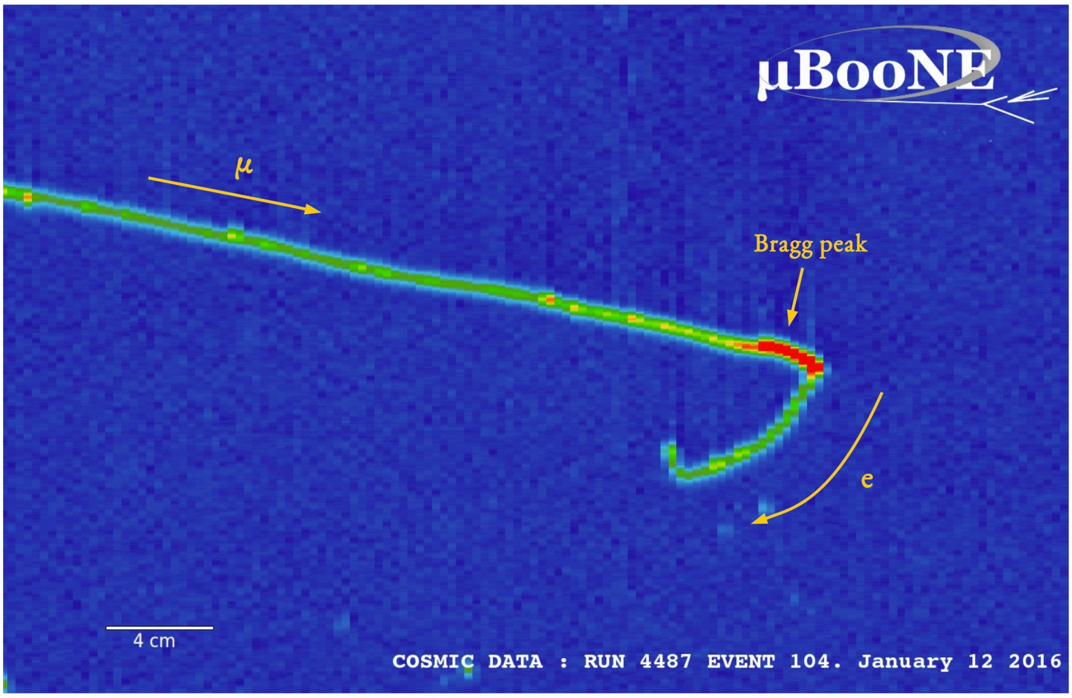

Figure 3.2. An event display of MicroBooNE data showing a cosmic-ray muon event from a small region of the TPC volume. The muon produces a long ionising track which stops in the TPC and decays to a positron (Michel electron) and neutrinos, creating a Bragg peak shown in red at the end of the track. The red colour at the end of the track indicates a large amount of energy being deposited. Highly ionising segments appear in yellow and red along the muon track, indicating δ-rays produced by the muon while traversing the detector [83].

The charged particles interact within the LArTPC, losing energy over time as they travel through the medium. The Bethe-Bloch formula [41] models the average energy deposition per unit length, dE/dx, along the resulting tracks. It can be expressed as follows, representing the energy loss due to ionisation and atom excitation:

$$\left\langle -\frac{dE}{dX} \right\rangle = K\ z^2\ \frac{Z}{A}\frac{1}{\beta^2}\left[\frac{1}{2}\ \ln\ \frac{2m_e c^2\beta^2\gamma^2 W_{max}}{I^2} - \beta^2 - \frac{\delta(\beta\gamma)}{2}\right], \qquad (3.1)$$

where $K = 4\pi N_A r_e^2 m_e c^2 = 0.307075$ MeV mol^{-1} cm^2, $N_A = 6.023 \times 10^{23}$ mol^{-1} is Avogadro's number, $r_e = \frac{e^2}{4\pi\epsilon_0 m_e c^2}$ is the classical radius of electron orbit, z is the charge number of the incident particle, and Z and A are the atomic numbers and the atomic mass of the traversed medium respectively. Additionally, $\beta = v/c$, where v is the particle velocity, and $\gamma = 1/\sqrt{1 - \frac{v^2}{c^2}}$. The term W_{max} is the maximum energy transfer to an ionisation electron in a single collision, while I denotes the mean excitation energy. The quantity $\delta(\beta\gamma)$ represents the density effect correction to ionisation energy loss.

Equation 3.1 remains applicable within the range of $0.1 \lesssim \beta\gamma \lesssim 1000$. This equation describes the mass stopping power, measured in MeV g^{-1} cm^2. The linear stopping power, denoted as $\rho \langle dE/dx \rangle$, is expressed in MeV/cm, where ρ is the density of the medium in g/cm^3. Figure 3.3 illustrates the Bethe-Bloch curves for muons, pions, and protons in various mediums are exactly the same if the x-axis is plotted as a function of p/Mc, where p is the momentum and M is the mass of the particle. The corresponding momentum of these particles, which depends on their particle masses, is also indicated on the secondary x-axis. The average energy loss relies on both the particle type and the detector medium. Most relativistic particles, such as cosmic-ray muons, have energy loss rates close to the minimum and are known as minimum ionising particles (MIPs). At low $\beta\gamma$, the energy loss increases much faster with the decrease of the momentum than at high $\beta\gamma$. Consequently, as particles decelerate, they exhibit an increasing ionisation effect, depositing a significant amount of energy at the end of the track when they come to a stop. This energy loss peak formed at the end of the track is known as the Bragg peak. The particles that emerge from accelerator neutrino interactions in LArTPCs span a range of energies, from approximately a hundred MeV to several GeV. As a result, muons and pions are primarily produced in the region where ionisation is minimised, whereas protons are often produced in the low-momentum region and exhibit high ionisation. The average energy loss per unit distance (dE/dx) for a minimum-ionising particle in liquid argon is approximately 2.1 MeV/cm [84].

The ionisation energy loss (dE/dx) of the charged particles in the medium follows a Landau distribution [85]. Large energy transfers from the particle to the atom of liquid argon can result in the emission of electrons with sufficient energy

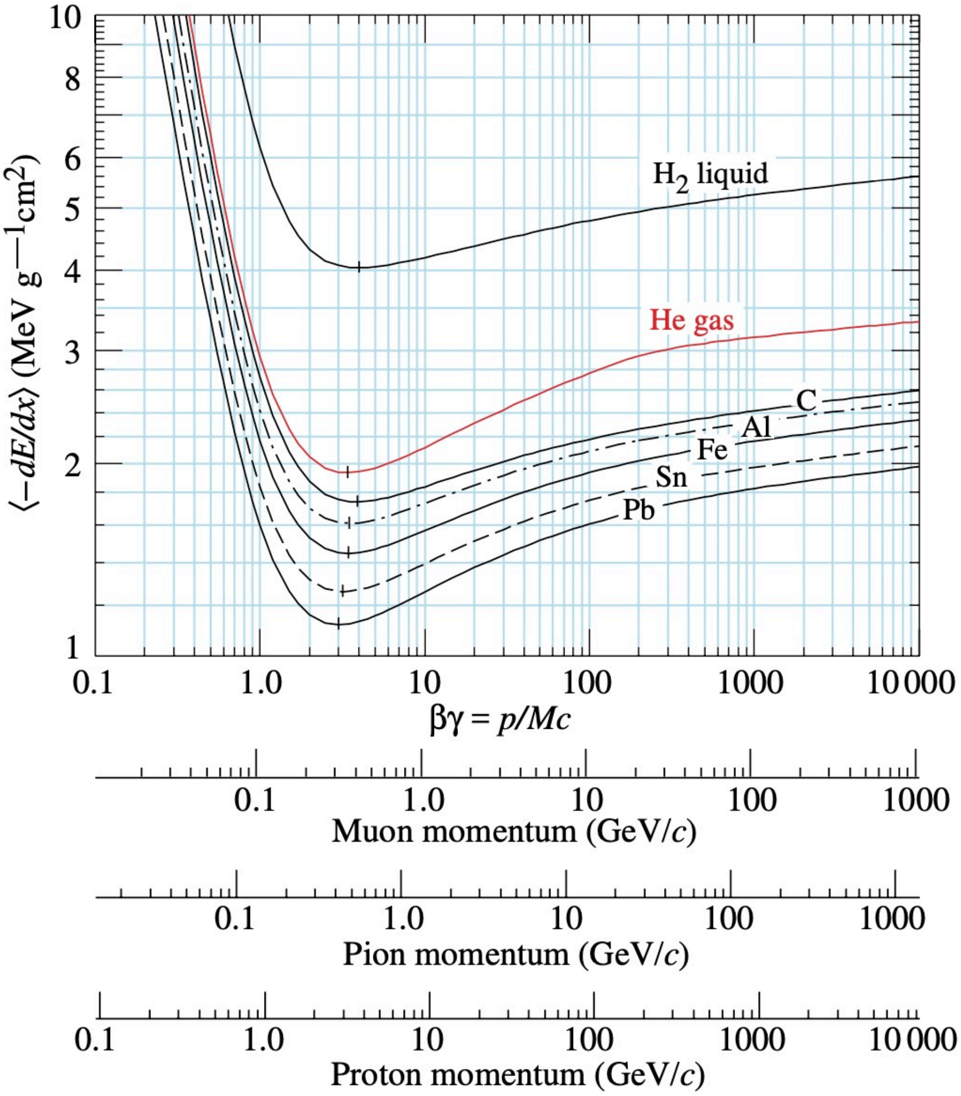

Figure 3.3. The Bethe-Bloch curves illustrate the average energy loss experienced by muons, pions, and protons in different media, depending on their momentum. Different x-axes show the momentum of different particle types [41].

to produce further ionisation. These emitted electrons are commonly known as knock-on electrons or δ-rays [86]. Figure 3.2 illustrates instances of δ-ray activity occurring at various points along the muon's ionising track. Depending on the energy of the emitted δ-ray, there are two possible outcomes: either a couple of anode plane sense wires will register a higher dE/dx, or in the case of higher energies, a distinct track will be formed, which can be detected by multiple anode plane wires.

3.2.2 Shower formation: electrons and photons

The electromagnetic (EM) showers are generated by electrons and photons. These showers consist of a series of secondary particles that are produced within a medium when high-energy ($E > 100$ MeV) electrons or photons interact. At such high energies, electrons primarily lose their energy through radiation, usually bremsstrahlung, while photons lose their energy by generating an electron-positron pair through pair production.

At low energies, electrons and positrons experienced multiple Coulomb scattering (MCS) effects. As electrons traverse a medium, they are deflected by many small-angle scatters, with most of the deflection resulting from Coulomb scattering off nuclei [87, 88, 89, 90]. These Coulomb scattering are well described by Molière's theory [91]. The cumulative effect of these interactions significantly alters the electrons' paths, broadening their overall trajectory in the medium.

In terms of the shower's behaviour within a detector, electrons and positrons exhibit similar characteristics. Figure 3.4 shows the electron kinetic energy contribution to the collision (ionisation) and radiation processes. Figure 3.5 illustrates the dependence of cross section on the photon energy for different interaction types in liquid argon. At low energies ($E < 0.1$ MeV), photons make a more significant contribution to the overall cross section through photoelectric absorption. As the energy increases, Compton scattering becomes the dominant process. Above about 20 MeV, pair production becomes the primary interaction mechanism for photons in liquid argon.

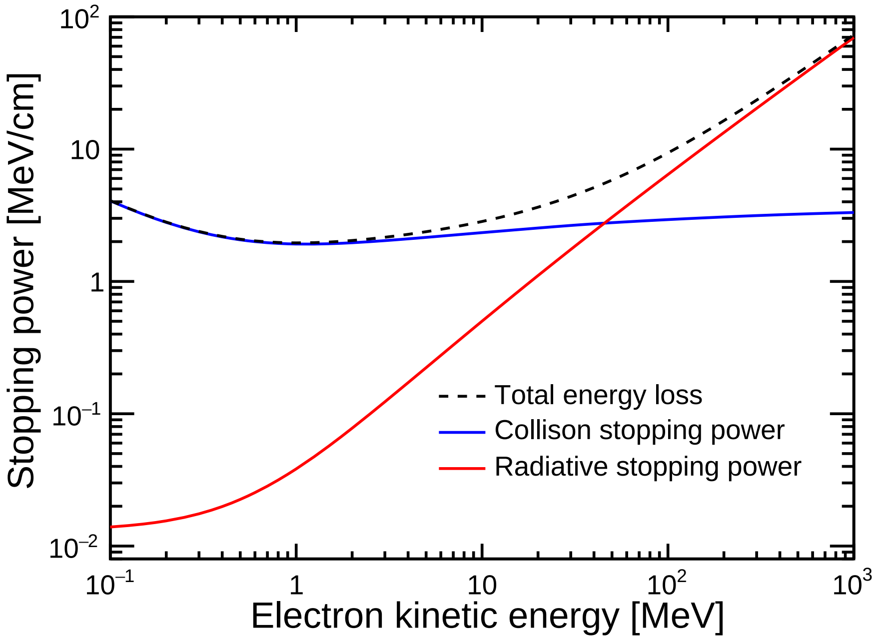

Figure 3.4. Energy loss for electrons in argon obtained from NIST ESTAR tables [92]. The density of liquid argon is taken as 1.39 g/cm^3.

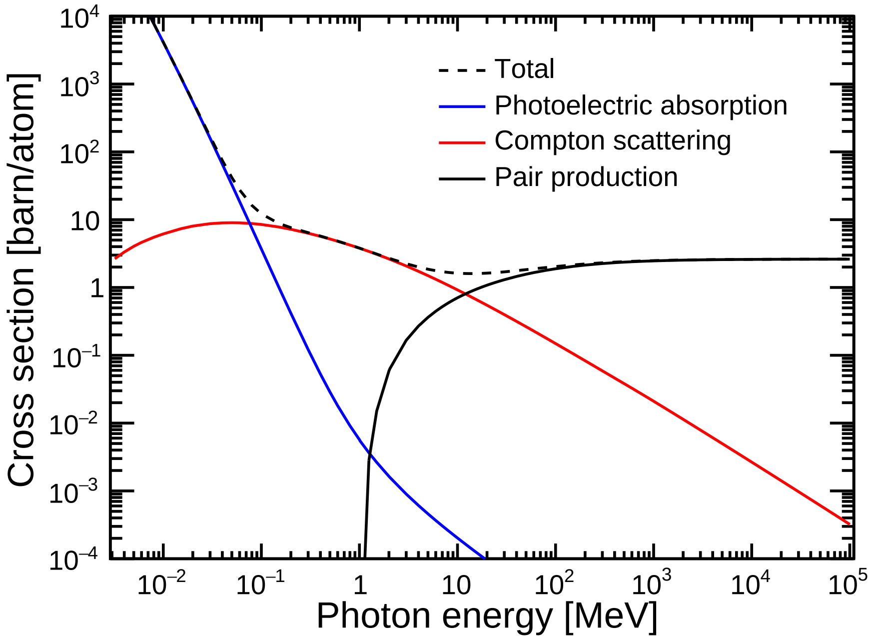

Figure 3.5. Cross sections of photon interactions in liquid argon obtained from NIST XCOM tables [93].

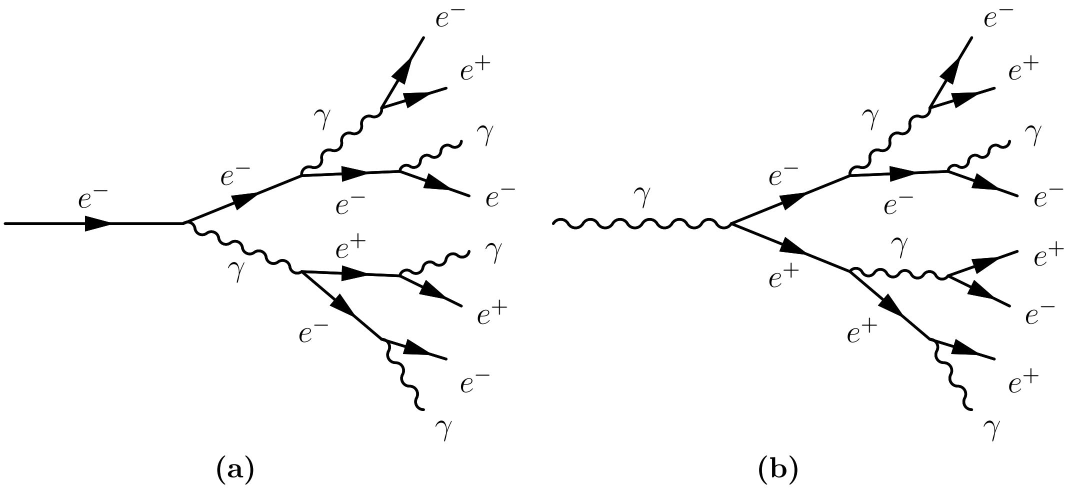

Figure 3.6. The development of electromagnetic showers: a) initiated by an electron, b) initiated by a photon. These two showers can be separated by analysing the energy loss at the start of the shower. In the case of electron shower, the energy loss is given by a single MIP particle whereas for photon shower it is given by two MIP particles.

Figure 3.6 shows an electromagnetic cascade that is initiated by an electron and a photon. The shower continues to grow until radiation losses become equal to ionisation/excitation. The showers produced by electrons and photons can be distinguished by analysing the energy loss at the beginning of the shower. For an electron shower, energy loss is given by a single MIP particle while for a photon shower, it is given by two MIP particles. In LArTPC detectors, electromagnetic cascades manifest as showers composed of electrons and positrons. Figure 3.7 presents an observed event of a charged pion interaction within the ProtoDUNE detector. It showcases two distinct electromagnetic showers originating from photons from the decay process of $\pi^0 \to 2\gamma$. Additionally, the interaction results in two resembling tracks: one from the primary π^+ and another from the secondary proton that is produced by the π^+. Moreover, there is a cosmic ray muon overlapping with the incident π^+.

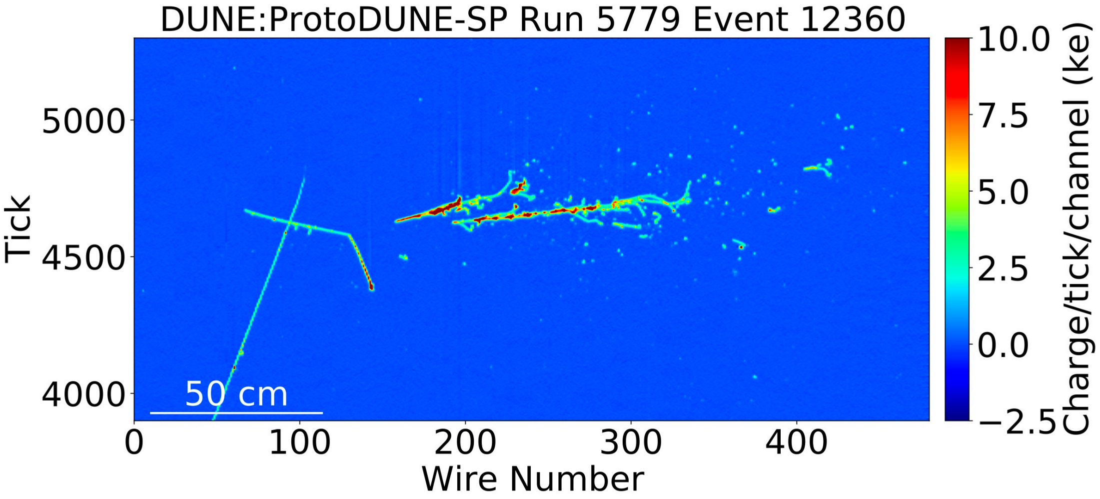

Figure 3.7. An event display showing a π^+ interacting in the ProtoDUNE-SP LArTPC. During this occurrence, a π^+ travels into the detector from the left side and engages in a charge exchange process. This interaction leads to the production of a proton and a π^0. The proton comes to rest, while the π^0 undergoes decay, generating two photons that cause electromagnetic showers. Additionally, there is an overlapping cosmic ray muon alongside the incoming π^+. The figure is taken from Ref. [94].

3.3 Ionisation signals: formation and implications

3.3.1 Charge production

During ionisation, pairs of e^- and Ar^+ are produced. For an incident particle, X, interacting with liquid argon, the ionisation process is

$$X + \mathrm{Ar} \to e^- + \mathrm{Ar}^+ + X'. \tag{3.2}$$

The ionisation energy of liquid argon is 23.6 ± 0.3 eV [95]. Therefore, 1 MeV of deposited energy can produce $\sim$ 40,000 electron-ion pairs if all of this energy is utilised in ionisation. However, a fraction of this energy goes into the excitation of argon, producing scintillation light. The energy carried by electrons within a cluster of ionisation charge is insufficient to induce further ionisation. When a minimum ionising particle (MIP) which has an energy loss rate close to the minimum (Figure 3.3), like a low-energy muon, traverses liquid argon at a temperature of approximately 87 K, it deposits 2.1 MeV of energy per centimetre of track length [84]. In the case of a minimum ionising particle subjected to an electric field of 0.5 kV/cm, the measured electron yield is $\sim\ 29,000\ e^{-}$/MeV [96].

In the absence of an electric field, the ionisation electrons e^{-} and Ar^{+} ions recombine, resulting in the creation of argon atoms and the emission of scintillation light. However, when an electric field is present, a fraction of the ionisation pairs separate before recombination. The ionisation electrons move towards the anode plane wires, while the Ar^{+} ions move towards the cathode plane. The quantity of charge gathered at the anode plane wires is influenced by the strength of the electric field. LArTPC detectors typically maintain an electric field strength of 0.5 kV/cm. This value is selected to strike a balance between the energy transferred to the ionisation electrons and the production of scintillation light. At very low electric fields, only a small amount of charge is collected, whereas, at high electric fields, the production of scintillation light is minimal. Recombination is also affected by the density of ionisation charge [97], with higher ionisation charge densities leading to a greater likelihood of recombination. The density of ionisation electrons e^{-} and Ar^{+} ions produced is higher when a highly ionising particle, such as a proton, interacts with LAr. Figure 3.8 shows the recombination factor as a function of applied electric field for 364 KeV from ^{113}Sn [98], 976 KeV electron from a ^{207}Bi [99] radioactive sources. The recombination factor is defined as $Q = \mathcal{R} \times Q_0$; where Q is collected charge, Q_0 is the intial ionisation, and $\mathcal{R}$ is recombination factor. Q_0 is related to the energy needed to produce an electron pair (ionisation energy)[100].

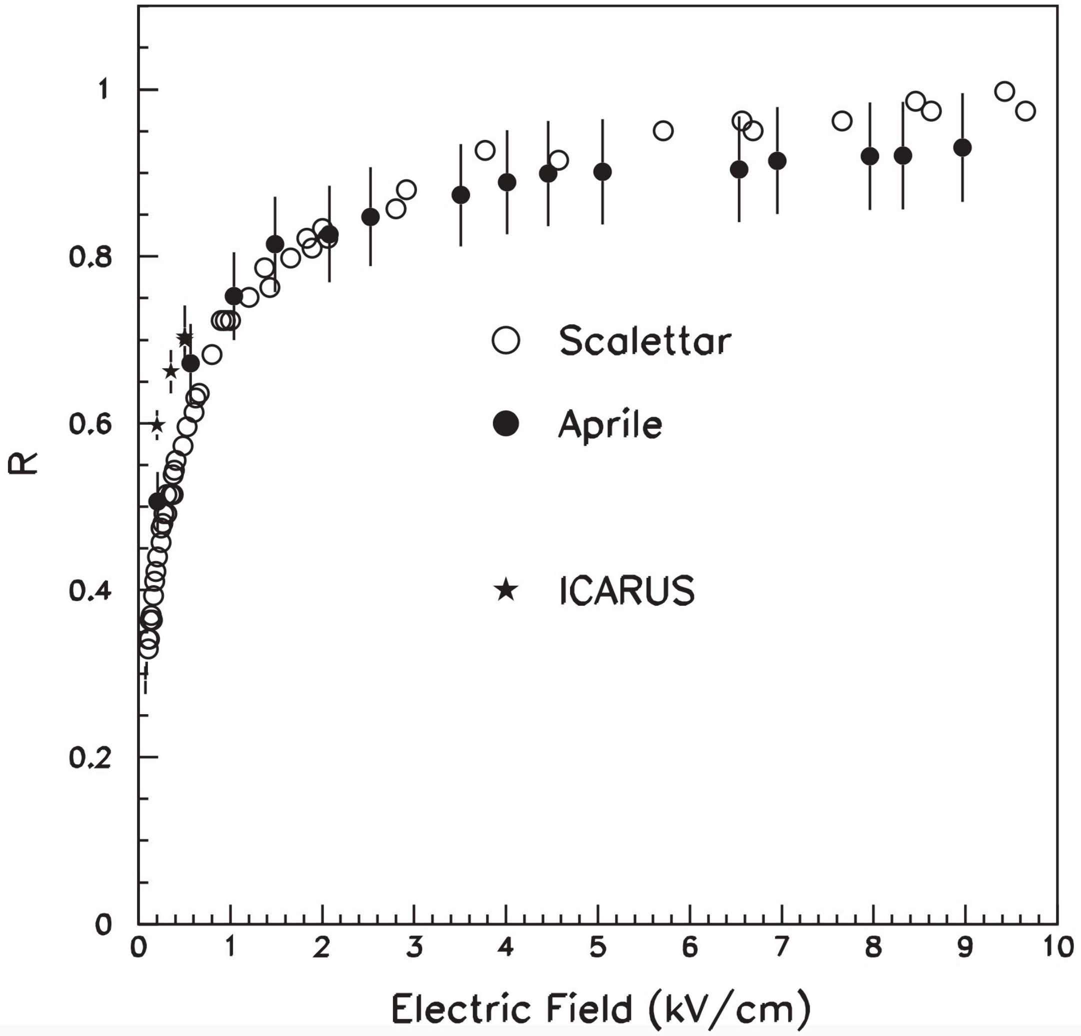

Figure 3.8. Recombination factor as a function of the electric field for 364 KeV electrons • [98], 976 KeV electrons ∘ [99], and minimum ionising particles (ICARUS). The figure is taken from Ref. [100].

3.3.2 Ionisation charge drift

The free electrons e^- and argon Ar^+ pairs that escape the recombination travel towards the anode and cathode respectively under the influence of the applied electric field. The drift velocity depends on the applied electric field as well as the temperature of the medium [101]. At a temperature of $T = 87$ K and at electric field 0.5 kV/cm, the electron drift velocity is measured as $v_{e^-} = 1.6 \times 10^3$ m/s (1.6 mm/μs), while the positive ions have a drift velocity of 8×10^{-3} m/s (8×10^{-6} mm/μs) [102].

Electronegative impurities like oxygen and water, found in liquid argon, have the ability to capture drifting electrons. As a result, the amount of charges accumulated on the anode wires is reduced, leading to a decrease in signal amplitude. This effect is given by the formula [94]:

$$Q(t) = Q_0 \exp\left(-(t_{\text{hit}} - t_0)/\tau\right), \tag{3.3}$$

where $Q(t)$ represents the charge detected on an anode wire, and Q_0 represents the initial charge resulting from argon ionisation. t_0 denotes the time of ionisation, and t_{hit} signifies the time when the drifting charge reaches the anode wire. The symbol τ refers to the lifetime of drift electrons. A greater τ value indicates a purer liquid argon state, as fewer drifting electrons will adhere to impurities during their journey towards the anode wire. An infinite electron lifetime implies that there are no impurities present in the liquid argon. Through argon purification systems as used in ProtoDUNE, contemporary LArTPCs can attain electron lifetime ~ 100 ms, corresponding to an impurity level in the detector of approximately 3 parts per trillion (ppt) of oxygen equivalent [94].

Electron clouds originating from the ionisation point can spread out (diffuse) while propagating toward the anode plane. The electric field causes the diffusion to be anisotropic. Electrons that diffuse parallel to the drift direction are referred to as 'longitudinal diffusion', while those diffusing perpendicular to the drift direction are termed 'transverse diffusion'. Electron clouds originating near the cathode are most affected by diffusion since they have the furthest distance to propagate. The spatial resolution of a LArTPC in the plane perpendicular to the anode wire plane is influenced by longitudinal diffusion, which causes the signal waveforms to spread out as the drift time increases. Close to the anode, where the drift time is short, the waveform has a high amplitude and small width. However, as the drift time lengthens, the pulses become of lower amplitude and wider [103]. The spatial resolution in the plane parallel to the readout wire plane is influenced by the transverse component. Transverse diffusion causes electrons to spread across multiple readout wires, resulting in an averaging effect that can modify the observed shape of the energy deposition per unit length (dE/dx). This effect is particularly significant close to the Bragg peak, where the dE/dx changes rapidly. The Bragg peak is described in Section 3.2.1. Consequently, this phenomenon has the potential to distort the distribution of dE/dx in this region more than in other areas, thus affecting the particle identification capabilities of LArTPCs [104, 105]. In most substances, transverse diffusion is more than the longitudinal diffusion [105]. The longitudinal and transverse diffusion coefficient at an electric field of $E = 0.5$ kV/cm and a temperature of $T = 87$ K in liquid argon have been calculated to be 6.6 cm^2/s and 13.2 cm^2/s respectively [106].

The Ar^+ ions have a drift velocity approximately $2 - 4 \times 10^5$ times slower than that of ionisation electrons when subjected to an electric field of 0.5 kV/cm. As a result, over the time scale of electron drift in a TPC, the Ar^+ ions will appear to be motionless. These positively charged ions can accumulate in the detector over time, leading to distortion of the electric field. This phenomenon is referred to as the space charge effect (SCE). These distortions in the electric field can alter the trajectory of ionisation electrons during their drift within the detector. Consequently, the reconstructed positions of the ionisation charge may differ from their actual origin in the detector. Furthermore, the electric field distortions can impact the recombination of electrons and ions at locations where energy is deposited in the detector. Additionally, the accumulated Ar^+ ions can attach to drifting electrons from subsequent events. These effects can modify both the particle's energy loss per unit distance dE/dx and its trajectory, resulting in complications in identifying particles within a LArTPC detector. The SCE becomes particularly significant when the LArTPC is exposed to a high flux of cosmic rays, which leads to a substantial production of Ar^+ ions [107]. This is especially relevant for detectors located at the surface of the Earth or at shallow depths.

3.3.3 Ionisation charge detection: signal formation

The drifted ionisation electrons approach the LArTPC anode planes in the presence of the uniform external electric field. The TPC anode consists of three parallel planes of sense wires (sensitive to the ionisation charge) and one plane of shielding wires that are perpendicular to the electric field direction. The wire plane arrangement begins with an outermost layer consisting of an uninstrumented shielding (grid) plane, succeeded by two induction planes, and ultimately concluded with the collection plane. These four planes are biased at different potentials, causing electric field lines to terminate only at the last collection plane, where they collect electrons. Meanwhile, the other two induction planes allow electrons to pass through, remaining transparent to drifting electrons. As drifting electrons travel through the first two induction planes, a bipolar signal is induced. When the drifting electrons are collected on the wires of the collection plane, they induce a unipolar signal. Figure 3.9 shows the field simulation and an illustration of the signal observed on the anode wire planes. The shield plane primarily serves the purpose of pulse-shaping and remains disconnected from the electronics readout. This arrangement prevents signal induction until the charge surpasses the shield plane, leading to a more clean bipolar signal. Without the shield plane, the signal becomes noticeably asymmetric, with the first part of its bipolar shape spreading over a longer time. The DUNE SP LArTPC detectors utilise these shield planes to simplify and enhance the reconstruction of the ionisation signal. However, other studies [108, 109] opt not to employ them, partially due to the cost and complexity involved in manufacturing the additional wire plane that lacks instrumentation.

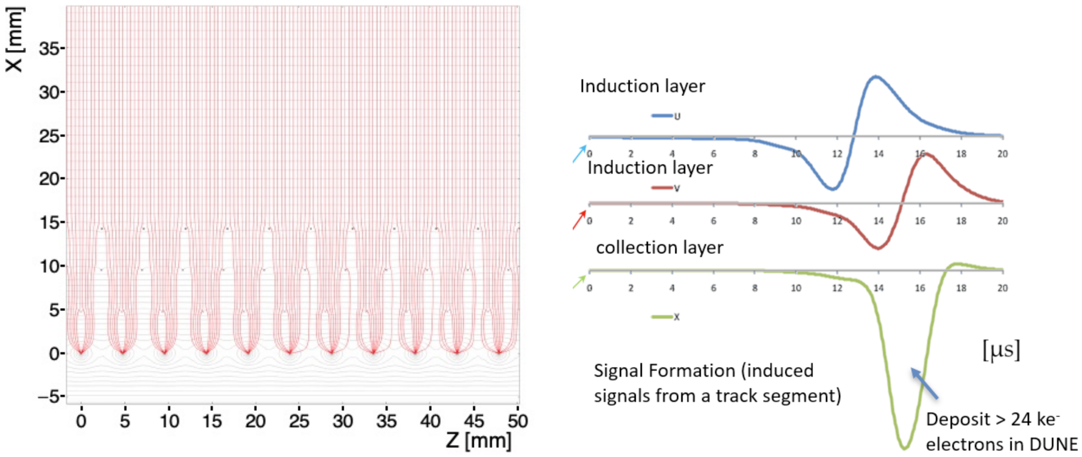

(a) **(b)**

Figure 3.9. An illustration of electric field lines (i.e., electron trajectories) and signal formation of a LArTPC SP HD in DUNE: a) electric field lines [4], b) signals induced on wires of anode planes by an ionising track [110]. The drifted ionisation electrons induce a bipolar signal on the wires of the induction planes u and v, which are then collected on the wires of the collection plane x resulting in a large unipolar signal. X represents the drift direction and Z is the direction perpendicular to the wires in the collection plane. The wire pitch of the induction planes and collection plane in the DUNE HD FD is 4.7 mm and 4.8 mm respectively. The distance between the wire planes is 4.8 mm. The wires in the induction plane u and v are inclined at ± 37.5 degrees with respect to wires in the x plane.

LArTPCs act as multi-channel waveform recorders, recording the signal induced on wires within a predefined time window. To generate a three-dimensional representation of interacting particles within the LArTPC, a minimum of two sensitive wire planes must be employed. These two planes enable the determination of two-dimensional coordinates within the wire plane. By combining the wire coordinates from two different planes, a two-dimensional reconstruction can be achieved in the plane perpendicular to the drift direction. For 3D reconstruction, the charge drift time needs to be calculated by knowing the charged particle's arrival time in the TPC (t_0) and the electron's arrival time at the anode. This determines the location of interacting particles in the direction of the electric field, and hence the third coordinate is determined. The most modern LArTPC detectors, such as DUNE and ProtoDUNE, use three instrumented planes. Even when the particle is moving parallel to the wires in one of the planes, this technology provides precise three-dimensional imaging.

The quantity of charge induced or collected on the wires is directly proportional to the amount of energy deposited by traversing particles into the detector. An estimate of the charge signal size on the collection plane can be given for a track that is parallel to the wire plane and perpendicular to the wires, as follows [4, 111]:

- For a MIP, the most probable energy loss of 170 keV/mm, a 5 mm track will produce 170 keV/mm × 5 mm/(23.6 eV/e) = 3.60×10^4 electrons = 5.76 fC.
- Following the occurrence of an initial recombination loss (at an electric field strength of 0.5 kV/cm), the expected outcome would be as: 3.60×10^4 electrons × 0.70 = 2.52×10^4 electrons = 4.04 fC. Tracks in proximity to the wire planes would exhibit the maximum signal.
- Considering the simulated electron lifetime $\tau = 3$ ms in DUNE FD SP LArTPC, the fraction of electrons which survive after drift time 2.19 ms (maximum drift distance 3.5 m with drift speed 1.6 mm/μs) calculated using Equation 3.3 is $\sim$ 0.482.
- The expected signal for 5 mm wire spacing is then 2.52×10^4 electrons × 0.482 = 1.21×10^4 electrons = 1.94 fC.
- The induction signals on the first and second wire planes are smaller as shown in Figure 3.9.

  To detect the small charge signal collected on the collection wires and the even lower current induced on the induction wires by drifting ionisation charge, low electronic noise is required. The development of cold electronics is a key breakthrough, achieving a very good signal-to-noise ratio. A key feature of the DUNE far detector design is the use of cryogenic (cold) electronics [111, 4] on the TPC wire planes, ensuring very low noise levels in charge readout and high signal-to-noise ratios for signal events of interest.

The particle energy loss per unit distance, dE/dx, is calculated using the collected charge or the number of electrons collected on the wires of the anode plane.

3.4 Scintillation light signal

3.4.1 Production

The production of scintillation light in liquid argon occurs as a result of the ionisation and excitation of charged particles traversing through it. An excited argon atom (Ar^*) combines with a neutral argon atom (Ar) and forms an excited argon dimer (Ar_2^*). This dimer then decays, emitting a scintillation photon. The process can be represented as follows [112]:

$$\mathrm{Ar}^* + \mathrm{Ar} \rightarrow \mathrm{Ar}_2^* \rightarrow 2\mathrm{Ar} + \gamma. \tag{3.4}$$

Additionally, the ionised argon atom (Ar^+) can pair with a neutral argon atom and produces an ionised argon dimer (Ar_2^+),

$$\mathrm{Ar}^+ + \mathrm{Ar} \rightarrow \mathrm{Ar}_2^+. \tag{3.5}$$

The ionised argon dimer can further recombine with the ionisation electron and produces an excited argon dimer (Ar_2^*), which subsequently de-excites by emitting a scintillation photon,

$$\mathrm{Ar}_2^+ + e^- \rightarrow \mathrm{Ar}_2^* \rightarrow 2\mathrm{Ar} + \gamma. \tag{3.6}$$

The scintillation light produced in both the above processes has a wavelength of 128 nm Vaccum Ultra-Violet (VUV) photon.

Excited argon dimers form singlet or triplet excited states. When these states return to the ground state, scintillation light is emitted. The singlet state has a relatively short lifetime of about 6 ns (τ_{fast}), while the triplet state has a longer mean lifetime of approximately 1.5 μs (τ_{slow}) [4]. These two states are commonly referred to as the fast (or prompt) and slow (or late) components, respectively. In the context of underground neutrino detectors, scintillation light serves as a trigger for detecting proton decay, supernova neutrinos, and atmospheric neutrinos [112]. Additionally, in neutrino and dark matter experiments, scintillation light proves valuable for particle identification. The proportion of fast to slow component intensities is influenced by the ionisation density of LAr and varies depending on the ionising particle. Highly ionising particles generate a greater concentration of electrons locally compared to cosmic-ray muons, resulting in an increased rate of singlet decay. The ratio of singlet to triplet decays, therefore, offers a means to distinguish highly ionising particles from muons and assists in the rejection of cosmic-ray spallation backgrounds [113].

Liquid argon emits about 40,000 photons per MeV of energy deposited by minimum ionising particles in the absence of an external electric field [4]. The presence of an electric field suppresses electron recombination, which leads to the formation of excited argon dimers, and consequently reduces the photon yield. For the DUNE SP HD LArTPC, which operates at an electric field strength of 0.5 kV/cm, the photon yield is approximately 24,000 photons per MeV. The presence of impurities in the argon, such as nitrogen or oxygen, can absorb scintillation photons produced during the de-excitation of argon dimers, further reducing the total photon yield [96, 114].

3.4.2 Transmission

The scintillation light emitted by excited argon dimers can travel long distances within liquid argon due to its high transparency to the light [82]. The mean free path of the emitted photons is primarily influenced by Rayleigh scattering and absorption caused by impurities. Although Rayleigh scattering does not affect the number of photons in transit, it does alter their trajectory [115]. Depending on their position and the distance they travel, this scattering can either impede or enhance the chances of light reaching photon detectors. The light that scatters before reaching a photon detector takes a longer path compared to directly propagating light. As a result, there is a significant variation in the arrival times of photons, which can be interpreted as a lengthening effect, particularly for the fast component of scintillation light. Consequently, the travel time of scintillation light in large-scale liquid argon detectors can vary from a few to several tens of nanoseconds.

3.4.3 Detection

To detect the scintillation light in LArTPC detectors, the use of photon detectors (PDs) capable of functioning at extremely low temperatures ($\sim$ 87K) is necessary. The prevailing technology employed in LArTPC detectors [116, 117, 118] for photon detection is the cryogenic photomultiplier tube (PMT). While these PMTs offer quantum efficiencies (QE) of up to 30%, their substantial dimensions pose challenges in terms of integration and impact the active space within the LAr. However, there has been a growing interest in employing silicon photomultipliers (SiPM) due to their advantages, including low power consumption, compact size, excellent noise performance at liquid argon temperatures, and high QE of up to 40% [119]. Current and future detectors such as ProtoDUNE [120] and DUNE [4] are shifting towards using Silicon Photomultipliers (SiPMs). Light guide bars or light trap devices, like the ARAPUCA or X-ARAPUCA devices [121], can amplify light collection via SiPMs in LArTPC detectors.

To detect the VUV light, the prevailing approach involves applying a coating of a wavelength-shifting (WLS) compound on the PDs. This compound converts the 128 nm light to a longer wavelength, which can be detected by a PMT [122]. By absorbing the VUV light and emitting light in the UV spectrum, the WLS compound enables PDs to detect it effectively. However, due to the random scattering of the re-emitted light, WLS-coated PDs experience a reduction in efficiency of approximately 50% as the emitted light deviates from the active surface. In the case of large-scale LArTPC used in neutrino detectors, PDs are typically positioned behind planes of instrumented wires [120, 4].

Chapter 4

Deep Underground Neutrino Experiment

The Deep Underground Neutrino Experiment (DUNE) [1, 2, 3, 4] is a cutting-edge experiment for neutrino science and nucleon decay searches. DUNE is currently under construction in the USA and involves two sites; Fermilab and Sanford Underground Research Facility (SURF). DUNE will employ the LArTPC technology at an unprecedented scale. DUNE will capture and reconstruct neutrino interactions in the $\sim$GeV range and above to study neutrinos and search for new physics using neutrinos from a Fermilab-generated beam and from the atmosphere. This includes long-baseline neutrino physics, which involves exploring phenomena such as neutrino oscillations, CP violation, and mass hierarchy. DUNE's dynamic range also allows sensitivity to neutrinos with energies around 5 MeV, enabling it to detect bursts of neutrinos expected from a galactic core-collapse supernova. Additionally, DUNE will investigate beyond the standard model (BSM) physics, including the search for nucleon decay.

This chapter commences with the experimental design of DUNE, outlined in Section 4.1. The description of the neutrino beam is presented in Section 4.2, while Section 4.3 briefly discusses the design of the DUNE near detector (ND). The research undertaken in this thesis centres on studies within the framework of the DUNE far detector (FD). A comprehensive description of the DUNE FD is presented in Section 4.4. Finally, Section 4.5 discusses the physics goals of DUNE, including neutrino oscillation, proton decay, low energy physics searches, and physics beyond the standard model.

4.1 Experimental design

The DUNE comprises a near detector at Fermilab, a far detector located 1.5 km underground and 1300 km away from the near detector at SURF, and the neutrino beam, originating from Fermilab. Figure 4.1 shows a schematic of the facilities at the two sites. Following an upgrade from its initial power of 1.2 MW to 2.4 MW, the beam will become the most intense neutrino beam ever operated. The neutrino beamline and conventional facilities, such as excavation and installation of detectors for the ND and FD, will be provided by the Long-Baseline Neutrino Facility (LBNF) project [1]. The far detector is designed to comprise four modules [2]. The first module will be a single-phase (SP) horizontal drift (HD) LArTPC, with a total mass of 17.5 kton of liquid argon and a minimum fiducial mass of 10 kton, followed by a SP vertical drift (VD) LArTPC [123] for the second module. The design of the third and fourth modules will remain flexible, allowing us to incorporate lessons learned during the construction of the initial two modules.

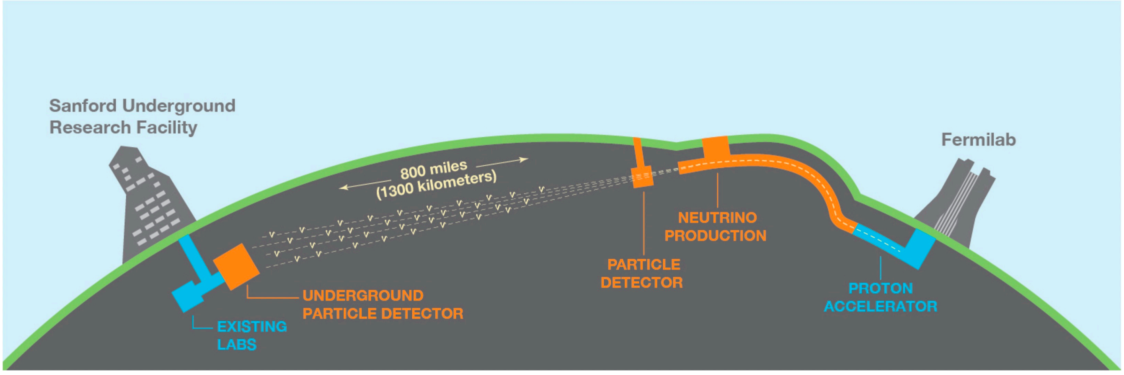

Figure 4.1. Schematic of the DUNE project: Fermilab, the host lab and the house of the ND are shown on the right. The neutrino beam will be produced at the Fermilab. The SURF laboratory is shown on the left. DUNE FD at SURF will receive the neutrino beam from Fermilab, 1300 km away. The distance between the ND and FD will define the baseline for neutrino oscillation [1].

4.2 Neutrino beam

The neutrino beam for DUNE will be produced at Fermilab's neutrino complex. A proton beam with an energy 120 GeV and a beam power of 1.2 MW will be generated at the start of the DUNE operations. A total of 1.1×10^{21} protons on target (POT) per year will be delivered with a proton beam momentum of 120 GeV/c [2]. The high-energy proton beam strikes a graphite target, producing

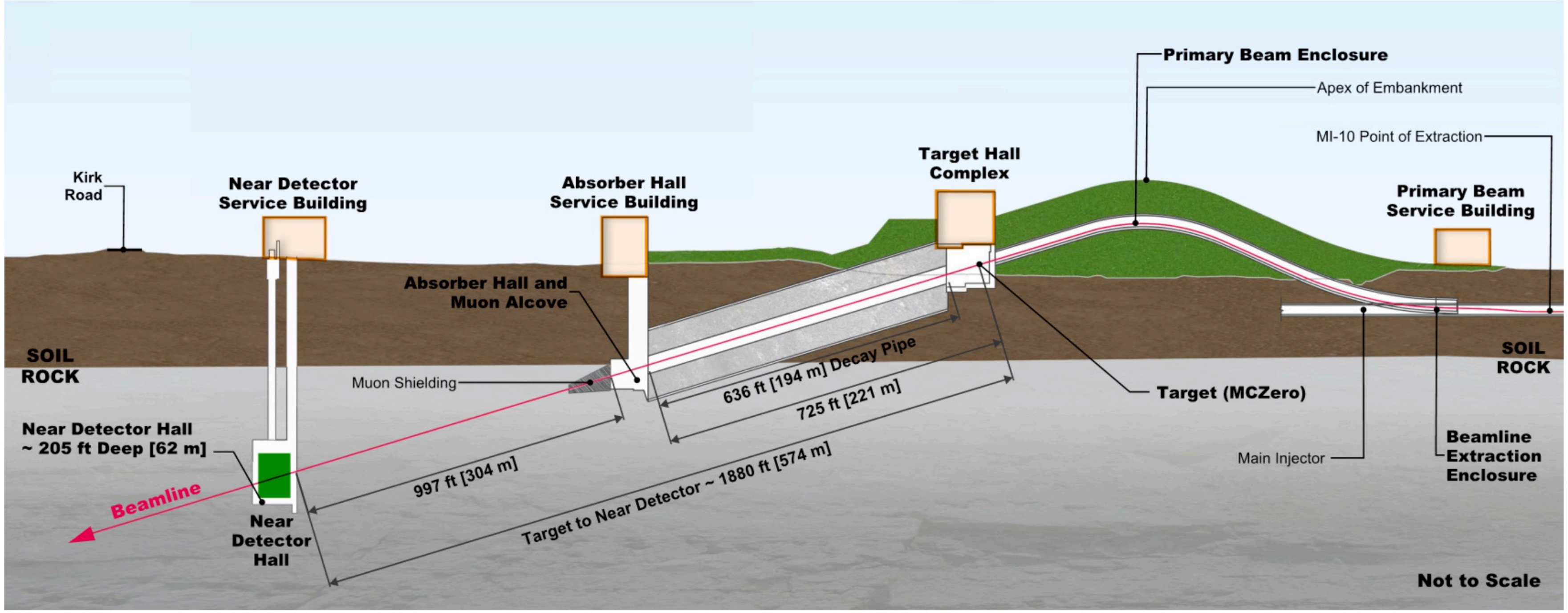

Figure 4.2. Neutrino beamline and DUNE ND hall at Fermilab [1].

hadronic showers of pions. Magnetic horn will focus these pions into a 194 m long decay pipe, where hadrons decay into muons and muon neutrinos. By choosing the polarity of the magnetic focusing horns, the selection of positive and negative pions is made, allowing the beam to run in neutrino or antineutrino mode. To address potential contamination of electron neutrinos produced in muon decay, muons are stopped in a shielding after the decay pipe. Figure 4.2 illustrates the neutrino beamline at the DUNE ND site. The neutrino flux will be first measured at ND and then detected at FD for precision oscillation measurements. Figure 4.3 shows the neutrino energy spectra at DUNE FD while the beam operates in neutrino and antineutrino modes.

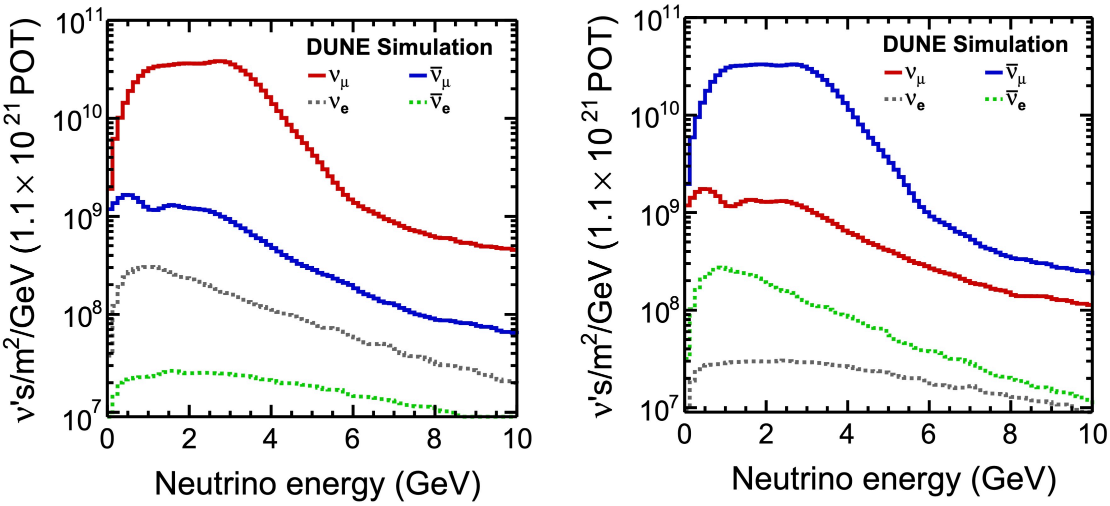

(a) **(b)**

Figure 4.3. Neutrino fluxes at DUNE FD operating at different modes: a) neutrino mode, b) antineutrino mode. The figure is taken from [124].

4.3 Near detector

The Near Detector plays a crucial role in the DUNE experiment, functioning as both an experimental control centre and a valuable component of the experiment. It measures and monitors the beam, and constrains systematic uncertainties [2]. The near detector measures various critical parameters, including the total beam neutrino flux, the rate of unoscillated neutrino interactions, and the initial energy spectra of unoscillated neutrinos or antineutrinos, all in proximity to the production point. The measurements conducted in the ND hold immense importance in establishing the oscillation signal spectrum within the FD.

As depicted in Figure 4.2, the ND will be positioned 574 m downstream from the beam source. This detector setup will comprise three distinct detectors. Two of them are capable of off-axis movement, allowing for exploring diverse neutrino energy spectra. The three detectors, ND-LAr, multi-purpose detector (MPD), and System for on-Axis Neutrino Detection (SAND), are strategically positioned along the neutrino beam direction [2]. Figure 4.4 shows the arrangement of these detectors, with the beam direction oriented from right to left. A brief description of each is provided below.

1. **ND-LAr:** ND-LAr consists of 35 LArTPCs and is constructed using ArgonCube technology [2, 125]. The fiducial mass of ND-LAr is 67 ton, with dimensions of 5 m (in beam direction) × 7 m × 3 m (height). ND-LAr dimensions were carefully chosen to optimise the containment of complex hadronic showers that may result from neutrino interactions within the LArTPC active volume. While closely resembling the FD, ND-LAr modifies the charge readout system due to the need to handle a high rate of interactions. Neutrino interactions produce high-energy leptons, mainly GeV-scale muons and recoil hadrons. The acceptance for highly energetic muons above 0.7 GeV/c in standalone ND-LAr starts to decrease due to limitations in containment. Given that muon momentum and charge are crucial for neutrino energy determination, a magnetic spectrometer is essential downstream of ND-LAr to measure these parameters precisely.

2. **MPD:** MPD will be positioned directly downstream to determine the charge and momenta of muons escaping ArgonCube. The MPD is composed of a high-pressure gaseous argon Time Projection Chamber (HPgTPC) surrounded by an electromagnetic calorimeter (ECAL) within a 0.5 T magnetic field. Utilising high-pressure gaseous argon time projection chambers (HPgTPCs) offers better measurement precision, particularly at lower energies, when compared to LArTPCs. Furthermore, these HPgTPCs offer enhanced identification capabilities, particularly for charged pions and protons. These advanced capabilities are crucial for imposing tighter constraints on systematic uncertainties for the long-baseline oscillation analysis.

   ND-LAr and MPD are notably equipped with a flexible rail system, enabling them to move off-axis by up to 33 meters. This system, known as DUNE PRISM [2], provides adaptability that allows for measuring neutrino flux from various angles. This flexibility separates neutrino fluxes and interaction cross-sections, contributing to a more comprehensive analysis.

3. **SAND:** The System for on-Axis Neutrino Detection (SAND) is the third detector, serving as a neutrino spectrum monitor [2] and remains in a fixed position. SAND comprises 3D scintillator trackers within a superconducting magnet at 0.6 T. Its primary function is to monitor the neutrino flux on-axis while ND-LAr and MPD are positioned off-axis. SAND is an alternative detector technology that uses a different target than the far detector, allowing for comparisons and systematic cross-checks with the neutrino flux determinations from ND-LAr.

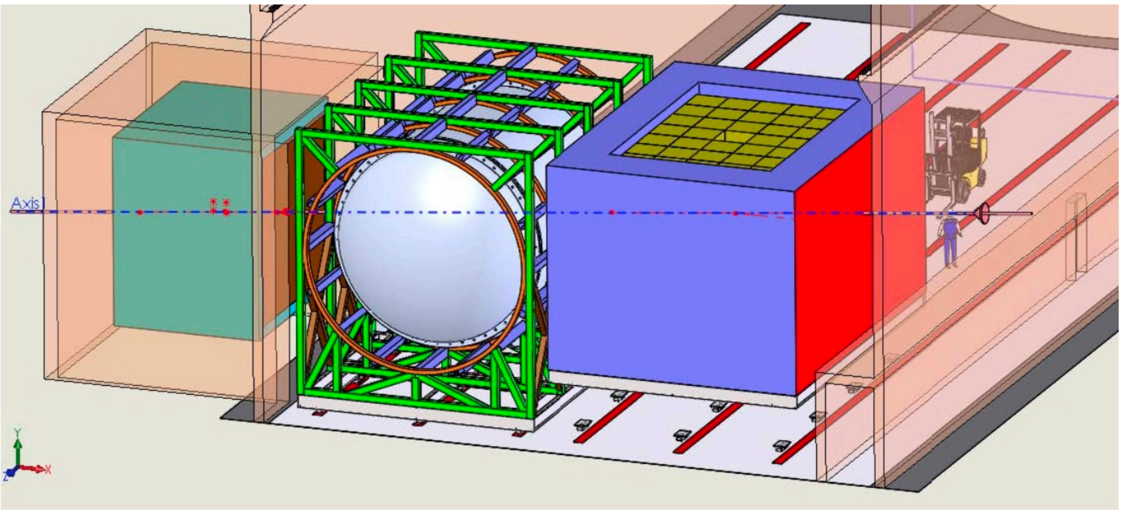

Figure 4.4. An illustration of the ND hall showcases the various detector subcomponents. ND-LAr is the foremost component in the direction of the beam, which travels from right to left in this image. Immediately downstream from ND-LAr is MPD, which functions as a muon spectrometer for ND-LAr. Extending further beyond MPD is SAND [2].

4.4 Far detector

4.4.1 Overview of the far detector

The primary purpose of the Far Detector (FD) is to fulfil the core physics objectives outlined in Section 4.5. A crucial prerequisite for the success of DUNE's scientific goals lies in the FD's ability to reconstruct neutrinos with exceptional efficiency and achieve precise energy resolution across a broad spectrum of energies [2, 4]. The significance of this detector is emphasised by its ability to provide millimetre-level spatial precision for tracking the trajectories of charged particles. This characteristic holds the potential for precise reconstruction of neutrino interactions and the investigation of rare interactions. The detector design is aimed to identify interactions down to the MeV scale, encompassing both solar and Supernova Burst (SNB) neutrino energies.

The DUNE FD will comprise four modules, each with a 10 kt fiducial mass [4]. The LArTPCs fit inside a cryostat which is 65.84 m long, 18.94 m wide, and 17.84 m high [3]. The cryostat is filled with liquid argon with a total mass of 17.5 kton. Each cryostat will be enclosed within an insulated double membrane, employing a technology frequently used in industrial settings to contain liquefied natural gas. Figure 4.5 shows the cavern layout for the DUNE FD. The first detector module will be placed in the east end of the north cavern, whilst the second will be installed in the east end of the south cavern. The first two detector modules have distinct designs. The first detector module utilises the single-phase horizontal drift technology (FD1-HD). This technology has been used successfully in several previous experiments including ProtoDUNE, SBND and MicroBooNE [108, 109, 120]. The second far detector module implements the single-phase vertical drift technology (FD2-VD) [123].

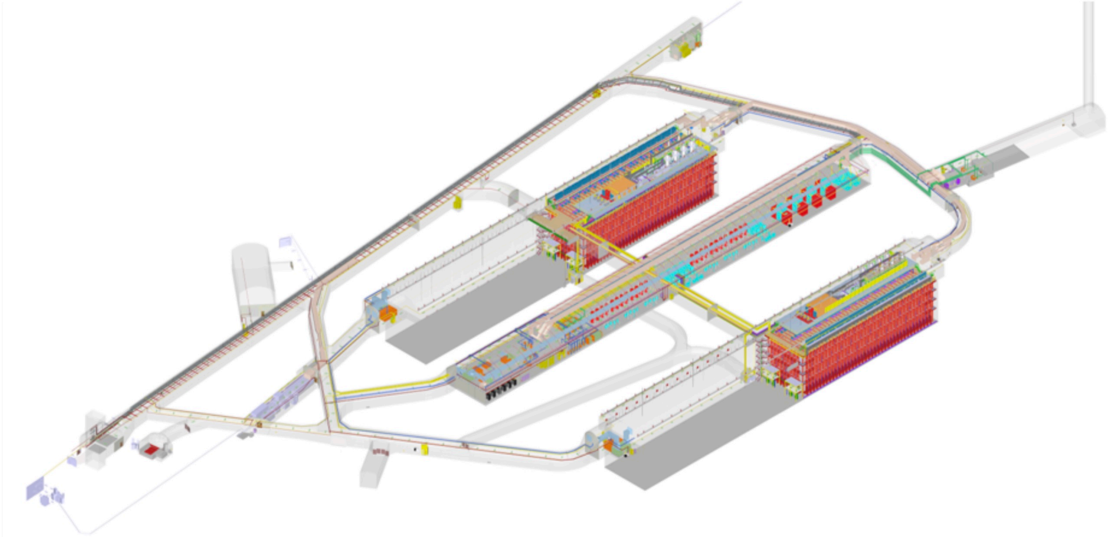

Figure 4.5. Underground cavern and cryogenics systems at SURF in South Dakota. The large red boxes illustrate the first two far detector modules. Situated amidst the two cryostat caverns, the central cavern hosts the data acquisition (DAQ) system and cryogenic facilities. The Ross Shaft, the vertical shaft providing access to the DUNE underground area, appears on the right [123].

4.4.2 Single-phase horizontal drift

A comprehensive description of LArTPC technology used in the far detector can be found in Chapter 3. The FD active volume measures 12.0 m ×14.0 m × 58.2 m [4]. This volume is partitioned into four drift regions, each with a drift length of 3.5 m, and has five alternating anode and cathode walls, each wall measuring 58 m × 12 m. In the DUNE FD, starting from the anode, there are three anode and two cathode walls. The cryostat encompasses the LArTPCs module, as depicted in Figure 4.6, with the LAr maintained at a temperature of 88 K (−185°C). An electric field is applied between the anode plane assembly (APA) and the cathode plane assembly (CPA) to create the drift region within the active volume. Each cathode wall in a module is called a CPA array. The CPA is a 1.2 m × 4 m panel from which the CPA arrays are formed, with each array containing 150 CPAs. The anode walls are each made up of 50 APA units, each measuring 6 m × 2.3 m. The APAs hang vertically, with each anode wall consisting of two APAs in height and 25 APAs in width. There will be 150 APAs and 300 CPAs in a 10 kt module of DUNE FD. The critical parameters of the SP HD module are listed in Table 4.1.

Table 4.1. Key specification of 10 kt SP HD FD module. The U and V are induction planes, X is the collection plane and G is the shielding plane of an APA [4, 3].

Item	Quantity
TPC size	12.0 m × 14.0 m × 58.2 m
Nominal fiducial mass	10 kt
APA size	6.0 m × 2.3 m
CPA size	1.2 m × 4.0 m
Number of APAs	150
Number of CPAs	300
U, V plane wire spacing	4.669 mm
X, G plane wire spacing	4.790 mm
Number of X-ARAPUCA PD bars	1500
X-ARAPUCA PD bar size	209 cm × 12 cm × 2 cm
Design drift voltage	- 180 kV
Design drift field	500 V/cm
Drift length	3.5 m
Drift speed	1.6 mm/μs

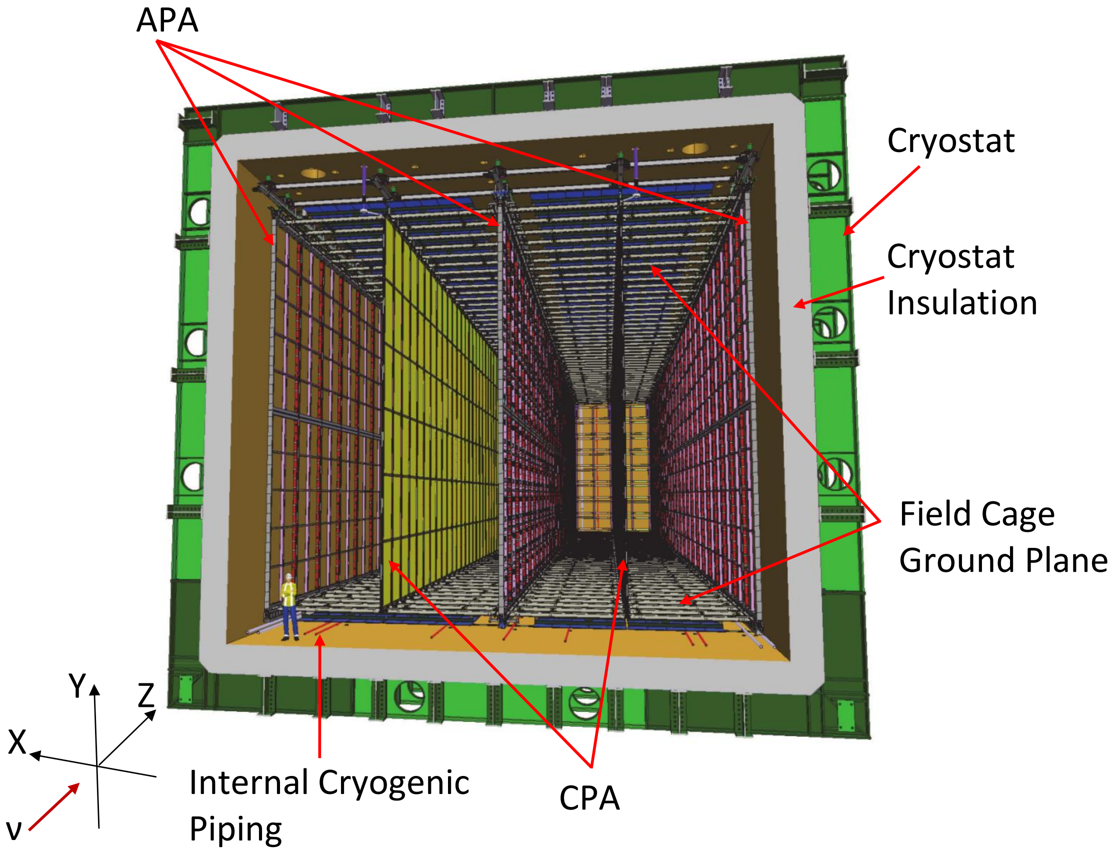

Figure 4.6. Schematic of a 10 kt DUNE FD SP module illustrates the arrangement of alternating APAs and CPAs, accompanied by the field cage, detector support system, and cryostat. The detector module is segmented into four drift volumes. Each drift volume has dimensions 58.2 m long, 3.5 m wide, and 12.0 m high. The figure is adopted from [3].

4.4.3 Anode plane assembly

The anode plane assembly is designed with two sides, featuring three active wire planes and an additional shielding layer known as the grid layer [4]. The plane wires are wrapped around the frame maintaining ~ 5 mm wire spacing on the layers. Figure 4.7 shows a schematic of an APA. The first wire plane encountered by drifting electrons is the grid plane (G). Its function is to shield against charges that are far away, promoting greater field line stability near the wire planes. Notably, the grid wire plane is not connected to the readout system. Following the grid plane, the subsequent planes are induction wire planes (U and V). These planes have a bias voltage such that electrons will not be collected but will induce charge when drifting electrons pass through the planes. The U and V planes are completely transparent to the drifting electrons. The last wire plane, a collection wire plane (X), collects the drifted electrons. Table 4.2 shows the bias voltages of wire planes of an APA. The X wires are oriented parallel to the y-axis of the detector, while the U and V wires are wrapped around at a relative angle of ± 35.7° with respect to the X wire orientation. This strategic configuration guarantees that every X wire intersects with each U and V wire exactly once. This intersection pattern facilitates the precise mapping of ionisation depositions onto the yz plane, which corresponds to the face of the APA. Figure 4.8 shows a completed APA covered in a protective layer produced at Daresbury laboratory in the United Kingdom (UK).

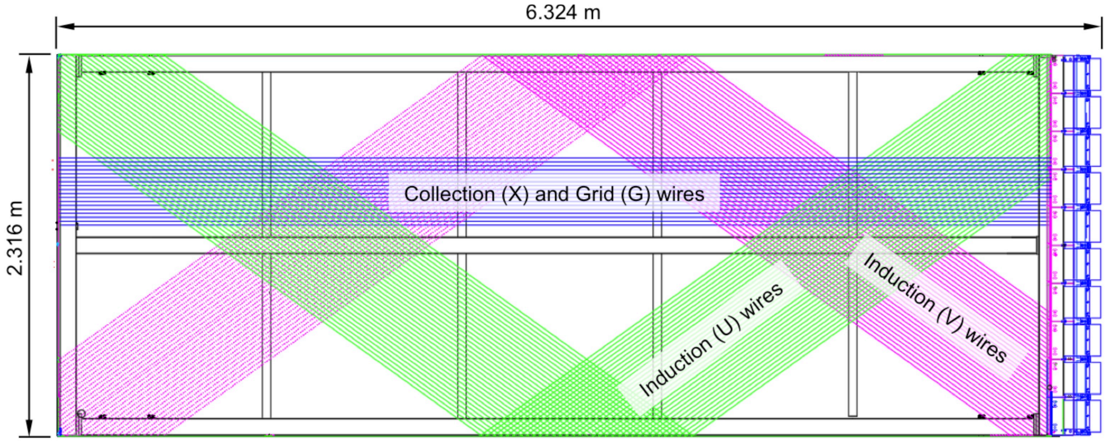

Figure 4.7. An illustration of the DUNE APA structure and wire wrapping scheme showing small portions of the wires. Each APA comprises four wrapped induction wire planes and two collection wire planes. The photon detector is sandwiched between two collection wire planes that span the width of an APA [4].

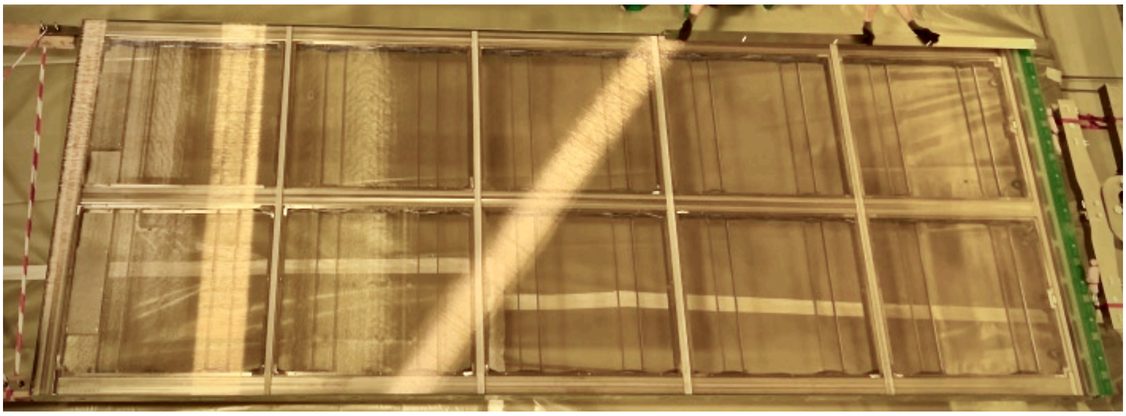

Figure 4.8. A completed APA built at the Daresbury APA production factory in the UK [126].

Table 4.2. Baseline bias voltages for the wire planes of an APA [4].

Anode Plane	Bias Voltage
G - Grid	− 665 V
U - Induction	− 370 V
V - Induction	0 V
X - Collection	820 V
Grounding Mesh	0 V
Cathode	− 180 kV

The photon detection system is integrated into an APA frame to measure interaction time. Figure 4.9a illustrates the integration of the photon detectors within the APAs. An individual PD unit comprises a light guide and 12 Silicon Photomultipliers (SiPMs) [4]. Each APA frame contains ten equally spaced PD units. A wavelength shifter plate is used in the PD system, which converts the 127 nm scintillation photons into UV light of wavelength 430 nm. A specially designed device called X-ARAPUCA collects this wavelength-shifted light illustrated in Figure 4.9b.

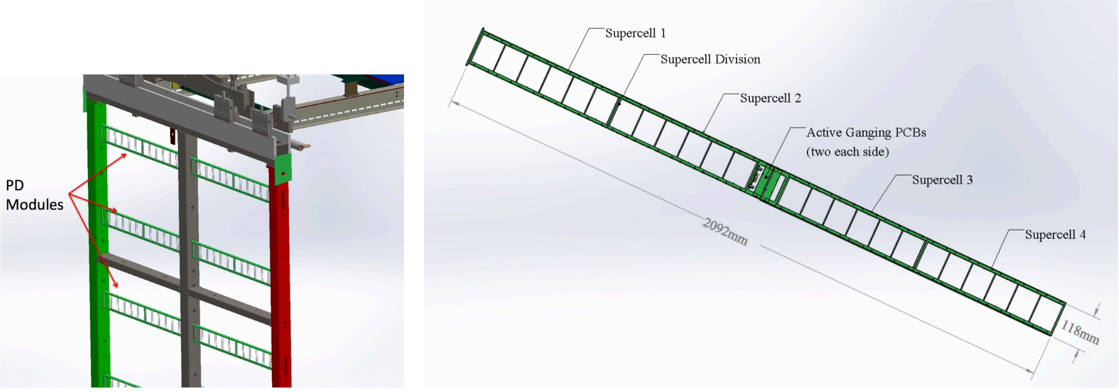

(a) **(b)**

Figure 4.9. Photon detection system in APA modules: a) the photon detectors, X-ARAPUCA mounted inside an APA, b) X-ARAPUCA module spanning the width of an APA. There are 24 X-ARAPUCA cells grouped into four supercells [4].

4.4.4 Cathode planes and high voltage

The single-phase DUNE FD has two cathode plane assembly arrays formed from 150 CPAs (50 along the length, stacked three high) as shown in Figure 4.6. Each CPA has an independent high voltage (HV) supply of −180 kV [4]. With the APA arrays held close to the ground, this setup creates a uniform electric field of 500 V/cm across the drift volume. A typical minimum ionising particle passing through the argon produces about 60,000 ionisation electrons per centimetre, which drift toward the anodes at approximately 1.6 mm/μs [4]. The time to cover the full drift distance is about 2.2 ms.

4.4.5 Field cage

In the single-phase DUNE FD module, a field cage (FC) covers the top, bottom, and end walls of all the drift volumes as depicted in Figure 4.6. This setup provides the necessary boundary conditions to ensure a uniform electric field, unaffected by the presence of the cryostat walls. The FC is constructed from adjacent extruded aluminium open profiles (electrodes) running perpendicular to the drift field. These electrodes are set at increasing potentials along the 3.5 m drift distance, from the CPA HV (−180 kV) to ground potential at the APA sensor arrays [4].

4.5 Physics goals of DUNE

The DUNE includes a wide range of physics programmes [2]. As a long-baseline neutrino experiment, the primary goals of DUNE include measuring CP violation in the leptonic sector and determining the neutrino mass ordering through high-precision measurements of neutrino oscillation parameters. Among other DUNE primary objectives are nucleon decay searches across various decay modes and detecting and precisely measuring the neutrino flux originating from core-collapse supernova bursts.

Beyond its primary objectives, the DUNE science programs include further accelerator-based search for the BSM phenomena [2]. These include measurements related to charge, parity, and time reversal symmetry (CPT), investigations into sterile neutrinos, heavy neutral leptons, and the measurement of tau neutrino appearance. Moreover, DUNE includes the measurement of neutrino oscillation phenomena through the study of atmospheric neutrinos, dark matter searches, and non-accelerator searches for neutron-antineutron oscillation as part of its BSM physics efforts. The ND is also involved in additional neutrino interaction physics programs, spanning a diverse range of neutrino cross-section measurements and studies of nuclear effects. Some of the key physics goals of DUNE are briefly discussed in the subsequent subsections.

4.5.1 Neutrino oscillation physics at DUNE

Neutrino oscillation confirms the non-zero neutrino mass and manifests CP violation in the lepton sector [5, 21, 127, 128]. To determine the neutrino mass ordering (hierarchy) and quantify the CP violation parameters, DUNE will take a comprehensive study of ν_μ disappearance and ν_e appearance using ν_μ and $\bar{\nu}_\mu$ beam from Fermilab [2]. The two measurements will be repeated, looking for $\bar{\nu}_\mu$ disappearance and $\bar{\nu}_e$ appearance [124]. The concept of “disappearance” arises from the observation that the DUNE neutrino beam primarily consists of muon neutrinos. Consequently, the far detector is anticipated to register a diminished count of muon neutrinos compared to the near detector, attributable to neutrino oscillations. The neutrino energy spectra at DUNE FD are shown in Figure 4.3 illustrating the beam operation in neutrino and antineutrino modes. The “appearance” study will measure the increased rate of electron neutrinos as a consequence of the oscillation of muon neutrinos into electron neutrinos. For the appearance studies, DUNE will look at the appearance of ν_e and ν_τ from the ν_μ beam.

Figures 4.10a and 4.10b present the oscillation probability of ν_μ converted into ν_e, $P(\nu_\mu \to \nu_e)$, and $\bar{\nu}_\mu$ converted into $\bar{\nu}_e$, $P(\bar{\nu}_\mu \to \bar{\nu}_e)$, respectively, at the far detector location. Both distributions are constructed assuming the normal ordering of the neutrino mass hierarchy.

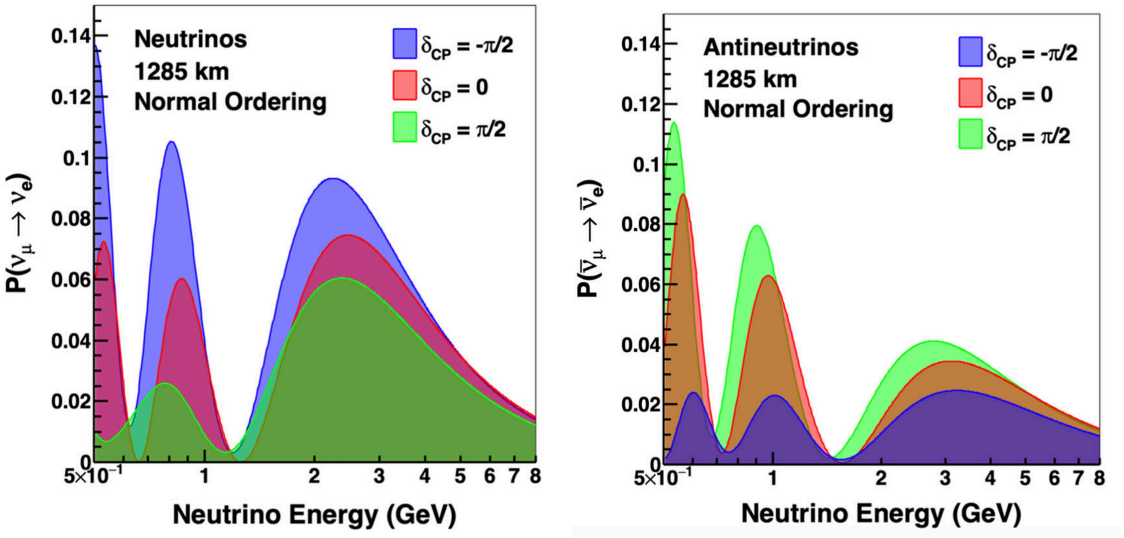

(a) (b)

Figure 4.10. Appearance probability at a baseline of 1285 km in DUNE as a function of neutrino energy for δ_{cp} values $-\pi/2$, 0, and $\pi/2$: a) ν_μ being converted into ν_e, b) $\bar{\nu}_\mu$ being converted into $\bar{\nu}_e$ [124].

The sensitivities to the mass hierarchy and CP violation are determined by comparing oscillated far detector spectra in each oscillation channel to unoscillated near detector spectra, taking into account the systematic uncertainties [124]. Figure 4.11 shows the simulated sensitivity with which CP violation can be observed as a function of true δ_{CP} values. Figures 4.11a and 4.11b represent the sensitivity for exposures corresponding to seven and ten years of data in normal ordering and inverted ordering, respectively [124]. The DUNE experiment follows a staging plan, which involves running the experiment with varying exposure over different years. The sensitivity exhibits a distinctive double-peak pattern which arises due to the fact that CP violation is maximal at $\delta_{\text{CP}} = \pm\, \pi/2$ and decreases around the CP conserving value of $\delta_{\text{CP}} = 0$. Following an exposure of seven years under normal ordering, the median CPV sensitivity attains a 5σ for a small range of values. However, with extended exposure of ten years, the median CP violation sensitivity achieves a 5σ significance level across a broader range of δ_{CP} values. In inverted ordering, DUNE exhibits slightly stronger sensitivity to CP violation and achieves a 5σ significance for a wide range of values after seven years of exposure.

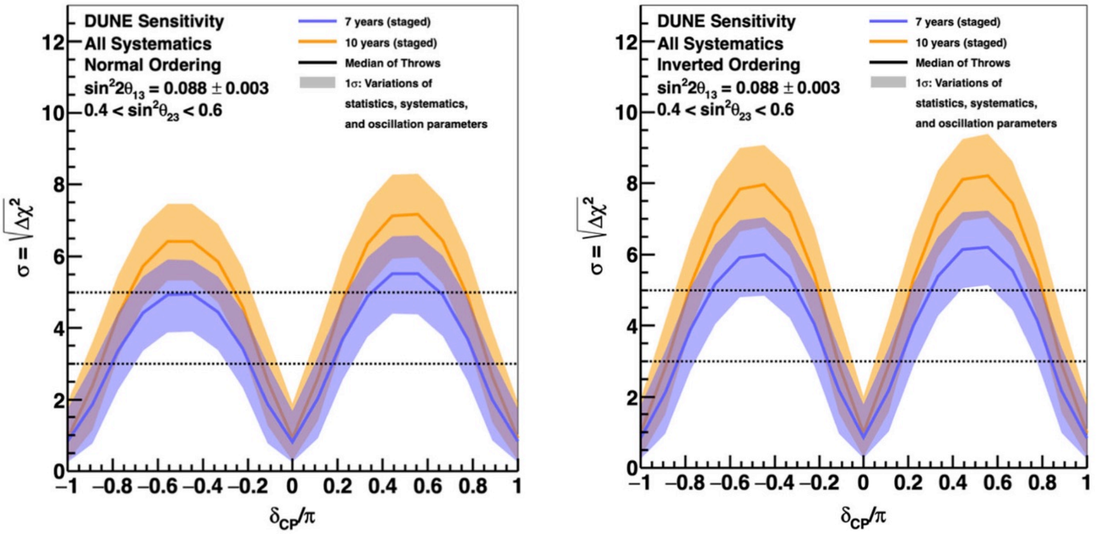

(a) **(b)**

Figure 4.11. The significance of the CP violation ($\delta_{\mathrm{CP}} \neq 0$ or π) discovery by DUNE as a function of the true value of δ_{CP}: a) normal ordering, b) inverted ordering. The width of the transparent bands covers 68% spread of the value. The solid lines show the median sensitivity [124].

Figure 4.12 shows the sensitivity of the DUNE for neutrino mass ordering as a function of true δ_{CP} values for exposures of seven and ten years [124]. Figure 4.12a shows the significance with which normal mass ordering can be observed, while Figure 4.12b illustrates the significance of inverted ordering. DUNE would achieve a significance above 5σ regardless of the value of δ_{CP}. The distinctive shape arises due to the degeneracy between matter and the CP violation effect. For normal ordering, it occurs close to $\delta_{\mathrm{CP}} = \pi/2$ while for inverted ordering δ_{CP} is close to $-\pi/2$.

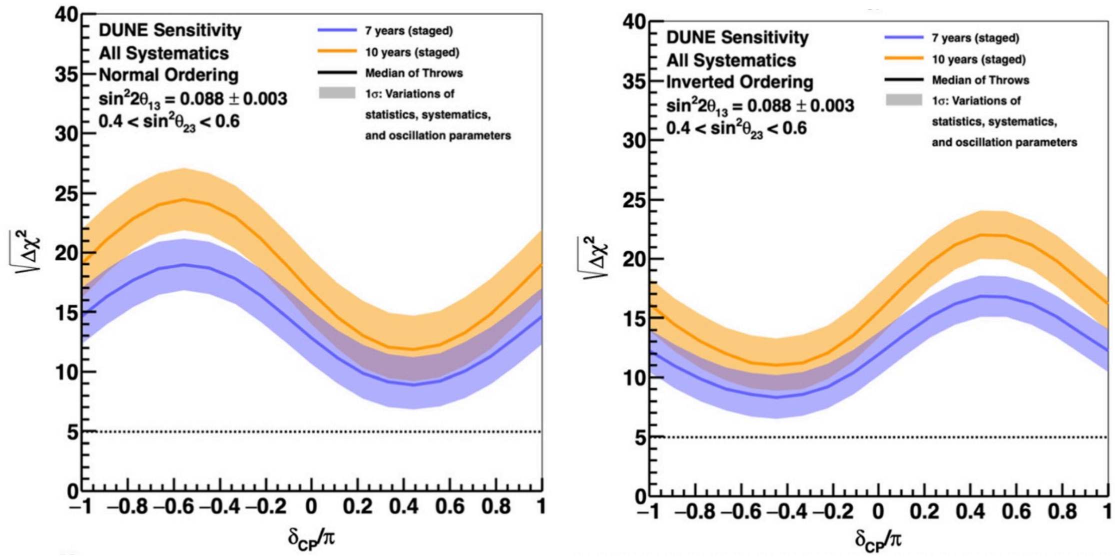

(a) **(b)**

Figure 4.12. The significance of the determination of normal mass ordering by DUNE as a function of the true value of δ_{CP}: a) normal ordering, b) inverted ordering. The width of the transparent bands covers 68% spread of the value. The solid lines show the median sensitivity [124].

Figure 4.13 shows the significance with which CP violation and mass ordering can be observed as a function of exposure in kt · MW · years [124]. Figure 4.13a shows the significance with which CP violation can be determined assuming normal mass ordering for 75% and 50% of δ_{CP} values, and when $\delta_{\mathrm{CP}} = -\pi/2$. The width of the band shows the impact of applying an external constraint on θ_{13} [2]. The observation of CP violation can achieve a 5σ significance level in approximately seven years (equivalent to 336 kt · MW · years) when δ_{CP} is set to $-\pi/2$. Similarly, when considering 50% of δ_{CP} values, CP violation can be detected with 5σ significance in approximately ten years (equivalent to 624 kt·MW·years). Finally, CP violation can be observed at a 3σ significance level for 75% of δ_{CP} values after a running period of about thirteen years. Figure 4.13b shows the significance with which normal mass ordering can be determined for 100% of δ_{CP} values, and when $\delta_{\mathrm{CP}} = -\pi/2$. The width of the band shows the impact of applying an external constraint on θ_{13}. The observation of mass ordering can achieve a 5σ significance level after exposure of 66 kt · MW · years corresponding to 2 years of data taking for all δ_{CP} values [124].

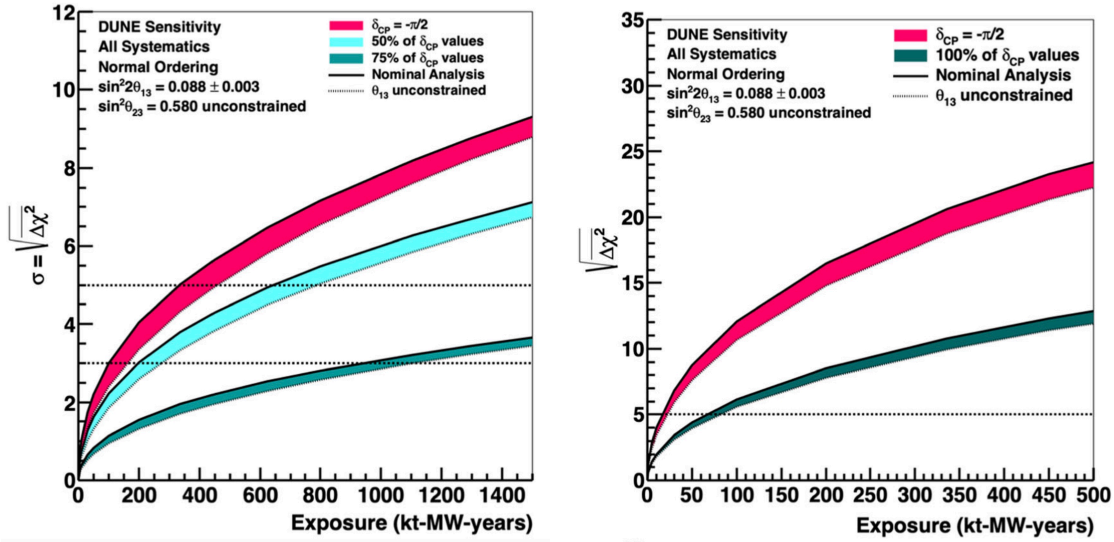

(a) **(b)**

Figure 4.13. a) The significance of the CP violation as a function of exposure in kt · MW · years for the case when $\delta_{\mathrm{CP}} = -\pi/2$, for 75% and 50% of δ_{CP} values. b) The significance of the determination of normal mass ordering as a function of exposure in kt · MW · years for the case when $\delta_{\mathrm{CP}} = -\pi/2$, and for 100% of δ_{CP} values. The width of the band shows the impact of applying an external constraint on θ_{13} [124].

4.5.2 Proton decay searches at DUNE

Nucleon decay is a rare event in high energy physics predicted by several grand unified theories (GUTs) [129, 130, 131] beyond the SM. Nucleon decay searches provide the most direct way to probe baryon number conservation in the SM and test the GUTs in the energy scale $10^{15} - 10^{16}$ GeV. This energy range cannot be achieved by accelerators. However, it can be studied by large underground detectors. The DUNE has the ability to probe different nucleon decay channels due to the size of the fiducial mass, excellent imaging and particle identification capabilities with the LArTPC technology. The two dominant decay modes predicted by GUT models are $p \to e^+ + \pi^0$ and $p \to K^+ + \bar{\nu}$ [132, 133, 134, 135].

The proton decay mode $p \to e^+ + \pi^0$ is often predicted to have a high branching ratio of the two decay modes. In this decay, the mass of a proton is converted into electromagnetic shower energy of π^0 and e^+. This channel is a comparably more straightforward experimental signature for water Cherenkov detectors like Super-Kamiokande, where electromagnetic showers produce a ring of Cherenkov light and signal can be identified [136]. In the case where a neutral pion interacts in the nucleus by absorption, scattering, or charge exchange after a proton decay event, the correct reconstruction of proton mass and momentum (which is expected to close to zero) becomes challenging. However, a water molecule, having two free protons, remains unaffected by such pion interaction, contributing to the high efficiency of water Cherenkov detectors. In the LAr, the detection efficiency for the $p \rightarrow e^+ + \pi^0$ is limited due to inelastic intra-nuclear scattering of the neutral pion. DUNE will have the capability to detect this mode but it is less likely to outperform the limit placed by the Super-Kamiokande and Hyper-Kamiokande experiments [136, 137]. Figure 4.14 shows a lifetime comparison of experimental limits on key decay modes predicted by GUTs [2]. A more complete analysis gave a less favourable prediction for the mode with a kaon [138].

The proton decay mode $p \rightarrow K^+ + \bar{\nu}$ is particularly interesting in DUNE since LArTPCs can detect and identify the K^+ produced in this channel by its distinctive dE/dx signature [2]. The kaon produced in this decay has energy below the Cherenkov threshold and cannot produce Cherenkov light, hence, it cannot be detected by the Cherenkov detector. LArTPC provides the opportunity to observe all decay modes with a charged kaon in the final state. The K^+ produced in this channel has a higher ionisation density than lower mass particles such as pions and muons which results in higher detection efficiency in LArTPC compared to water Cherenkov, and many final state K^+ decay would be fully reconstructable in LArTPC. Given a signal efficiency of 30% and an anticipated background rate of one event per $\mathrm{Mt} \cdot \mathrm{year}$, the experiment can set a 90% confidence level (CL) lower limit on the proton lifetime for the $p \rightarrow K^+ + \bar{\nu}$ decay channel which is 1.3×10^{34} years [138], assuming no signal is observed over ten years of running with a 40 kt of fiducial mass. The current lifetime limit placed by Super-K for this decay channel is 5.9×10^{33} years [136].

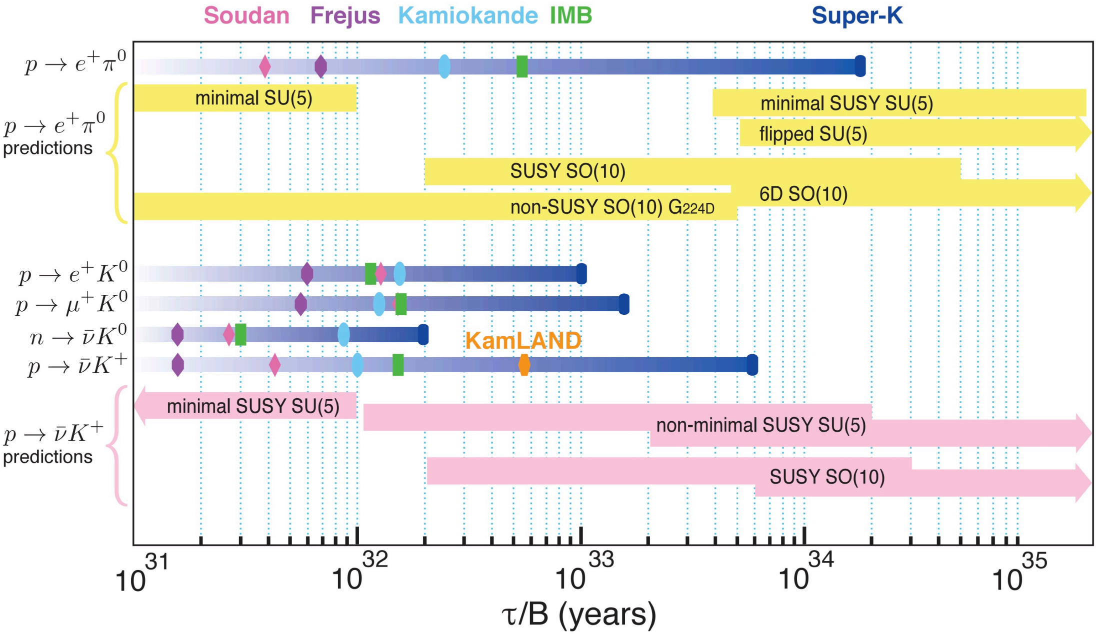

Figure 4.14. Summary of experimental nucleon decay searches and predicted lifetime limits from past and currently running experiments. The limits shown are 90% confidence level (CL) lower limits on the partial lifetimes; τ/B, where τ is the total mean lifetime and B is the branching fraction. Marker symbols indicate published experimental limits as labelled by the colours on top of the figure. The figure is taken from [2].

4.5.3 Low energy physics searches at DUNE

DUNE will be capable of detecting low-energy (∼5–100 MeV) astrophysical neutrinos from supernovae and the Sun [139, 140, 2]. DUNE will also look for physics beyond the standard model, such as dark matter searches. This includes the detection of weakly interacting massive particles (WIMPs) through low-energy nuclear recoils (∼100 keV) in the detector [141]. Figure 4.15 shows the low-energy physics targets and their energy ranges. Radiological backgrounds have a critical role in detecting these experiments. Important backgrounds and sources are also shown in the figure. Some of the low-energy physics searches at DUNE are discussed next. A discussion of the radiological backgrounds of these experiments can be found in Ref. [141].

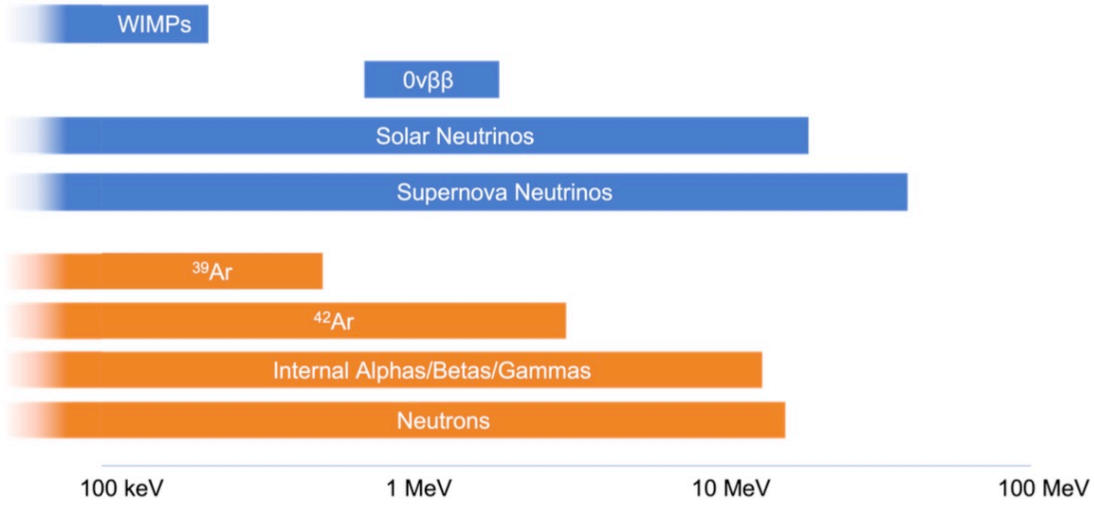

Figure 4.15. Low energy physics targets and their energy ranges with primary radiological backgrounds of these experiments [141].

1. **Supernova neutrino searches at DUNE:**

   One of the primary physics goals of DUNE is to detect and measure the ν_e flux from a core-collapse supernova within our galaxy. A core-collapse supernova occurs when a massive star reaches the end of its life. The core-collapse neutrino signal primarily composed of ν_e from the reaction $e^- + p \rightarrow \nu_e + n$ [139]. Liquid argon is particularly sensitive to the ν_e component of a supernova neutrino burst, through the dominant interaction, CC absorption of ν_e on ^{40}Ar, represented as: $\nu_e + {}^{40}\text{Ar} \rightarrow e^- + {}^{40}\text{K}^*$. The observable outcome of this interaction is the electron plus de-excitation products from the excited $^{40}\text{K}^*$ final state. DUNE will bring unique ν_e sensitivity via ν_e charged-current (ν_eCC) interactions from around 5 MeV to several tens of MeV. The most famous supernova in particle physics, Supernova 1987A, released a burst of neutrinos that travelled 50 kiloparsecs before reaching the Earth [142, 143]. A few dozen antineutrinos were detected between Kamiokande-II, IMB, and Baksan [144]. Should a supernova occur during DUNE's lifetime, DUNE will be able to make leading observations of supernova features [2]. The neutrinos from a supernova burst (SNB) carry intrinsic information about the progenitor star, the collapse, the explosion, and the outcome of the supernova—whether a neutron star or black hole forms.

2. **Solar neutrino searches at DUNE:** Solar neutrinos originating from the Sun, are produced as a byproduct of nuclear fusion in its core. Detecting solar neutrinos is uniquely challenging due to their very low energies

($< \sim$18 MeV) [145]. DUNE is sensitive to ν_e in the MeV range ($>$ 5 MeV) making it a prime candidate for detecting solar neutrinos [2]. At DUNE, solar neutrinos can be detected by the CC interaction: $\nu_e + {}^{40}\text{Ar} \rightarrow e^- + {}^{40}\text{K}^*$. Above 5 MeV electrons can be detected with high efficiency in DUNE. The solar neutrino event rate in a 40 kt LArTPC is $\sim$100 per day [2]. DUNE can measure solar mass splitting Δm^2_{21} and mixing angle $\sin^2\theta_{12}$ with higher precision than previous measurements [52, 54, 55, 61, 146, 147], which can explain the anomaly of the Δm^2_{21} value between solar and reactor measurements [2, 64, 140]. Also, DUNE is in a competitive position to make the first measurement of the *hep* neutrino flux, ^{8}B neutrino flux, and potentially measure the CNO neutrino flux, a sub-dominant helium production mechanism in the Sun [2, 140]. Measuring the CNO flux would also help to assess the Sun's metallicity.

4.5.4 Beyond the standard model physics

DUNE could perform a wide range of additional beyond standard model searches. Some of these are discussed below.

1. **Search for active-sterile neutrino mixing:** Experimental results that question the three-neutrino-flavor paradigm, potentially indicating mixing between the known active neutrinos and one or more sterile states [148, 149]. This has prompted a rich and diverse program of searches for oscillations into sterile neutrinos. DUNE is sensitive to a wide range of potential sterile neutrino mass splittings by looking for the disappearance of charged current, and neutral current interactions over the long distance between the near detector and the far detector [2]. With a longer baseline, a more intense beam, and a high-resolution large-mass far detector compared to previous experiments, DUNE offers a unique opportunity to significantly improve the sensitivities of the existing probes [2]. This greatly enhances the ability to explore the extended parameter space if a sterile neutrino is discovered.

2. **Search for light-mass dark matter:** Cosmological and astrophysical evidence strongly supports the existence of dark matter (DM), constituting about 27% of the universe's mass-energy. However, its nature and potential non-gravitational interactions with regular matter remain unknown [48]. The lack of evidence for WIMPs at direct detection has prompted a reconsideration of the WIMP paradigm. DUNE, with its high-flux neutrino beam, can probe dark matter parameter space that cannot be covered by either direct

detection or collider experiments [150, 151, 152, 2]. In DUNE, light-mass dark matter (LDM) may be produced through proton interactions in the target and detected in the near detector through neutral current-like interactions with either electrons or nucleons in the detector material via elastic scattering. This makes DUNE's search for LDM both competitive and complementary to other experiments.

3. **Search for boosted dark matter:** A representative model consists of heavy and light dark matter components, with the lighter one produced from the annihilation of the heavier one in locations such as the Sun or galactic centre [153, 154, 155]. The relativistic lighter dark matter component, boosted dark matter (BDM), can be detected via its interaction with the standard model particle in the detector [156, 157]. BDM energetically scatters off the nucleus inside the detector and can be observed through the signature of electron or nucleon recoil. DUNE will be able to search for boosted dark matter using its large detector modules [2]. The low energy detection threshold of DUNE has the ability to probe the BDM, allowing various physics opportunities within BDM.

Chapter 5

Simulation and reconstruction of the DUNE FD

In modern physics experiments, simulations play a crucial role in the development and understanding of event reconstruction, event selection, and achievable physics outcomes. These simulations rely heavily on Monte Carlo (MC) methods [158], which involve random sampling from predefined distributions to generate results that closely resemble experimental data. DUNE benefits from a standardised approach to simulation and reconstruction across experiments, facilitated by the widely used LArSoft [159] software package. LArSoft represents a comprehensive simulation, reconstruction, and analysis package developed for LArTPCs [160], and it serves various experiments such as MicroBooNE [108], ICARUS [161], SBND [109], ProtoDUNE [94] and DUNE [2]. The architecture of LArSoft is built on the *art* [162] particle physics event processing framework which is written in C++ [163]. LArSoft seamlessly integrates external packages such as GENIE [164], CORSIKA [165] and MUSUN [166] for particle generation, GEANT4 [167] for particle propagation, and the Pandora [168] pattern recognition package for particle reconstruction and identification.

To provide a comprehensive overview, the chapter focuses on simulation and reconstruction in LArTPC detectors, with an emphasis on the techniques employed by the DUNE experiment. Following the structure of LArSoft simulation, it covers event generation, particle propagation, charge and light simulation, detector response simulation, and reconstruction.

5.1 Monte Carlo simulation

The Monte Carlo (MC) simulation process in DUNE FD comprises three key stages. Firstly, in the particle generation stage, kinematic properties such as momenta are assigned to primary particles, establishing their initial states. These properties serve as inputs for the second stage, where particle propagation takes place. During this stage, the initial particle states interact with the detector material, generating secondary particles based on established cross-sections and physical laws. Lastly, the third stage involves simulating the detector's response to the signals produced by different particles and their energy depositions.

5.1.1 Particle generation

LArSoft is designed to incorporate several external packages, including GENIE for studying neutrino interactions and nucleon decays, CRY [169] and CORSIKA [165] for simulating cosmic ray events at surface detector locations. Additionally, users have the option to utilise a single particle generator, allowing them to specify particle types, initial momenta, positions, and directions as needed. Furthermore, a muon generator MUSUN [166, 170] is available, which uses the output of MUSIC [171]. MUSIC first propagates muons through a user-defined medium for given initial energies. The work presented in this thesis utilises MUSUN to simulate cosmic-ray muons at the deep underground location in the DUNE FD. Details about MUSUN are provided in Chapter 6.

5.1.2 Particle propagation

At the next stage, particles are propagated through the detector and surrounding materials using GEANT4 [167]. Each particle is transported using the step method which is determined by the possible physics processes (interactions or decay) of a particular particle in liquid argon and hence their trajectory is tracked. The selection of the physics process and the number of steps are determined based on the output necessary for the simulation. After each step information such as particle position, energy and momentum are recorded and the particle trajectory is determined. The process stops when the particle energy reaches a threshold below which the energy deposited by the particle is undetectable, or when the particles leave the detector. All secondary particles resulting from interactions during the propagation are preserved and later simulated using the same approach, with tracking of their corresponding parent particle. The energy deposited by the particle is utilised to compute the production of both ionisation charge and scintillation light, which are subsequently employed in the detector simulation.

5.2 Detector simulation: charge and light

The interactions within the detector lead to the production of signals, such as scintillation light or ionisation charge as described in Chapter 3. The ionisation charge produced by a charged particle induces a current on the induction wire plane while drifting toward the collection plane. This process produces signals on the wire planes. The charge ionisation and signal formation are already discussed in Section 3.3. The current i induced on a wire is proportional to drifting charge q given as [2, 172, 173]:

$$i = -q \cdot \vec{E_w} \cdot \vec{v_q} \tag{5.1}$$

where $\vec{E_w}$ and $\vec{v_q}$ are weighting field at the location of charge and the velocity of drifting charge respectively. The $\vec{E_w}$ depends on the geometry of the electrode while $\vec{v_q}$ depends on the external electric field. The function describes the induced current at a given wire, and the drift path over a period of time is characterised by the field response function, which is simulated using 2D Garfield [174]. Each plane has a separate field response function. The response function is further used in the TPC detector signal simulation. The energy deposited by a particle is taken as an input for the detector signal simulation and outputs a digitised waveform using an analogue-to-digital converter (ADC). The detector signal simulation incorporates effects such as noise which is mostly generated due to readout electronics and other detector effects as discussed in Chapter 3.

The produced scintillation light propagates towards the photon detectors. The generation of scintillation light in LArTPC is discussed in Section 3.4. For the response of photon detectors, the detector is divided into small volumes which are called voxels [2]. A pre-generated photon library is used to determine the probability of a photon reaching any of the photon detectors (PDs). The library also encompasses the relationship between the response and the position of the PDs, which accounts for the attenuation occurring between the photon emission point and its detection by the silicon photomultipliers (SiPMs).

5.3 Event reconstruction in the DUNE FD

The simulated events and data follow the same reconstruction procedure. To achieve effective LArTPC reconstruction, it is essential to accurately reconstruct tracks and showers in three dimensions, identify particles, and determine particle momentum and energy. The reconstruction process starts by detecting signals on individual wires surpassing a specified threshold and then constructing "hits" from each signal pulse. There are different reconstruction methods available for DUNE FD such as Wire-Cell, TrajCluster and Pandora [2]. This section will centre on charge signal reconstruction using Pandora, which is pertinent to the research presented in the thesis.

5.3.1 Signal processing and hit finding

The signal produced on each wire in a plane is converted into a raw waveform in the format of ADC counts as a function of the TPC tick and is recorded by the data acquisition system (DAQ). ADC counts define the amplitude of the signal and a tick is a detector timing unit which corresponds to 0.5 μs on each plane in the DUNE FD [2]. The reconstruction procedure starts with the identification of ionising electrons arriving at the anode planes. This is done by using a deconvolution algorithm. The recorded signal is a convolution of noise, electronic responses and detector effects as mentioned in the previous section and discussed in Chapter 3. The process used to correct for these detector effects is called deconvolution. Figure 5.1 illustrates the induction U-plane signal processing. After the deconvolution process, the bipolar signal is transformed into a unipolar signal, thereby simplifying the hit-finding procedure [2].

Following the processing of raw signals, the next step involves the procedure of hit finding. A "hit" is a 2D object representing the charge deposited on a single wire at a given time. Hence signal on a wire can be considered as a hit(s). The width of a hit is calculated using the Gaussian fit of a waveform peak produced on a wire. The area of each hit is proportional to the amount of charge deposited on a wire. Figure 5.2 displays the hit reconstruction of a deconvolved waveform using Gaussian fitting. In this example, a total of three hits are reconstructed. The signal on a waveform is fitted to a Gaussian. The total charge is represented by the area and the mean of the Gaussian represents the hit peak time. For the measured waveform, the unit is ADC and for the deconvolved waveform, the unit is

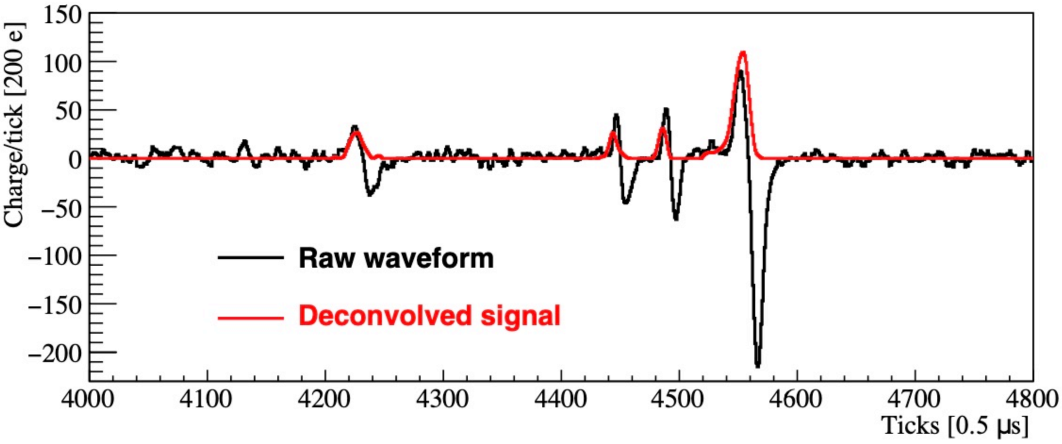

Figure 5.1. A measured raw waveform (black) and deconvolved waveform (red) from induction U-plane of ProtoDUNE-SP before and after the signal processing procedure. After the deconvolution process, bipolar signal shapes are converted into unipolar signal shapes [2].

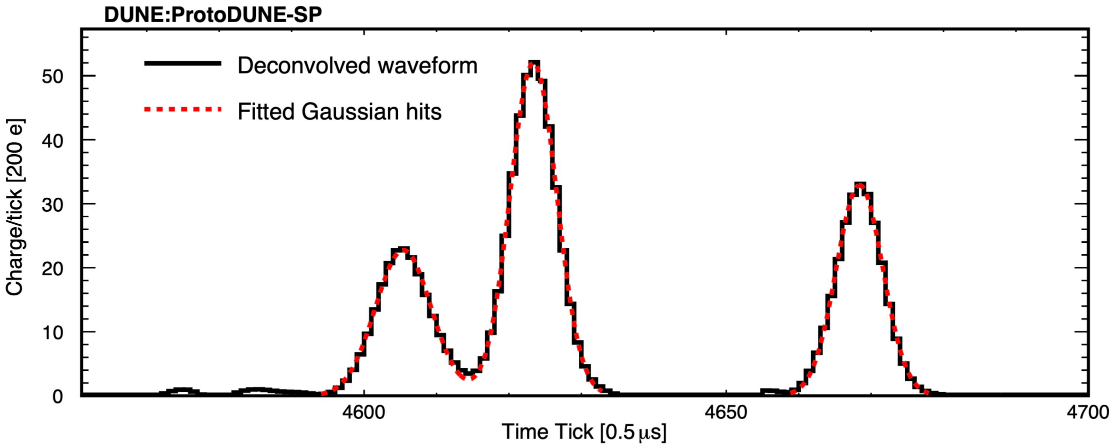

Figure 5.2. Hit reconstruction on a single wire from ProtoDUNE-SP data [94]. Three hits are reconstructed out of a waveform produced on a single wire.

the number of electrons. A calibration constant is used to convert ADC values to a number of electrons. The calibration studies are performed in Chapter 8.

5.3.2 Pandora overview

The Pandora software development kit [168] is a multi-algorithm framework for the pattern recognition used in the various LArTPC experiments such as MicroBooNE [83], ProtoDUNE [94] and DUNE [2]. Pandora takes the reconstructed hits as input and advances through the following key stages:

1. **Hit clustering:** The first stage of Pandora pattern recognition is the clustering of hits for each wire plane independently, referred to as 2D reconstruction. It begins with simple clustering, where hits forming a continuous straight line are grouped, assuming a track-like structure for simplicity. This process aims to group hits that are supposed to have originated from the same interacting particle. Subsequently, a sequence of algorithms is employed to merge these clusters across gaps in the detector and address ambiguities arising from factors like intersecting or interacting particles. Then Pandora starts matching for the 2D cluster in all three wire planes by finding candidate clusters in other planes. Once clusters are identified, Pandora proceeds to establish a 3D position for each hit, termed a space point.

2. **Track reconstruction:** The track reconstruction by Pandora is performed using clustered hits. The track reconstruction is processed by identifying the combination of hit clusters on each plane representing the same track-like particle. This is achieved by selecting two clusters on different planes and predicting the potential 3D cluster projection onto the third plane. The projected position is then compared with nearby reconstructed 2D clusters on that plane. Pandora lists all hit clusters as reconstructed "PFParticles". Here PF denotes particle flow. Each different track or shower is assigned with PFParticle which is associated with the list of hit clusters. Characterisation algorithms play a crucial role in classifying each cluster as either track-like or shower-like at different stages of the reconstruction procedure.

3. **Shower reconstruction:** Pandora uses a series of metrics to identify whether a hit cluster is track-like or shower-like. It employs the track reconstruction algorithm to determine the initial vertex and trajectory of the shower. Subsequently, the reconstruction of the shower revolves around this initial axis, achieved by recognising adjacent clusters of hits exhibiting shower-like characteristics. This reconstruction is extended until the termination point of the shower is reached.

5.3.3 Pandora reconstruction chains

Pandora has over 100 algorithms that can be used. Each algorithm is developed for a specific role in the reconstruction chain. Two distinct Pandora reconstruction pathways are defined by default in the DUNE FD [2, 168]: PandoraCosmic and

PandoraNu. Both reconstruction pathways utilised a chain of various algorithms. Many algorithms are shared between the two pathways.

1. **Cosmic reconstruction chain (CRC):** The reconstructed hits are processed by PandoraCosmic reconstruction. The set of algorithms used in this reconstruction pathway is strongly track-oriented and mainly developed for the reconstruction of cosmic-ray muons assuming particles will leave a long track in the detector volume. The showers produced are assumed to be an activity of delta electrons that are produced by muons ionising the argon and transferring a significant fraction of their energy to delta electrons and considered as a daughter particle of the cosmic-ray muon. The reconstructed vertex of an object is presumed to be positioned at a higher value of the detector y-coordinate.

2. **Neutrino reconstruction chain (NRC):** The reconstructed hits are processed by PandoraNu. This reconstruction utilizes a set of algorithms to identify the vertex of a neutrino interaction, which is then used to assist in reconstructing all particles originating from that vertex. Special attention is dedicated to reconstructing both tracks and showers. Initially, particles identified as emerging from the interaction vertex are considered, and the particle exhibiting the highest consistency with being an incoming particle is identified as the primary particle. Parent-child relationships are then established between the primary particle and the other particles originating from the interaction vertex.

The characterisation of tracks and showers of both the cosmic reconstruction chain and neutrino reconstruction chain is carried out in Section 6.6 including an event display from both reconstruction pathways.

5.4 Energy reconstruction

To measure dE/dx of showers and tracks, the process begins by measuring the charge deposition per unit length dQ/dx on a single wire at the collection plane. The charge dQ is determined as the area of the Gaussian fit to the hit, initially expressed in units of ADC as discussed in Section 5.3.1. The distance dx is then calculated using the shower (electron) or track direction to determine the actual distance that the particle traverses in the TPC between adjacent wires. This distance is calculated as the wire pitch divided by the cosine of the angle between the track direction and the direction normal to the wire in the wire plane [94]. The conversion from dQ/dx to dE/dx utilises the calibration constants. The ProtoDUNE-SP has employed the modified box model developed by the ArgoNeuT collaboration [97] to obtain the calibration constant. Calibration studies, including the modified box model for the DUNE FD, are discussed in Chapter 8.

Chapter 6

Muon production

Cosmic-ray muons are a naturally occurring source capable of penetrating deep underground and can be used for different studies such as detector calibration. Cosmic-ray muons are also a background in experiments looking for rare events such as nucleon decay deep underground. Muons can be used as a standard candle because they have a well-understood energy loss profile. The uniformity of the detector response can be calibrated using through-going and stopping muons. Stopping muons are used to determine the energy scale. Muons inside the detector may produce both charged and neutral pions. These pions can be utilised for calibrating the DUNE FD, specifically for the detector's response to electromagnetic shower activity and the energy scale. Using the MUon Simulation UNderground (MUSUN) particle generator, cosmic muons have been simulated and analysed within the dedicated software framework for liquid argon experiments, LArSoft. These simulated cosmic muons are used in calibrating the DUNE far detector (FD).

This chapter begins with a discussion of cosmic muon production in the atmosphere in Section 6.1 and their characteristics are discussed in the context of surface and underground experiments in Sections 6.2 and 6.3, respectively. The simulation of muons in DUNE FD is covered in Section 6.4, including a discussion of the muon particle generator MUSUN. Section 6.5 discusses muon distributions at the DUNE FD, including the characterisation of cosmic muon events and different particles produced in the LArTPC. Section 6.6 discusses the two different reconstruction chains used in the reconstruction process, including the event displays for each case. Finally, Section 6.7 provides a summary of this chapter.

6.1 Muon production in the atmosphere

The high-energy primary cosmic rays, which consist of charged energetic particles and nuclei, incident on the top of the atmosphere and produce secondary particles when interacting with atmospheric nuclei. The predominant particles produced in the cosmic ray interactions are pions and kaons. Muons are produced from the decay of pions and kaons around 15 km above the Earth's surface. Muons can travel deep underground due to their relative stability and small interaction cross-sections. The main process involved in the production of cosmic-ray muons with the decay probabilities are [47]:

$$\pi^{\pm} \rightarrow \mu^{\pm} + \nu_{\mu}(\bar{\nu}_{\mu}) \qquad \sim 100\% \tag{6.1}$$

$$K^{\pm} \rightarrow \mu^{\pm} + \nu_{\mu}(\bar{\nu}_{\mu}) \qquad \sim 63.5\%. \tag{6.2}$$

The mean lifetime of the muon is 2.2 μs and high-energy muons survive the distance to the Earth's surface and deep underground due to the time-dilation effect.

Charged pions are unstable and produce muons as they decay [47]:

$$\pi^{+} \rightarrow \mu^{+} + \nu_{\mu}, \tag{6.3}$$

$$\pi^{-} \rightarrow \mu^{-} + \bar{\nu}_{\mu}. \tag{6.4}$$

Lower energy muons from the interactions 6.3 and 6.4 decay in flight into [47]:

$$\mu^{+} \rightarrow e^{+} + \nu_{e} + \bar{\nu}_{\mu}, \tag{6.5}$$

$$\mu^{-} \rightarrow e^{-} + \bar{\nu}_{e} + \nu_{\mu}. \tag{6.6}$$

producing electrons, positrons, and neutrinos. Electrons and positrons further produce low-energy electromagnetic showers.

6.2 Cosmic-ray muons at the Earth's surface

The cosmic muon energy spectrum at the production of muons at a given height in the atmosphere can be derived by using two-body decay kinematics of the parent mesons $\pi \rightarrow \mu + \nu$ and $K \rightarrow \mu + \nu$ with their production spectrum [175]. Muons lose about 2 GeV to ionisation before reaching the Earth. The muon flux or intensity depends on the energy and angle.

The cosmic-ray muon flux at sea level is given by modified Gaisser's parametrisation which includes large zenith angles (Earth curvature) [176] and muon decay in the atmosphere (low energy) as [177, 178, 170]:

$$\begin{aligned}\frac{dI_{\mu_0}}{dE_{\mu_0}d\Omega}(E_{\mu_0},\theta_0) \approx & \frac{0.14 \times A \times E_{\mu}^{'\,-\gamma}}{\mathrm{cm}^2 \cdot \mathrm{s} \cdot \mathrm{sr} \cdot \mathrm{GeV}} \times P_d \\ & \times \left\{ \frac{1}{1 + \frac{1.1 E_{\mu}^{'} \cos\theta^*}{115 GeV}} + \frac{0.054}{1 + \frac{1.1 E_{\mu}^{'} \cos\theta^*}{850 GeV}} + R_c \right\},\end{aligned} \tag{6.7}$$

where $\frac{dI_{\mu_0}}{dE_{\mu_0}d\Omega}(E_{\mu_0},\theta_0)$ is the differential muon intensity at sea level in units of $\mathrm{cm}^{-2}\cdot\mathrm{s}^{-1}\cdot\mathrm{sr}^{-1}\cdot\mathrm{GeV}^{-1}$, E_{μ_0} is the muon energy in GeV at the surface, θ_0 is the muon zenith angle at the surface, θ^* is the muon zenith angle at the height of muon production. The relationship between θ_0 and θ^* is given by $\cos\theta^* = \sqrt{1 - 0.99(1 - \cos^2\theta_0)}$. $E_{\mu}^{'}$ is the muon energy at the height of the production, $E_{\mu}^{'} = E_{\mu_0} + \Delta E_{\mu_0}$, where $\Delta E_{\mu_0} = 2.06 \times 10^{-3}(1030/\cos\theta^* - 120)$ is the muon energy loss in the atmosphere, which is the correction term for low energy muons [179]. P_d is the survival probability of muons in the atmosphere which can be expressed as $P_d = a^b$, where $a = \frac{120}{1030/\cos\theta^*}$ and $b = \frac{1.04}{\cos\theta^*(E_{\mu_0} + \Delta E_{\mu_0}/2)}$ as mentioned by [179, 180].

The first term inside the bracket describes the muon contribution from the pion decay ($\epsilon_{\pi} = 115$ GeV), and the second term describes the muon contribution from the kaon decay ($\epsilon_K = 850$ GeV), where ϵ denotes the critical energy. Here, the critical energy is defined as the energy at a particular height where the probability of decay is similar to the probability of interaction. R_c is the ratio of prompt muons to pions. Prompt muons are produced in charmed particle decays. Charmed particles are produced together with pions and kaons, but have much shorter lifetimes and decay immediately. An upper limit on $R_c = 2 \times 10^{-3}$ was set by the LVD experiment [178], although the prompt muon flux does not contribute significantly to the intensities at large depths underground.

The normalisation factor A and spectral index γ can be determined according to the best fit of the particular experimental data. The Gaisser recommendation of these parameters for shallow depths (less than 1-1.5 km w. e. at vertical) is A =1, $\gamma = 2.70$. For larger depths, the best-fitted values of γ vary from 2.75 – 2.78. In many deep underground laboratories for depths greater than 3 km w. e., values of A =1.95 and $\gamma = 2.78$ provide a good fit of the data as obtained in the LVD experiment based on muon intensities measurement at Gran Sasso laboratory [180]. The muon energy spectra at sea level from the LVD [180], MSU [181], ASD [182], and MACRO [183] experimental datasets are shown in Figure 6.1. The best fits were calculated using Equation 6.7. The upper and lower solid curves represent the errors in parameters.

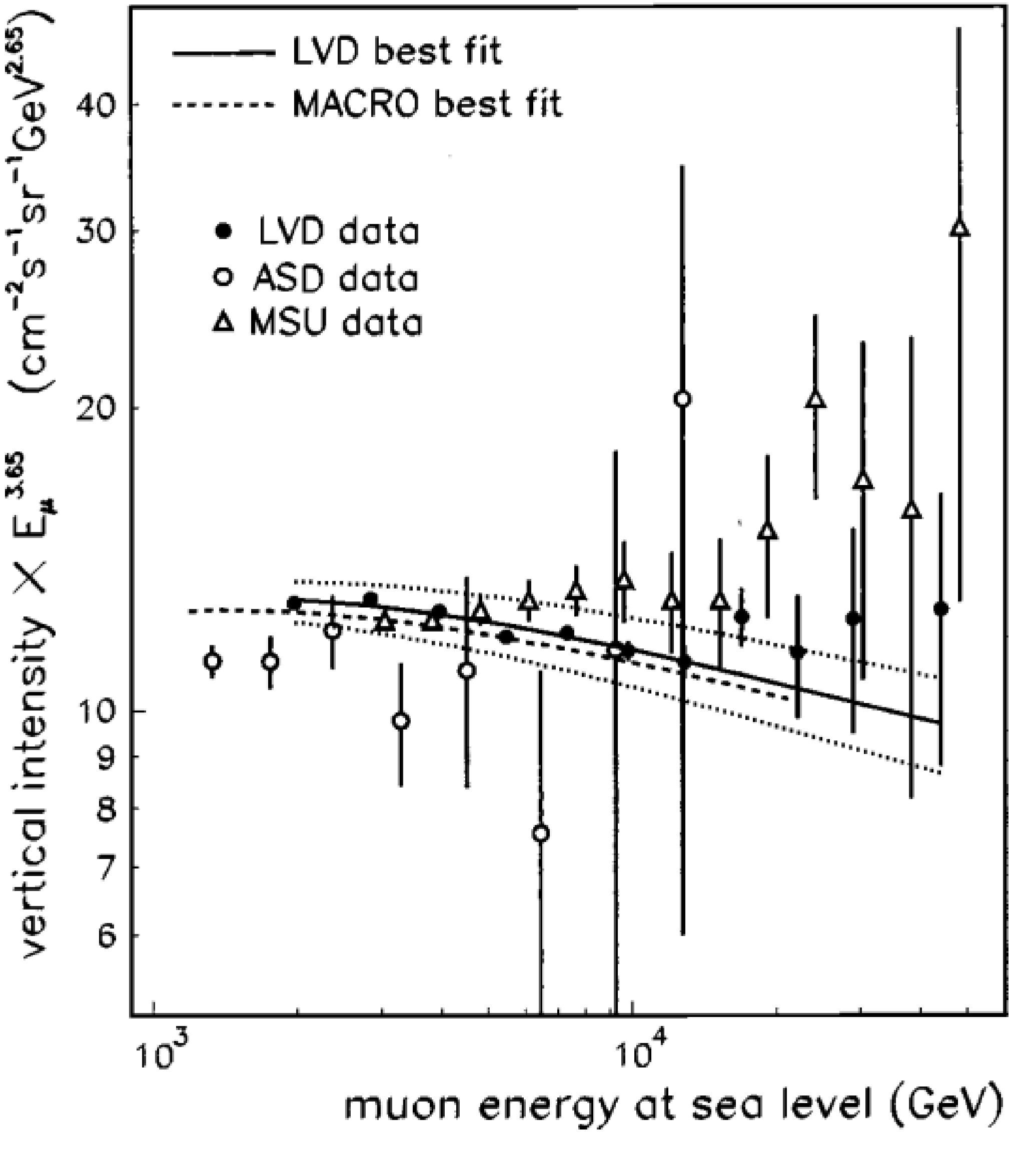

Figure 6.1. Vertical muon energy spectra at sea level measured in different experiments. The different data • [180], ○ [182], △ [181] are represented with different symbols from different experiments. The solid curve represents the best fit from LVD [180] using modified Gaisser's Equation 6.7 and the dashed curve shows MACRO [183] best fit. The upper and lower solid curves represent the errors in parameters. The figure is taken from Ref. [180].

6.3 Muon distributions underground

6.3.1 Cosmic-ray muon in underground experiments

Muon transport through matter and their properties underground play various roles in many areas of particle and astroparticle physics. Two important roles played by cosmic-ray muons in deep underground experiments are a) a source of background for many physics measurements and b) a standard candle for detector calibrations. Cosmic-ray muons are the main source of background for the deep underground experiments looking for rare events such as proton decay, neutrino oscillation studies, dark matter experiments, neutrino-less double-beta decay ($0\nu\beta\beta$), and other neutrino searches [184]. Muons can be mis-reconstructed which can mimic neutrino-induced events in a search for astrophysical neutrinos at GeV-TeV energies. At higher energies (GeV) neutrons from muons can produce a signature similar to proton decay for the decay channel $p \to \bar{\nu} + K^+$, where K^+ is the only signal in the detector. A cosmic muon can mimic the signal by producing a long-lived neutral kaon K_L^0 outside the detector. The kaon can propagate into the detector and it could produce K^+ in a charge exchange and be misidentified as K^+ from the $p \to \bar{\nu} + K^+$.

6.3.2 Muon propagation through matter

All charged particles lose energy in traversing through different types of materials. Muons are charged particles and they interact mainly via the electromagnetic force with nuclei and atomic electrons in a medium. Muons lose energy in two ways: ionisation (and excitation) when muon interacts with atomic electrons and due to radiative processes when muon interacts with an atomic nucleus or electrons. In general, the mean energy loss rate of muons is given by [84]:

$$\left\langle -\frac{dE}{dx} \right\rangle = a(E) + b(E)E. \tag{6.8}$$

where x represents the path length (in units of g/cm^2), E is the total energy, $a(E)$ is the electronic losses (ionisation + excitation) and $b(E)$ accounts for the radiative losses. The two processes are discussed next.

1. **Ionisation**

   Muons travel through the medium and transfer their energy to atomic electrons, ionising or exciting the atom depending on the energy and proximity of the muon. The energy loss of a muon of energy E due to ionisation and excitation is described by the Bethe-Bloch formula [41], as discussed in Section 3.2.

2. **Radiative processes**

   Muons lose energy through radiative processes such as bremsstrahlung, pair production, and photonuclear interactions. At very high energy (momentum > 100 GeV/c), radiative contribution becomes significant [185]. The function $b(E)$ of Equation 6.8 can be expressed as:

$$b \equiv b_{brems} + b_{pair} + b_{nucl} \tag{6.9}$$

   (a) **Bremsstrahlung:** As the muon passes close to the atomic nucleus it decelerates in the electric field produced by the nucleus or atomic electrons and radiates a photon. The energy of the radiated photon is the same as the energy loss of muon. High-energy radiated photons may also produce electron-positron pairs.

   (b) **Pair-production:** A muon can radiate a virtual photon in the electromagnetic interaction. The virtual photon associated with muon converts into a real electron-positron pair:

$$\mu + nucleus \rightarrow \mu + e^{+} + e^{-} + nucleus. \tag{6.10}$$

   (c) **Photonuclear interaction:** The photonuclear interaction is the process of inelastic lepton-nucleon scattering,

$$\mu + N \rightarrow \mu + (hadrons), \tag{6.11}$$

   where N denotes a nucleon.

In Equation 6.8, both terms $a(E)$ and $b(E)$ are slowly varying functions of E. The energy at which radiative and ionisation losses become equal is defined as the critical energy E^{c}_{μ}. E^{c}_{μ} depends on the material through which the muons propagate. The critical energies for standard rock and liquid argon are given in Table 6.1 with their material properties. The energy losses of muons in these two materials are also shown.

Table 6.1. Muon energy loss rate and critical energy for the standard rock and liquid argon with their material properties. The average atomic number is considered for the standard rock [84].

Material	Atomic number	Density [g/cm^3]	Critical energy [GeV]	Energy loss [MeV cm^2/g]
Standard rock	11	2.650	693	1.688
Liquid argon	18	1.396	483	1.508

Figure 6.2 shows the muon intensity vs depth. Muon intensity decreases as the thickness of the rock increases. After a depth of around 11 km w. e., the neutrino-induced muons dominate.

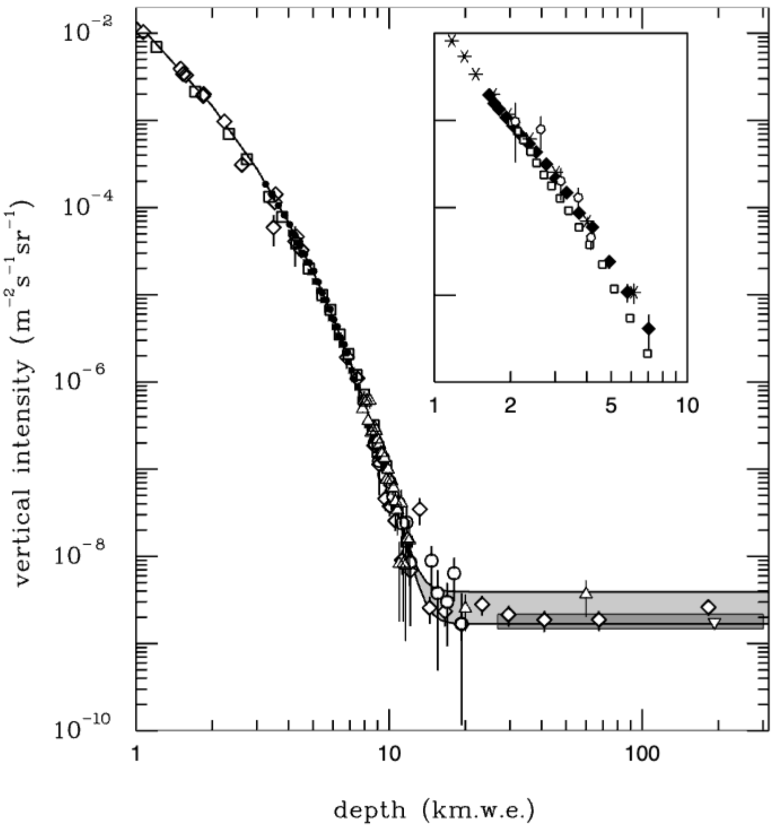

Figure 6.2. Underground depth dependence of the muon intensity. The experimental data is compiled from: △: SNO [186], ○: LVD [187], •: MACRO [183], □: Baksan [188], ■: FREJUS [189] and ◊: Crouch [190]. The shaded region at large depth is for neutrino-induced muons of $E_\mu > 2$ GeV. The upper line represents horizontal neutrino-induced muons while the lower one represents vertically upward muons. The DUNE FD will be at a depth of approximately 4 km w. e. considering rock density = 2.70 g cm^{-3} and depth = 1478 m. The figure is taken from Ref. [191].

6.4 Simulation of muons in the DUNE FD using MUSUN

6.4.1 Muon generator MUSUN

MUSUN (MUon Simulation UNderground) [166] is the muon generator useful for sampling muons in underground laboratories according to their energy and angular distributions. MUSUN uses the results of muon transport through matter carried out with MUSIC (MUon SImulation Code) [171, 192]. MUSIC first propagates muons through a user-defined medium for given initial energies. At the first stage, muons with various energies in the range 10^2 GeV and 10^7 GeV with a step of $\Delta \log E = 0.025$ are propagated through matter and their energy distributions are stored at depths from the initial point to distances ranging from 100 m w. e. to 15000 m w. e. Energy losses due to all processes mentioned in Section 6.3.2 are considered. The output of MUSIC, along with the surface profile, rock composition, etc. is then used by MUSUN to generate muons with energy and angular distributions at a given detector location. MUSUN is incorporated into the DUNE software framework — LArSoft. LArSoft has been discussed in Chapter 5.

6.4.2 Generating muons

The DUNE FD is located 1480 m underground at Sanford Underground Research Facility (SURF) [193]. The global coordinates of the DUNE are $44°20'45.2''$ North and $103°45'16.13''$ West [194]. The dimensions of the DUNE FD with cryostat are 63.6 m long, 16.7 m wide, and 15.6 m high. The average rock composition is calculated as $< Z > = 12.09$ and $< A > = 24.17$ using Refs. [195, 196]. The average density of rock is taken to be 2.70 g/cm^3 in the MUSIC simulation for the SURF. The vertical muon flux measurement at SURF at a depth of 1480 m performed by the active veto system of the Davis' experiment is 5.38×10^{-9} cm^{-2}·s^{-1}·sr^{-1} [197]. This result agrees very well with the vertical muon flux calculated for the Davis cavern by MUSIC/MUSUN, which is 5.18×10^{-9} cm^{-2}·s^{-1}·sr^{-1} [170].

Muons were transported through the rock deep underground using MUSIC. After the muon transport the differential muon intensities underground, $\frac{dI_\mu}{dE_\mu d\Omega}(E_\mu, \theta)$, were calculated using equation [194, 198, 170]:

$$\frac{dI_\mu}{dE_\mu d\Omega}(E_\mu, \theta) = \int_0^\infty P(E_\mu, X(\theta), E_{\mu_0}) \, \frac{dI_{\mu_0}}{dE_{\mu_0} d\Omega}(E_{\mu_0}, \theta_0) \, dE_{\mu_0}, \tag{6.12}$$

where $\frac{dI_{\mu 0}}{dE_{\mu_0} d\Omega}(E_{\mu 0}, \theta_0)$ is the muon spectrum at the surface modified for large zenith angle, taking into account the curvature of the Earth, given by Equation 6.7 and $P(E_\mu, X(\theta), E_{\mu_0})$ is the probability of a muon with initial energy at surface E_{μ_0} to have an energy E_μ at a depth X.

The simulated muons for DUNE FD are sampled on the top and side of the surface of a box enclosing the detector geometry. The box is chosen so that muons would travel at least 7 m of rock above the cavern and 5 m of rock around the cavern. The dimensions of the box which the muons are sampled from are 77.22 m long, 29.54 m wide, and 30.18 m high. This is to ensure that muons pass through a sufficient amount of rock to produce particle showers. The energy range of simulated muons using MUSUN ranges from 1 GeV – 10^6 GeV. Figure 6.3 shows the positions of 10^5 sampled muons over and around the box enclosing the DUNE FD as generated by LArSoft using the MUSUN generator. The initial positions of muons are shown as red points. The black box represents the cryostat encompassing DUNE FD TPCs and every single box in blue represents the individual TPCs. Muons are sampled according to their energy spectrum, the vertical depth of the laboratory, and the range of zenith angle and azimuthal angle. The charge of the generated muons is defined in accordance with the ratio measured for the high-energy muons, and the ratio is taken to be $\mu^+/\mu^- \approx 1.38$ [199]. The rate of generated cosmic muons through the box upon which muons are sampled is 0.164 Hz or 14,118 per day. The muon rate inside the TPC is 0.054 Hz. A total of 1.85×10^6 muons are generated which corresponds to 131 days of data at the DUNE FD.

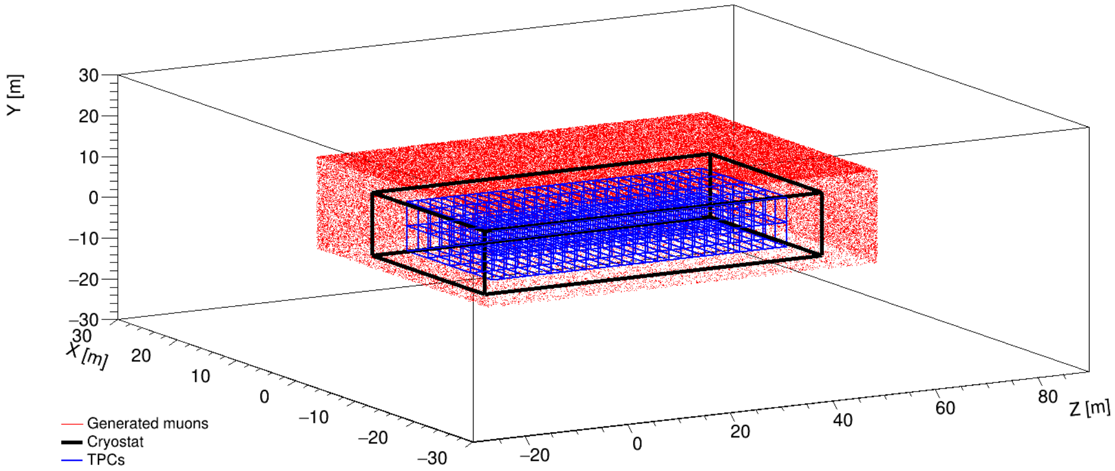

Figure 6.3. The initial positions of 10^5 muons sampled over and around the DUNE FD. The initial positions of sampled muons are shown in red points. The cryostat box encompassing the detector is shown in black. Each TPC is shown in blue boxes.

6.5 Muon distributions at the DUNE FD

The event statistics of different particles produced in the sample are shown in Table 6.2. The energy distribution of generated muons at the DUNE FD is shown in Figure 6.4. The mean energy of the generated muons is 284 GeV. Generated muons that enter the active volume of the DUNE TPCs are termed primary muons. The energy distribution of primary muons at the start of the active volume of DUNE FD is shown in Figure 6.4 (in black) and compared with generated muons (in red). About one-third of the simulated muons passed through the active volume of the detector. Muons with larger zenith angles fail to hit the detector.

Table 6.2. Event statistics of the generated cosmic muon sample for the DUNE FD. The characterisation of different particles produced in the sample in active volume is described in the first column. The second column shows the number of counts. Per-day statistics in the third column is calculated using the rate of the sampled muons. The fraction in the last column is calculated with respect to primary muons reaching the active volume except the fraction of primary muons in the active volume which is calculated with respect to the total number of generated muons. The data corresponds to 131 days of live time at the DUNE FD.

Characterisation	Total number	Per day	Fraction [%]
Total generated events	1.85×10^6	1.41×10^4	
Primary μ in TPC	6.24×10^5	4.76×10^3	33.72 ± 0.04
Any stopping μ in TPC	2.28×10^4	174	3.65 ± 0.02
Primary stopping μ in TPC	1.13×10^4	86	1.81 ± 0.02
All Michel electrons in TPC	2.01×10^4	153	3.21 ± 0.02
Michel from primary μ in TPC	6.84×10^3	52	1.10 ± 0.01
π^0 in TPC	2.76×10^4	210	4.42 ± 0.03
Events in which π^0 are produced	4.89×10^3	37	0.78 ± 0.01
Stopping π^+ in TPC	2.72×10^4	207	4.35 ± 0.03
Events in which π^+ are produced	4.71×10^3	36	0.75 ± 0.01
Stopping π^- in TPC	3.15×10^4	240	5.04 ± 0.03
Events in which π^- are produced	4.90×10^3	37	0.78 ± 0.01
Stopping protons in TPC	3.32×10^5	2.53×10^3	53.20 ± 0.09
Events in which protons are produced	2.05×10^4	156	3.28 ± 0.02
Stopping K^+ in TPC	1.50×10^3	11	0.24 ± 0.01
Events in which K^+ are produced	5.66×10^2	4	0.09 ± 0.00
Stopping K^- in TPC	6.68×10^2	5	0.11 ± 0.00
Events in which K^- are produced	3.38×10^2	3	0.05 ± 0.00

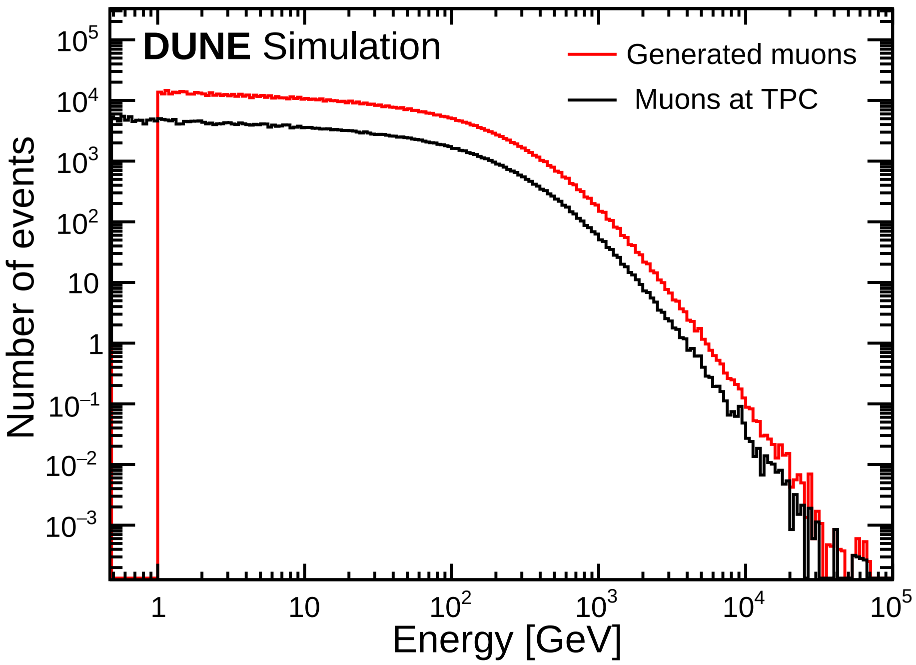

Figure 6.4. The energy distributions of generated muons (red) and the primary muons as they enter the DUNE TPCs (black). A total of 1.85×10^6 simulated muon events are used. About 33% of muons enter into the DUNE FD.

The surface profile of a region 4×4 km^2 above the location of the DUNE FD SP is shown in Figure 6.5a [194], where the centre of the map is the location of the detector. Each quadrant of the map is divided into 22.5° intervals for comparison with the azimuthal angle distribution in Figure 6.5b. Figure 6.5b shows the two-dimensional distributions of the zenith and azimuthal angle of generated muons. The azimuthal angle is calculated from East (pointing to the right in Figure 6.5a) to North in the counterclockwise direction reflecting the surface profile above the DUNE FD. The troughs and peaks in the muon azimuthal angle distribution correspond to the peak and trough of the surface profile moving from East to North. Figure 6.6a shows the zenith angle distribution of generated and muons that entered the TPC. The zenith angle distribution depicts the fact that most of the muons inside active volume are directed vertically downwards reflecting cosmic muons encounter the least rock overburden. Figure 6.6b shows the distribution of the azimuthal angle of generated and muons that enter the TPC.

The path length distribution of muons in argon in the TPCs is shown in Figure 6.7. The peak of this distribution is about 12 m. The peak corresponds to the height of the detector's active volume which is 12 m. The average path length

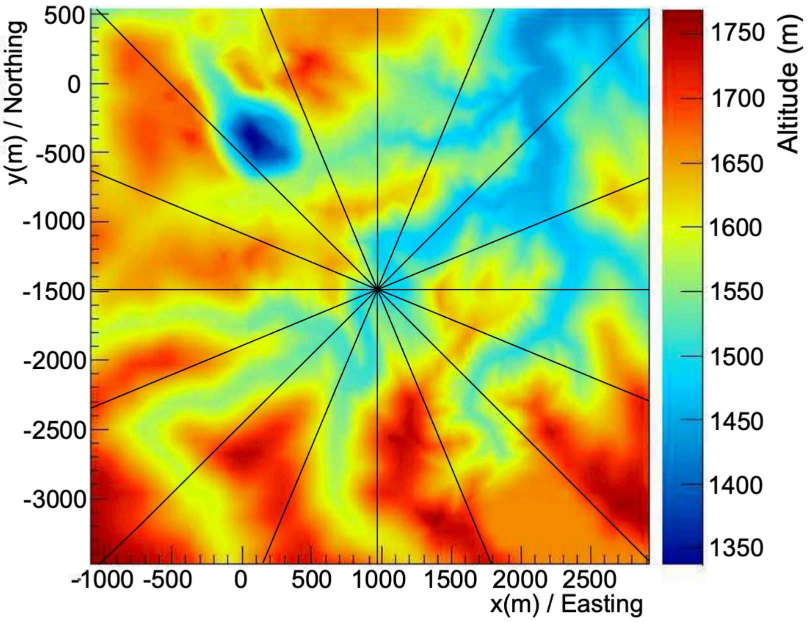

(a) The surface profile above the DUNE FD site at SURF [194].

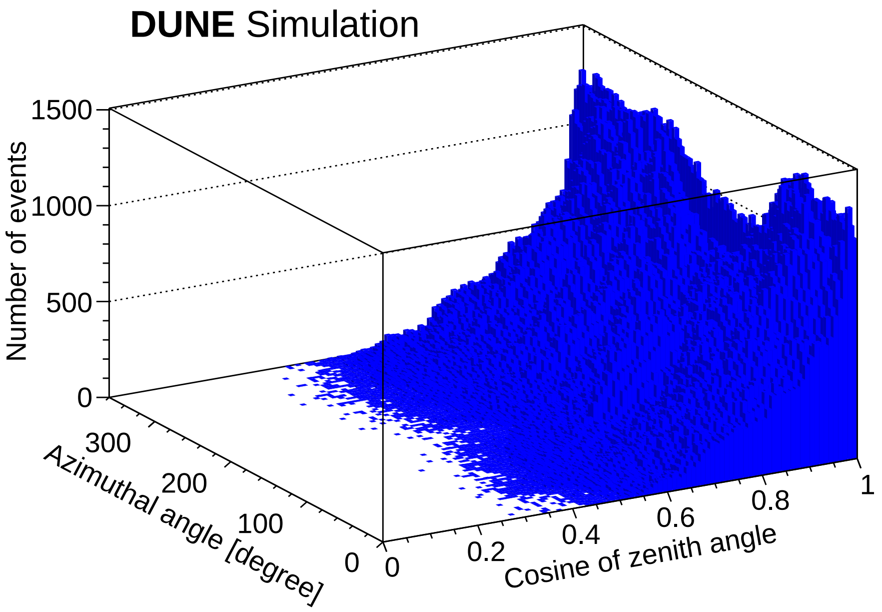

(b) Two-dimensional representation of zenith and azimuthal angle distribution of generated muons.

Figure 6.5. The correlation between the surface profile and azimuthal angle distribution of 1.85×10^6 generated muons at the DUNE FD site. The surface profile quadrant is divided in the step of 22.5° moving from East (horizontal line to the right) to North in the counterclockwise direction. The troughs and peaks in the surface profile (Figure 6.5a) correspond to peaks and troughs in the azimuthal angle distribution of Figure 6.5b.

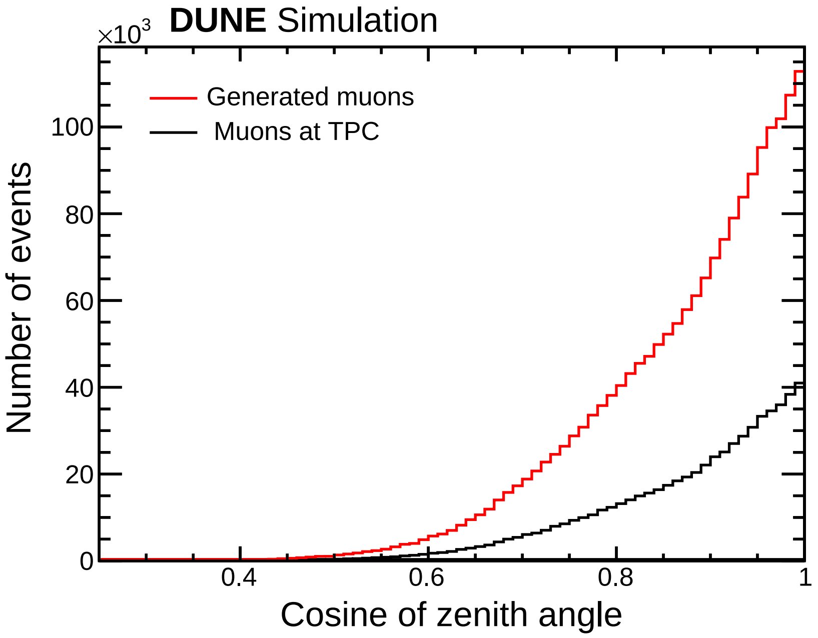

(a) The zenith angle distribution of generated muons.

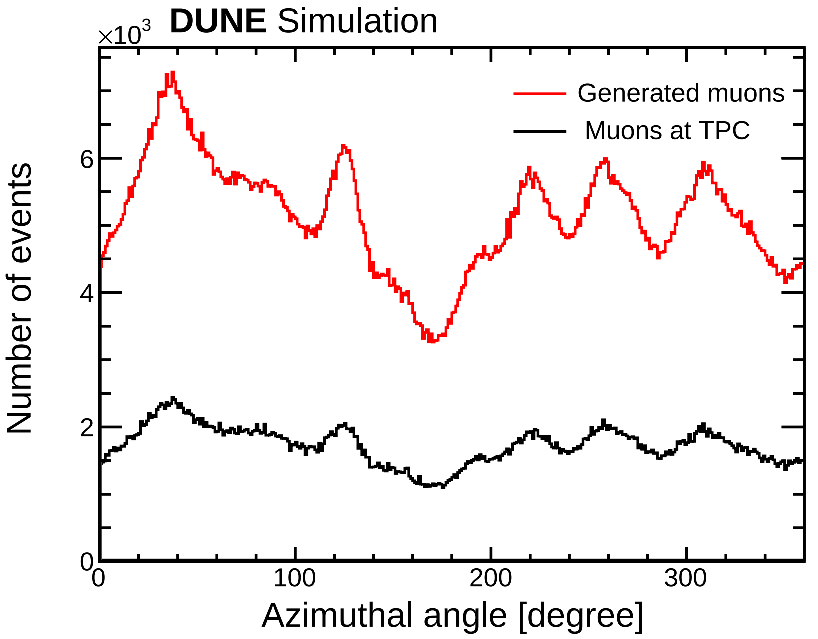

(b) The azimuthal angle distribution of generated muons.

Figure 6.6. Angular distributions of 1.85×10^6 generated muons over and around the DUNE FD. a) Zenith angle distribution of generated and muons that enter the TPC. Most of the muons are directed vertically from the top of the detector. b) Azimuthal angle distribution of generated and muons that enter the TPC reflect the surface profile at the DUNE FD.

of about 10.5 m. The energy loss distribution of muons that enter the TPC is shown in Figure 6.8. The mean energy loss is 3.66 GeV. The peak around 3.5 GeV is because most of the muons are vertical and through-going and therefore they travel approximately the same distance in the detector. Muons that enter from the sides of the DUNE FD have a short track length and lose a smaller amount of energy thus energy loss corresponding to these muons is less than 3.5 GeV. Some muons which pass diagonally through the detector lose more energy due to longer tracks. Some more energetic muons can also lose large amounts of energy in a single interaction with nuclei where they usually initiate particle showers. Figure 6.9 shows the distribution of energy loss of muons that enter the TPC per unit path length inside the active volume. The mean value of this distribution is 3.52 MeV/cm and peaked at around 2.5 MeV/cm.

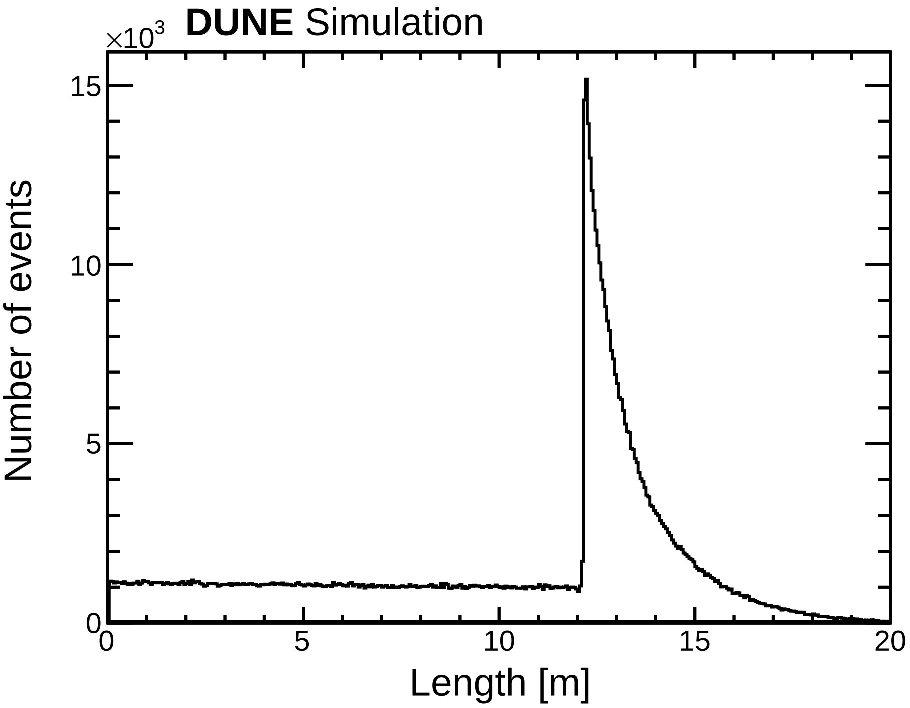

Figure 6.7. Distribution of path length of 6.24×10^5 muons that enter the TPC volume of the DUNE FD.

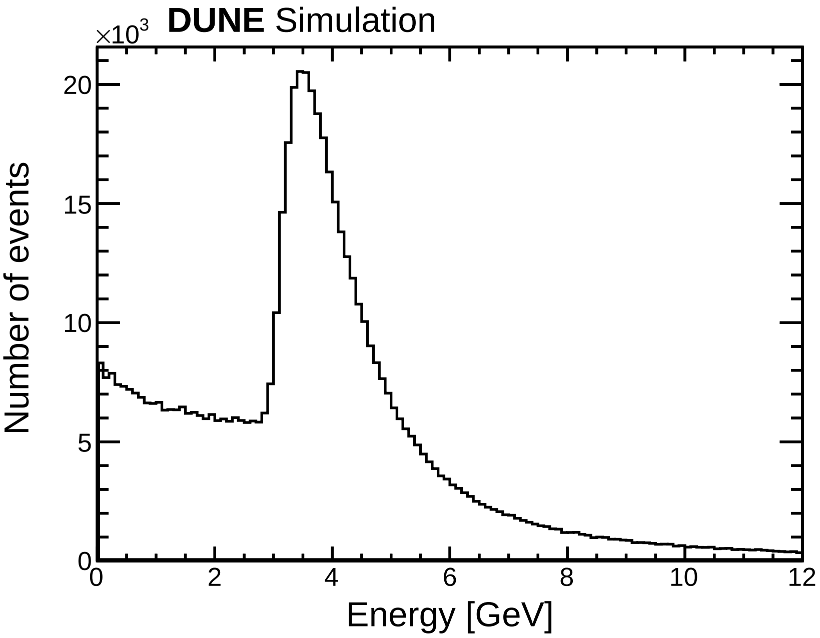

Figure 6.8. Energy loss distribution of 6.24×10^5 muons that enter the TPC volume of DUNE FD.

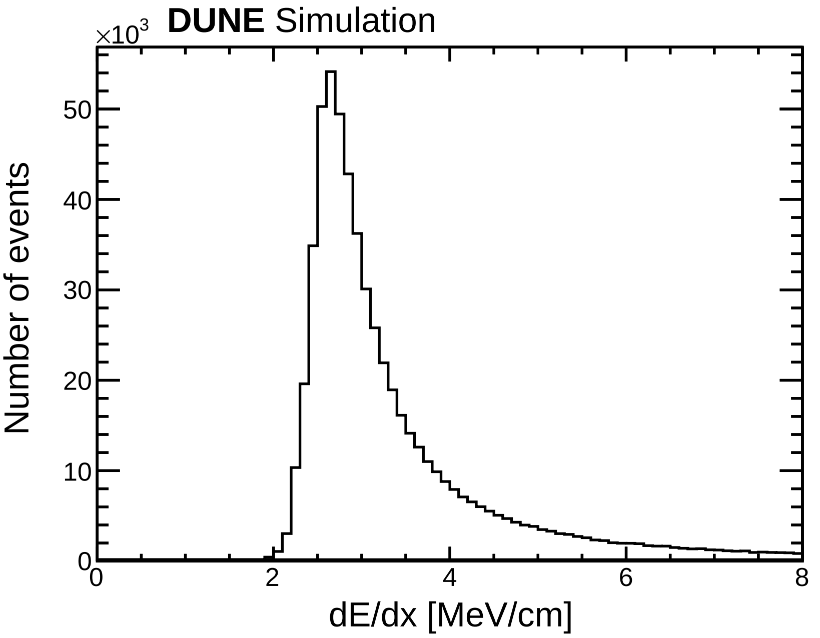

Figure 6.9. Energy loss per unit path length of 6.24×10^5 muons that enter the TPC volume of DUNE FD.

6.6 Cosmic muon events in different reconstructions

6.6.1 Cosmic and neutrino oriented reconstruction methods

Generated muon events are propagated through the detector using GEANT4 [167]. A full detector simulation, including detector response, is carried out. These simulated events were reconstructed using Pandora [168] software which is integrated into LArSoft as discussed in Chapter 5. Two distinct methods are used to reconstruct an event: the cosmic reconstruction chain (CRC) and the neutrino reconstruction chain (NRC). The neutrino reconstruction chain is tuned to reconstruct neutrino interactions whilst the cosmic reconstruction chain is tuned to reconstruct cosmic-ray muons and other particles produced by muons that leave mainly tracks in the TPC. These two reconstructions are discussed in Section 5.3.2. A sample of muons reconstructed with the NRC contains 1.48×10^6 events equivalent to 105 days of data at DUNE FD whilst the events reconstructed with the CRC contain 3.71×10^5 events equivalent to 26 days of data at DUNE FD. In the cosmic-oriented reconstruction, showers are fragmented and some showers are also reconstructed as tracks. Thus the number of tracks and showers reconstructed in the cosmic oriented chain is significantly larger than in the neutrino oriented reconstruction. Table 6.3 compares cosmic muon events analysed using these two reconstruction methods.

Table 6.3. Event statistics of generated cosmic muon sample in two reconstruction methods for the DUNE FD. The NRC events correspond to 105 days of live time at DUNE FD and CRC events correspond to 26 days of live time at DUNE FD. Fraction is calculated with primary muons in TPC except the fraction of primary muons in TPC which is calculated with respect to total generated events. For reconstructed tracks and showers, the fraction represents the number of reconstructed tracks and showers per primary muon event.

Characterisation	Total number		Daily rate		Fraction [%]	
	NRC	CRC	NRC	CRC	NRC	CRC
Total generated events	1.48×10^6	3.71×10^5	1.41×10^4	1.41×10^4		
Primary μ in TPC	4.98×10^5	1.26×10^5	4.74×10^3	4.84×10^3	33.64	33.96
Reconstructed tracks	9.19×10^5	1.88×10^6	8.75×10^3	7.23×10^4	1.84	14.92
Reconstructed showers	8.37×10^5	3.26×10^6	7.97×10^3	1.25×10^5	1.68	25.87

Figures 6.10 and 6.11 show the number of reconstructed tracks and showers in the NRC and the CRC respectively. In the cosmic-oriented reconstruction, showers are fragmented and some showers are also reconstructed as tracks.

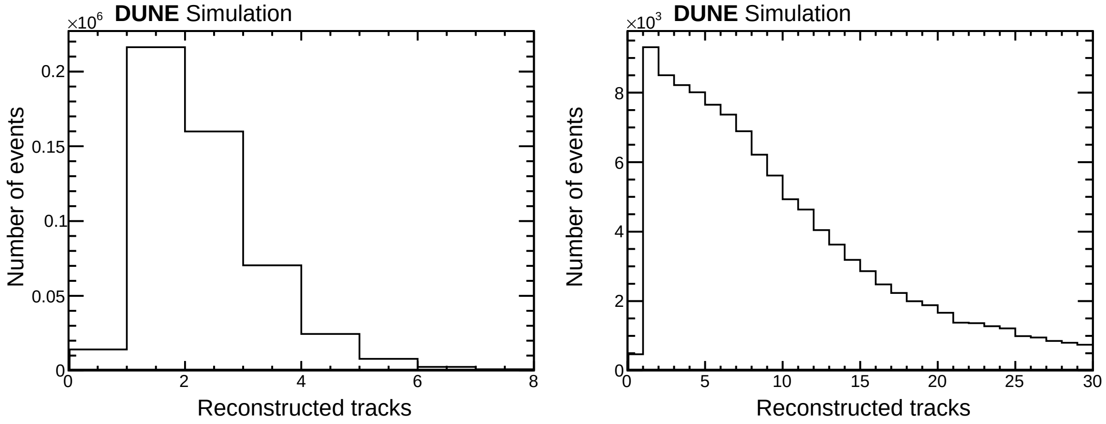

(a) Reconstructed tracks of NRC events. **(b)** Reconstructed tracks of CRC events.

Figure 6.10. The number of reconstructed tracks in 1.26×10^5 CRC and 4.98×10^5 NRC events in TPCs. a) Reconstructed tracks of NRC events. b) Reconstructed tracks of CRC events.

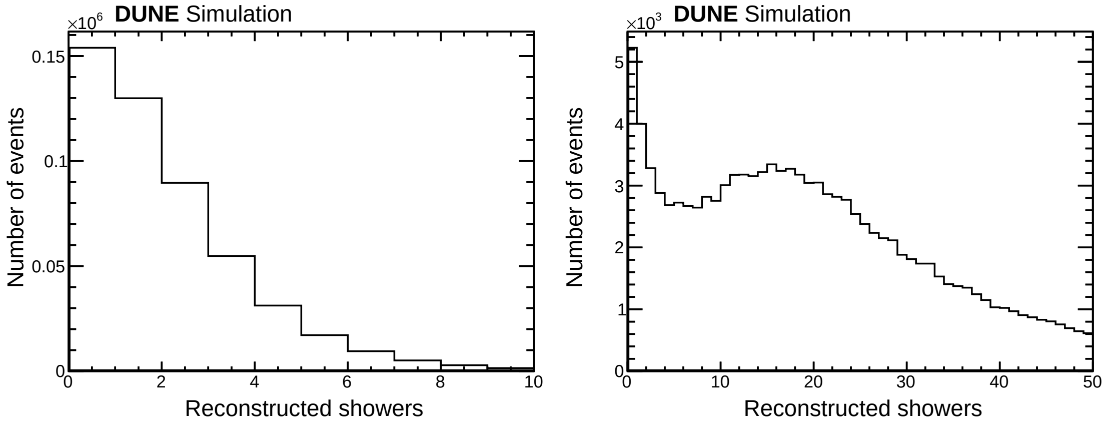

(a) Reconstructed showers of NRC events. **(b)** Reconstructed showers of CRC events.

Figure 6.11. The number of reconstructed showers in 1.26×10^5 CRC and 4.98×10^5 NRC events in TPCs. a) Reconstructed showers of NRC events. b) Reconstructed showers of CRC events.

6.6.2 Event display

Simulated events in LArTPCs can be visualised using Pandora pattern recognition. Figure 6.12 shows the event display of a cosmic muon event simulated in the DUNE FD using the NRC and CRC. Figure 6.12a shows the neutrino oriented reconstruction of a cosmic muon event. Different colours show different particle tracks and showers. Showers produced by photons from π^0 decay are shown in triangles. The Pandora NRC algorithm merges different particle tracks with shower as shown by sky blue. Figure 6.12b shows the cosmic oriented reconstruction of the cosmic muon event. The cosmic oriented chain fragments one shower into many. Yellow, green, pink, and teal inside the triangle are fragmented showers which are produced by a photon. The fragmentation of showers and tracks occurs significantly more frequently in CRC events which are shown in Table 6.3 and Figures 6.10 and 6.11. The track reconstruction is more effective in CRC whilst the shower reconstruction is more effective in NRC.

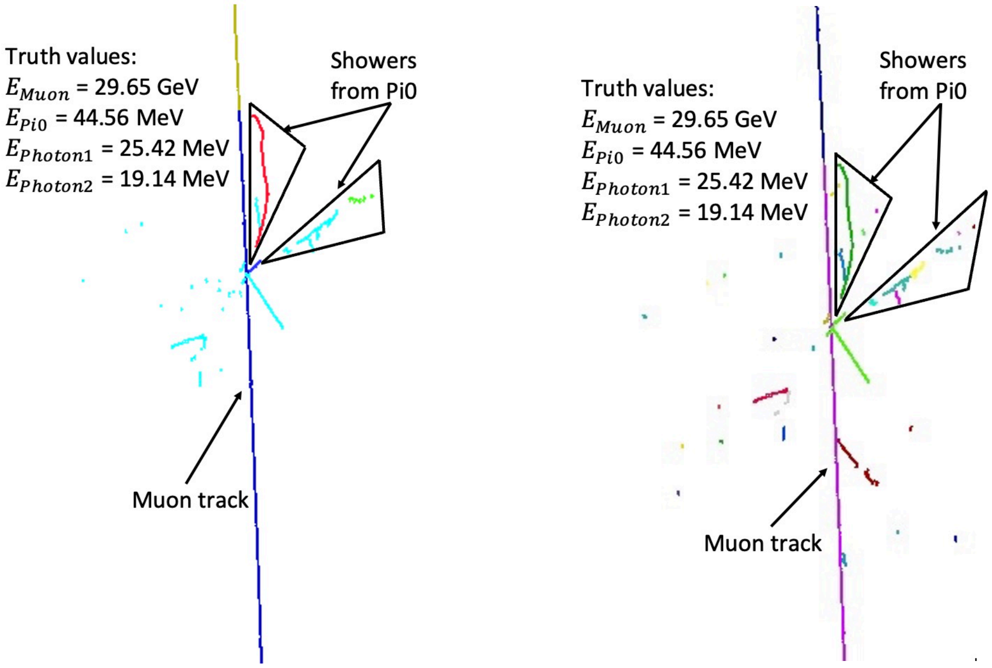

(a) Reconstructed NRC event. **(b)** Reconstructed CRC event.

Figure 6.12. Event display of a reconstructed cosmic muon event in a DUNE FD TPC. The muon interaction inside the TPC produces a π^0. Two showers emerging from π^0 are shown in triangles. Different colours represent different tracks and showers. a) The reconstruction is performed with the NRC. Parts of the showers from one photon are merged with other showers and tracks as shown by the sky blue. b) An event display of the same cosmic muon reconstructed with the CRC. The CRC often fragments one shower into many.

6.7 Summary

Cosmic-ray muon events are simulated with the MUSUN generator within the DUNE FD. A total of 1.86×10^6 cosmic muons are generated corresponding to 131 days of data at DUNE FD. The rate of muons entering the DUNE FD is 4.76×10^3 per day. About 33 % of generated muon enters into the DUNE FD. The mean energy of muons that entered the DUNE FD is 283 GeV. The mean energy loss inside the DUNE FD of muons is 3.66 GeV. The mean energy loss of muon per unit length inside DUNE FD is 3.52 MeV/cm. The characterisation of various particles produced in liquid argon is carried out. The event displays of the two distinct reconstruction chains: CRC and NRC, provide valuable insights into the reconstruction processes. The event display shows the neutrino-oriented algorithm merges different particle showers and tracks into one whilst cosmic-oriented chain fragments one shower into many. The fragmentation of showers occurs significantly more frequently in CRC events than in NRC events. For showers, the NRC is more effective, as it exhibits less shower fragmentation than the CRC. Conversely, for tracks, the CRC is more effective because it reconstructs particle tracks more efficiently than the NRC, which sometimes merges tracks with showers.

Chapter 7

Neutral pion analysis

A critical aspect of conducting neutrino oscillation studies in DUNE is to have a comprehensive understanding of how the detector responds to the particles produced in the neutrino interactions, all of which have energy dependence. Accurate energy reconstruction is necessary for measuring CP violation and fully exploiting the capabilities of the detector. Two principles which are important to DUNE involve the neutral pion (π^0). First, the neutral pion is the major background to the electron neutrino appearance signal. The π^0 produced in the neutral current neutrino interaction: $\nu_\mu + p \rightarrow \nu_\mu + p + \pi^0$ can mimic the neutrino appearance signal: $\nu_e + n \rightarrow p + e^-$ if the showers produced by $\pi^0 \rightarrow 2\gamma$ are mis-reconstructed either by two showers reconstructed as one or only one shower is reconstructed. Hence, a careful study is required in order to reduce systematic uncertainties. Second, its decay signature $\pi^0 \rightarrow 2\gamma$ provides a means for calibrating the energy of electromagnetic showers. The determined mass of the reconstructed π^0 relies on the overall energy scale of its γ showers. The true mass of π^0 can be used as a standard candle for calibration. By comparing the reconstructed mass to the true π^0 mass, a scale factor can be obtained and utilised to correct the shower energy. In DUNE, the reconstructed neutrino energy is calculated from the reconstructed energy of its interaction products, including showers. Hence electromagnetic shower calibration is important in DUNE. This chapter presents the analysis of $\pi^0 \rightarrow 2\gamma$ produced in cosmic-ray muon events, demonstrating the reconstruction of the π^0 mass from the reconstructed energy of two showers emerging from the $\pi^0 \rightarrow 2\gamma$ and its use in shower energy calibration.

The chapter begins with a brief introduction to neutral pions including their kinematics and their production in the DUNE FD. The next Section 7.2, describes a layout of the analysis and discusses its procedure. Truth-level properties of neutral pions are discussed in Section 7.3. A detailed study of reconstructed photon showers from $\pi^0 \rightarrow 2\gamma$ focussing on angle and energy reconstruction is carried out in Section 7.4. The π^0 invariant mass is reconstructed using the energy and opening angle of the photon showers from the $\pi^0 \rightarrow 2\gamma$ decay, this is discussed in Section 7.5. Finally, Section 7.6 summarises this chapter.

7.1 The neutral pion

The neutral pion is the lightest strongly interacting particle observed in nature [200]. Neutral pions are commonly produced in hadronic, photonuclear, and neutrino interactions [35, 201]. It has zero electric charge and has a mass of 135 MeV/c^2. Neutral pions decay quickly as they have a very short lifetime $8.4 \pm 0.6 \times 10^{-17}$ s [202] and hence they do not travel a considerable distance before decaying. Two foremost decay modes of π^0 exist. The most dominant decay of neutral pion is $\pi^0 \rightarrow 2\gamma$ with a branching ratio of 0.98823. In LArTPCs, this decay ideally translates to two electromagnetic showers originating from the same vertex. The second most important decay channel of the neutral pion is $\pi^0 \rightarrow e^+ + e^- + \gamma$ with a branching ratio of 0.01174, resulting in up to three showers within the detector. This decay channel is not considered in this analysis due to its rarity.

Neutrino interactions lead to the creation of π^0 via two different mechanisms as mentioned in [35, 203] including references therein:

$$\nu + N \rightarrow l + \Delta \rightarrow l + \pi^0 + N \qquad (resonant) \tag{7.1}$$

$$\nu + A \rightarrow \nu + A + \pi^0 \qquad (coherent) \tag{7.2}$$

where N denotes a nucleon (proton or neutron), l is the outgoing charged lepton (neutrino) in CC (NC) interactions and A is a nucleus.

In resonant π^0 production, a(n) (anti) neutrino interacts directly with a nucleon, exciting the nucleon into a baryonic resonance Δ^+ or Δ^0 particle depending on the charge of the nucleon. This excited state regains the original form by producing a π^0. In coherent π^0 production, a small amount of energy is exchanged between the (anti)neutrino and the nucleon and the neutrino excites the whole nucleus. Thus nucleus is left intact and a π^0 is produced.

In DUNE FD, π^0 is also produced by cosmic-ray muons in photonuclear interaction and subsequently hadronic interaction by the process of lepton-nucleon scattering:

$$l + N \rightarrow l + X \tag{7.3}$$

where l, N, and X denote leptons, nucleons, and hadrons, respectively. The hadrons produced in this interaction include π^0, π^+, and π^-. Charged pions interact with nucleons in nuclei of LAr and produce neutral pions as follows:

$$\pi^+ + n \rightarrow \pi^0 + p, \tag{7.4}$$

$$\pi^- + p \rightarrow \pi^0 + n. \tag{7.5}$$

7.1.1 Neutral pion kinematics

The $\pi^0 \rightarrow 2\gamma$ decay kinematics are shown in Figure 7.1. In the rest frame of the π^0, each photon shares exactly half of the π^0 mass in the form of energy. These photons are emitted in the opposite direction to conserve the system's momentum. In the lab frame (detector frame), the vector sum of the photon's momenta from the π^0 decay is non-zero. The photons produced from the $\pi^0 \rightarrow 2\gamma$ decay are boosted in the direction of their parent particle. The energy of emitted photons in the lab frame depends on the angle of the photon from the π^0 direction (θ^*) of the rest frame:

$$E_{1,2} = \frac{\gamma\ m_{\pi^0}}{2}(1 \pm \beta \cos\theta^*) \tag{7.6}$$

where E_1 and E_2 correspond to the energy of the leading and subleading photons respectively in the lab frame, $\beta = v/c$ where v is the velocity of the π^0 and $\gamma = 1/\sqrt{1-\beta^2}$ is the Lorentz factor. In the special case where $\beta = 0$ or $\theta^* = 90°$, the energy of both photons becomes $\gamma m_{\pi^0}/2$.

The angle between two photons (opening angle) from a π^0 decay in the lab frame can be expressed in terms of the π^0 energy as follows:

$$\cos\theta = 1 - \frac{2m_{\pi^0}^2}{E_{\pi^0}^2(1-\alpha^2)} \tag{7.7}$$

where

$$\alpha = \frac{E_1 - E_2}{E_1 + E_2} \tag{7.8}$$

and θ is the opening angle between two photons and E_{π^0} is the neutral pion energy in the lab frame. The parameter α represents the asymmetry between the two photons and is defined in terms of their energy. As the initial π^0 energy increases,

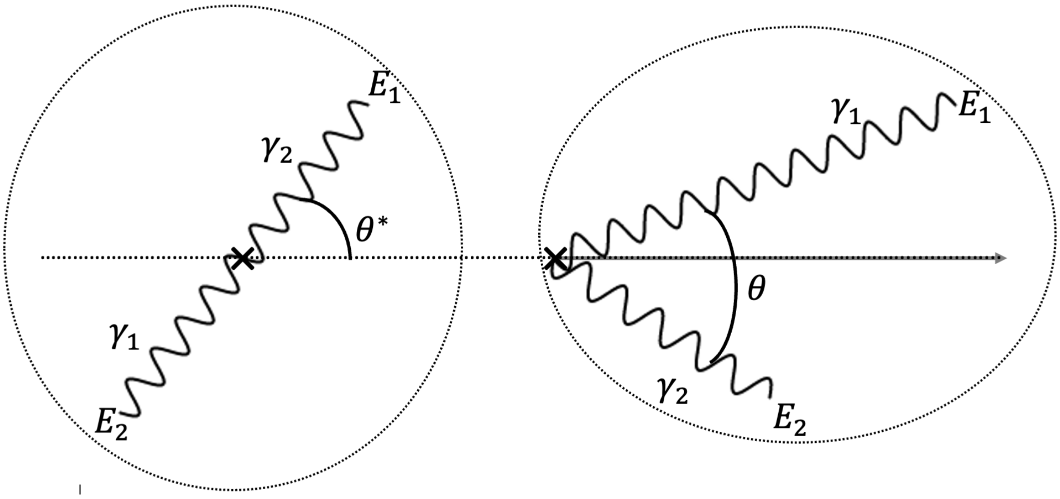

Figure 7.1. A graphical representation illustrating the kinematics of π^0 decay. The process $\pi^0 \to 2\gamma$ decay observed in the particle rest frame (left) and in the lab frame (right) where π^0 has some momentum. E_1 and E_2 denote the momentum of two photons γ_1 and γ_2 respectively. θ^* denotes the angle of the photon from π^0 direction in the rest frame and θ is the opening angle between two photons from $\pi^0 \to 2\gamma$ decay in the lab frame.

the opening angle between the two photons decreases asymptotically, eventually approaching near 0.

The invariant mass of the π^0 can be determined using the energies and opening angle of the two photons of $\pi^0 \to 2\gamma$, and this quantity can be expressed as follows:

$$m_{\pi^0} = \sqrt{2E_1E_2(1 - \cos\theta)}. \tag{7.9}$$

The mass of the neutral pion remains unaffected by the particle's kinetic energy and the decay photons' angle. This property enables the energy calibration of the reconstructed quantities, particularly the photons' reconstructed energy.

7.1.2 Neutral pion in the DUNE FD

The electromagnetic showers produce two photons from π^0 decay and serve as the primary signature for detecting the presence of π^0 in the detector. Figure 7.2 depicts the formation of an electromagnetic shower from a π^0 decay. A photon from the π^0 decay undergoes electron-positron pair production and $e^{\pm}$ splits further producing bremsstrahlung photons [204]. Every particle undergoes a splitting after travelling a distance. The number of particles grows by 2^n after n splitting. The pair production and bremsstrahlung stop when the individual energy of $e^{\pm}$ drops below the critical energy where the ionisation losses begin to exceed radiative losses.

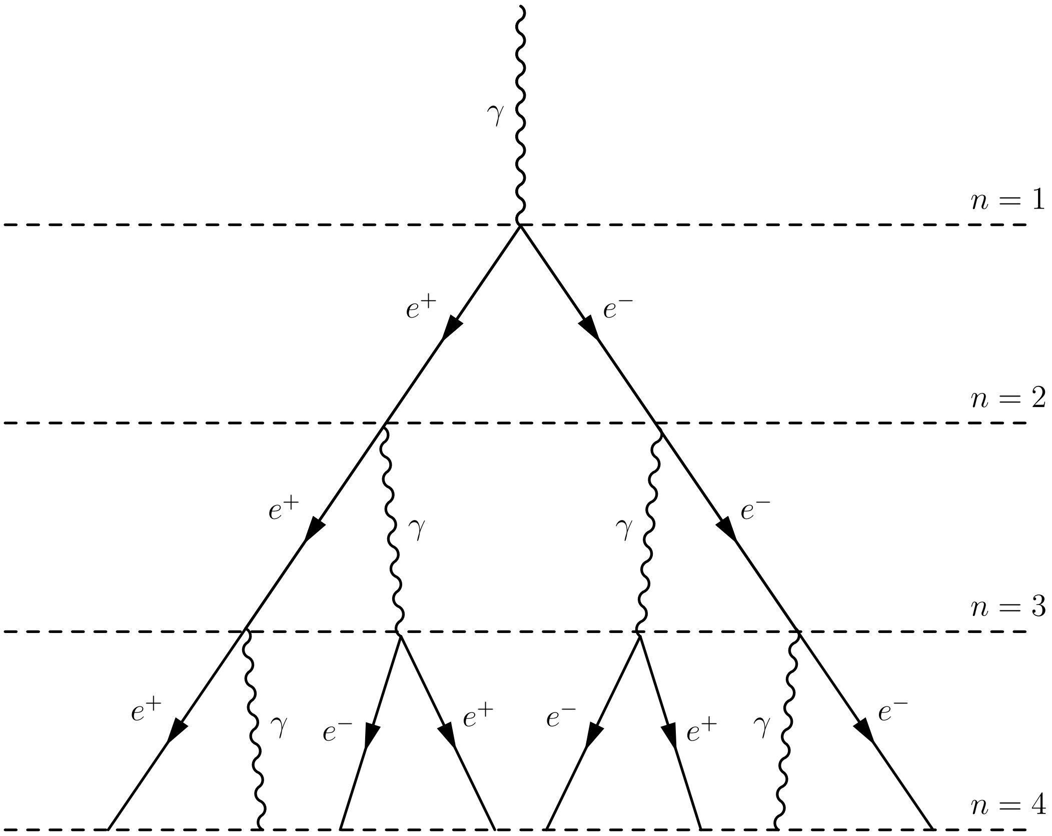

Figure 7.2. A schematic of an electromagnetic shower. The incoming photon is a decay product of a π^0. The photon creates an e^+e^- pair at level $n = 1$. Both the electron and positron generate photons via bremsstrahlung radiation at level $n = 2$. These photons also create electron-positron pairs at level $n = 3$, leading to more bremsstrahlung photons, which will again generate more e^+e^- pairs. This process ceases if the energy of $e^\pm$ is not sufficient anymore for the bremsstrahlung process. The figure is not to scale.

Two characteristics of the π^0 decay complicate matters inside DUNE FD. Firstly, showers exhibit a scattered hit distribution in comparison to tracks. They are made up of numerous individual particles (depending on the energy of photons) which make showers more cloud-like than track-like. Photons produced within the showers may travel a significant distance before creating a sub-shower and thus create a substantial gap between shower hits. The disconnected clustering of showers makes it challenging for Pandora to properly reconstruct hits within the same object. This also makes it challenging to identify the starting point and the direction of the shower. This impacts the reconstruction of energy and opening angle and ultimately the reconstructed invariant mass of the π^0 as mentioned in Equation 7.9.

Secondly, a complication arises from the fact that photons from π^0 decays travel undetected until they interact with the liquid argon in the DUNE FD. This separates the shower from its parent particle π^0 origin as well as the showers from one another and makes it more difficult to recognise that the showers originated from the same vertex. Showers from photons that travel far from the π^0 vertex before interacting may fail to be identified as a daughter of their true origin by Pandora.

Figure 7.3 shows an event display of a reconstructed muon event in DUNE FD. A cosmic muon enters from the top of the DUNE FD and produces a neutral pion after interacting with liquid argon. The neutral pion further decays to two photons γ_1 and γ_2 which produce electromagnetic showers in the detector.

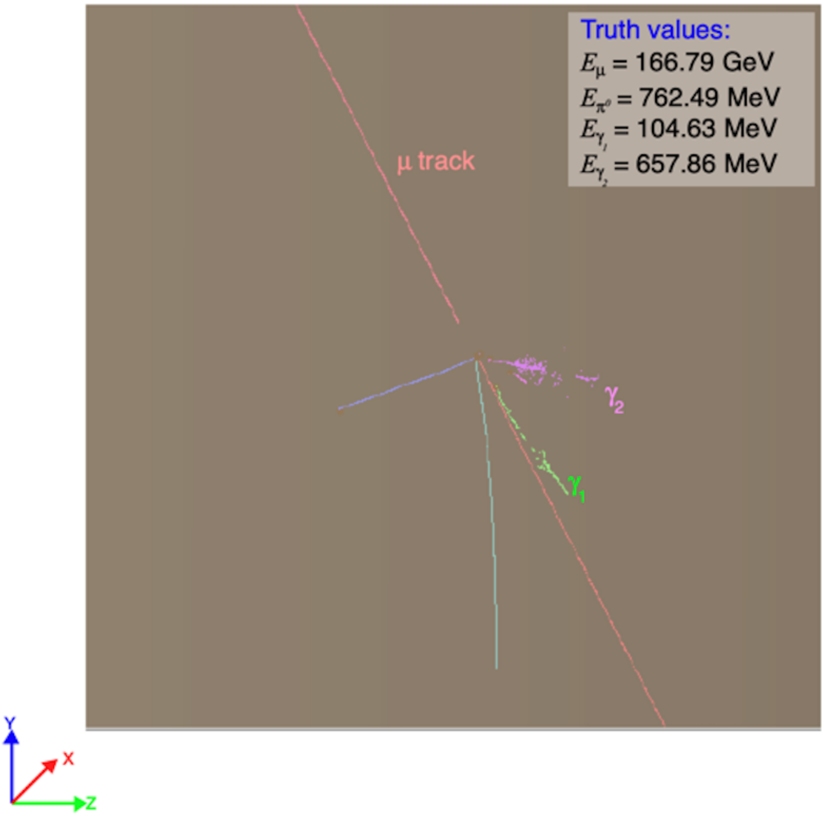

Figure 7.3. Event display of a reconstructed muon event in the DUNE FD. The muon interaction inside TPC produces a π^0. The muon track is shown in light magenta. The neutral pion decays to two photons γ_1 and γ_2. Two showers emerging from π^0 are shown in green and light pink.

7.2 Analysis framework

Simple analysis can be directly performed within LArSoft modules. LArSoft has pre-written analysis modules for specific or general purposes. The main challenge arises when complex or dedicated studies have to be performed. The number of simulated events used in the analysis is large, containing 1.5 million events. Each reconstruction file contains 500 simulated cosmic muon events and has a size of ∼1.8 gigabytes. These events on average stored approximately thousands of Monte Carlo (MC) particles and hundreds of true and reconstructed hits. This makes the analysis a lengthy and time-consuming process running on the Fermilab computing facilities. For these reasons, a custom LArSoft analysis module is written for a particular analysis and is used exclusively for the extraction of relevant particles and their information based on the analysis goal from the main reconstruction file. The analysis module writes the values of relevant quantities of each event in a simple ROOT [205] file having a tree-structured format. Most of the information from the reconstruction file can be copied without any changes such as position, direction, particle data group (PDG) code [202] and basic information on their hits. To avoid storing all MC hit information, simple calculations are performed to store quantities such as purity and completeness of reconstructed objects. These quantities are defined in Section 7.4.1. ROOT tree-based parameters can be easily accessed in a later stage for plotting histograms and calculating other analysis-specific quantities such as opening angle and reconstructed invariant mass using ROOT scripts. A graphical representation of the analysis framework is shown in Figure 7.4. Green boxes represent the earlier stages which are already performed for the studies described in Chapter 5.

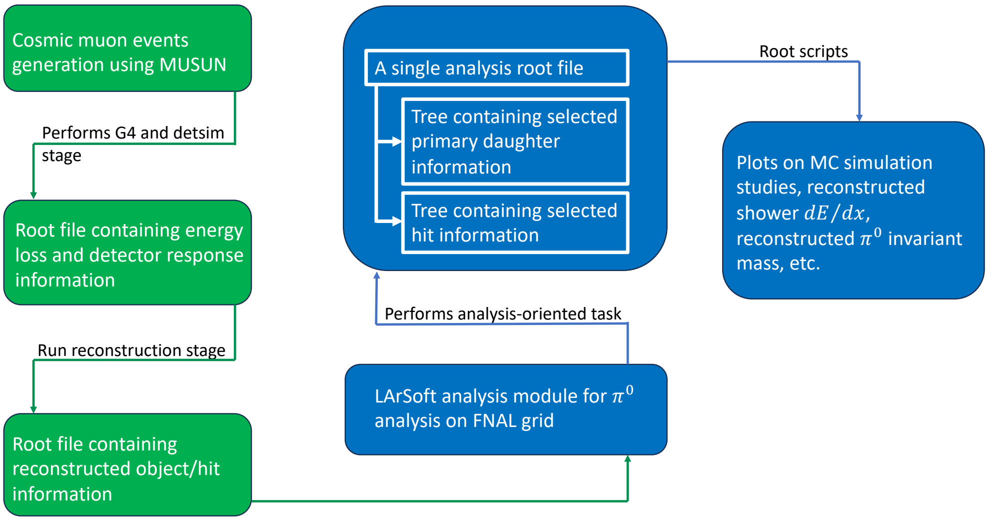

Figure 7.4. Analysis layout of π^0 used in this chapter. Green boxes represent the earlier stages that have already been performed for the studies described in Chapter 5, whilst blue boxes represent the stages which are carried out for the π^0 analysis.

7.3 Monte Carlo simulation studies

Simulated cosmic muon events in the DUNE FD are the source of the π^0 sample for this study. In this section, various parameters are analysed considering only the truth information of simulated events. Cosmic muon events are reconstructed using two different algorithm chains, neutrino-oriented and cosmic-oriented reconstruction. These two reconstruction chains have been discussed in Section 6.6. For this study, 1.48×10^6 neutrino-oriented reconstructed events which correspond to 105 days of data at DUNE FD are considered. A sample of 3.20×10^5 cosmic-oriented reconstructed events which correspond to 22 days of data at DUNE FD is also considered for the comparison. Table 7.1 analyses the π^0 statistics in the sample.

Table 7.1. Event statistics of the generated cosmic muon sample used in this study. The second column shows the number of counts in neutrino and cosmic-oriented reconstruction. Daily rate statistics in the third column is calculated using the rate of the sampled muons. The fraction in the last column is calculated with respect to muons reaching the active volume, except for the fraction of muons in TPC volume which is calculated with respect to the total number of generated muons.

Characterisation	Total number		Daily rate		Fraction [%]	
	NRC	CRC	NRC	CRC	NRC	CRC
Generated events	1.48×10^6	3.20×10^5	1.41×10^4	1.41×10^4		
Muons in TPC	4.99×10^5	1.08×10^5	4.76×10^3	4.77×10^3	33.69 ± 0.06	33.81 ± 0.12
Events with π^0	3.92×10^3	9.54×10^2	37.36	42.09	0.79 ± 0.01	0.88 ± 0.03
π^0 in TPC	2.27×10^4	4.97×10^3	2.17×10^2	2.19×10^2	4.56 ± 0.03	4.59 ± 0.07

The first step of this study is to select events containing at least one π^0. Higher-energy muons can generate particle cascades in the detector. This can lead to more than one neutral pions in an event. The 3D location of each π^0 particle's vertex produced in the DUNE FD is shown in Figure 7.5. Figure 7.6a shows the distribution of neutral pions multiplicities produced in each event inside the DUNE FD. The zenith angle distribution of the π^0 sample is shown in Figure 7.6b. Most of the neutral pions are pointing downwards following the direction of the interacting muons. The mean of the cosine of the zenith angle is -0.47.

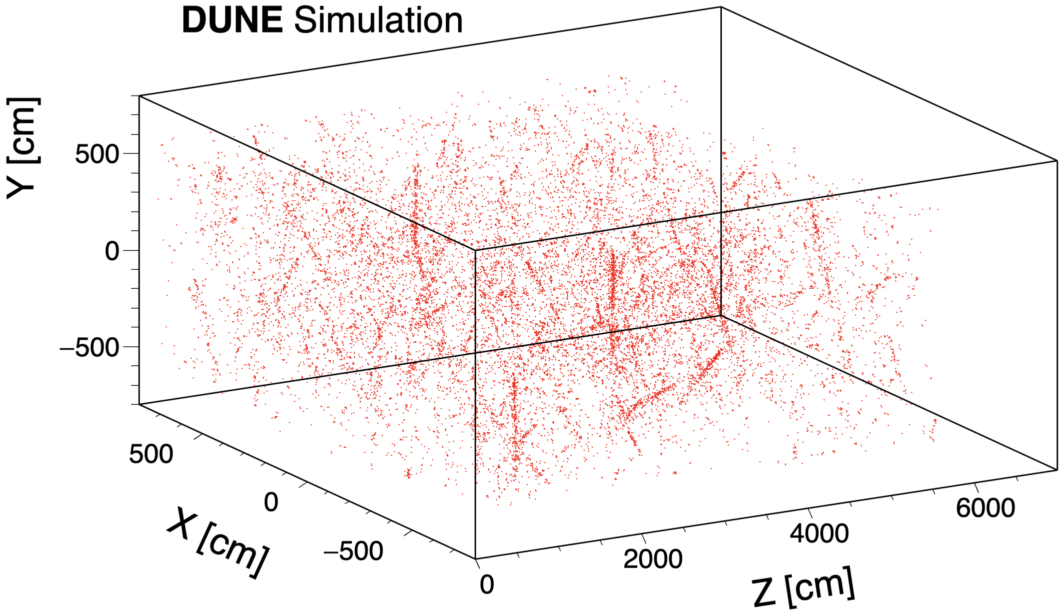

Figure 7.5. Location of π^0 particles produced in the DUNE FD. Each red dot represents the 3D location of the π^0 particle's vertex. Some of the muon events produce hadronic cascades and thus generate several neutral pions.

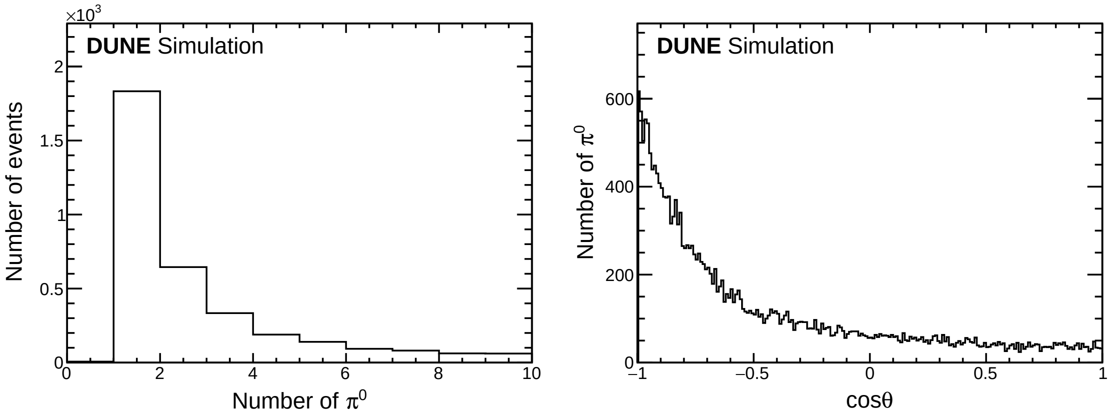

(a) (b)

Figure 7.6. Multiplicity and zenith angle distributions of neutral pions inside the DUNE FD: a) The number of neutral pions produced in each event, b) the zenith angle distribution of π^0. The majority of the events have one π^0 but there are a few events which have several π^0 particles. Most of the pions are directed vertically downward following the direction of parent muons.

The total energy of neutral pions and their photon daughters are shown in Figure 7.7. The π^0 energy produced in an event ranges from a few MeV to tens of

GeV. The rest mass is the minimum energy a particle can have; hence, the energy spectrum of the neutral pion starts from 135 MeV/c^2. The energy spectrum of π^0 is shown in Figure 7.7a. The mean energy is 0.53 GeV. Neutral pion energy is distributed asymmetrically between its two daughter photons. Figure 7.7b shows the energies of the leading and subleading photons from the π^0 decay. Higher energy photon in $\pi^0 \rightarrow 2\gamma$ decay is termed as leading photon whilst lower energy photon is termed as subleading photon. The distribution of subleading photon energies peaks at 60 MeV, presenting a significant challenge in the reconstruction of these showers. Electromagnetic showers have a nebulous nature in LArTPC, making it difficult for the clustering algorithm to identify smaller shower objects and distinguish them from the noise. Reconstructed parameters will be discussed in the coming sections.

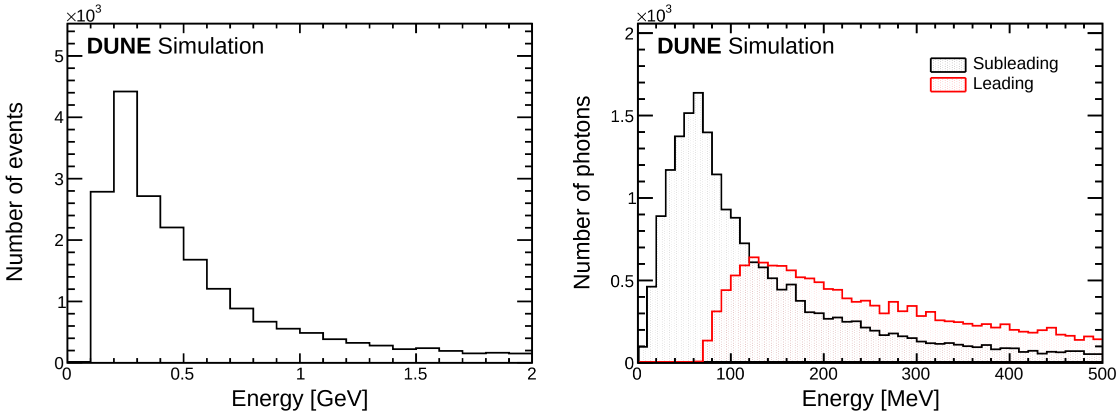

(a) **(b)**

Figure 7.7. Energy distribution of neutral pions and their daughter photons inside the DUNE FD: a) energy distribution of π^0, b) energy distribution of leading and subleading photons.

The last parameter used to reconstruct the π^0 mass is the opening angle of two daughter photon showers coming from π^0 decay as shown in Figure 7.8a. Showers that emerge at very low opening angles may overlap with the second shower from π^0 decay, hence reconstructed shower energy may be imperfectly reconstructed. This issue is also discussed in later sections. The calculated π^0 mass using the truth values of the opening angle and energy of two photons from $\pi^0 \rightarrow 2\gamma$ decay using Equation 7.9 is shown in Figure 7.8b. The peak at 135 MeV/c^2 shows the correct matching of two decaying photons with π^0, hence giving the correct π^0 rest mass.

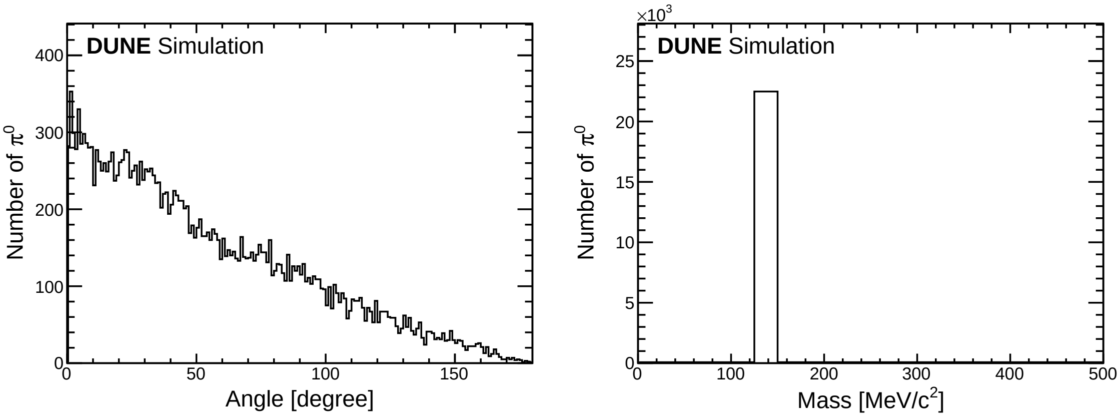

(a) **(b)**

Figure 7.8. Opening angle of two photons from $\pi^0 \to 2\gamma$ decay and π^0 mass distributions inside the DUNE FD: a) opening angle distribution of two photons, b) true π^0 mass calculated from the truth values of opening angle and energy of two photons using Equation 7.9. The peak at 135 MeV/c^2 shows the rest mass of π^0.

The link between simulated and reconstructed particles is not directly built into the reconstruction chain for the simulated events. However, there is a useful feature called BackTracker [206] which is separately incorporated in LArSoft. The BackTracker identifies the origin of each reconstructed hit [2] object by finding the match with the simulated charge depositions. These simulated charges have links to potential MC particle objects. A reconstructed object is a collection of hits that may have originated from different sources. Hence a reconstructed object is a cluster of particle traces. Individual MC particle hits may scatter far apart, leading to their division into multiple reconstructed objects. Consequently, in this chapter, each reconstructed shower selected is associated with a single MC particle chosen based on the total number of hits contributed to that reconstructed shower.

7.4 Reconstruction studies

7.4.1 Completeness and purity

The reconstructed invariant π^0 mass mainly depends on how track and shower reconstructions are accomplished. Before considering whether a particle is successfully reconstructed, it is essential to evaluate the quality of the reconstruction process itself. The quantities which define the properties of reconstruction are completeness and purity [2]. These two quantities can be determined after establishing links between the reconstructed object (track or shower) and an MC particle. The completeness of a reconstructed object is defined as the fraction of hits created by the corresponding MC particle that are successfully captured by the reconstructed object. A completeness of 1 indicates that the reconstructed object includes all of the particle hits. The purity of the reconstructed object is defined as the fraction of hits within the reconstructed object that originated from the linked MC particle. Their definitions are described in Equations 7.10 and 7.11.

$$\text{Completeness} = \frac{\text{Number of shared hits between reconstructed and MC objects}}{\text{Number of hits in MC object}} \tag{7.10}$$

$$\text{Purity} = \frac{\text{Number of shared hits between reconstructed and MC objects}}{\text{Number of hits in the reconstructed object}} \tag{7.11}$$

To understand completeness and purity qualitatively and quantitatively, a simplified event display is considered. Figure 7.9 illustrates the Pandora event display of a cosmic event in which a neutral pion is produced and decays to two photons. Both photons produce EM showers in the detector which are shown in triangles. Different colours represent different reconstructed tracks and showers. Each small rectangular box represents hits reconstructed by Pandora. On the left part of the figure, a back-tracked hit cluster algorithm is used within Pandora which matches the reconstructed hits with MC objects and then hits are clustered as reconstructed objects. On the right part of the figure, the hits are reconstructed without the back-tracked hit cluster algorithm. In the case of photon 1, Pandora creates shower objects out of selected hits (small blue rectangles on the right part). Only 78 out of 98 original photon hits are captured in the reconstructed objects, calculating the completeness $78/98 = 0.8$. A few hits from another particle (hits circled in blue) are included in the shower object, making the purity $78/104$, approximately 0.75.

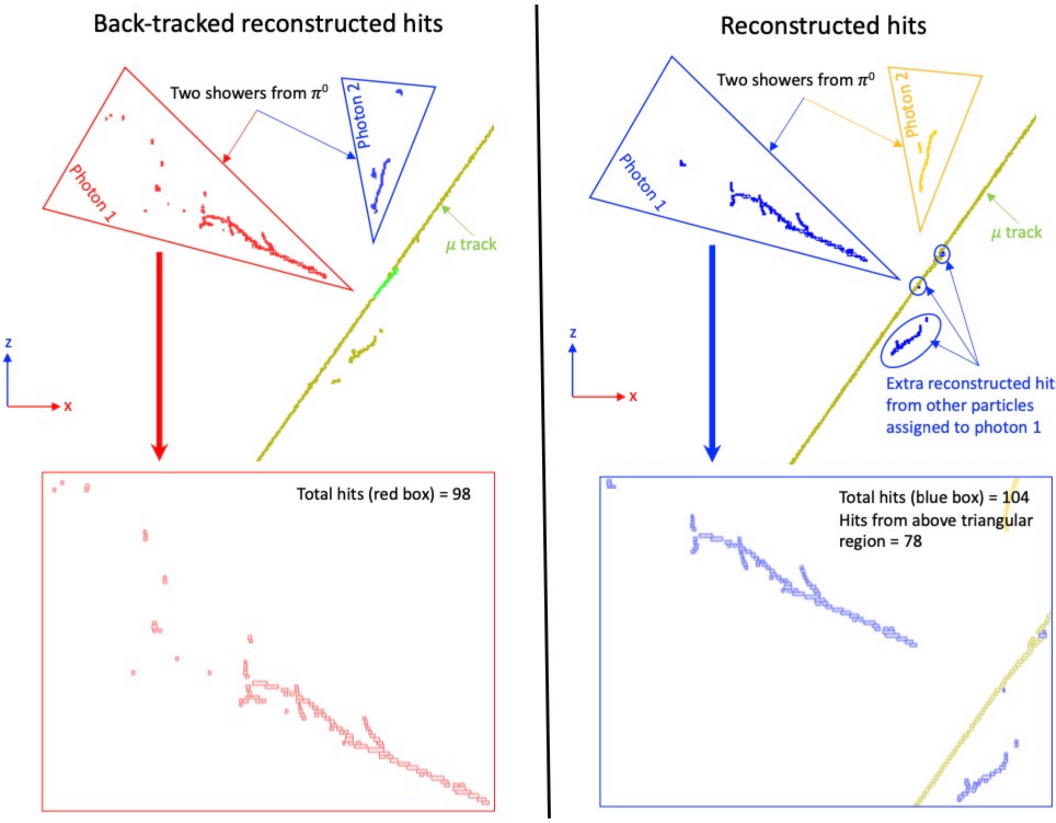

Figure 7.9. An elucidated event display of a reconstructed cosmic muon event in the DUNE FD producing a single π^0 that subsequently decays into two photons. The invisible photons generate electromagnetic showers in the detector, which are represented by triangles. Different colours distinguish various tracks and showers. Each small rectangular box corresponds to hits reconstructed by Pandora. On the left side of the figure, Pandora utilises a back-tracked hit cluster algorithm, matching reconstructed hits with MC objects. On the right side of the figure, no back-tracked information is used for reconstruction. For photon 1, Pandora generates shower objects including hits from the other particles circled in blue.

Figure 7.10 shows the distribution of completeness and purity of reconstructed photons produced from $\pi^0 \rightarrow 2\gamma$ in the events. It includes all π^0 where either or both photons are reconstructed from the π^0 decay, as well as all showers in case of multiple showers reconstructed for a photon. It can be noticed that only 50 % of reconstructed showers have a purity > 0.8. The completeness distributions show a dual peak structure which can be due to the contribution of leading showers towards higher value since leading showers have better completeness than subleading showers. The extent of completeness directly impacts the process of energy reconstruction — the higher the completeness the better the energy of the reconstructed shower. Sub-leading photon showers are not well reconstructed since they have low energy compared to leading photon showers. Figure 7.11 shows the completeness and purity of leading and subleading photon showers from π^0 decay, where both photons are reconstructed from the π^0 decay. The number of π^0 in which both photons are reconstructed is lower compared to the total number of π^0 produced in the DUNE FD, as shown in Table 7.2. In the case of multiple shower formation by Pandora, the maximum energy shower is selected.

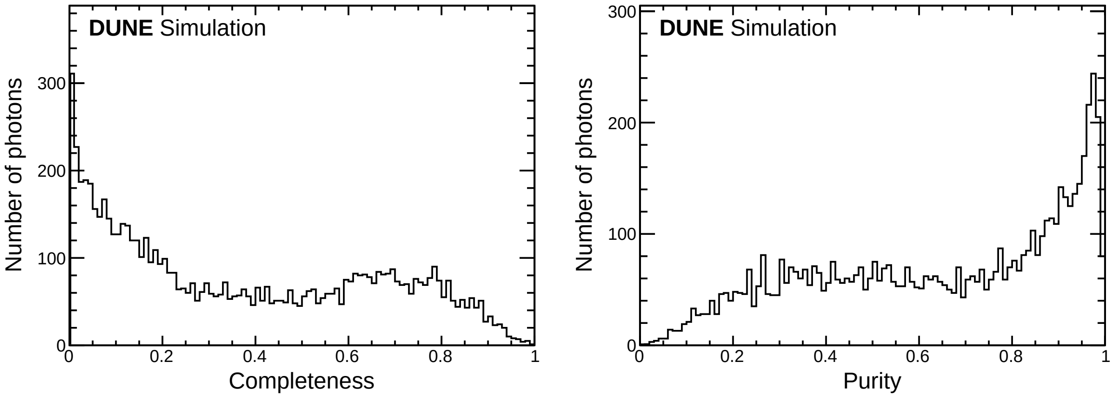

(a) (b)

Figure 7.10. Completeness (a) and purity (b) distribution of reconstructed photons from $\pi^0 \rightarrow 2\gamma$ in DUNE FD, where either or both of the photons are reconstructed from the π^0 decay.

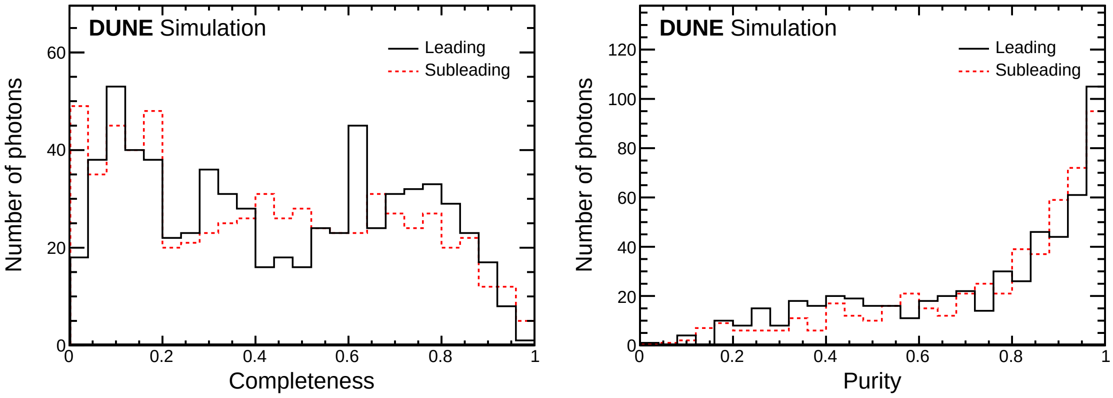

(a) (b)

Figure 7.11. Completeness (a) and purity (b) distribution of leading and subleading reconstructed photons from $\pi^0 \rightarrow 2\gamma$ decay in DUNE FD, where both photons are reconstructed from the π^0 decay.

Completeness and purity are significantly influenced by the size of the reconstructed shower. Smaller showers tend to have lower completeness because their shape is not well defined and becomes challenging for reconstruction. Conversely, larger showers tend to overlap with other objects, leading to a decrease in their purity. Figure 7.12 shows the completeness and purity of reconstructed showers of leading and subleading photons based on their size of hits. Linking truth and reconstructed information can be beneficial as it allows for the selection of well-reconstructed objects with high accuracy, even in cases where truth information is not available. By using such links, more complete photon showers can be effectively chosen through a cut on the minimum number of hits.

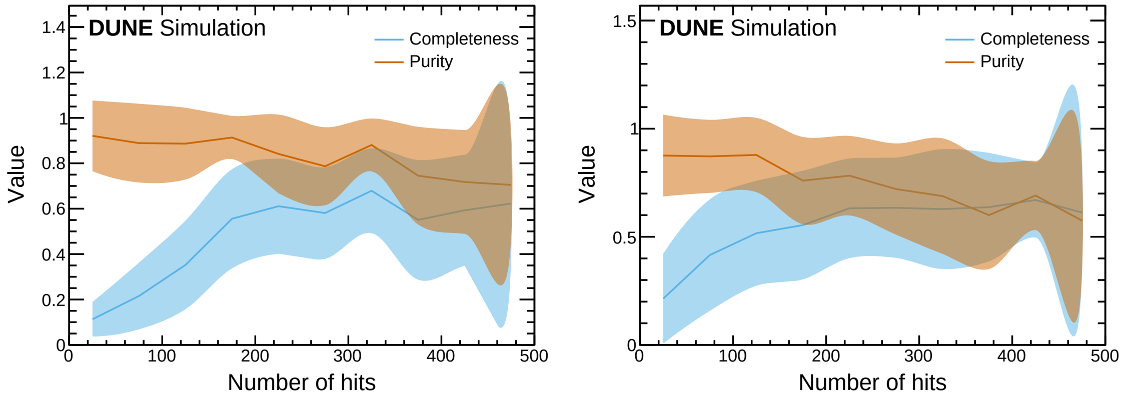

(a) **(b)**

Figure 7.12. Completeness and purity distribution of leading and subleading reconstructed photons from $\pi^0 \to 2\gamma$ decay as a function of the number of hits in the reconstructed objects: a) leading photon, b) subleading photon. The colour band shows a 1σ spread of the values in each bin.

7.4.2 Reconstructed showers

The reconstructed shower energy is the essential quantity to reconstruct the π^0 invariant mass. Biases in the photon energy reconstruction can be understood by correlating the true and reconstructed π^0 mass. A table containing statistics of the reconstructed showers is shown in Table 7.2. Figure 7.13 shows the distribution of the number of reconstructed showers produced in an event containing π^0 in CRC and NRC samples. In many cases, Pandora does not identify the showers from a π^0, resulting in significantly reduced matching of reconstructed showers with true photons for events $\pi^0 \to 2\gamma$. These events are also included in the figure. The single π^0 events are simpler and the identification of the shower is easier. Events that have exactly one neutral pion are also included in the figure. The cosmic-oriented sample has more reconstructed showers in an event. It can be due to the Pandora algorithm being more tuned to track like objects rather than shower objects and hence one big shower may be reconstructed as many small shower objects.

Table 7.2. An extended version of event statistics presented in Table 7.1 including reconstructed shower quantities. The second column shows the number of counts produced in NRC and CRC samples. The daily rates shown in the third column are calculated using the rate of sampled muons. The fraction in the last column is calculated with respect to muons reaching the active volume except the fraction of muons in TPC which is calculated with respect to the total generated muons. The fraction of the total number of events $\pi^0 \to 2\gamma$ and shower matched with photons is calculated with respect to the total events with π^0 and the fraction for the last three characterisations is calculated with respect to the total number of π^0 in TPC.

Characterisation	Total number		Daily rate		Fraction [%]	
	NRC	CRC	NRC	CRC	NRC	CRC
Generated events	1.48×10^6	3.20×10^5	1.41×10^4	1.41×10^4		
Muons in TPC	4.99×10^5	1.08×10^5	4.76×10^3	4.77×10^3	33.69 ± 0.06	33.81 ± 0.12
Events with π^0	3.92×10^3	9.54×10^2	37.36	42.09	0.79 ± 0.01	0.88 ± 0.03
π^0 in TPC	2.27×10^4	4.97×10^3	2.17×10^2	2.19×10^2	4.56 ± 0.03	4.59 ± 0.07
Reconstructed showers associated with π^0	7.62×10^3 (Per $\pi^0 = 0.33$)	1.60×10^4 (Per $\pi^0 = 3.21$)	72.69	7.05×10^2	1.53 ± 0.02	14.76 ± 0.13
Number of events with $\pi^0 \to 2\gamma$ where showers are matched with photons	6.25×10^2	6.85×10^2	5.96	30.22	15.96 ± 0.67	71.80 ± 3.60
Number of π^0 which decay to 2γ where showers are matched with photons	6.67×10^2	1.46×10^3	6.36	64.37	2.93 ± 0.12	29.37 ± 0.87
Number of π^0 which decay to 2γ and exactly 1 shower is matched with photon	5.32×10^2	1.86×10^2	5.07	8.21	2.34 ± 0.10	3.74 ± 0.28
Number of 1 π^0 events with $\pi^0 \to 2\gamma$ where showers are matched with photons	2.35×10^2	2.56×10^2	2.24	11.29	1.03 ± 0.07	5.15 ± 0.33

Photons from $\pi^0 \to 2\gamma$ may have multiple reconstructed showers by Pandora. The fragmentation of the shower affects reconstructed photon energy and opening angle and consequently reconstructed π^0 mass. Figure 7.14 shows the distribution of the number of reconstructed showers produced from a photon in two different samples. The cosmic oriented reconstruction sample has more shower fragmentation, resulting in a long tail in the distribution shown in Figure 7.14b.

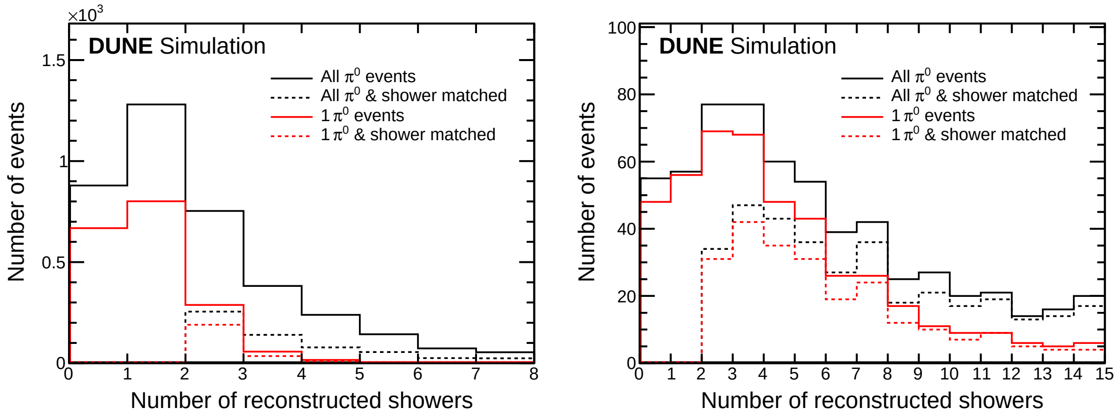

(a) (b)

Figure 7.13. Distributions of reconstructed showers in $\pi^0 \to 2\gamma$ events in two samples with different reconstruction algorithms: a) neutrino oriented reconstruction sample corresponding to 105 days at DUNE FD, b) cosmic oriented reconstruction sample corresponding to 22 days at DUNE FD. Events containing at least one π^0 are shown by a solid black histogram and the dashed black histogram represents an additional selection if both photons have at least one matched reconstructed shower. Events containing exactly one π^0 are shown in a solid red histogram and the dashed red histogram represents an additional selection if both photons have exactly one matched reconstructed shower.

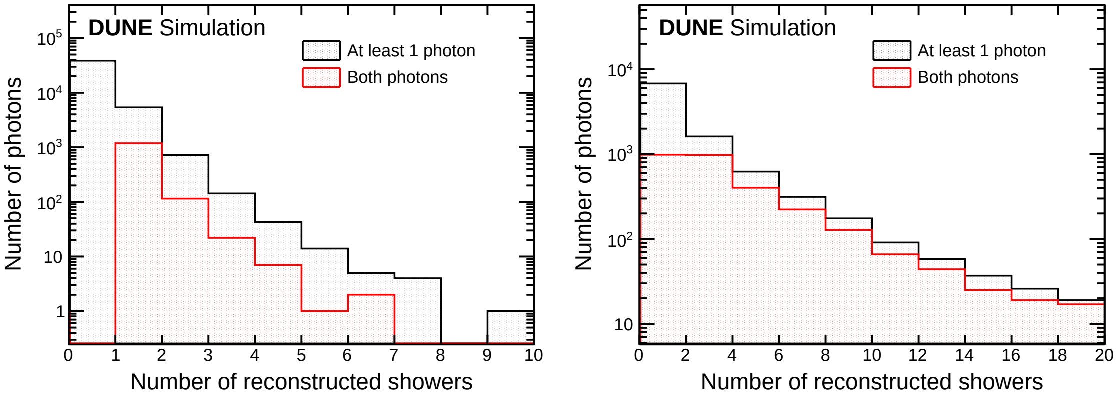

(a) (b)

Figure 7.14. Reconstructed shower multiplicity of photons from $\pi^0 \to 2\gamma$ in two samples with different reconstruction algorithms: a) neutrino oriented reconstruction sample, b) cosmic oriented reconstruction sample. The grey shaded area represents cases where either photon from $\pi^0 \to 2\gamma$ has at least one matching reconstructed shower, while the red shaded area indicates cases where both photons from $\pi^0 \to 2\gamma$ have at least one matching reconstructed shower.

7.4.3 Reconstructed shower energy

The reconstructed shower energy of photons from $\pi^0 \to 2\gamma$ with various selections is shown in Figure 7.15. Low energy photons seem not well reconstructed as many of the showers in the figure have very low values. In cosmic-oriented reconstruction, the shower's energy peaks near zero. This is because in cosmic reconstruction, shower fragmentation is higher and as a result, each fragmented shower has a low reconstructed energy value. Many of the photons from π^0 have not been associated with reconstructed showers. Using a selection on π^0 with at least one matching shower to photons from $\pi^0 \to 2\gamma$ reduces the π^0 statistics to 3% of the total π^0 produced in the DUNE FD. Single neutral pion events are simpler and the identification of showers is easier. Selecting only one π^0 event further reduced the statistics to 1% of the total π^0 produced in the DUNE FD.

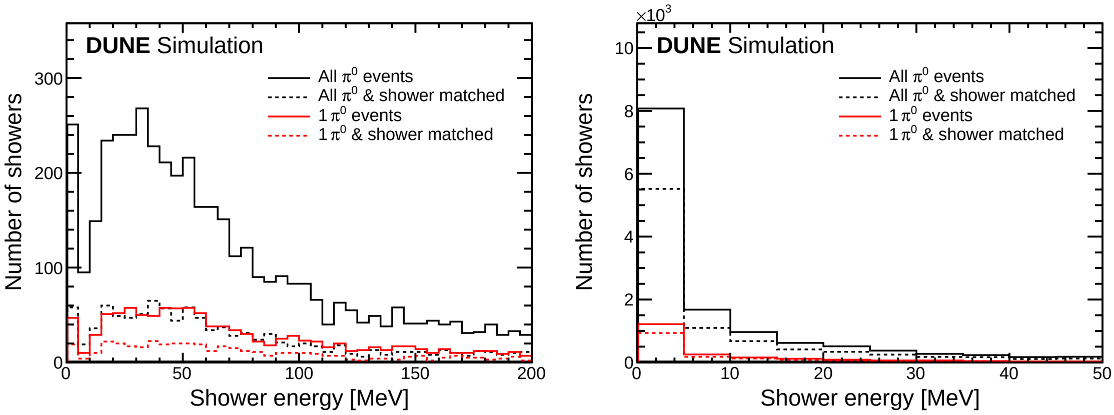

(a)

(b)

Figure 7.15. Reconstructed shower energy distribution from $\pi^0 \to 2\gamma$ events in two samples with different reconstruction algorithms: a) neutrino oriented reconstruction sample, b) cosmic oriented reconstruction sample. The solid black histogram shows at least one reconstructed shower matched with either photon and the dashed black histogram represents an additional selection if both photons from $\pi^0 \to 2\gamma$ have at least one matching reconstructed shower. The solid red histogram shows one π^0 event and reconstructed shower matched with either photon from π^0 and the dashed red histogram represents an additional selection if both photons from $\pi^0 \to 2\gamma$ have a matching reconstructed shower.

The bias of shower energy reconstruction with respect to the photon energy can be further analysed with leading and subleading true photons from neutral pions decaying to 2γ. The energy distribution of leading and subleading photons and reconstructed showers are shown in Figure 7.16. Subleading showers have low energy reconstruction performance in comparison to leading showers. The highest energy shower is selected in case of multiple reconstructed showers associated with a photon from $\pi^0 \rightarrow 2\gamma$ in all figures.

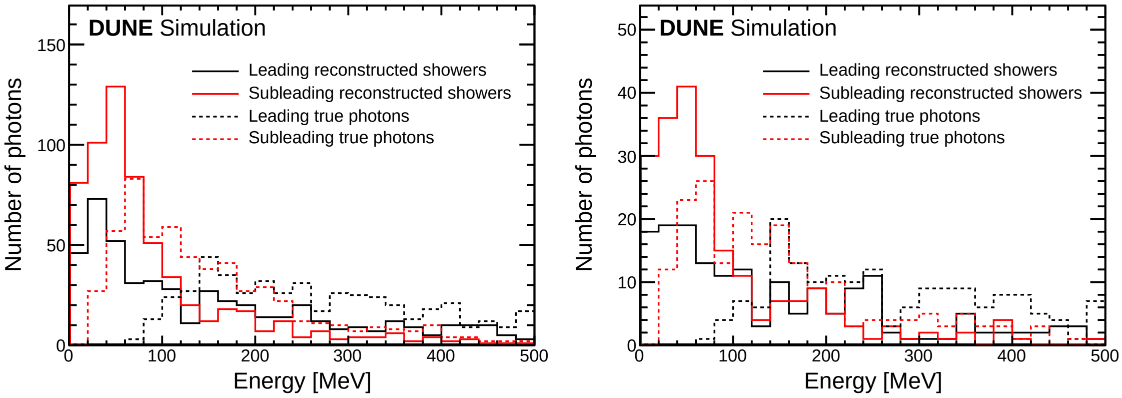

(a) **(b)**

Figure 7.16. True and reconstructed shower energy distribution of leading and subleading photons from $\pi^0 \rightarrow 2\gamma$ events in two samples with different reconstruction algorithms: a) neutrino oriented reconstruction sample, b) cosmic oriented reconstruction sample. The events are selected with $\pi^0 \rightarrow 2\gamma$ and at least one shower is matched with either photon. The maximum shower energy is chosen in case of multiple reconstructed showers associated with a photon.

A comparison between true and reconstructed photon energy is useful to understand how well the photon energy is reconstructed. Figure 7.17 shows the distribution of reconstructed shower energy as a function of true photon energy. The red line denotes the average of the values in each bin. It can be seen that the neutrino-oriented reconstruction sample has a better correlation between reconstructed and true photon energy than the cosmic-oriented reconstruction sample due to less fragmentation of showers in the neutrino-oriented reconstruction sample. Many of them pile up near low energy indicating the poor performance of reconstruction.

To evaluate the quality of the photon shower energy reconstruction, a valuable metric is the relative difference between the reconstructed and true (MC), expressed as $(E_{\text{reconstructed}} - E_{\text{MC}})/E_{\text{MC}}$. Figure 7.18 shows the relative difference between reconstructed and true photon energy. The peak near -1 ($E_{\text{reconstructed}} = 0$) indicates that the energy reconstruction does not perform very well for many of the showers. In the cosmic reconstruction sample, it even gets more shifted near -1 indicating the energy reconstruction is not well performed. Considering the limitations of

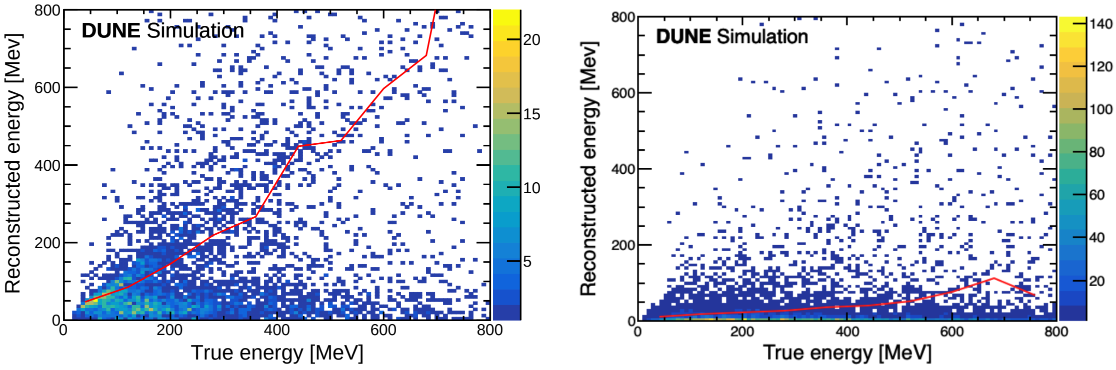

(a) (b)

Figure 7.17. True and reconstructed shower energy distribution from $\pi^0 \to 2\gamma$ events in two samples with different reconstruction algorithms: a) neutrino-oriented reconstruction sample, b) cosmic-oriented reconstruction sample. The events are selected in which $\pi^0 \to 2\gamma$ and at least one reconstructed shower are associated with either photon. The red line denotes the average of the values in each bin. The neutrino-oriented reconstruction sample shows a better correlation between true and reconstructed shower energy than the cosmic-oriented reconstruction sample.

previous studies on the cosmic-oriented sample, which did not perform well in terms of shower reconstruction, only the neutrino-oriented reconstruction sample is considered for the analysis moving forward.

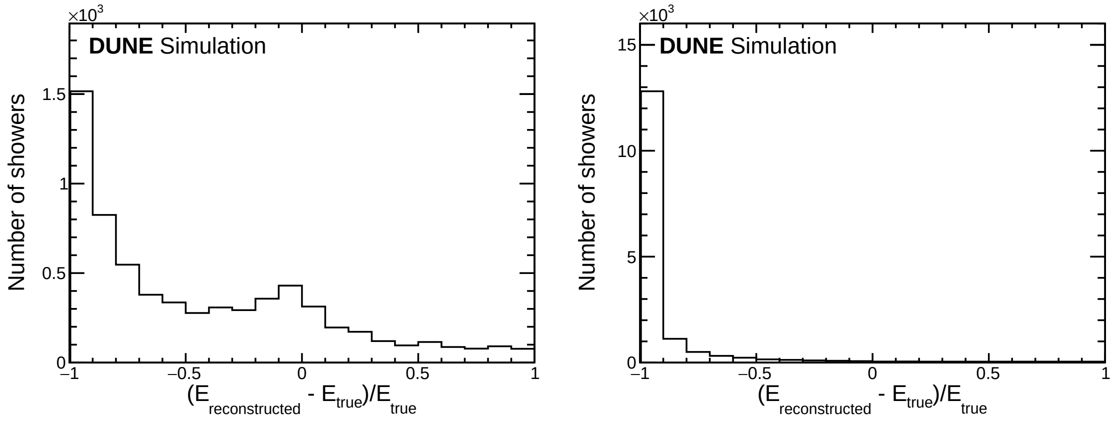

(a) (b)

Figure 7.18. The relative difference between reconstructed and true energy $(E_{\text{reconstructed}} - E_{\text{MC}})/E_{\text{MC}}$ from $\pi^0 \to 2\gamma$ events in two samples with different reconstruction algorithms: a) neutrino oriented reconstruction sample, b) cosmic oriented reconstruction sample. The events are selected in which $\pi^0 \to 2\gamma$ and at least one shower is associated with either photon.

The metric $(E_{\text{reconstructed}} - E_{\text{MC}})/E_{\text{MC}}$ is considered as a function of the number of hits in Figure 7.19. From the plot, it is evident that small shower objects have energies that fall below the true energy of the photon, mainly because of their low completeness. On the other hand, larger objects show an energy surplus, which can be attributed to the reduction in purity. The reconstructed energy rises to a value above the original photon energy when the shower mistakenly includes the other particle hits. The relative energy difference approaches 0 for showers containing 150 or more hits for the leading showers and 100 or more hits for the subleading showers. The selection of the number of hits improves the quality of reconstructed showers, leading to an enhancement in the reconstructed π^0 mass as discussed in a later section. However, implementing cuts on these hits reduces the statistics.

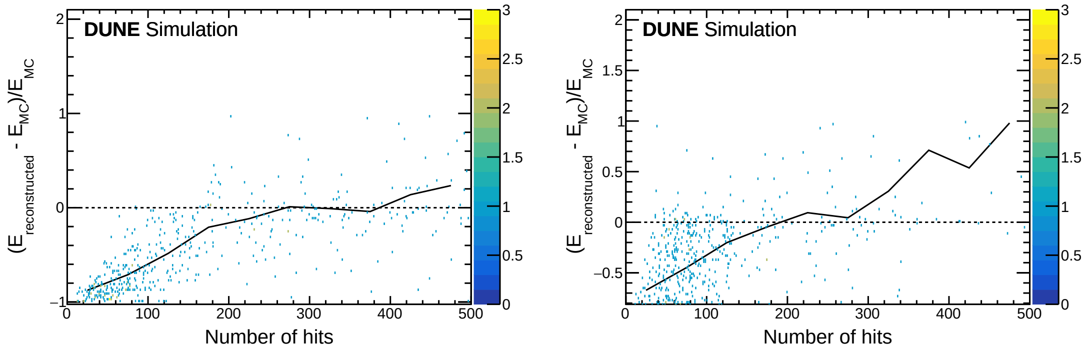

(a) **(b)**

Figure 7.19. The distribution of relative energy difference $(E_{\text{reconstructed}} - E_{\text{MC}})/E_{\text{MC}}$ of leading and subleading photons as a function of the number of hits from $\pi^0 \rightarrow 2\gamma$ events: a) leading photons, b) subleading photons. The solid black line denotes the average of the values in each bin. The black dashed line shows the perfect match at 0. Only π^0's that have at least one matching reconstructed shower for both photons are selected.

7.4.4 Reconstructed opening angle

The opening angle between photons from $\pi^0 \rightarrow 2\gamma$ decay provides the last ingredient for the reconstruction of the neutral pion mass. Obtaining an accurate reconstructed opening angle requires that the direction of each reconstructed shower represents that of its parent photon. Figure 7.20a shows the angle between π^0 daughter photons and their associated reconstructed objects for leading and subleading showers. In the case of multiple shower formation for a photon, the maximum energy shower is selected. It can be seen that many of the showers have an angle greater than 90 degrees. This could be because Pandora wrongly identified the shower direction or maybe showers were reconstructed backwards. To examine further whether it depends on the case where multiple showers are reconstructed for either photon from $\pi^0 \rightarrow 2\gamma$ decay, Figure 7.20b displays the photon-shower angle for leading and subleading photons when exactly one shower is reconstructed for each photon from $\pi^0 \rightarrow 2\gamma$. This also follows a similar trend.

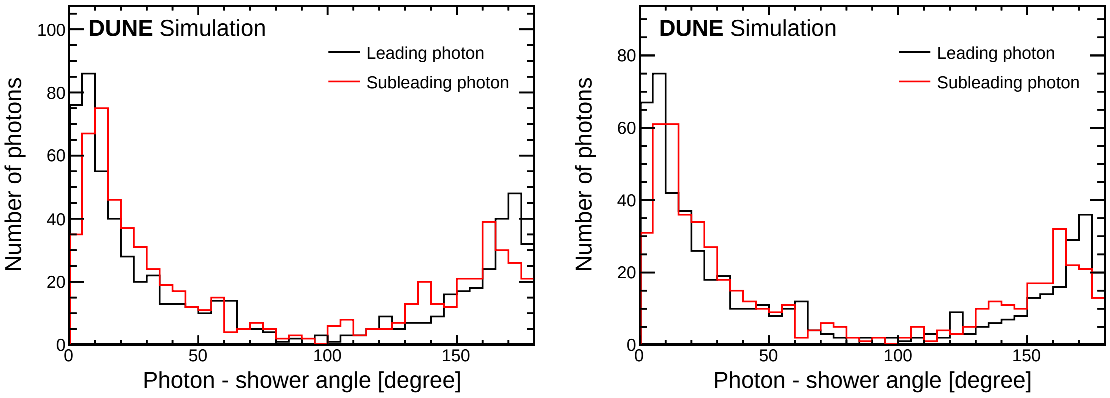

(a) **(b)**

Figure 7.20. The three-dimensional angle between photons and their associated shower objects from $\pi^0 \rightarrow 2\gamma$ decay for leading and subleading photons: a) including multiple reconstructed showers from either photon, b) only one shower reconstructed for each photon.

The photon-shower angle is further analysed with the number of hits which make up the reconstructed showers. Figure 7.21 shows the angle between photons and their associated reconstructed objects from $\pi^0 \rightarrow 2\gamma$ decay as a function of the number of collection plane hits contained within the shower object. The plot exhibits a similarity between the leading and subleading π^0 daughter photons, apart from the shortage of large subleading showers. This also follows a similar trend as in Figure 7.20. Many of the showers are reconstructed backwards, significantly towards lower numbers of hits.

The distribution of reconstructed and true opening angle between two photons from $\pi^0 \rightarrow 2\gamma$ decay is shown in Figure 7.22. Figure 7.22a shows the opening angle of reconstructed showers from $\pi^0 \rightarrow 2\gamma$ decay. The mean of the angle distribution is 68 degrees. To analyse shower angle reconstruction performance, the distribution of the reconstructed opening angle as a function of the true opening is shown in Figure 7.22b. At a low angle, the reconstructed shower opening angle is more populated at higher values indicating that at a low opening angle, the shower angle reconstruction is not well performed.

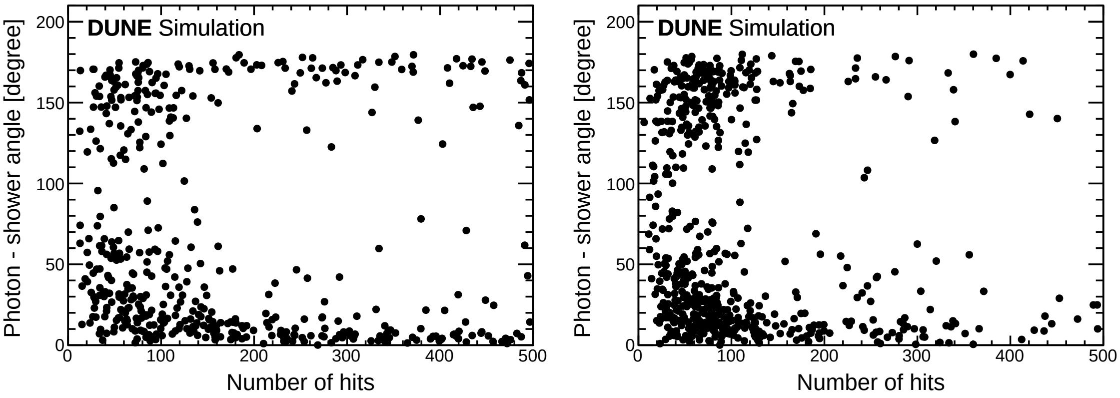

(a) **(b)**

Figure 7.21. The angle between photons and their associated shower objects from $\pi^0 \rightarrow 2\gamma$ decay as a function of the number of hits: a) leading photons, b) subleading photons.

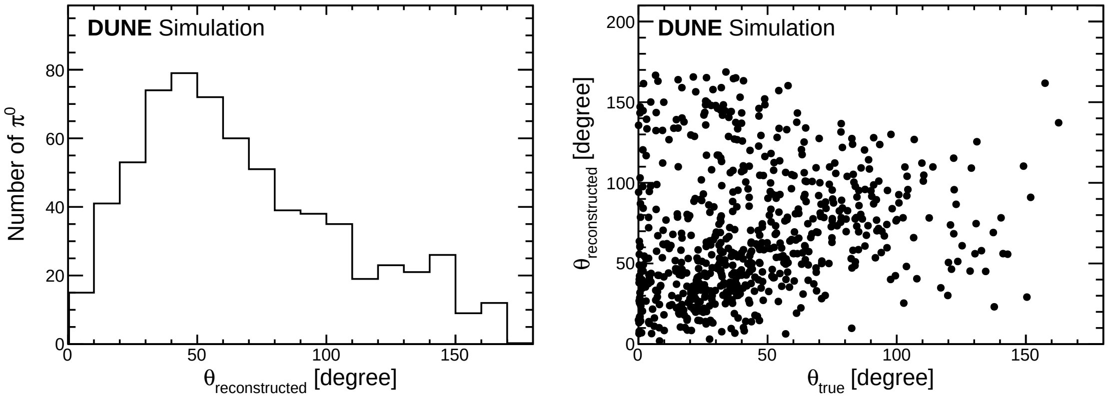

(a) **(b)**

Figure 7.22. The distribution of true and reconstructed opening angle between photons from $\pi^0 \rightarrow 2\gamma$ decay: a) reconstructed opening angle, b) reconstructed opening angle vs. true opening angle.

The quality of the reconstructed opening angle θ between two-photon showers from the $\pi^0 \rightarrow 2\gamma$ decay can be evaluated using various methods. Figure 7.23 presents two such approaches: the absolute difference between the reconstructed and true opening angles and a metric more suited for reconstructing the π^0 invariant mass.

In particular, the factor C, defined as $C = 1 - \cos\theta$, plays a direct role in the calculation of the invariant mass as described in Equation 7.9. Both distributions in Figure 7.23 show peaks around 0, indicating that the reconstructed opening angles are generally close to the true values. However, the wide spread of the distributions suggests that there are variations in the reconstructed opening angles. The comprehensive studies on shower reconstruction performance carried out in previous sections may account for this variation in the reconstructed opening angles.

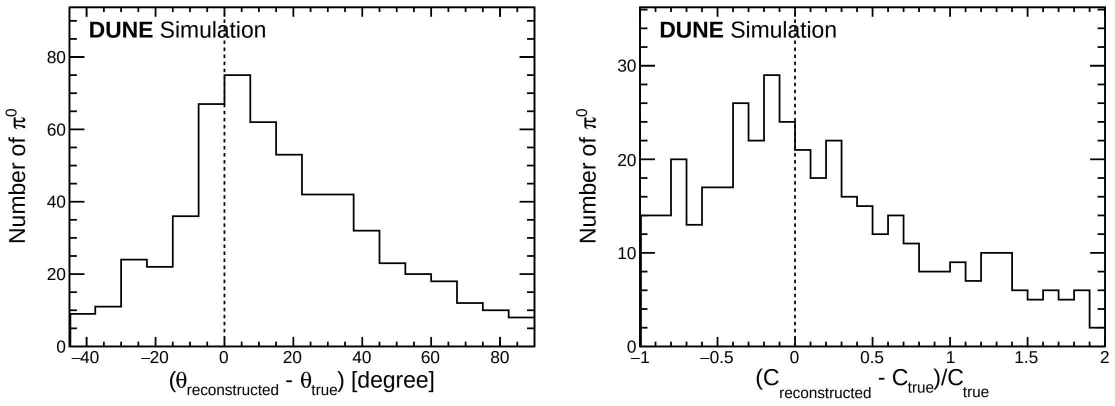

(a)

(b)

Figure 7.23. The difference between reconstructed and true opening angles of photon showers from $\pi^0 \to 2\gamma$ decay: a) the absolute difference between reconstructed and true opening angles and b) the relative difference between reconstructed and true $C = 1 - \cos\theta$. The black dashed line shows the perfect reconstruction.

Figure 7.24 explores the poorly reconstructed opening angles by examining the relative difference in factor C as a function of the reconstructed opening angle. The plot reveals that reconstruction is poor for all angles, and angles below $\sim 20°$ degrees tend to exhibit a higher tendency to be less well-reconstructed.

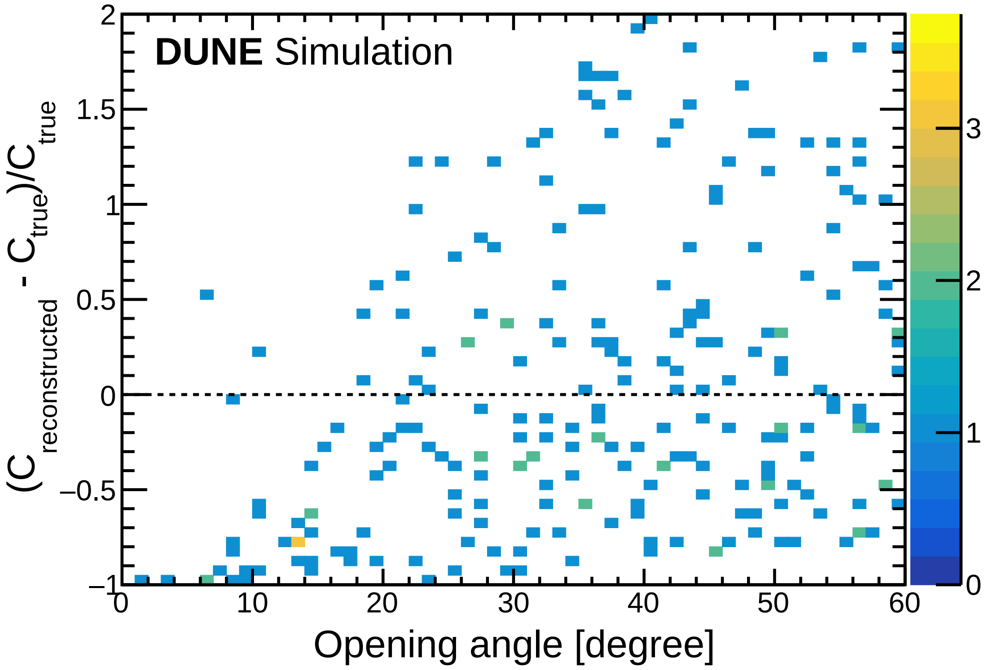

Figure 7.24. The relative difference between reconstructed and true $C = 1 - \cos\theta$ as a function of the reconstructed opening angle. Notably, the reconstructed opening angles below $\sim 20°$ have a high tendency of being imperfectly reconstructed. The black dashed line shows the perfect reconstruction.

7.5 Reconstructed π^0 mass

To select the best fraction of the sample, given the performance of the reconstruction, the selection can be made on the number of shower hits and the reconstructed opening angle of photons showers. These selections reduce the π^0 statistic significantly. Table 7.3 shows the cuts applied on different quantities and the number of π^0 being left after the cuts applied for the reconstructed neutral pion invariant mass studies. The total number of π^0 before these two cuts is 667 with a daily rate of 6.36, which has at least one matching reconstructed shower for both photons in $\pi^0 \to 2\gamma$. The cosmic muon event sample taken for this analysis is mentioned in Table 7.1

Table 7.3. The cuts applied on different quantities. The total number of π^0 before these cuts is 667. The cut on the number of reconstructed shower hits reduces statistics significantly. These two cuts together reduce π^0 number to 156 which corresponds to a daily rate of 1.49.

Quantities	Cuts	Number of π^0	Daily rate
Number of shower hits	> 100	187	1.78
Reconstructed opening angle	$> 20°$	611	5.83

The distribution of reconstructed mass using Equation 7.9 after selection mentioned in Table 7.3 is shown in Figure 7.25. To quantify the results, a Gaussian fit was performed within the range (135 ± 115) MeV/c^2. The reconstructed mass has a mean (136 ± 7) MeV/c^2, which is consistent within the statistical uncertainty of 5% with the expected π^0 mass [124]. The standard deviation of the fit is (54 ± 7) MeV/c^2.

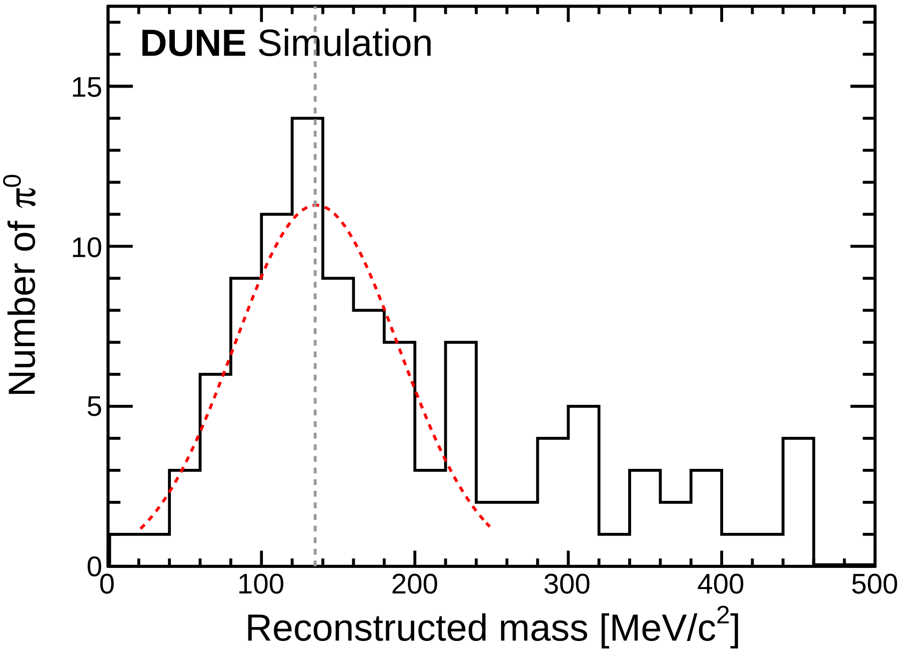

Figure 7.25. The reconstructed mass of π^0 determined from reconstructed shower pairs from $\pi^0 \to 2\gamma$. The shower pairs shown here are subjected to two requirements: an opening angle greater than 20° and a minimum of 100 collection plane hits per shower. The shower pairs are matched with photons from $\pi^0 \to 2\gamma$. The red dashed line shows a Gaussian fit applied within the range (135 ± 115) MeV/c^2. The true π^0 mass is shown with a vertical dashed line.

7.6 Summary

The reconstruction of neutral pion is important in the DUNE FD as it serves as a background for the electron neutrino appearance signal. Additionally, it can be used as a means of calibrating electromagnetic showers. Studies were performed on neutral pion reconstruction produced in cosmic-ray muon events in DUNE FD. The mean value of the reconstructed invariant π^0 mass after applying the Gaussian fit is reconstructed as (136 ± 7) MeV/c^2, which is consistent within the statistical uncertainty of 5% with the expected π^0 mass. Several improvements are needed especially in shower energy reconstruction. The shower clustering and direction reconstruction algorithm is not perfectly tuned by Pandora. The two selections are applied to reconstructed showers: an opening angle greater than 20° and containing at least 100 collection plane hits per shower. In the DUNE FD, the daily rate of neutral pions that decay to 2γ, and each photon has at least one matching reconstructed shower, is 6.36. After applying these two selections, the daily rate reduces significantly to 1.49. Further enhancing the energy and direction reconstruction of photon showers may lead to improvements in the accuracy of the reconstructed invariant mass measurement. By achieving a more accurate and precise reconstruction, the resulting peak in the reconstructed invariant mass distribution becomes sharper and better defined which will allow more reliable electromagnetic shower energy calibration.

Chapter 8

Energy calibration of the DUNE FD using stopping particles

This chapter presents the energy calibration methods developed and employed for the DUNE FD, with a primary focus on utilising stopping cosmic-ray muons as a standard candle for energy scale calibration and subsequent validation with charge pions and protons. Section 8.1 discusses the specifics of energy calibration using stopping muons, starting with the selection of stopping muon events. Section 8.2 presents energy calibration techniques developed for the DUNE FD, utilising stopping cosmic-ray muons. The first method discussed is model-dependent, employing the modified box model that was first developed in the ArgoNeuT experiment [207] and is now implemented for the first time in the DUNE experiment. Conversely, the second method, termed the absolute energy scale method, stands as an independent development by the author, and is implemented in the DUNE for the first time. Furthermore, the same calibration method is applied to charged pions and protons for dE/dx reconstruction, establishing a relation for translating reconstructed charge to energy for these particles, discussed in Section 8.3 and Section 8.4, respectively. Section 8.5 presents a comparison between theoretical dE/dx and reconstructed dE/dx as a function of different variables such as kinetic energy, residual range, and p/m for stopping muons, pions, and protons. The good agreement between theoretical and reconstructed dE/dx validates the absolute energy calibration method for particles in LArTPC. Section 8.6 presents a comparison of reconstructed dQ/dx as a function of different quantities such as kinetic energy, residual range, and p/m for stopping muons, pions, and protons. Finally, Section 8.7 summarises this chapter.

8.1 dE/dx calibration using stopping muons

8.1.1 Introduction

The fundamental strengths of LArTPC technology include its exceptional ability to precisely reconstruct both the direction of particle tracks and their energy. However, various factors, including space charge effects, electron attenuation, diffusion, and recombination, can potentially degrade the energy resolution of the detector. These effects are discussed in detail in Chapter 3. Therefore, precise detector calibration is essential, particularly for accurate dE/dx (energy loss per unit track length) measurements. This calibration is crucial for particle identification, particularly in the distinction of muons, pions and protons in liquid argon.

Stopping muons prove an invaluable calibration source for LArTPCs due to their well-understood energy loss in liquid argon. Muons that come to a stop within the active volume prove to be effective calibration tools, enabling a detailed study of the detector response to specific energy depositions. Determining their energy at any point along the trajectory, measured by the distance from the end of the track, known as the ‘residual range’, allows for a more detailed understanding of how the detector responds to the energy deposition by particles. A calibration constant is determined to convert ionisation charge per unit length dQ/dx to particle energy loss per unit length dE/dx.

8.1.2 Event selection

For this study, a sample of 3.62×10^5 simulated cosmic-ray muon events of cosmic-oriented reconstruction which correspond to 25 days of data at DUNE FD is considered. The simulation and types of reconstruction used in generating cosmic muon event and their characterisation are discussed in detail in Chapter 6. For the selection of truth stopping muons, the first step is to select all muons tagged as primary particles, which means that they do not originate from any other particle. After selecting primary muons (generated muons that entered the DUNE FD), events are confirmed as stopping muons if the particle’s truth end position (x, y, z) is within the TPC. Reconstruction will identify primary cosmic-ray muons by recognizing tracks that have entered the TPC volume from the outside (track-related energy deposition at the edge of the TPC). This process results in a total of 2169 stopping muons in the active volume consisting of 1284 μ^+ and 885 μ^-. All μ^+ produces a

Michel electron after decaying

$$\mu^+ \rightarrow e^+ + \nu_e + \bar{\nu}_\mu, \tag{8.1}$$

while μ^- either decays or is captured by the nucleus. Out of 885, 229 μ^- are decays as

$$\mu^- \rightarrow e^- + \bar{\nu}_e + \nu_\mu, \tag{8.2}$$

and 656 μ^- are captured by a proton in the nucleus as

$$\mu^- + p \rightarrow \nu_\mu + n. \tag{8.3}$$

The capture of μ^- has a rate of 74%. These values of decay and captured events of μ^+ and μ^- are consistent with cosmic muons data analysed by the ICARUS liquid argon TPC [208].

8.1.3 Reconstructed track selections

For the selection of reconstructed muon, the following criteria are used for stopping muon selection:

1. **Volume criteria:** The selected reconstructed track should match with truth stopping muons, which originate outside the TPC volume and stop inside the TPC volume.

2. **Angular criteria:** The reconstruction capability of a LArTPC is limited for tracks passing parallel to a wire or in the plane containing drift direction and a wire. For such tracks, all the charge from the incident particle gets deposited in a single wire thus leading to the poor reconstruction of the deposited charge. The two angles θ_{xz} (which is the angle made by the projection of a track on the xz plane with the z-direction) and θ_{yz} (which is the angle made by the projection of a track on the yz plane with the z-direction) are defined. Figure 8.1 shows θ_{xz} and θ_{yz} for the coordinate system used in DUNE SP HD. The distribution of average dQ/dx vs θ_{xz} and θ_{yz} for the collection plane using stopping cosmic-ray muons is shown in Figure 8.2. Many tracks, mainly short and broken, are mis-reconstructed as backward-going tracks. These tracks are further removed as discussed in the next selection criteria. From the figure, it is evident that the tracks at certain angular orientations have a very low dQ/dx. The angular cuts are data-driven and different for various

wire planes. Following are the angular cuts for the collection plane that are used to remove events from further analysis:

- $-115° < \theta_{xz} < -60°$ or $65° < \theta_{xz} < 120°$.
- $-105° < \theta_{yz} < -83°$ or $65° < \theta_{yz} < 110°$.

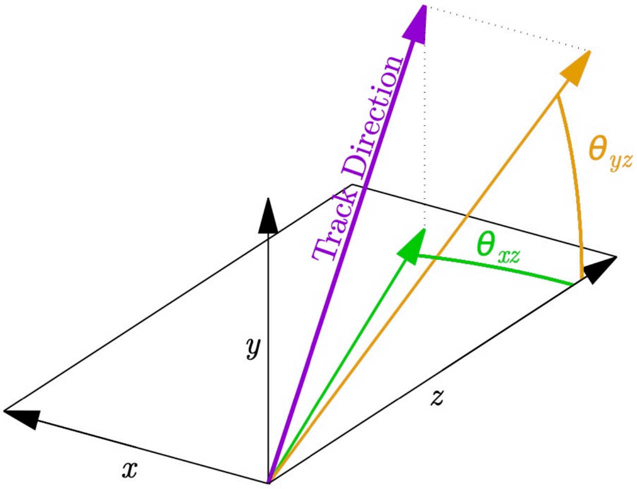

Figure 8.1. The track direction angles θ_{xz} and θ_{yz} defined in DUNE FD [94].

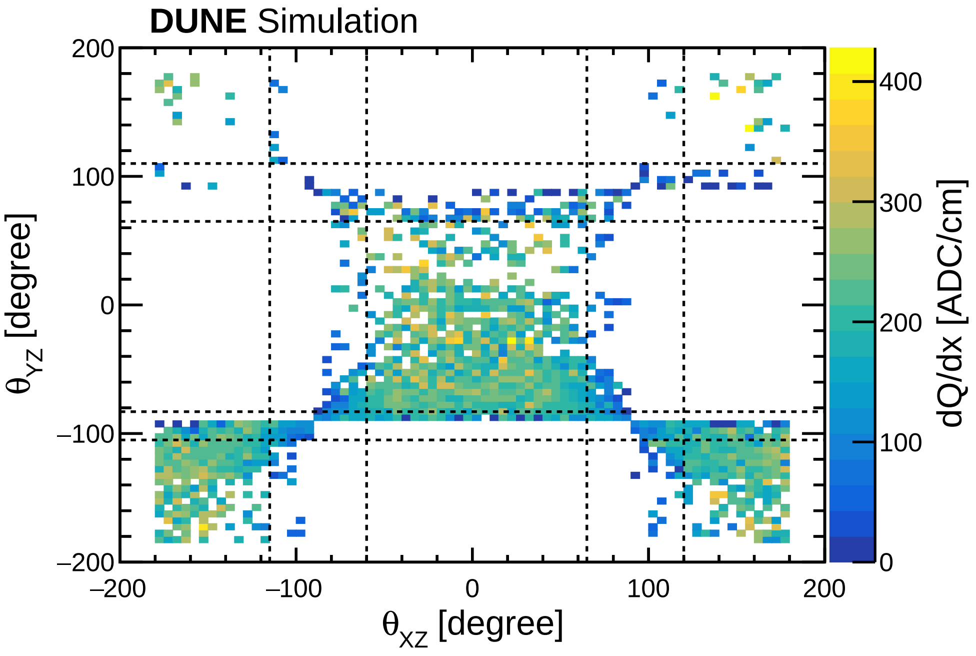

Figure 8.2. Average dQ/dx distribution as a function of θ_{xz} and θ_{yz} in the collection plane. The colour scale represents the average dQ/dx for a track in each bin. The common regions of the dashed lines show the track incident angles excluded for the selection of stopping muon track.

3. **Removing broken tracks:** Due to reconstruction inefficiencies, certain particle trajectories are mistakenly reconstructed as two or more tracks, creating an appearance of a stopping muon even if the particle did not stop inside the TPC. To obtain a pure sample of stopping reconstructed muons, it is necessary to eliminate such tracks. Figure 8.3 shows the distribution of the reconstructed track for each truth stopping muon in the TPC. In cases where multiple tracks are reconstructed for a single muon, the tracks which have minimum y-coordinates are selected considering the cosmic-ray muons travel vertically downward.

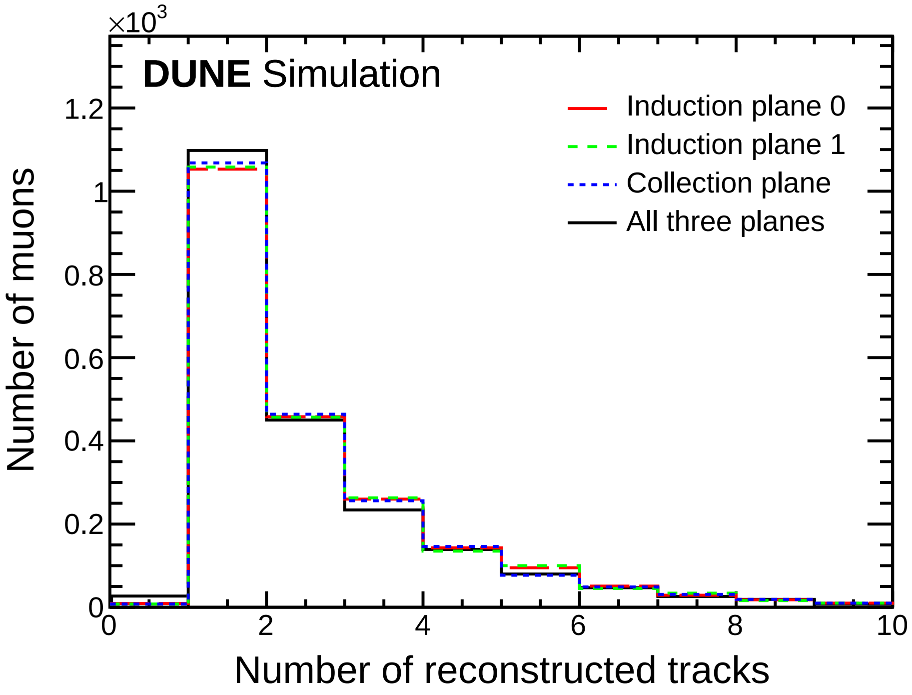

Figure 8.3. Reconstructed track multiplicity of stopping muons. In some cases of stopping muons, no track has been reconstructed, whilst some of them have more than one reconstructed track. The distributions show if a stopping muon track has been reconstructed in each plane and all three wire planes.

4. **Selecting best plane tracks:** Many of the tracks have been reconstructed in all three planes differently as shown in Figure 8.3. The number of broken tracks is different for different planes and thus the number of hits of a stopping track is different in all three wire planes. The wire plane which has the maximum number of reconstructed hits of a track is selected.

A total of 2140 muon tracks have successfully passed all the cuts.

8.2 Analysis methods

The tracks that successfully pass the selections outlined in Sections 8.1.2 and 8.1.3 are utilised in the dE/dx calibration. The Landau-Vavilov theory accurately predicts the theoretical most probable dE/dx for stopping muon in liquid argon [85, 209]. Figures 8.4a and 8.4b show the theoretical most probable dE/dx as a function of kinetic energy and residual range, respectively. This chapter presents two methods for energy calibration. The first one is model-dependent and is referred to as the modified box model. The second method is the absolute energy scale, which is independent of any specific model.

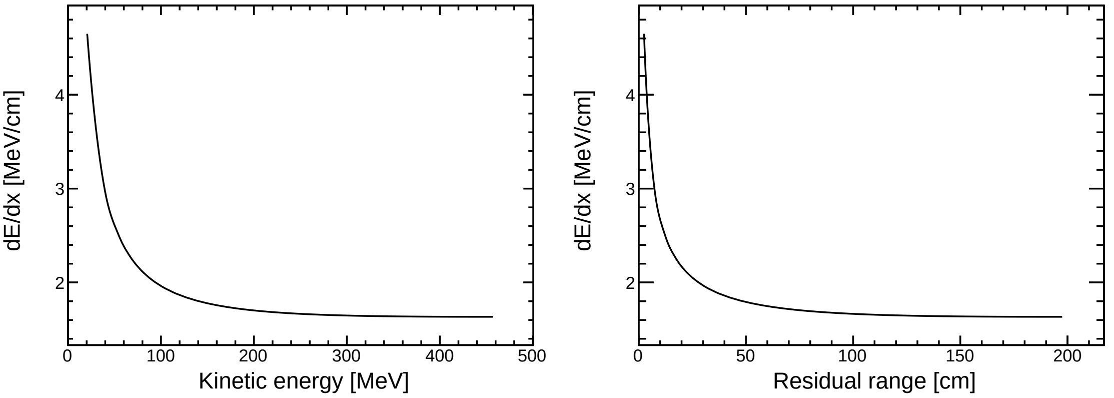

(a) (b)

Figure 8.4. The theoretical most probable of stopping muons based on Landau-Vavilov theory [85, 209] obtained from the data [210]: a) dE/dx vs. kinetic energy, b) dE/dx vs. residual range.

8.2.1 Model dependent: modified box model

The experimental dE/dx values are derived from dQ/dx values using the modified box model [207] with the calibration constant treated as a free parameter. Equation 8.4 describes the modified box model equation.

$$\left(\frac{dE}{dx}\right)_{\text{calibrated}} = \left(\exp\left(\frac{\left(\frac{dQ}{dx}\right)_{\text{calibrated}}}{C_{\text{cal}}}\frac{\beta' W_{\text{ion}}}{\rho\mathcal{E}}\right) - \alpha\right)\left(\frac{\rho\mathcal{E}}{\beta'}\right), \tag{8.4}$$

where

C_{cal} = Calibration constant used to convert ADC values to the number of electrons,

$W_{\text{ion}} = 23.6 \times 10^{-6}$ MeV/electron, is the work function of argon,

$\mathcal{E} = 0.50$ kV/cm (DUNE FD drift electric field),
$\rho = 1.39$ g/cm^3 (LAr density at temperature 87 K),
$\alpha = 0.93$, and
$\beta' = 0.2.12$(kV/cm)(g/cm^2)/MeV.
The last two parameters α and β' are measured by the ArgoNeuT experiment at an electric field strength of 0.481 kV/cm [207].

As per the given equation, the accurate determination of the calibration constant C_{cal}, which translates "ADC/cm" to "number of electrons/cm" is crucial for establishing the absolute energy scale. The objective of dE/dx calibration is to determine the calibration constant C_{cal}. The calibration constant C_{cal} is normalised such that the unit ("ADC × tick") corresponds to 200 electrons, where 1 tick corresponds to 500 ns of sampling time of an ADC. In the ideal case of a perfectly modelled detector response (e.g., in simulation), C_{cal} should be exactly $1/200 = 5 \times 10^{-3}$ADC × tick/e [94]. To obtain the calibration constant, we perform a fit of the dE/dx derived from the dQ/dx along the muon track in the minimum ionising region (corresponding to 120 to 200 cm from the stopping point of the track). In this fit, C_{cal} is treated as a free parameter, and the fit is carried out through χ^2 minimisation. The methodology for the energy calibration using the modified box model is outlined as follows:

1. For every track that satisfies the selection criteria mentioned in Section 8.1.3, the first 200 cm from the end of the track is taken into consideration and divided into 5 cm bins based on the distance from the stopping point (residual range).

2. For every residual range bin, the value of dE/dx is calculated using Equation 8.4 with a chosen C_{cal} value. The distribution of resulting dE/dx is then plotted and fitted to a Landau function convolved with a Gaussian [211]. The C_{cal} value is randomly chosen from a range that is close to the minimum χ^2. The final χ^2 is obtained through χ^2 minimisation as discussed in the next steps. This fitting process aims to determine the most probable dE/dx value (MPV) for a specific residual range bin. Figure 8.5 illustrates the dE/dx distribution for a particular residual range bin (ranging from 85 to 90 cm) along with the corresponding Landau-Gaussian fit, utilised to extract the most probable dE/dx value.

3. For every residual range bin, the mid value of the bin is selected as the representative residual range, and this value is then transformed into kinetic

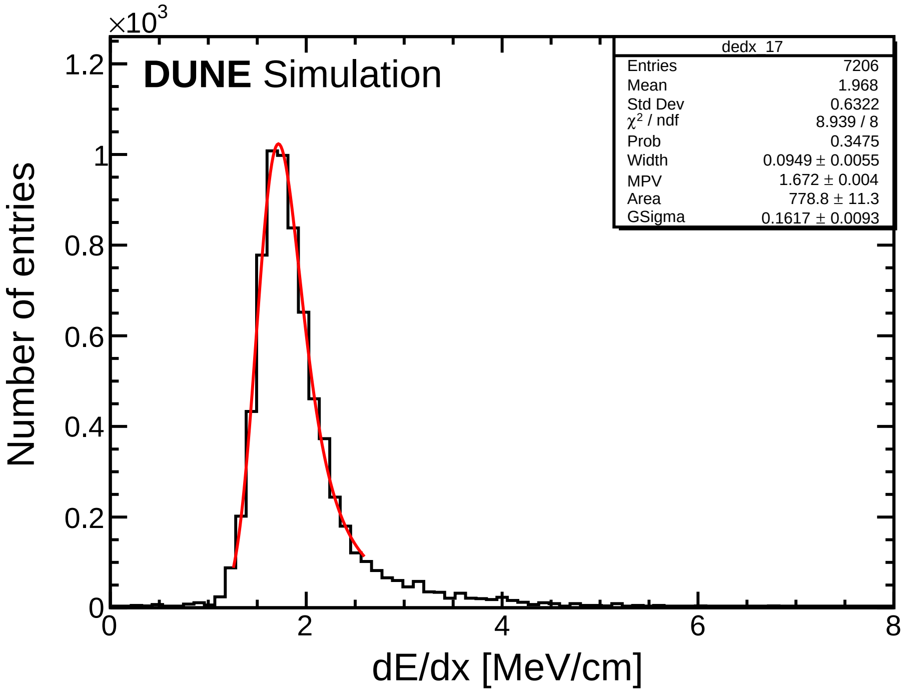

Figure 8.5. Distribution of dE/dx in the residual range between 85 cm to 90 cm, fitted to a Landau function convolved with a Gaussian.

energy using a cubic spline interpolation of kinetic energy versus residual range values mentioned in [84]. The referenced [84] dataset serves as a representation of the anticipated profile of kinetic energy vs. residual range for stopping muons in liquid argon.

4. For bins with a residual range between 120 cm and 200 cm (or kinetic energy between 250 MeV and 450 MeV), the values obtained in the previous step are compared with the prediction made by the Landau-Vavilov theory [85, 209] and the χ^2 value is calculated for a broad range of calibration constants. These constants are chosen arbitrarily such that χ^2 spans to a minimum value. The χ^2 is computed using the following relation:

$$\chi^2 = \sum \left(\frac{(\mathrm{MPV}(dE/dx)_{\mathrm{prediction}} - \mathrm{MPV}(dE/dx)_{\mathrm{measured}})^2}{\sigma^2} \right) \tag{8.5}$$

where $\sigma^2 = \sigma_{\mathrm{fit}}^2$. Here summation is over the bins ranges from kinetic energy 250 MeV to 450 MeV and σ_{fit} is the uncertainty associated with the most probable value of the dE/dx distribution extracted by fitting a Landau function convolved with a Gaussian to the dE/dx distribution.

Figure 8.6 illustrates the χ^2 values corresponding to various calibration constants. The optimal or best-fit value is the one that yields the minimum χ^2, indicating the calibration constant that provides the most favourable agreement between the data and the theoretical model. Figure 8.7 shows the $\chi^2 - \chi^2_{\text{min}}$ values for different calibration constants. To estimate the statistical uncertainty, C_{cal} values are determined for $\chi^2 - \chi^2_{\text{min}} = 1$. The derived calibration constant value is $(5.469 \pm 0.003) \times 10^{-3}$ ADC × tick/e.

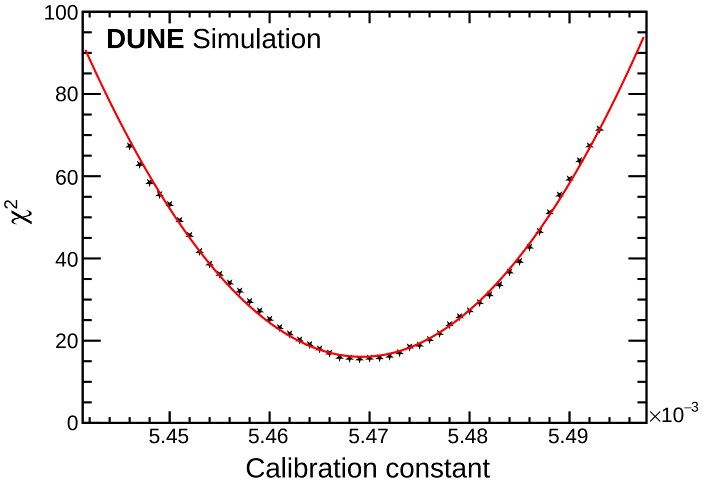

Figure 8.6. Distribution of χ^2 vs. calibration constant for stopping muons fitted with a suitable polynomial function.

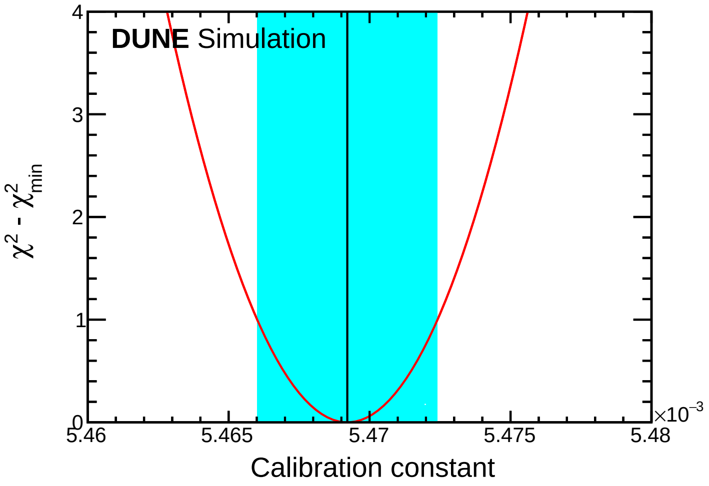

Figure 8.7. Distribution of $\chi^2 - \chi^2_{\text{min}}$ vs. calibration constant. The black solid line represents the calibration constant at minimum χ^2. The colour bands show the uncertainty associated with a calibration constant C_{cal}.

Figure 8.8 shows the comparison between the theoretical and reconstructed MPV of dE/dx as a function of kinetic energy using the derived value of the calibration constant. Figure 8.9 shows the comparison of reconstructed and theoretical MPV of dE/dx as a function of residual range using the same derived value of the calibration constant. Figure 8.10 shows the colour plot of the reconstructed dE/dx vs. residual range of stopping muon tracks with the comparison of reconstructed and theoretical MPV of dE/dx. Most of the reconstructed values agree very well with the theoretical values. However, some differences between reconstructed and theoretical values become apparent at lower residual ranges.

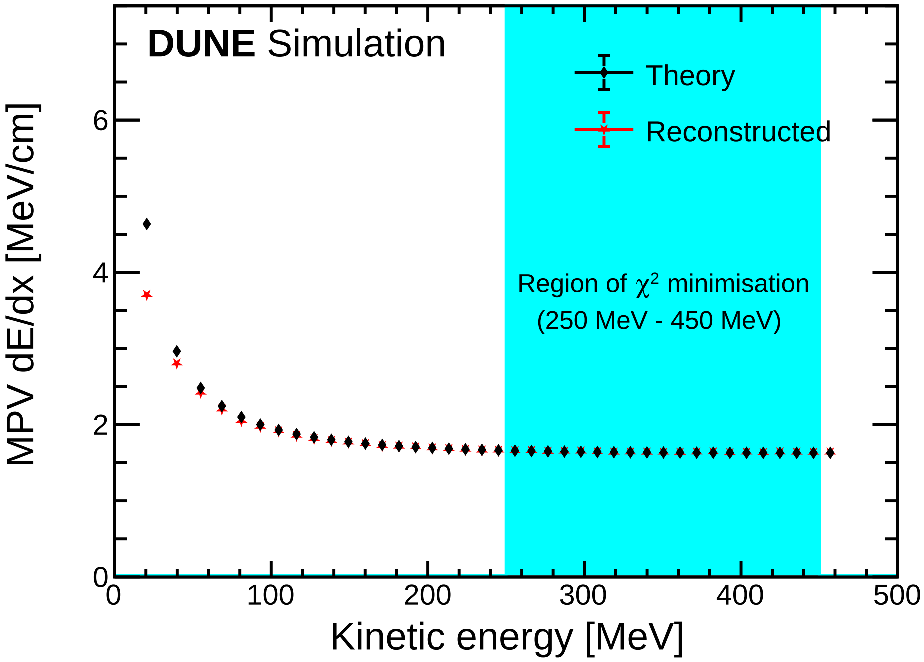

Figure 8.8. Comparison between the reconstructed and Landau-Vavilov theory most probable value dE/dx vs. kinetic energy for stopping muons. The magnitude of the error is too small to be visible in the reconstructed values.

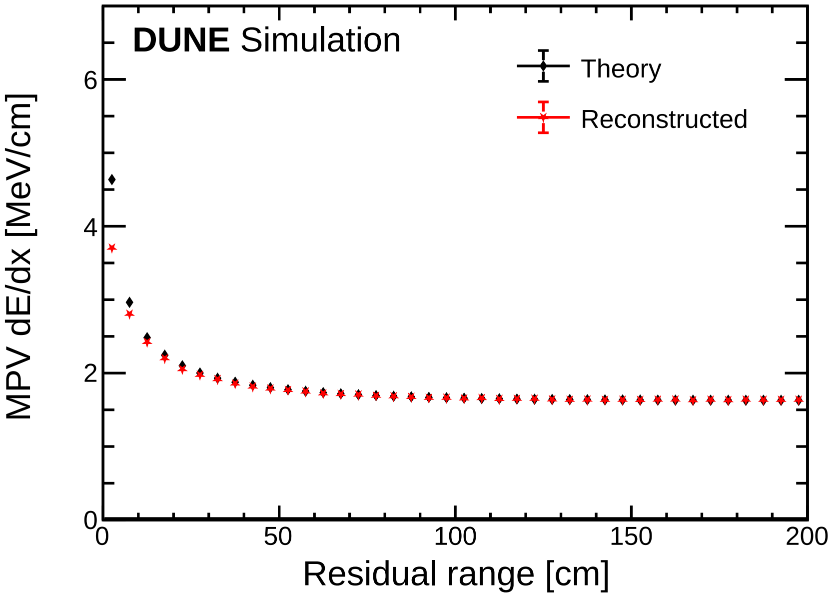

Figure 8.9. Comparison between the reconstructed and Landau-Vavilov theory most probable value dE/dx vs. residual range for stopping muons. The magnitude of the error is too small to be visible in the reconstructed values.

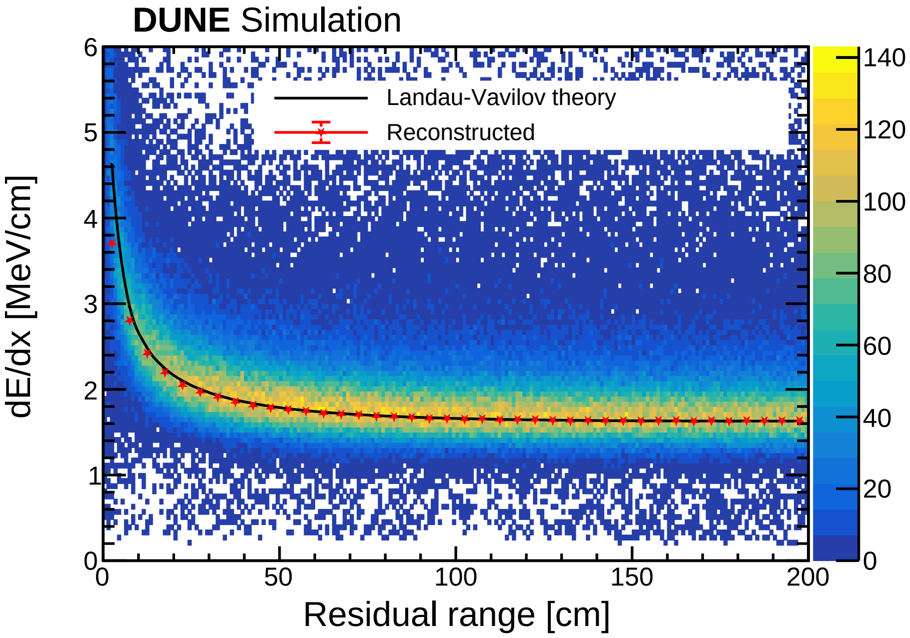

Figure 8.10. The colour plot of reconstructed dE/dx vs. residual range of stopping muon tracks. The reconstructed and theoretical most probable dE/dx vs. residual range is also presented. The magnitude of the error is too small to be visible in the reconstructed values.

8.2.2 Model independent: absolute energy scale

In this analysis method, the author have developed a scaling procedure that is independent of any specific model and relies on the residual range for translating dQ/dx to dE/dx. The event selections as detailed in Sections 8.1.2 and 8.1.3 are used for this analysis method. The methodology for this absolute energy scale calibration method is outlined as follows:

1. For every track, the first 200 cm or less from the end of the track is taken into consideration and divided into 5 cm bins based on the distance from the stopping point (residual range).
2. For each residual range bin, the reconstructed dQ/dx distribution is plotted and fitted to a Landau function convolved with a Gaussian to determine the most probable value of dQ/dx for that specific residual range bin. Figure 8.11 shows the colour plot of reconstructed dQ/dx vs. residual range of stopping muons. In Figure 8.12, the dQ/dx of a particular residual range bin, ranging from 65 cm to 70 cm, is shown fitted to a Landau function convolved with a Gaussian. The simulated energy resolution of the detector calculated from the figure is 11.78%.

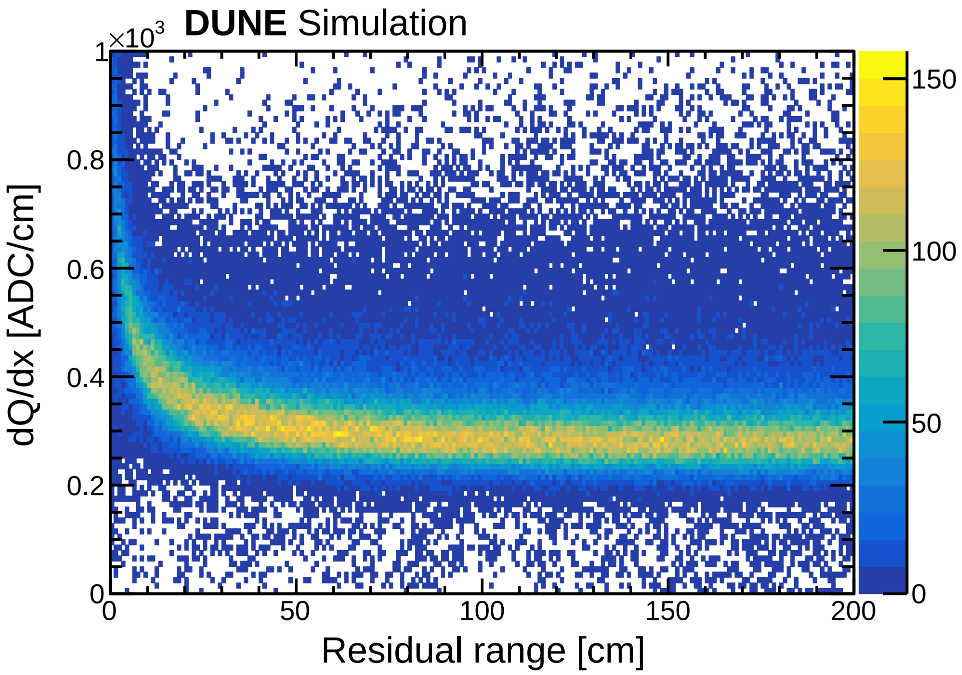

Figure 8.11. The colour plot of reconstructed dQ/dx vs. residual range of stopping muon tracks.

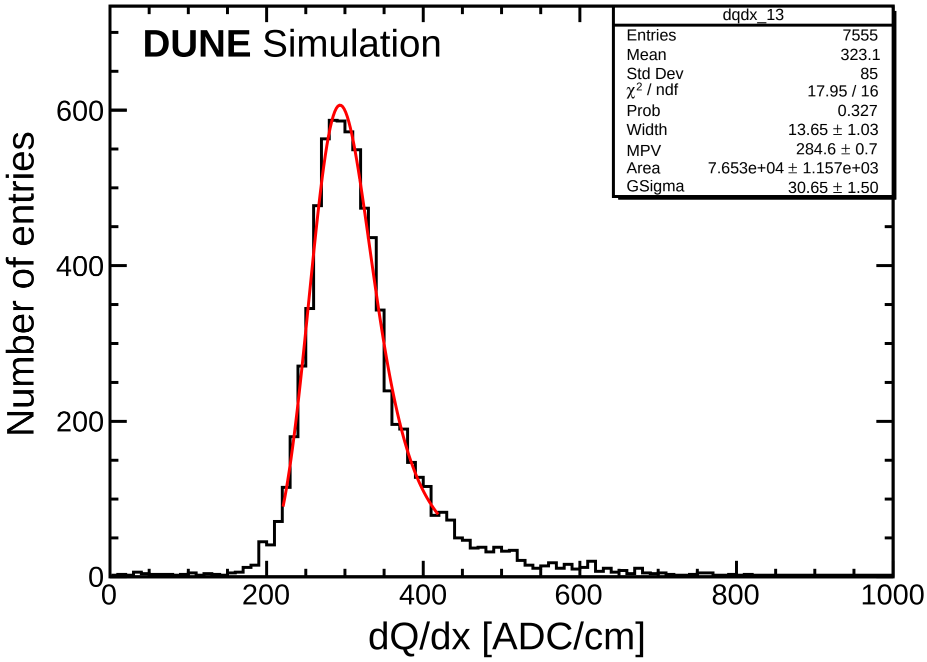

Figure 8.12. Reconstructed dQ/dx distribution fitted to a Landau function convolved with a Gaussian for residual range 65 cm to 70 cm.

3. For each residual range bin, the mid value of the bin is taken as a representative residual range value of that bin and the corresponding theoretical most probable value of dE/dx is calculated based on the Landau-Vavilov theory [85, 209]. The theoretical dE/dx as a function of the residual range is shown in Figure 8.4b.

4. For each residual range bin, the ratio of the MPV of $(dE/dx)_{\text{theoretical}}$ to MPV of $(dQ/dx)_{\text{reconstructed}}$ is calculated. The ratio is then plotted against the residual range and fitted with a suitable function. Figure 8.13 shows the ratio of the MPV $(dE/dx)_{\text{theoretical}}$ to the MPV $(dQ/dx)_{\text{reconstructed}}$ vs. residual range of each bin together with the fit to a function:

$$f(r) = p_0 \ + \ p_1 \times 1/r \ + \ p_2 \times r. \tag{8.6}$$

Thus, a relation between $\text{MPV}(dQ/dx)_{\text{reconstructed}}$ and $\text{MPV}(dE/dx)_{\text{reconstructed}}$ is obtained:

$$\frac{\text{MPV}(dE/dx)_{\text{reconstructed}}}{\text{MPV}(dQ/dx)_{\text{reconstructed}}} = p_0 + p_1 \times 1/r + p_2 \times r, \tag{8.7}$$

where r represents residual range and p_0, p_1 and p_2 are the fitting parameters. The values of the parameters of the fit function are shown in Table 8.1.

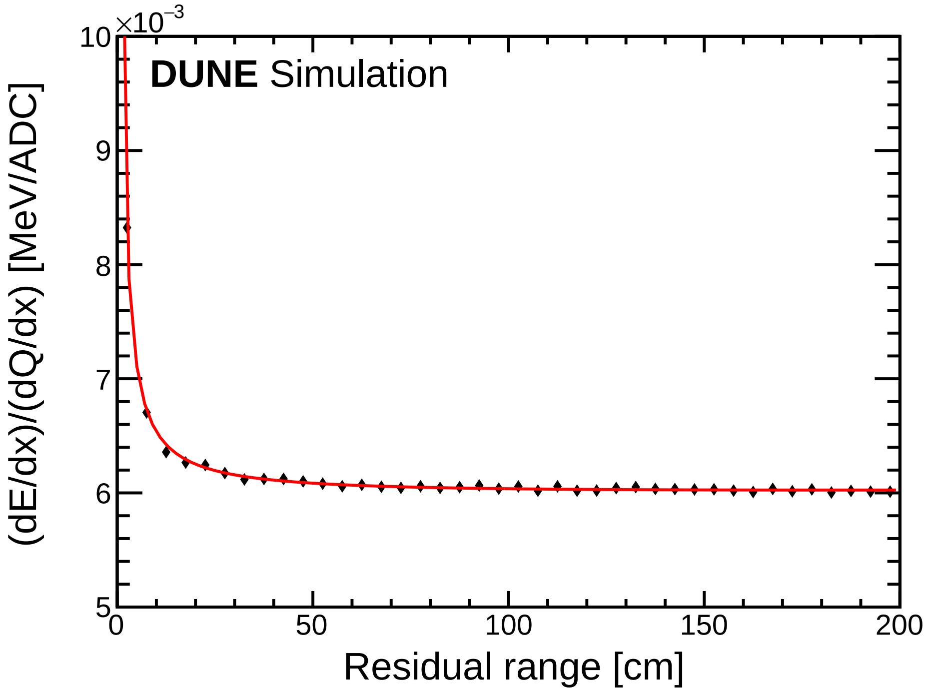

Figure 8.13. The ratio of theoretical dE/dx to reconstructed dQ/dx of stopping muons as a function of residual range and fitted with the function as described by Equation 8.6. The magnitude of the error is too small to be visible in the reconstructed values.

Table 8.1. The value of the parameters of the fit function shown in Figure 8.13

	Fit parameters		
	p_0	p_1	p_2
Value	$(5.962 \pm 0.007) \times 10^{-3}$	$(5.731 \pm 0.087) \times 10^{-3}$	$(1.613 \pm 0.499) \times 10^{-7}$

5. The reconstructed dQ/dx is converted to reconstructed dE/dx using Equation 8.7 and fit parameters obtained in Table 8.1. Figure 8.14 shows the reconstructed MPV of dE/dx as a function of kinetic energy using the derived relation from Equation 8.7 that translates dQ/dx to dE/dx compared with the theoretical curve. Figure 8.15 shows the comparison of reconstructed and theoretical MPV of dE/dx as a function of residual range. Figure 8.16 shows

the colour plot of the reconstructed dE/dx vs. residual range of stopping muon tracks with the comparison of reconstructed and theoretical MPV of dE/dx. Most of the reconstructed values agree very well with theoretical values and significantly improve the agreement in the low residual range bin compared to the modified box model.

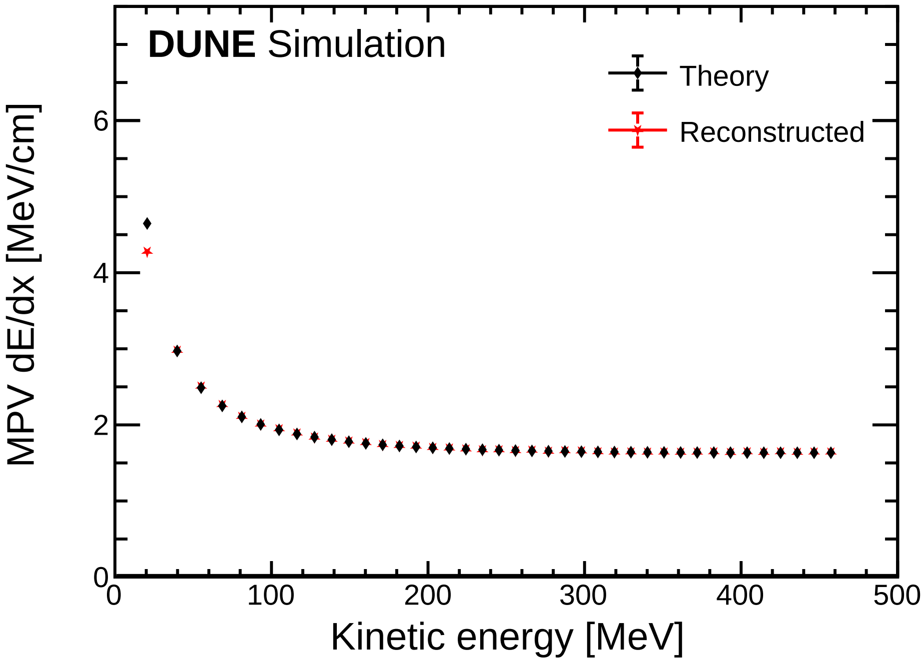

Figure 8.14. The reconstructed most probable dE/dx vs. kinetic energy for stopping muons and compared with the theoretical most probable dE/dx. The reconstructed values show good agreement with the theoretical prediction, even in the low kinetic energy. The reconstructed (red) and theoretical (black) points overlap for most ranges. The magnitude of the error is too small to be visible in the reconstructed values.

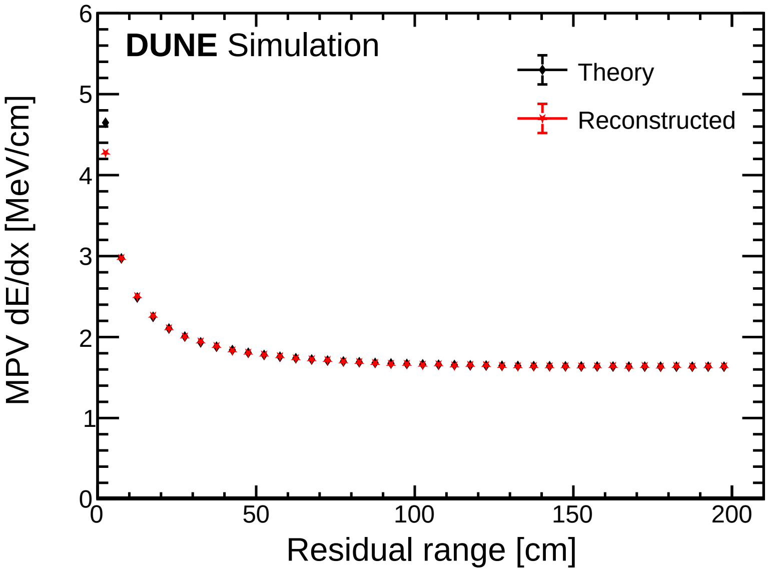

Figure 8.15. The reconstructed most probable dE/dx vs. residual range for stopping muons and compared with the theoretical most probable dE/dx. The reconstructed most probable values show good agreement with the theoretical prediction, even in the low residual range values. The reconstructed (red) and theoretical (black) points overlap for most ranges. The magnitude of the error is too small to be visible in the reconstructed values.

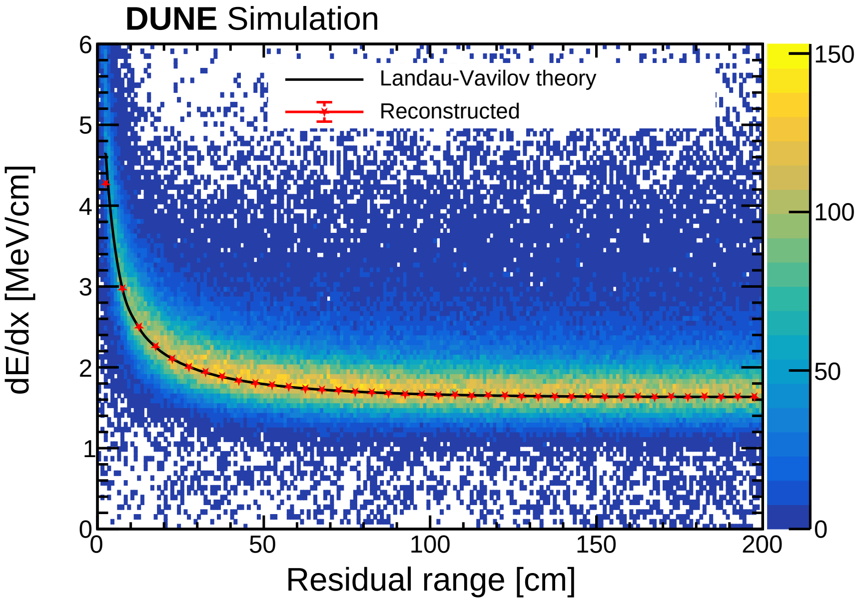

Figure 8.16. The colour plot of reconstructed dE/dx vs. residual range of stopping muon tracks. The reconstructed most probable dE/dx vs. residual range compared with the theoretical most probable dE/dx is also presented.

Further, to improve the agreement between theory and reconstruction at the low residual range value, a variable width is considered. For this, a 2 cm bin size is taken for the residual range 0 to 16 cm and a 5 cm bin size is taken for the residual range 20 to 200 cm. Figure 8.17 shows the reconstructed MPV of dE/dx as a function of kinetic energy using the derived relation from Equation 8.7 that translates dQ/dx to dE/dx compared with the theoretical value. Figure 8.18 shows the comparison of reconstructed and theoretical MPV of dE/dx as a function of residual range. Figure 8.19 shows the colour plot of the reconstructed dE/dx vs. residual range of stopping muon tracks with the comparison of reconstructed and theoretical MPV of dE/dx.

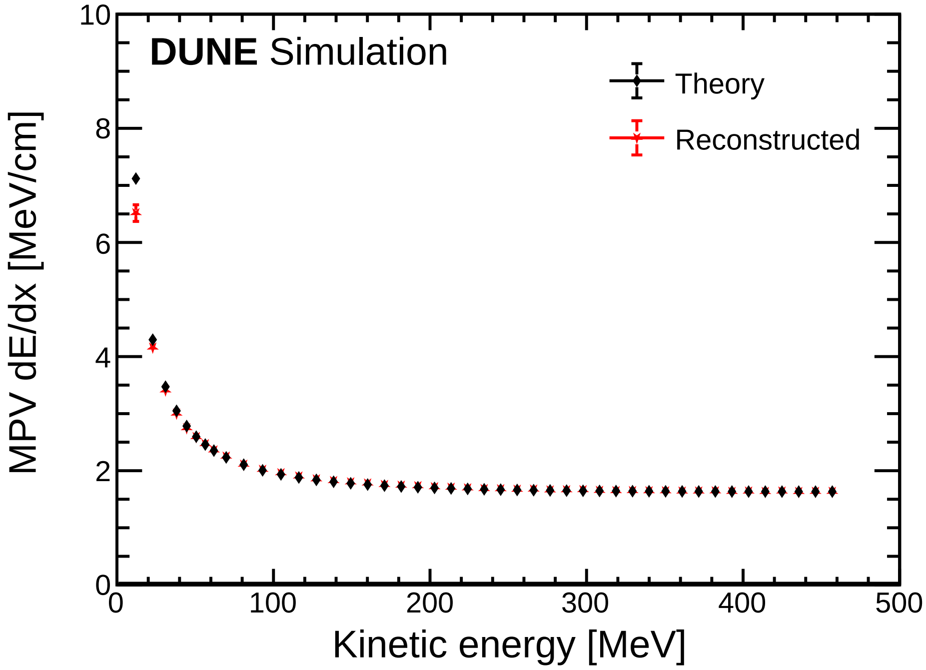

Figure 8.17. The reconstructed and theoretical most probable values of dE/dx vs. kinetic energy for stopping muons. The smaller kinetic energy bins have low statistics and higher statistical uncertainty compared to bigger kinetic energy bins.

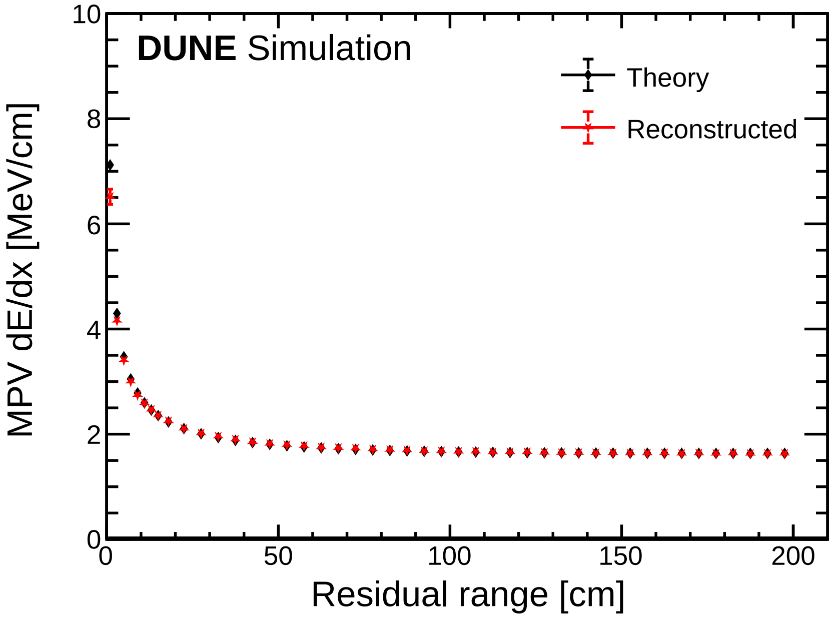

Figure 8.18. The reconstructed and theoretical most probable values of dE/dx vs. residual range for stopping muons. The smaller bin ranges have low statistics and higher statistical uncertainty compared to bigger residual range bins.

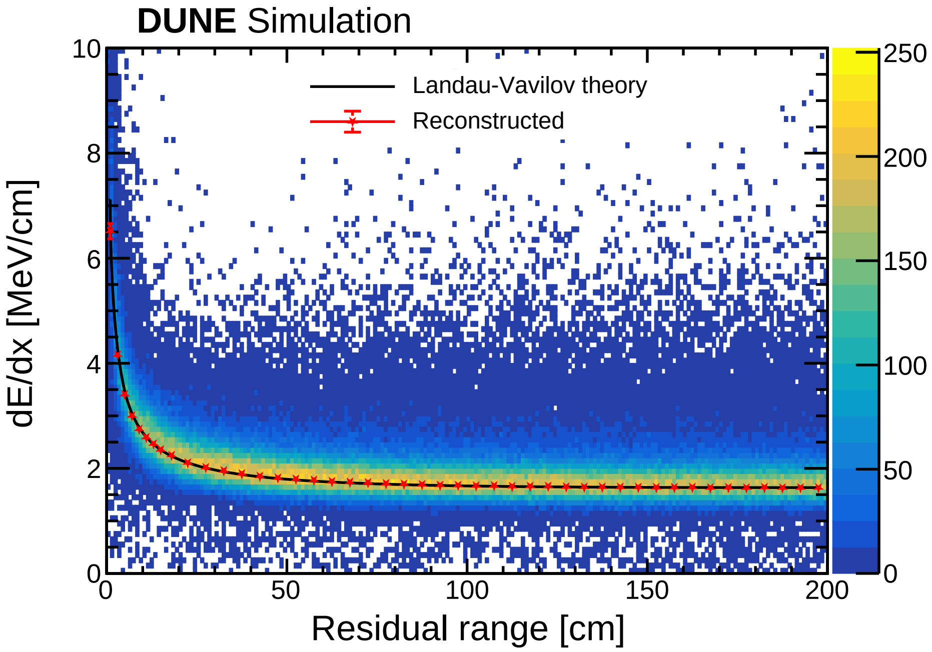

Figure 8.19. The colour plot of reconstructed dE/dx vs. residual range of stopping muon tracks. The reconstructed and theoretical most probable values of dE/dx vs. residual range for stopping muons are also presented.

The two dE/dx calibration methods, the modified box model, and the absolute energy scale, employed within the framework of the DUNE experiment, reveal that the absolute energy scale method demonstrates superior agreement, particularly in low residual ranges. The key advantage of the absolute energy scale lies in its independence from modelling and any parameters from other experiments. In contrast, the modified box model relies on pre-calibrated dQ/dx and parameters from another experiment before DUNE can perform these measurements itself. This emphasises the efficiency and autonomy of the absolute energy scale method, positioning it as a more favourable choice for dE/dx calibration in the DUNE experiment.

8.3 dE/dx reconstruction of stopping charged pions

After determining the absolute energy scale for stopping muons, as described in the previous sections, the next step involves assessing how the dE/dx calibration performs with pions (π^+ and π^-, unless otherwise stated). The dE/dx remains constant for a fixed p/m, where p and m are the momentum and mass of particles depositing energy in liquid argon, as described in Section 3.2. This verification procedure ensures the robustness and applicability of the absolute energy scale method for other particles in the DUNE FD.

8.3.1 Event selection

For the dE/dx calibration using charged pions, the analysis utilises the same sample of cosmic-ray muons employed in the study of stopping muons. This sample consists of 3.62×10^5 simulated cosmic-ray muon events with cosmic-oriented reconstruction which correspond to 25 days of data at DUNE FD. The charged pions produced by the cosmic-ray muons interacting in the liquid argon are considered for this study. The events are confirmed as stopping pions if the particle's truth end position (x, y, z) is within the TPC. The pions are also required to have originated inside the DUNE FD. A total of 9.30×10^3 charged pions are produced in the sample. The reconstructed pion track selection criteria are similar to stopping muons as mentioned in Section 8.1.3.

For the angular criteria of reconstructed pion tracks, the distribution of average dQ/dx vs. θ_{xz} and θ_{yz} is shown in Figure 8.20. The definition of θ_{xz} and θ_{yz} is shown in Figure 8.1. The tracks at certain angular orientations have a very low dQ/dx and were removed from the selection. Following are the angular cuts for the collection plane that are used to remove events from further analysis:

- $-105° < \theta_{xz} < -70°$ or $70° < \theta_{xz} < 110°$.
- $-115° < \theta_{yz} < -80°$ or $80° < \theta_{yz} < 110°$.

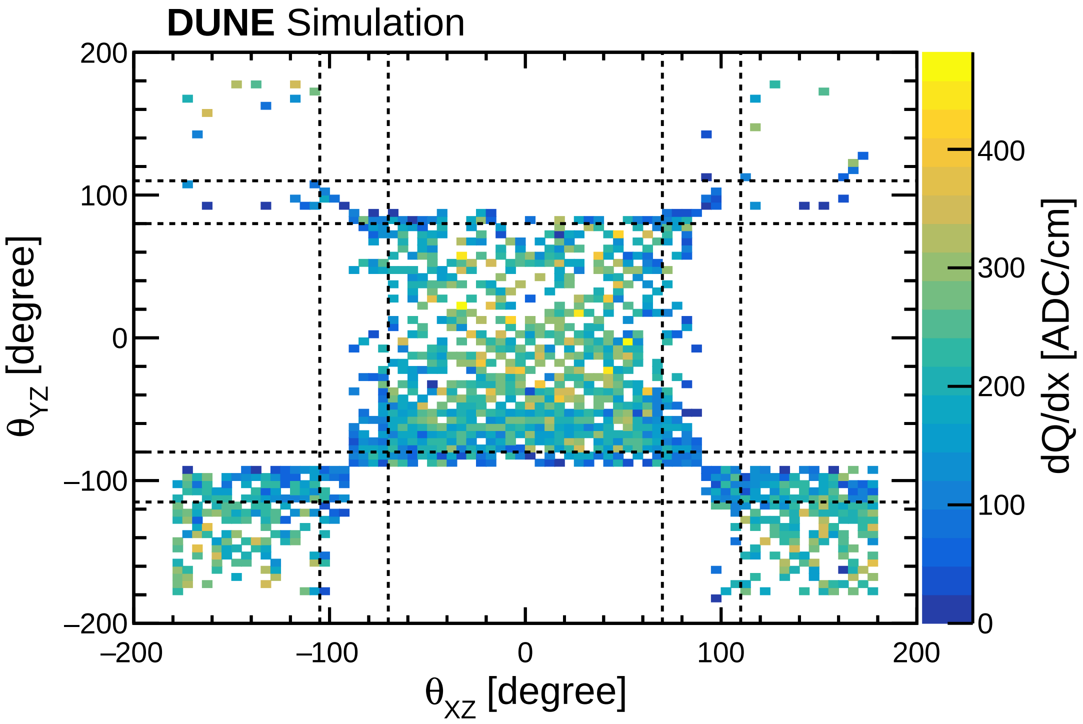

Figure 8.20. Average dQ/dx distribution as a function of θ_{xz} and θ_{yz} of pions in the collection plane. The colour scale represents the average dQ/dx for a track in each bin. The common regions of the dashed lines show the track incident angles excluded from the selection of pion tracks.

8.3.2 Analysis method

The selected tracks that pass the criteria mentioned in the above section are used for dE/dx reconstruction. The theoretical most probable energy loss of pions in liquid argon is calculated using Landau-Vavilov theory [85, 209] and then compared with reconstructed dE/dx using the same analysis method used for stopping muons described in Section 8.2.2.

For every track, the first 150 cm or less from the end of the track is considered and divided into variable bin sizes. For this, a 5 cm bin size is taken for the residual range 0 to 10 cm and a 10 cm bin size is taken for the residual range 10 to 150 cm. Figure 8.21 shows the distribution of reconstructed dQ/dx vs. residual range of stopping pion tracks. The dQ/dx of a particular residual range bin from 40 cm to 50 cm fitted to a Landau function convolved with a Gaussian is shown in Figure 8.22.

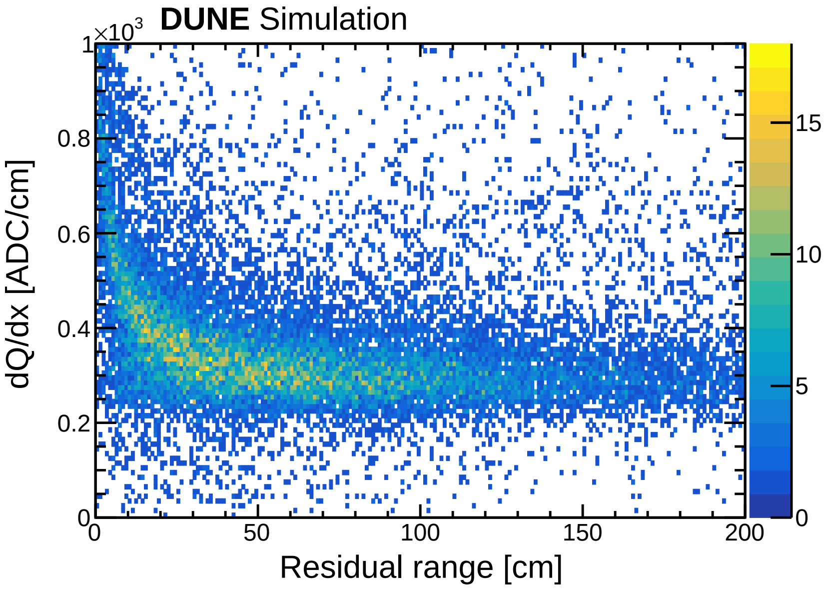

Figure 8.21. The colour plot of reconstructed dQ/dx vs. residual range of stopping pion tracks.

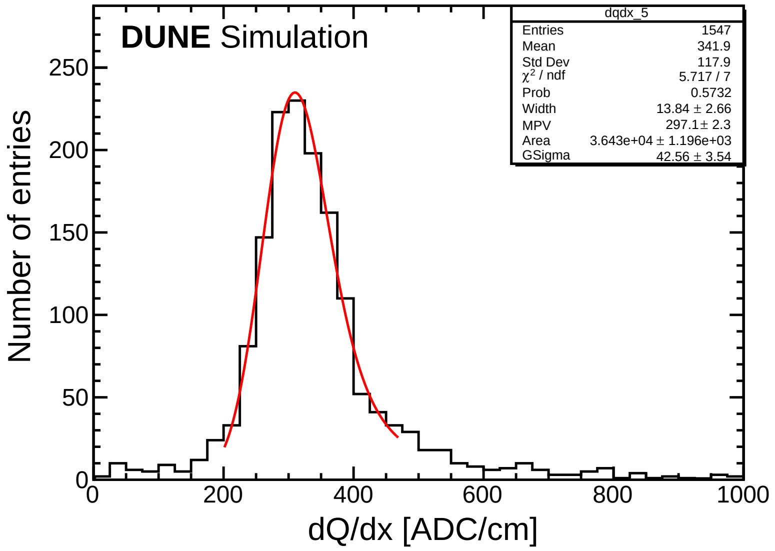

Figure 8.22. dQ/dx distribution of stopping pions fitted to a Landau function convolved with a Gaussian for residual range 40 cm to 50 cm.

For each residual range bin, the ratio of the MPV of $(dE/dx)_{\text{theoretical}}$ to MPV of $(dQ/dx)_{\text{reconstructed}}$ is calculated. The ratio is then plotted against the residual range and fitted with a suitable function. Figure 8.23 shows the ratio of the MPV of $(dE/dx)_{\text{theoretical}}$ to the MPV of $(dQ/dx)_{\text{reconstructed}}$ vs. residual range of each bin together with the fit to a function:

$$f(r) = p_0 \; + \; p_1 \times 1/r \; + \; p_2 \times r. \tag{8.8}$$

Thus, a relation between MPV$(dQ/dx)_{\text{reconstructed}}$ and MPV$(dE/dx)_{\text{reconstructed}}$ is obtained:

$$\frac{\text{MPV}(dE/dx)_{\text{reconstructed}}}{\text{MPV}(dQ/dx)_{\text{reconstructed}}} = p_0 + p_1 \times 1/r + p_2 \times r, \tag{8.9}$$

where r represents residual range and p_0, p_1 and p_2 are the fitting parameters. The values of the parameters of the fit function are shown in Table 8.2.

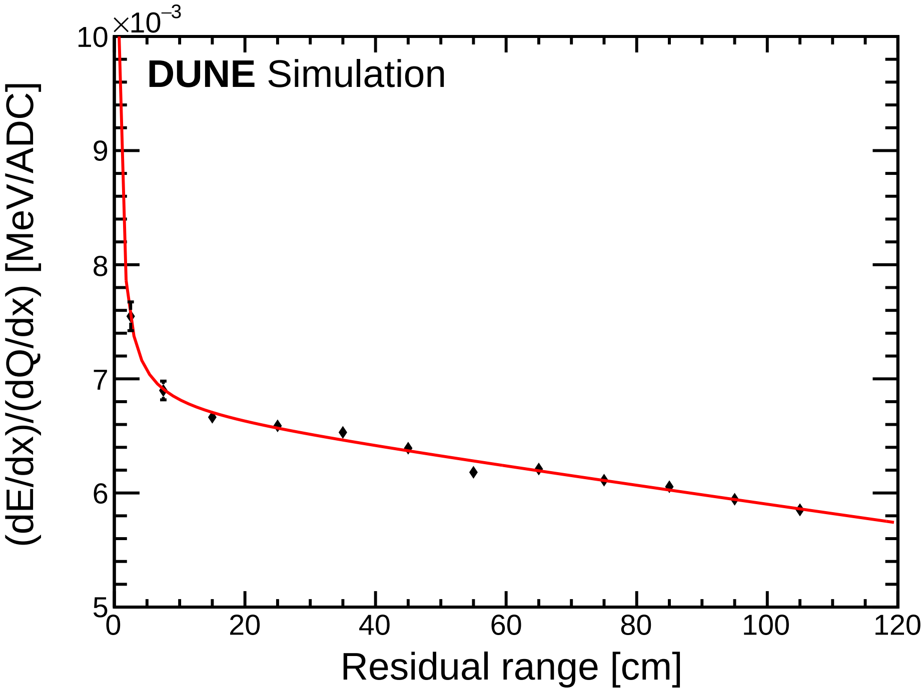

Figure 8.23. The ratio of theoretical dE/dx to reconstructed dQ/dx of stopping pions as a function of residual range and fitted with the function described in Equation 8.8.

Table 8.2. The value of the parameters of the fit function shown in Figure 8.23

	Fit parameters		
	p_0	p_1	p_2
Value	$(6.683 \pm 0.042) \times 10^{-3}$	$(2.149 \pm 0.350) \times 10^{-3}$	$(-8.031 \pm 0.532) \times 10^{-6}$

The reconstructed dQ/dx is converted to dE/dx using Equation 8.9 and fit parameters obtained in Table 8.2. Figure 8.24 shows the reconstructed MPV of dE/dx as a function of kinetic energy using the derived relation mentioned in Equation 8.9 that translates dQ/dx to dE/dx compared with the theoretical curve. Figure 8.25 shows the comparison of reconstructed and theoretical MPV of dE/dx as a function of residual range. Figure 8.26 shows the colour plot of the reconstructed dE/dx vs. residual range of stopping pion tracks with the comparison of reconstructed and theoretical MPV of dE/dx.

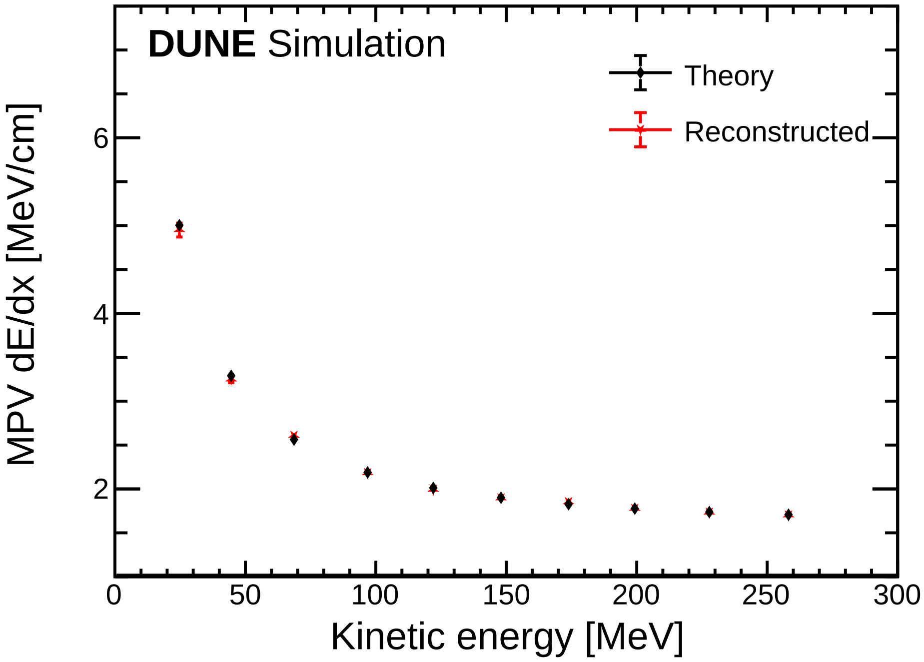

Figure 8.24. The reconstructed most probable value of dE/dx vs. kinetic energy of stopping pions compared with the theoretical prediction. The reconstructed most probable values show good agreement with the theoretical prediction, even in the low kinetic energy values.

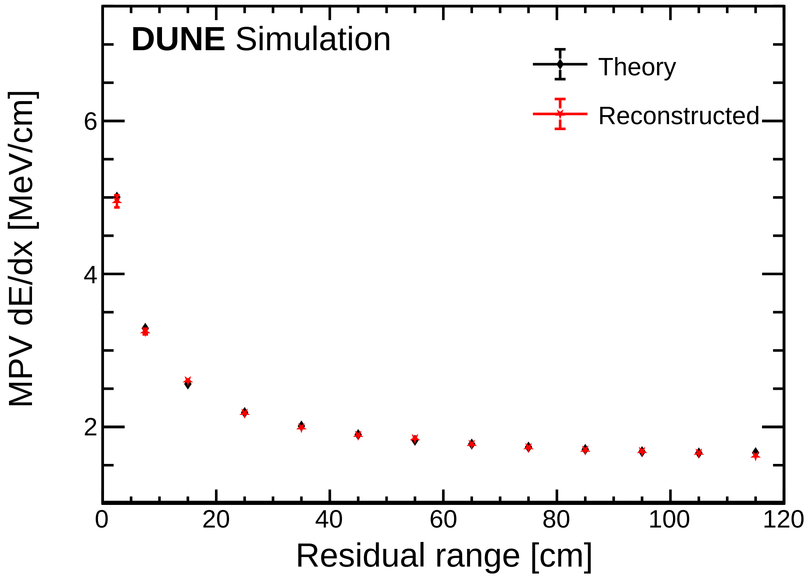

Figure 8.25. The comparison between the reconstructed and theoretical value of dE/dx vs. residual range for stopping pions. The reconstructed most probable values show good agreement with the theoretical prediction, even in the low residual range values.

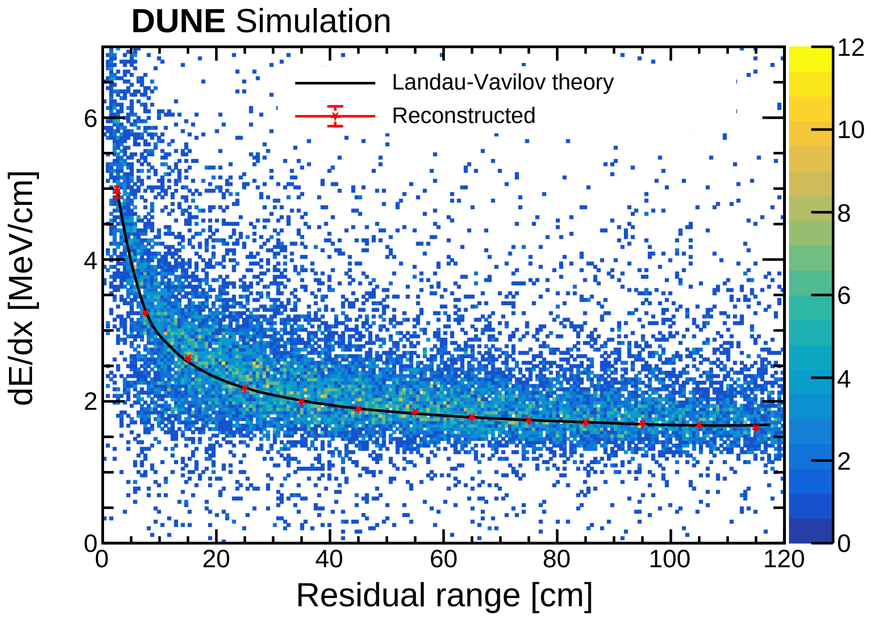

Figure 8.26. The colour plot of reconstructed dE/dx vs. residual range of stopping pion tracks. The reconstructed most probable values of dE/dx vs. residual range of stopping pions and comparison with the theoretical most probable values dE/dx are presented.

8.4 dE/dx reconstruction of stopping protons

After determining the absolute energy scale for stopping muons and pions as described in the previous sections, the analysis extends to stopping protons. A relation is established that translates the reconstructed dQ/dx to dE/dx. The reconstructed dE/dx values are then compared to the theoretical prediction of the most probable values of dE/dx based on the Landau-Vavilov theory [85, 209].

8.4.1 Event selection

For this study, the stopping protons produced by cosmic-ray muons interacting with liquid argon are considered. The same cosmic-ray muon sample used in the stopping muon study is employed for this analysis. A total of 5.43×10^4 stopping protons are selected. The selection criteria for reconstructed proton tracks are similar to stopping muons mentioned in Section 8.1.3.

For the angular criteria of proton tracks, the distribution of average dQ/dx vs. θ_{xz} and θ_{yz} is shown in Figure 8.27. The definition of θ_{xz} and θ_{yz} is shown in Figure 8.1. The tracks at certain angular orientations have a very low dQ/dx and were removed from the selection. Following are the angular cuts for the collection plane that are used to remove events from further analysis:

- $-105° < \theta_{xz} < -70°$ or $70° < \theta_{xz} < 110°$.
- $-115° < \theta_{yz} < -60°$ or $60° < \theta_{yz} < 110°$.

A total of 2281 stopping proton tracks are selected.

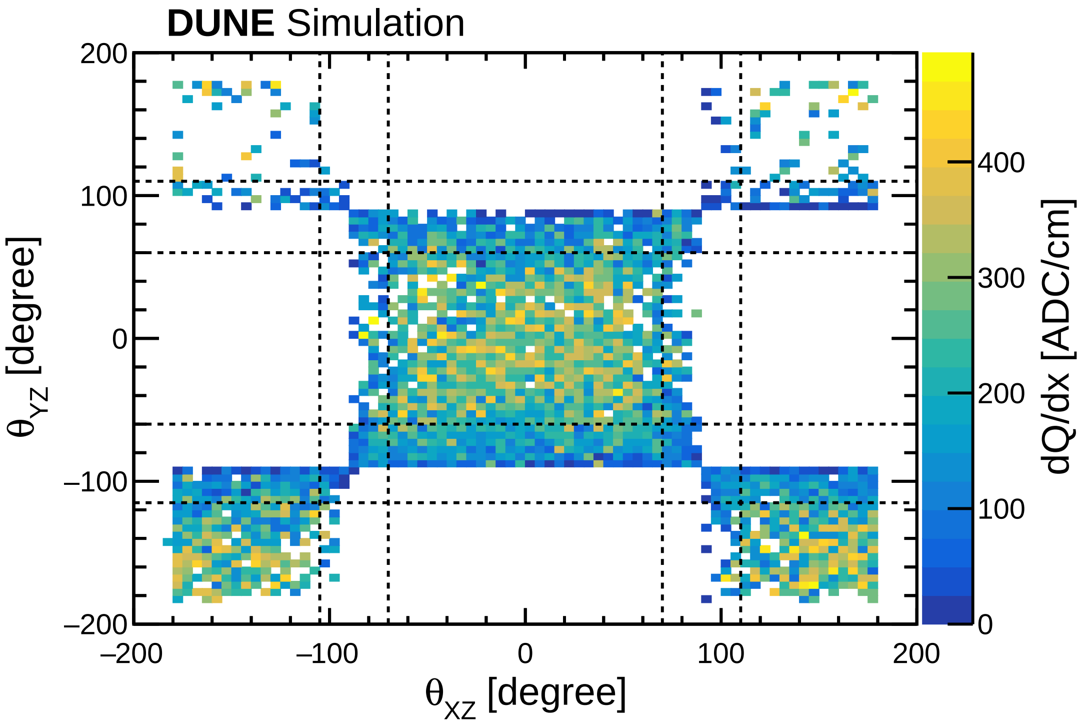

Figure 8.27. Average dQ/dx distribution as a function of θ_{xz} and θ_{yz} of protons in the collection plane. The colour scale represents the average dQ/dx for a track in each bin. The common regions of the dashed lines show the track incident angles excluded from the selection of proton tracks.

8.4.2 Analysis method

The tracks selected based on the criteria outlined in the previous section are utilised for dE/dx reconstruction. The analysis method employed for stopping protons follows a similar approach to that described in Section 8.2.2.

For every track, the first 100 cm or less from the end of the track is considered and divided into variable bin sizes. For this, a 2 cm bin size is taken for the residual range 0 to 10 cm and a 10 cm bin size is taken for the residual range 10 to 100 cm. Figure 8.28 shows the distribution of reconstructed dQ/dx vs. residual range of stopping proton tracks. The reconstructed dQ/dx of a particular residual range bin from 50 cm to 60 cm fitted to a Landau function convolved with a Gaussian is shown in Figure 8.29.

For each residual range bin, the ratio of the MPV of $(dE/dx)_{\text{theoretical}}$ to MPV of $(dQ/dx)_{\text{reconstructed}}$ is calculated. The ratio is then plotted against the residual range and fitted with a suitable function. Figure 8.30 shows the ratio of the MPV of $(dE/dx)_{\text{theoretical}}$ to the MPV of $(dQ/dx)_{\text{reconstructed}}$ vs. residual range of each bin

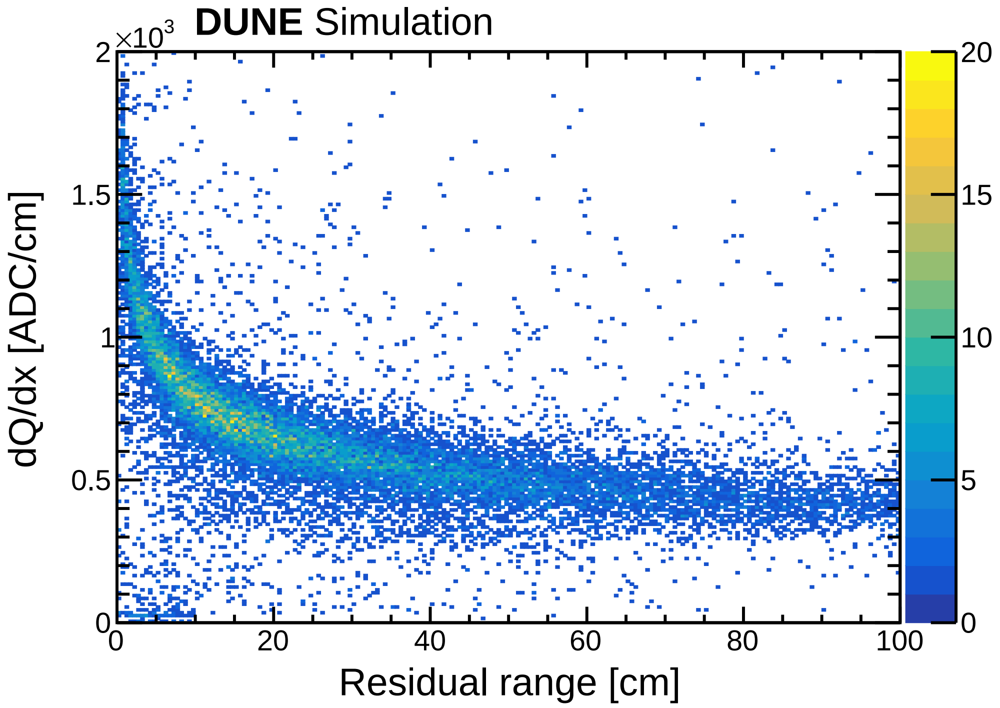

Figure 8.28. The colour plot of reconstructed dQ/dx vs. residual range of stopping proton tracks.

together with the fit to a function:

$$f(r) = p_0 \ + \ p_1 \times 1/r \ + \ p_2 \times r. \tag{8.10}$$

Thus, a relation between $\mathrm{MPV}(dQ/dx)_{\text{reconstructed}}$ and $\mathrm{MPV}(dE/dx)_{\text{reconstructed}}$ is obtained:

$$\frac{\mathrm{MPV}(dE/dx)_{\text{reconstructed}}}{\mathrm{MPV}(dQ/dx)_{\text{reconstructed}}} = p_0 + p_1 \times 1/r + p_2 \times r, \tag{8.11}$$

where r represents residual range and p_0, p_1, and p_2 are the fitting parameters. The values of the parameters of the fit function are shown in Table 8.3.

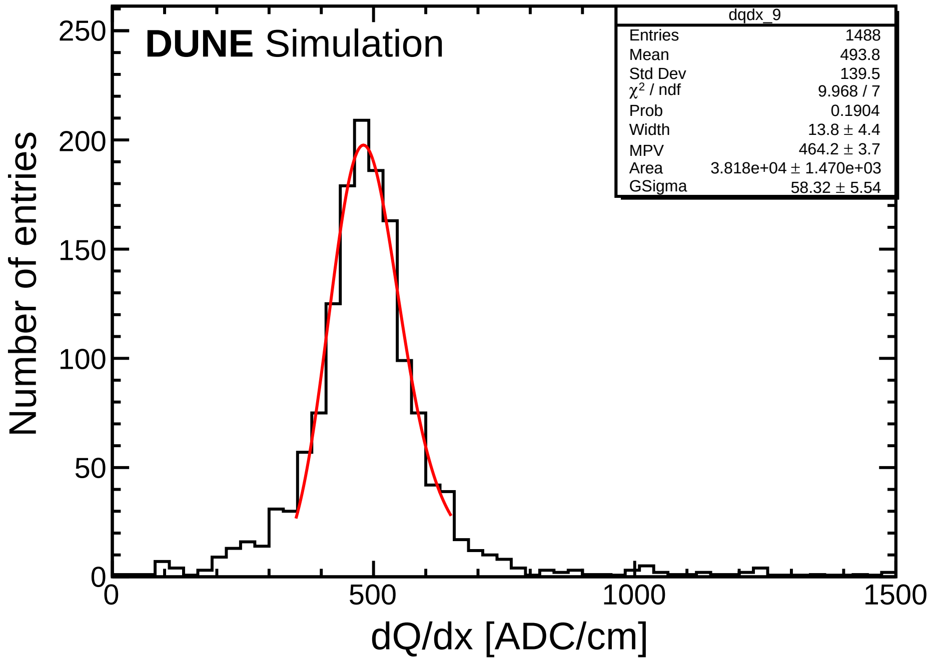

Figure 8.29. The reconstructed dQ/dx distribution fitted to a Landau function convolved with a Gaussian for the residual range 50 cm to 60 cm.

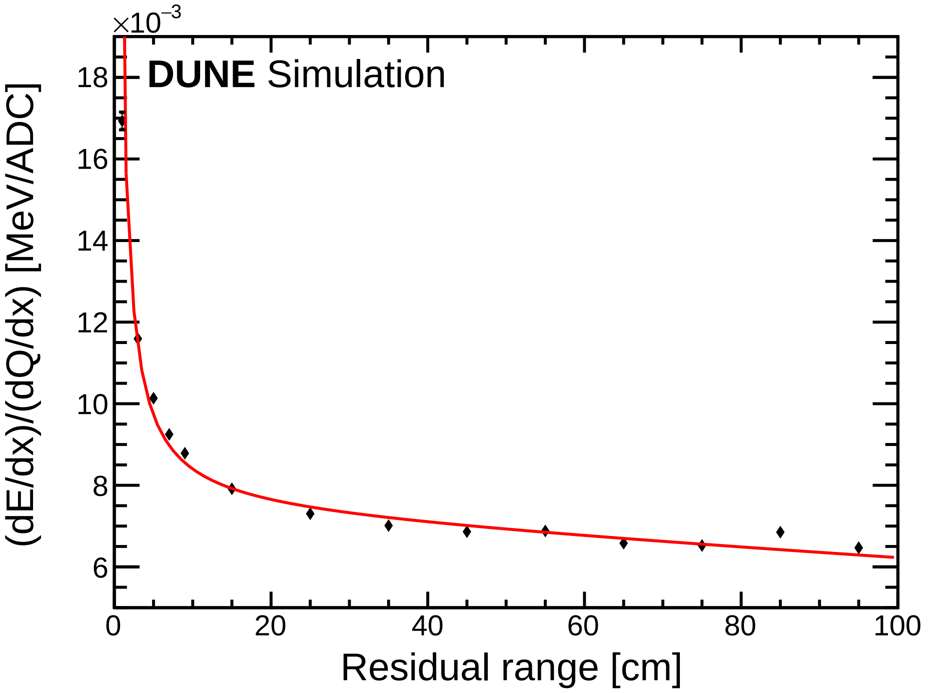

Figure 8.30. The ratio of theoretical dE/dx to reconstructed dQ/dx as a function of residual range for stopping protons and fitted with function as described in Equation 8.10.

Table 8.3. The value of the parameters of the fit function shown in Figure 8.30.

	Fit parameters		
	p_0	p_1	p_2
Value	$(7.253 \pm 0.023) \times 10^{-3}$	$(1.262 \pm 0.018) \times 10^{-2}$	$(-1.152 \pm 0.041) \times 10^{-5}$

The reconstructed dQ/dx is converted to dE/dx using Equation 8.11 and fit parameters obtained in Table 8.3. Figure 8.31 shows the reconstructed MPV of dE/dx as a function of kinetic energy using the derived relation mentioned in Equation 8.11 that translates dQ/dx to dE/dx. The reconstructed value is compared with the theoretical MPV of dE/dx. Figure 8.32 shows the reconstructed and theoretical MPV of dE/dx as a function of the residual range. Figure 8.33 shows the colour plot of the reconstructed dE/dx vs. residual range of stopping proton tracks with the comparison of reconstructed and theoretical MPV of dE/dx. Most of the reconstructed values agree very well with theoretical values. However, some differences between reconstructed and theoretical values become apparent at a lower residual range. This could be a result of inefficient reconstruction at the end of the tracks.

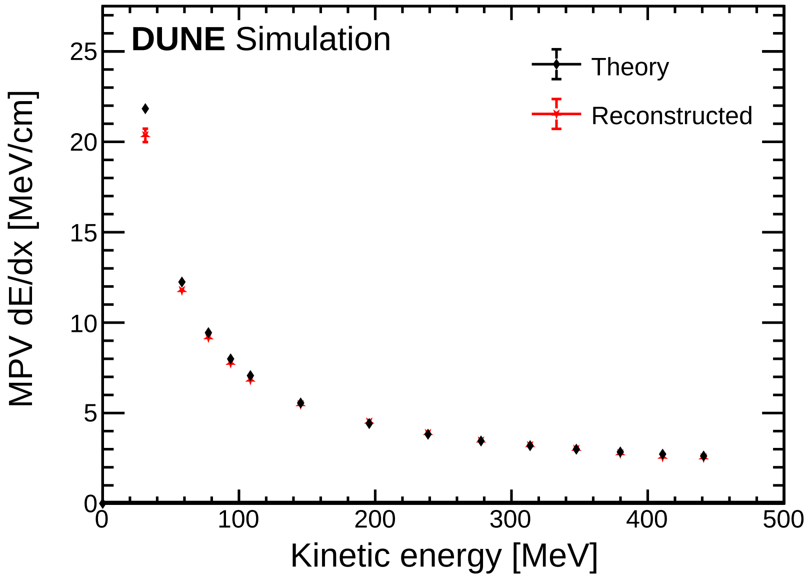

Figure 8.31. The reconstructed and theoretical most probable values of dE/dx vs. kinetic energy for stopping protons. The reconstructed values show good agreement with the theoretical prediction. At low kinetic energy, the reconstructed value is lower compared to the theoretical prediction.

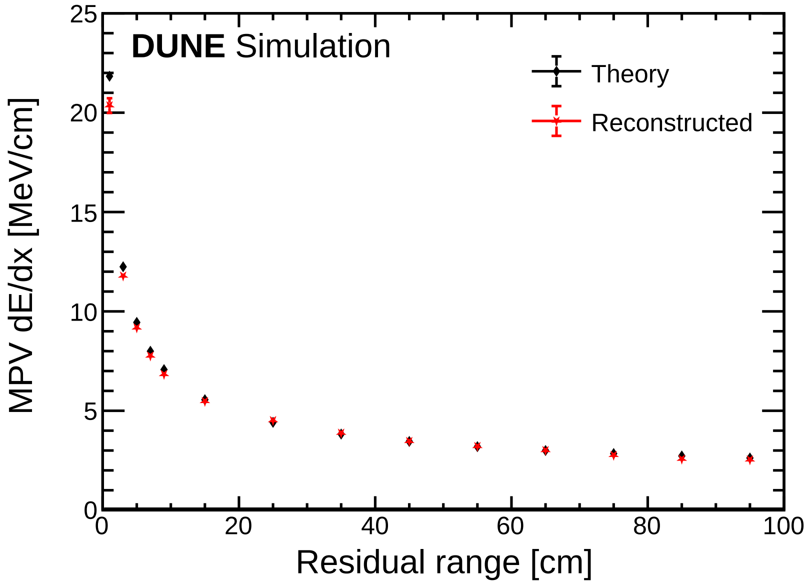

Figure 8.32. The reconstructed and theoretical most probable values of dE/dx vs. residual range for stopping protons. The reconstructed values show good agreement with the theoretical prediction. At a low residual range, the reconstructed value is lower compared to the theoretical prediction.

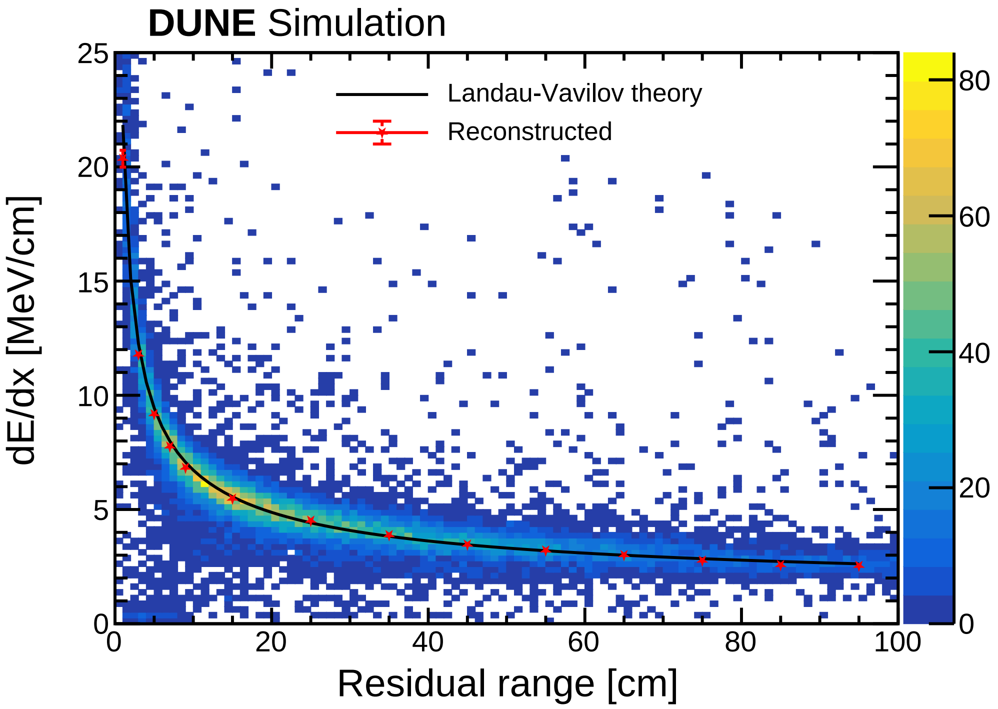

Figure 8.33. The colour plot of reconstructed dE/dx vs. residual range of stopping proton tracks. The reconstructed and theoretical most probable values dE/dx vs. residual range of stopping protons are shown with points and the curve, respectively.

8.5 Comparision of dE/dx reconstruction of stopping particles

Understanding how the energy loss varies for different particles is essential for characterising the behaviour of particles in the detector medium. In this section, the reconstructed dE/dx values as a function of different quantities such as residual range, kinetic energy, momentum and mass for stopping muons, pions and protons are compared. Figure 8.34 shows the comparison of reconstructed and theoretical dE/dx as a function of the kinetic energy of muons, pions and protons. The dependence of energy loss of a particle on its mass in a medium can be inferred from Equation 3.1. These particles show good agreement of reconstructed dE/dx with theoretical prediction as a function of kinetic energy. At low kinetic energy, protons show a difference between theoretical and reconstructed values. This could be a result of inefficient reconstruction at the end of the tracks.

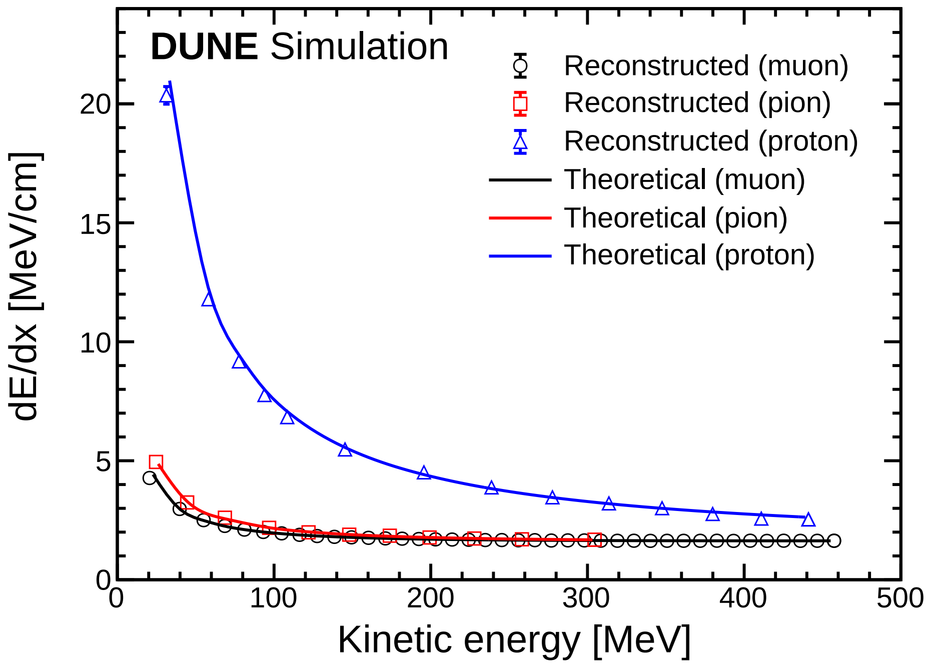

Figure 8.34. The reconstructed most probable dE/dx as a function of kinetic energy for muons, pions, and protons compared with theoretical values.

Figure 8.35 shows the comparison of reconstructed and theoretical dE/dx as a function of the residual range of muons, pions and protons. A good agreement is observed for reconstructed and theoretical dependences of dE/dx on the residual range and kinetic energy for muons, pions and protons, except probably some deviation for protons at low energy (residual range). This could be a result of inefficient reconstruction at the end of the tracks.

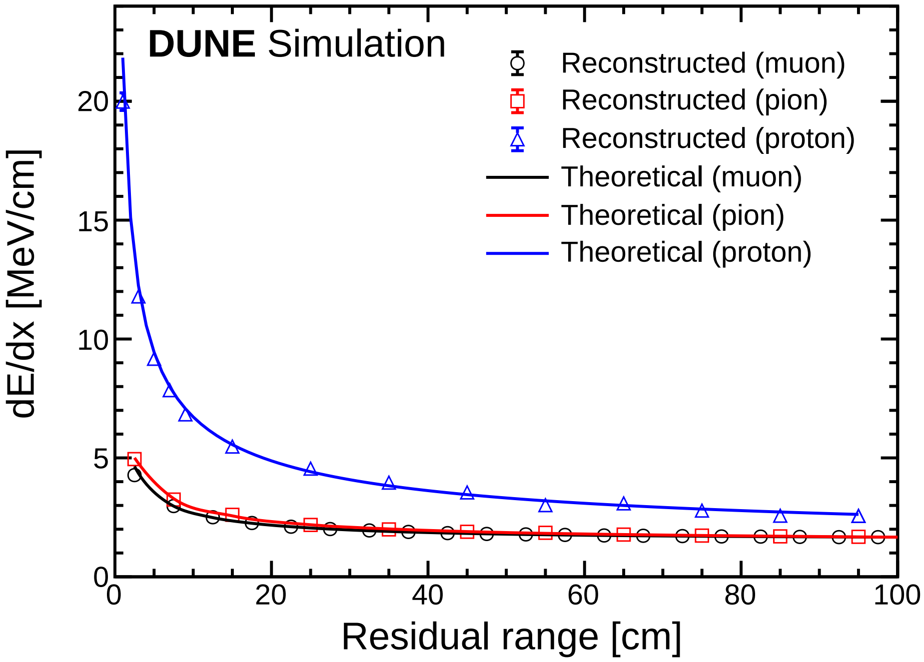

Figure 8.35. Reconstructed most probable dE/dx as a function of residual range for muons, pions, and protons compared with theoretical values. A good agreement is observed for reconstructed and theoretical prediction based on the Landau-Vavilov theory [85, 209].

The momentum-to-mass ratio (p/m) has the same values for different particles within the medium, as described by the Bethe-Bloch Equation 3.1 and illustrated in Figure 3.3. Figure 8.36 presents the reconstructed most probable of dE/dx as a function of p/m for stopping muons, pions and protons. These particles demonstrate the same p/m value (in natural units) in liquid argon. This, in turn, validates the calibration process using the absolute energy scale method employed in the conversion of dQ/dx to dE/dx for muons, pions and protons. The uniformity in the p/m behaviour across all three particles confirms the accurate translation of dQ/dx to dE/dx.

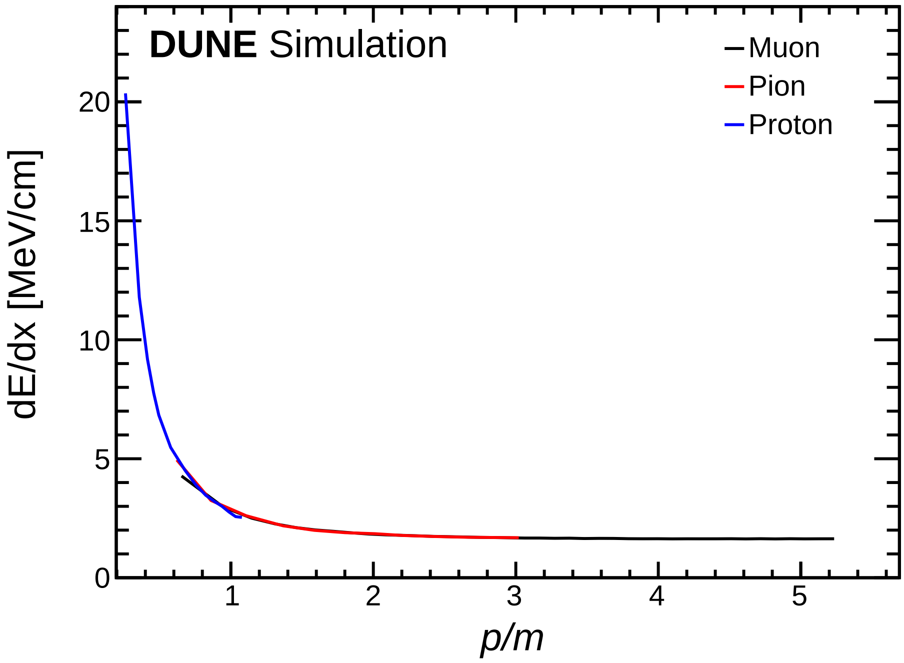

Figure 8.36. Reconstructed most probable dE/dx as a function of p/m. The p/m is almost the same for muons, pions and protons.

8.6 Comparision of dQ/dx reconstruction of stopping particles

To further observe how dQ/dx varies with residual range, kinetic energy, and p/m to understand its differences from dE/dx with these quantities, reconstructed most probable dQ/dx values are plotted against these quantities. Figures 8.37 and 8.38 show the reconstructed dQ/dx as a function of the kinetic energy and residual range of muons, pions, and protons, respectively. Figure 8.39 shows the reconstructed most probable dQ/dx as a function of p/m for stopping muons, pions, and protons. The reconstructed dQ/dx follows a similar trend of reconstructed dE/dx as a function of residual range, kinetic energy, and p/m.

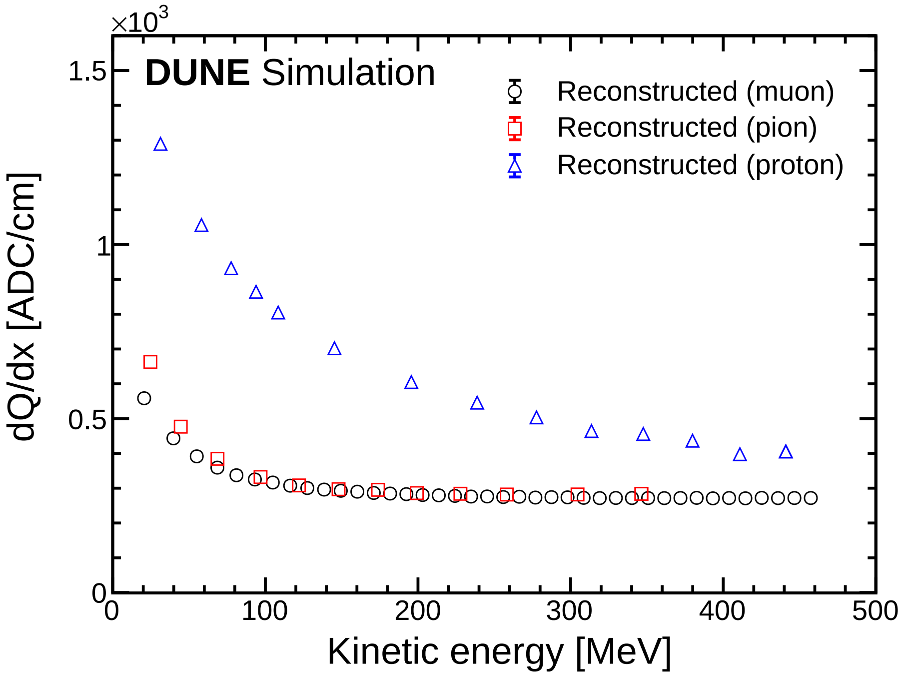

Figure 8.37. The reconstructed most probable dQ/dx as a function of kinetic energy for muons, pions, and protons.

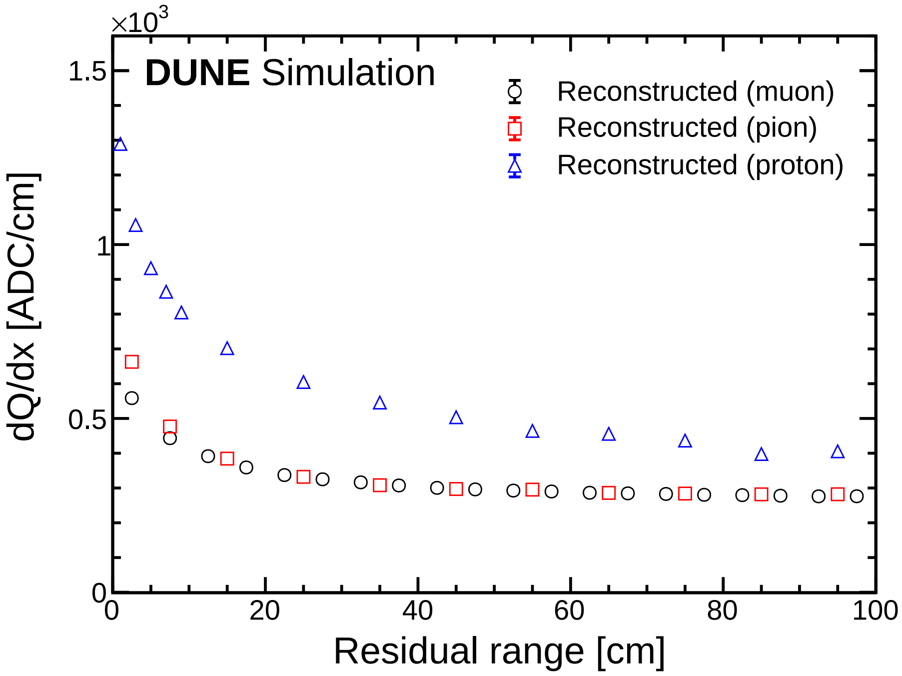

Figure 8.38. Reconstructed most probable dQ/dx as a function of residual range for muons, pions, and protons.

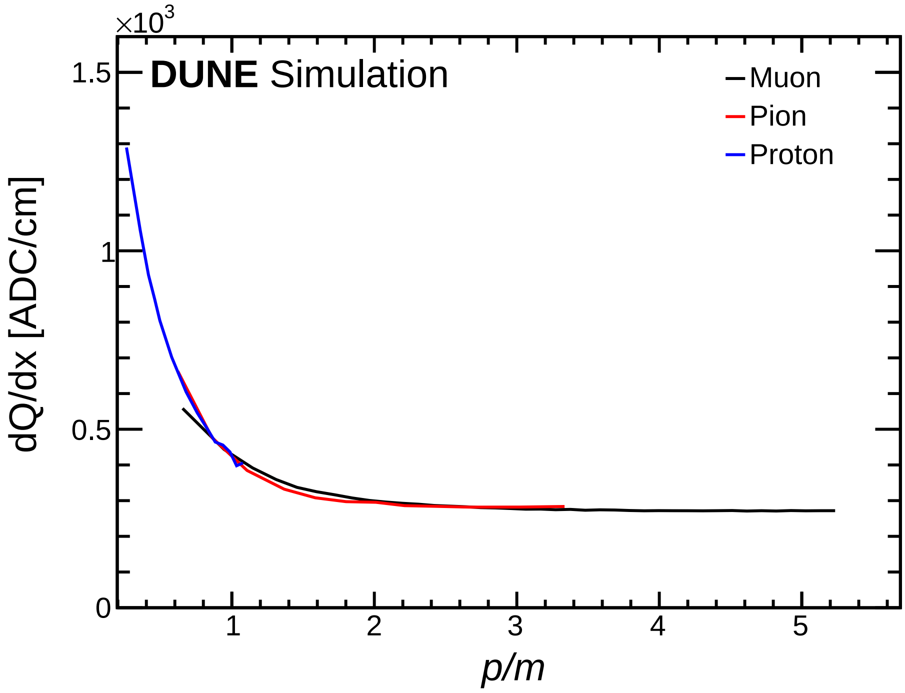

Figure 8.39. Reconstructed most probable dQ/dx as a function of p/m. The p/m is almost the same for muons, pions, and protons.

8.7 Summary

In the energy calibration process based on cosmic-ray muons, the author derived a calibration constant $C_{\text{cal}} = (5.469 \pm 0.003) \times 10^{-3}$ ADC × tick/e for the DUNE FD using stopping muons by the modified box model method as described in Equation 8.4. Additionally, a method for establishing the absolute energy scale was developed, enabling an accurate translation of dQ/dx to dE/dx for stopping muons. This absolute energy scale was subsequently applied to other particles, such as pions and protons, demonstrating good agreement between the reconstructed most probable dE/dx and the theoretical prediction from the Landau-Vavilov theory. This assumes that tracks of muons, pions, and protons can be identified before utilising specific dQ/dx to dE/dx conversion. Differentiating between muons, pions, and protons tracks may be relatively straightforward for cosmic-ray events, where it can be assumed that all sufficiently long tracks originating from outside the detector are muon tracks. Additionally, secondary tracks (excluding electrons, cascades, and protons, which should ideally be reconstructed as such) can be assumed to be pions. For neutrino events, muon calibration can likely be used for both muons and pions, especially when the track type is uncertain. This assumes, once again, that protons, electrons, and cascades can be reliably identified as such. A comparison was conducted for muons, pions, and protons with theoretical values, considering various quantities such as kinetic energy, residual range, and p/m. The consistent value for p/m across different particle types highlights the independence of the momentum-to-mass ratio from particle type, thereby validating the calibration method. This study demonstrates the versatility of the calibration techniques, applicable to LArTPC, and valid for different particles.

Chapter 9

Conclusion

This PhD thesis has presented different studies focusing on the DUNE FD, including the simulation and reconstruction of cosmic-ray muon events, the reconstruction of electromagnetic showers, and the calibration of the DUNE FD.

Cosmic-ray muons are a naturally available source, are capable of penetrating deep underground and can be used for different studies such as detector calibration. Muons can be used as a standard candle because they have a well-understood energy loss profile. Cosmic-ray muon events are simulated with the MUSUN generator in the DUNE HD FD. A total of 1.86×10^6 cosmic muons are generated corresponding to 131 days of data at DUNE FD. The rate of muons entering the DUNE FD is 4.76×10^3 per day. The energy of generated muons ranges from 1 GeV – 10^6 GeV. About 33 % of generated muon enters into the DUNE FD. The mean energy of muons that entered the DUNE FD is 283 GeV. The characterisation of various particles produced in liquid argon, with a special emphasis on cosmic muons is presented. The presented event displays showcased the effectiveness of two distinct reconstruction chains: CRC and NRC, providing valuable insights into the reconstruction processes. CRC is tuned to reconstruct cosmic muon tracks whilst NRC is tuned to reconstruct neutrino events. The event display shows that the neutrino-oriented algorithm merges different particle showers and tracks into one shower whilst the cosmic-oriented chain fragments one shower into many. The fragmentation of showers occurs significantly more frequently in CRC events than in NRC events. For showers, the NRC is more effective, as it exhibits less shower fragmentation than the CRC. Conversely, for tracks, the CRC is more effective because it reconstructs particle tracks more efficiently than the NRC, which sometimes merges tracks with showers.

In DUNE, a crucial component of conducting neutrino oscillation studies involve thoroughly examining the response of the detector to the particles produced in neutrino interactions. Accurate energy reconstruction is important for precisely measuring CP violation and fully utilizing the detector's capabilities. The production of π^0 in neutral current interactions is a background for the electron neutrino appearance signal. The reconstruction of π^0 becomes crucial, thus, requiring a detailed study to reduce systematic uncertainties. Additionally, the decay signature $\pi^0 \rightarrow 2\gamma$ provides a valuable means for calibrating the energy of electromagnetic showers. The neutral pion analysis involves the reconstruction of the π^0 mass from the reconstructed energy of two showers emerging from the $\pi^0 \rightarrow 2\gamma$ process, showcasing its application in shower energy calibration. The π^0 mass is reconstructed to be (136 ± 7) MeV/c^2. This result is consistent within the statistical uncertainty of 5% with the expected π^0 mass. Several improvements are needed, especially in shower energy reconstructions. The shower clustering and direction reconstruction algorithm is not yet perfectly functioning.

The accurate dE/dx reconstruction for particle tracks is important for measuring the total energy of stopping particles and for particle identification. Stopping muons proves to be invaluable as a calibration source for LArTPCs due to their well-understood energy loss in liquid argon. To convert charge per unit length (dQ/dx) to particle energy loss per unit length (dE/dx), a calibration constant is determined. In this study, a calibration constant $C_{\text{cal}} = (5.469 \pm 0.003) \times 10^{-3}\text{ADC} \times \text{tick/e}$ is derived for the DUNE FD using the modified box model method, translating dQ/dx to dE/dx for stopping muon tracks as described in Equation 8.4. Additionally, a method for establishing the absolute energy scale was developed, enabling an accurate translation of dQ/dx to dE/dx for stopping muons. This absolute energy scale was successfully applied to other particles, such as pions and protons, showing good agreement between the measured most probable dE/dx and the theoretical prediction from the Landau-Vavilov theory. A comprehensive comparison was conducted for muons, pions, and protons with theoretical values, considering various quantities such as kinetic energy, residual range, and p/m. The consistent value for p/m across different particle types highlights the independence of the momentum-to-mass ratio from particle type, validating the calibration method. This study demonstrates the versatility of the calibration technique, applicable to LArTPC and valid for all particle species.

The above-mentioned work carried out in this thesis has a significant and multifaceted impact on the DUNE experiment, both currently and in the future. A fundamental understanding of cosmic-ray muons and their interactions in liquid argon, particularly in the DUNE FD, plays a crucial role in enhancing the precision and accuracy of DUNE's neutrino experiments. The study of cosmic-muon rates and the secondary particles produced in the DUNE FD will aid various research areas, such as detector calibration. Cosmic-ray muons are beneficial for calibration, and certain classes of muon-induced events may serve as significant backgrounds for DUNE's physics analyses, especially in the search for proton decay. The development of reconstruction algorithms for cosmic-ray muon events will support the use of specific algorithms tailored to different analyses within DUNE. Furthermore, identifying issues in track and shower reconstruction will assist the DUNE reconstruction group in improving particle reconstruction techniques.

In DUNE, accurately identifying the type of interacting neutrino is only one aspect of the measurement process. Constructing a precise picture of neutrino oscillation parameters requires determining the energy of incoming particles with high accuracy. Neutral pions are produced in neutrino interactions in the DUNE FD. Energy reconstruction of electromagnetic showers is essential for accurately reconstructing the π^0 mass. Electromagnetic showers, a primary component of particle interactions in DUNE, require ongoing study in their reconstruction and characterisation. This research is vital for the classification of neutrino-induced interactions. As a crucial piece of the oscillation puzzle, it will ultimately aid DUNE in answering some of the most outstanding questions in particle physics.

Two energy calibration techniques have been developed for the DUNE FD, with the absolute energy calibration technique showing superior agreement with theoretical predictions and independence from modelling or parameters from other experiments. This advantage allows for precise calibration of the DUNE LArTPC detector. The versatility of this calibration technique means it can be adopted in other LArTPC experiments, such as ProtoDUNE. This capability will play a crucial role in making precise physics measurements at DUNE, such as determining the extent of CP violation in the neutrino sector, which requires accurate reconstruction of particle energies and other kinematic quantities.

References

[1] B. Abi *et al.* (DUNE Collaboration), “Volume I. Introduction to DUNE”, JINST **15**, T08008 (2020).

[2] B. Abi *et al.* (DUNE Collaboration), “Deep Underground Neutrino Experiment (DUNE), Far Detector Technical Design Report, Volume II: DUNE Physics”, arXiv:2002.03005v2 (2020).

[3] B. Abi *et al.* (DUNE Collaboration), “Volume III. DUNE far detector technical coordination”, JINST **15**, T08009 (2020).

[4] B. Abi *et al.* (DUNE Collaboration), “Volume IV. The DUNE far detector single-phase technology”, JINST **15**, T08010 (2020).

[5] P. Langacker, *The standard model and beyond* (CRC Press, USA, 2017).

[6] D. Griffiths, *Introduction to elementary particles* (Wiley-vch Verlag GmbH and Co. KGaA, Weinheim, 2008).

[7] J. Chadwick, “Intensitatsverteilung im magnetischen spektrum der β-strahlen von radium B + C”, Verhandlungen der deutschen physikalischen Gesellschaft **16**, 383 (1914).

[8] A. D. Franklin and A. D. Marino, *Are there really neutrinos?* (CRC Press, Boca Raton, 2020).

[9] A. de Gouvea, “2004 TASI lectures on neutrino physics”, arXiv:hep-ph/0411274 (2004).

[10] A. Franklin, “The machine speaks falsely”, Spontaneous Generations **4**, 1 (2010).

[11] C. D. Ellis and W. A. Wooster, “The average energy of disintegration of Radium E”, Proc. Roy. Soc. Lond. A **117**, 109 (1927).

[12] E. Fermi, “Tentativo di una teoria dei raggi beta”, Il Nuovo Cimento **9**, 1 (1934).

[13] J. Chadwick, “The existence of a neutron”, Proc. Roy. Soc. Lond. A **136**, 692 (1932).

[14] C. L. Cowan *et al.*, “Detection of the free neutrino: a confirmation”, Science **124**, 103 (1956).

[15] G. Danby, L. M. Lederman, *et al.*, “Observation of high-energy neutrino reactions and the existence of two kinds of neutrinos”, Phys. Rev. Lett. **9**, 36 (1962).

[16] K. Kodama *et al.* (DONUT Collaboration), “Observation of tau neutrino interactions”, Phys. Lett. B **504**, 218 (2001).

[17] R. Davis, Jr., D. S. Harmer, and K. C. Hoffman, “Search for neutrinos from the SUN”, Phys. Rev. Lett. **20**, 1205 (1968).

[18] J. N. Bahcall, N. A. Bahcall, and G. Shaviv, “Present status of the theoretical predictions for the ^{36}Cl solar-neutrino experiment”, Phys. Rev. Lett. **20**, 1209 (1968).

[19] J. Konijn, “The solar neutrino problem”, Eur. J. Phys. **20**, 399 (1999).

[20] V. Gribov and B. Pontecorvo, “Neutrino astronomy and lepton charge”, Physics Letters **28B**, 493 (1969).

[21] Q. R. Ahmad *et al.*, “Direct evidence for neutrino flavor transformation from neutral-current interactions in the Sudbury Neutrino Observatory”, Phys. Rev. Lett. **89**, 011301 (2002).

[22] Y. Fukuda *et al.* (Super-Kamiokande Collaboration), “Evidence for oscillation of atmospheric neutrinos”, Phys. Rev. Lett. **81**, 1562 (1998).

[23] K. S. Hirata *et al.*, “Observation of a small atmospheric ν_μ/ν_e ratio in Kamiokande”, Phys. Lett. B **280**, 146 (1992).

[24] S. L. Glashow, “Partial-symmetries of weak interactions”, Nucl. Phys. **22**, 579 (1961).

[25] S. Weinberg, “A model of leptons”, Phys. Rev. Lett. **19**, 1264 (1967).

[26] A. Salam, “Weak and electromagnetic interactions”, 969, Proc. of the 8th Nobel Symposium on ‘Elementary Particle Theory, Relativistic Groups and Analyticity’, Stockholm, Sweden, edited by N. Svartholm, 367 (1968).

[27] M. Peskin and D. Schroeder, *An introduction to quantum field theory* (Perseus Books Publishing, Reading, Massachusetts, 1995).

[28] C. Giunti and C. W. Kim, *Fundamentals of neutrino physics and astrophysics* (Oxford University Press, New York, 2007).

[29] S. Bilenky, *Introduction to the physics of massive and mixed neutrinos, lect. notes phys. 817* (Springer, Berlin Heidelberg, 2010).

[30] S. M. Bilenky, C. Giunti, and W. Grimus, “Phenomenology of neutrino oscillations”, Progress in Particle and Nuclear Physics **43**, 1 (1999).

[31] C. Giunti, “Theory and phenomenology of neutrino oscillations and masses”, Nuclear Physics B (Proc. Suppl.) **169**, 307 (2007).

[32] F. D. Lodovico *et al.*, “Experimental considerations in long-baseline neutrino oscillation measurements”, Annu. Rev. Nucl. Part. Sci. **73**, 69 (2023).

[33] J. A. Formaggio and G. P. Zeller, “From eV to EeV: Neutrino cross sections across energy scales”, Review of Modern Physics **84**, 1307 (2012).

[34] C. Giusti and M. V. Ivanov, “Neutral current neutrino-nucleus scattering: theory”, J. Phys. G: Nucl. Part. Phys. **47**, 024001 (2020).

[35] D. Rein and L. M Sehgal, “Neutrino-excitation of baryon resonances and single pion production”, Annals of Physics **133**, 79 (1981).

[36] B. Pontecorvo, “Inverse beta processes and nonconservation of lepton charge”, Sov. Phys. JETP **7**, 172 (1958).

[37] B. Pontecorvo, “Neutrino experiments and the problem of conservation of leptonic charge”, Sov. Phys. JETP **26**, 984 (1968).

[38] Z. Maki, M. Nakagawa, and S. Sakata, “Remarks on the unified model of elementary particles”, Progress of Theoretical Physics **28**, 870 (1962).

[39] Q. R. Ahmad *et al.* (SNO Collaboration), “Measurement of the rate of $\nu_e + d \to p + p + e^-$ interactions produced by ^{8}B solar neutrinos at the Sudbury Neutrino Observatory”, Phys. Rev. Lett. **87**, 071301 (2001).

[40] Q. R. Ahmad *et al.* (SNO Collaboration), “Direct evidence for neutrino flavor transformation from neutral-current interactions in the Sudbury Neutrino Observatory”, Phys. Rev. Lett. **89**, 011301 (2002).

[41] M. Tanabashi *et al.* (Particle Data Group), “Review of particle physics”, Phys. Rev. D **98**, 030001 (2018).

[42] H. Nunokawa, S. Parke, and J. W. Valle, “CP violation and neutrino oscillations”, Progress in Particle and Nuclear Physics **60**, 338 (2008).

[43] L. Wolfenstein, “Neutrino oscillations in matter”, Phys. Rev. D **17**, 2369 (1978).

[44] M. Bass *et al.*, “Baseline optimization for the measurement of CP violation, mass hierarchy, and θ_{23} octant in a long-baseline neutrino oscillation experiment”, Phys. Rev. D **91**, 052015 (2015).

[45] M. V. Diwan, “The case for a super neutrino beam”, Frascati Phys. Ser. **35**, 89 (2004).

[46] C. Jarlskog, “Commutator of the quark mass matrices in the standard electroweak model and a measure of maximal CP nonconservation”, Phys. Rev. Lett. **55**, 1039 (1985).

[47] R. L Workman *et al.* (Particle Data Group), “Review of particle physics”, Prog. Theor. Exp. Phys. **2022**, 083C01 (2022).

[48] N. Aghanim *et al.* (Plank Collaboration), “Planck 2018 results - VI. cosmological parameters”, Astronomy and Astrophysics **641**, A6 (2020).

[49] M. Aker *et al.* (KATRIN Collaboration), “Improved upper limit on the neutrino mass from a direct kinematic method by KATRIN”, Phys. Rev. Lett. **123**, 221802 (2019).

[50] P. de Salas *et al.*, “2020 global reassessment of the neutrino oscillation picture”, Journal of High Energy Physics **2021** (2021).

[51] S. F. King, “Unified models of neutrinos, flavour and CP violation”, Progress in Particle and Nuclear Physics **94**, 217 (2017).

[52] J. N. Abdurashitov *et al.* (SAGE Collaboration), “Measurement of the solar neutrino capture rate with gallium metal. iii: Results for the 2002–2007 data-taking period”, Phys. Rev. C **80**, 015807 (2009).

[53] F. Kaether, W. Hampel, G. Heusser, J. Kiko, and T. Kirsten, “Reanalysis of the GALLEX solar neutrino flux and source experiments”, Phys. Lett. B **685**, 47 (2010).

[54] B. Cleveland *et al.*, “Measurement of the solar electron neutrino flux with the Homestake chlorine detector”, Astrophys. J. **496**, 505 (1998).

[55] G. Bellini *et al.*, “Precision measurement of the ^{7}Be solar neutrino interaction rate in Borexino”, Phys. Rev. Lett. **107**, 141302 (2011).

[56] G. Bellini *et al.* (Borexino Collaboration), “Final results of Borexino Phase-I on low energy solar neutrino spectroscopy”, Phys. Rev. D **89**, 112007 (2014).

[57] Y. Fukuda *et al.* (Kamiokande Collaboration), “Solar neutrino data covering solar cycle 22”, Phys. Rev. Lett. **77**, 1683 (1996).

[58] J. Hosaka *et al.* (Super-Kamiokande Collaboration), “Solar neutrino measurements in Super-Kamiokande-I”, Phys. Rev. D **73**, 112001 (2006).

[59] J. P. Cravens *et al.* (Super-Kamiokande Collaboration), “Solar neutrino measurements in Super Kamiokande-II”, Phys. Rev. D **78**, 032002 (2008).

[60] K. Abe *et al.* (Super-Kamiokande Collaboration), “Solar neutrino results in Super-Kamiokande-III”, Phys. Rev. D **83**, 052010 (2011).

[61] B. Aharmim *et al.* (SNO Collaboration), “Combined analysis of all three phases of solar neutrino data from the Sudbury Neutrino Observatory”, Phys. Rev. C **88**, 025501 (2013).

[62] S. Abe *et al.* (The KamLAND Collaboration), “Precision measurement of neutrino oscillation parameters with KamLAND”, Phys. Rev. Lett. **100**, 221803 (2008).

[63] A. Gando *et al.* (The KamLAND Collaboration), “Constraints on θ_{13} from a three-flavor oscillation analysis of reactor antineutrinos at KamLAND”, Phys. Rev. D **83**, 052002 (2011).

[64] A. Gando *et al.* (KamLAND Collaboration), “Reactor on-off antineutrino measurement with KamLAND”, Phys. Rev. D **88**, 033001 (2013).

[65] G. Bak *et al.* (RENO Collaboration), “Measurement of reactor antineutrino oscillation amplitude and frequency at RENO”, Phys. Rev. Lett. **121**, 201801 (2018).

[66] D. Adey *et al.* (The Daya Bay Collaboration), “Measurement of the electron antineutrino oscillation with 1958 days of operation at Daya Bay”, Phys. Rev. Lett. **121**, 241805 (2018).

[67] K. Abe *et al.* (Super-Kamiokande Collaboration), “Atmospheric neutrino oscillation analysis with external constraints in Super-Kamiokande I-IV”, Phys. Rev. D **97**, 072001 (2018).

[68] M. G. Aartsen *et al.* (Super-Kamiokande Collaboration), “Measurement of atmospheric neutrino oscillations at 6–56 GeV with IceCube DeepCore”, Phys. Rev. Lett. **120**, 071801 (2018).

[69] M. G. Aartsen *et al.* (Super-Kamiokande Collaboration), “Measurement of atmospheric tau neutrino appearance with IceCube DeepCore”, Phys. Rev. D **99**, 032007 (2019).

[70] P. Dunne, *Latest neutrino oscillation results from T2K*, https://doi.org/10.5281/zenodo.3959558, 2020.

[71] M. H. Ahn *et al.* (K2K Collaboration), “Measurement of neutrino oscillation by the K2K experiment”, Phys. Rev. D **74**, 072003 (2006).

[72] P. Adamson *et al.* (MINOS Collaboration), “Combined analysis of ν_μ disappearance and $\nu_\mu \to \nu_e$ appearance in MINOS using accelerator and atmospheric neutrinos”, Phys. Rev. Lett. **112**, 191801 (2014).

[73] A. Himmel, *New oscillation results from the NOνA experiment*, https://www.osti.gov/biblio/1640225, 2020.

[74] K. Abe *et al.* (T2K Collaboration), “The T2K experiment”, Nucl. Instrum. Meth. Phys. Res., Sect. A **659**, 106 (2011).

[75] D. S. Ayres *et al.*, “The NOνA technical design report”, Tech. Rep. FERMILAB-DESIGN-2007-01, Fermilab (2007).

[76] M. A. Acero *et al.* (NOνA Collaboration), “Improved measurement of neutrino oscillation parameters by the NOνA experiment”, Phys. Rev. D **106**, 032004 (2022).

[77] K. Abe *et al.* (Hyper-Kamiokande Working Group), “A long baseline neutrino oscillation experiment using J-PARC neutrino beam and Hyper-Kamiokande”, arXiv:1412.4673v2 (2015).

[78] G. Charpak *et al.*, “The use of multiwire proportional counters to select and localize charged particles”, Nuclear Instruments and Methods **62**, 262 (1968).

[79] D. Nygren, “The time projection chamber: a new 4 pi detector for charged particles”, eConf **C740805**, 58 (1974).

[80] C. Rubbia, “The liquid-argon time projection chamber: a new concept for neutrino detectors”, CERN-EP-INT-77-8 (1977).

[81] C. E. Aalseth *et al.*, “DarkSide-20k: A 20 tonne two-phase LArTPC for direct dark matter detection at LNGS”, Eur. Phys. J. Plus **133**, 131 (2018).

[82] E. Aprile, A. E. Bolotnikov, A. I. Bolozdynya, and T. Doke, *Noble gas detectors* (Wiley-vch Verlag GmbH and Co. KGaA, Weinheim, 2006).

[83] R. Acciarri *et al.* (MicroBooNE Collaboration), “Michel electron reconstruction using cosmic-ray data from the MicroBooNE LArTPC”, JINST **12**, P09014 (2017).

[84] D. E. Groom, N. V. Mokhov, and S. I. Striganov, “Muon stopping power and range tables 10 MeV-100 TeV”, Atomic Data and Nuclear Data Tables **78**, 183 (2001).

[85] L. Landau, “On the energy loss of fast particles by ionisation”, J. Phys. U.S.S.R. **8**, 201 (1944).

[86] E. Aprile, W. H.-M. Ku, and J. Park, “Delta electron production and the ultimate energy resolution of liquid argon ionization detectors”, IEEE Trans. Nucl. Sci. **35**, 37 (1988).

[87] B. Rossi, *High energy particles* (Prentice-Hall, Inc., Englewood Cliffs, NJ, 1952).

[88] J. D. Jackson, *Classical electrodynamics, 3rd edition* (John Wiley and Sons, New York, 1998).

[89] W. T. Scott, “The theory of small-angle multiple scattering of fast charged particles”, Rev. Mod. Phys. **35**, 231 (1963).

[90] J. W. Motz, H. Olsen, and H. W. Koch, “Electron scattering without atomic or nuclear excitation”, Rev. Mod. Phys. **36**, 881 (1964).

[91] H. A. Bethe, “Moliere’s theory of multiple scattering”, Phys. Rev. **89**, 1256 (1953).

[92] M. Berger, J. Coursey, and M. Zucker, *ESTAR, PSTAR, and ASTAR: computer programs for calculating stopping-power and range tables for electrons, protons, and helium ions (version 1.21)*, http://physics.nist.gov/Star, 1999.

[93] M. Berger *et al.*, *XCOM: photon cross sections database (version 1.5)*, http://physics.nist.gov/xcom, 2010.

[94] B. Abi *et al.* (DUNE Collaboration), “First results on ProtoDUNE-SP liquid argon time projection chamber performance from a beam test at the CERN neutrino platform”, JINST **15**, P12004 (2020).

[95] M. Miyajima *et al.*, “Average energy expended per ion pair in liquid argon”, Phys. Rev. A **9**, 1438 (1974).

[96] R. Acciarri *et al.*, “Oxygen contamination in liquid argon: combined effects on ionisation electron charge and scintillation light”, JINST **5**, P05003 (2017).

[97] R. Acciarri *et al.*, “A study of electron recombination using highly ionising particles in the ArgoNeuT Liquid Argon TPC”, JINST **8**, P08005 (2013).

[98] R. T. Scalettar *et al.*, “Critical test of geminate recombination in liquid argon”, Phys. Rev. A **25**, 2419 (1982).

[99] E. Aprile *et al.*, “Energy resolution studies of liquid argon ionisation detectors”, Nucl. Instr. and Meth. A **261**, 519 (1987).

[100] S. Amoruso *et al.*, “Study of electron recombination in liquid argon with the ICARUS TPC”, Nucl. Instrum. Meth. Phys. Res. A **523**, 275 (2004).

[101] W. Walkowiak, “Drift velocity of free electrons in liquid argon”, Nucl. Instrum. Meth. Phys. Res., Sect. A **449**, 288 (2000).

[102] X. Luo and F. Cavanna, “Ion transport model for large LArTPC”, JINST **15**, C03034 (2020).

[103] P. Abratenko *et al.* (MicroBooNE Collaboration), "Measurement of the longitudinal diffusion of ionisation electrons in the MicroBooNE detector", JINST **16**, P09025 (2020).

[104] A. Lister and M. Stancari, "Investigations on a fuzzy process: effect of diffusion on calibration and particle identification in Liquid Argon Time Projection Chambers", JINST **17**, P07016 (2020).

[105] Y. Li *et al.*, "Measurement of longitudinal electron diffusion in liquid argon", Nucl. Instrum. Meth. Phys. Res., Sect. A **816**, 160 (2016).

[106] The Liquid Argon Technology @BNL, *Basic properties*, https://lar.bnl.gov/properties/basic.html, 2023.

[107] P. Abratenko *et al.* (MicroBooNE Collaboration), "Measurement of space charge effects in the MicroBooNE LArTPC using cosmic muons", JINST **15**, P12037 (2020).

[108] R. Acciarri *et al.* (MicroBooNE Collaboration), "Design and construction of the MicroBooNE detector", JINST **12**, P02017 (2017).

[109] R. Acciarri *et al.* (SBND Collaboration), "Construction of precision wire readout planes for the Short-Baseline Near Detector (SBND)", JINST **15**, P06033 (2020).

[110] S Gao and on behalf of the DUNE Collaboration, "Cold readout electronics for liquid argon TPCs in the DUNE experiment", J. Phys.: Conf. Ser. **2374**, 012075 (2022).

[111] H. Chen and V. Radeka, "Cryogenic electronics for noble liquid neutrino detectors", Nucl. Instrum. Meth. Phys. Res., Sect. A **1045**, 167571 (2023).

[112] D. Whittington, S. Mufsonb, and B. Howarda, "Scintillation light from cosmic-ray muons in liquid argon", JINST **11**, P05016 (2016).

[113] B. J. P. Jones *et al.*, "A measurement of the absorption of liquid argon scintillation light by dissolved nitrogen at the part-per-million level", JINST **8**, P07011 (2013).

[114] R. Acciarri *et al.*, "Effects of nitrogen contamination in liquid argon", JINST **5**, P06003 (2010).

[115] D. Garcia-Gamez, P. Green, and A. M. Szelc, "Predicting transport effects of scintillation light signals in large-scale liquid argon detectors", Eur. Phys. J. C **81**, 349 (2021).

[116] R. Acciarri *et al.*, "Demonstration and comparison of photomultiplier tubes at liquid argon temperature", JINST **7**, P01016 (2012).

[117] D. Kaleko (MicroBooNE Collaboration), "PMT triggering and readout for the MicroBooNE experiment", JINST **8**, C09009 (2013).

[118] A. Ankowski *et al.*, "Characterisation of ETL 9357FLA photomultiplier tubes for cryogenic temperature applications", Nucl. Instrum. Meth. Phys. Res., Sect. A **556**, 146 (2006).

[119] A. Gola *et al.*, “NUV-Sensitive silicon photomultiplier technologies developed at Fondazione Bruno Kessler”, Sensors **19**, 308 (2019).

[120] A. A. Abud *et al.* (DUNE Collaboration), “Design, construction and operation of the Proto-DUNE-SP Liquid Argon TPC”, JINST **17**, P01005 (2022).

[121] E. Segreto *et al.*, “First liquid argon test of the X-ARAPUCA”, JINST **15**, C05045 (2020).

[122] M. Kuźniak and A. M. Szelc, “Wavelength shifters for applications in liquid argon detectors”, Instruments **5**, 4 (2021).

[123] The DUNE Collaboration, “Deep Underground Neutrino Experiment Far Detector Conceptual Design Report: Single-Phase Vertical Drift Technology”, DUNE doc, 2022 (In preparation).

[124] B. Abi *et al.* (DUNE Collaboration), “Long-baseline neutrino oscillation physics potential of the DUNE experiment”, Eur. Phys. J. C **80**, 978 (2020).

[125] C. Amsler *et al.* (ArgonCube Collaboration), “ArgonCube: A novel, fully-modular approach for the realization of large-mass liquid argon TPC neutrino detectors”, Tech. Rep. CERN-SPSC-2015-009/SPSC-I-243 (2015).

[126] C. Touramanis, *APA activities and ProtoDUNE-HD*, https://indico.fnal.gov/event/50215/contributions/232416/attachments/151118/195286/APA-CM0122-CT.pdf, Presented at DUNE collaboration meeting at CERN, 2022.

[127] Y. Fukuda *et al.*, “Evidence for oscillation of atmospheric neutrinos”, Phys. Rev. Lett. **81**, 1562 (1998).

[128] G. C. Branco, “Leptonic CP violation”, Review of Modern Physics **84**, 515 (2012).

[129] J. Pati and A. Salam, “Is baryon number conserved?”, Phys. Rev. Lett. **31**, 661 (1973).

[130] H. Georgi and S. Glashow, “Unity of all elementary particle forces”, Phys. Rev. Lett. **32**, 438 (1974).

[131] H. Fritzsch and P. Minkowski, “Unified interactions of leptons and hadrons”, Annals of Physics **93**, 193 (1975).

[132] J. Hisano, “Proton decay in SUSY GUTs”, Prog. Theor. Exp. Phys. **12B**, 104 (2022).

[133] P. Langacker, “Grand unified theories and proton decay”, Phys. Rep. **72**, 185 (1981).

[134] D. H. Perkins, “Proton decay experiments”, Ann. Rev. Nucl. Part. Sci. **34**, 1 (1984).

[135] S. Dimopoulos, S. Raby, and F. Wllczek, “Proton decay in supersymmetric models”, Phys. Lett. **112B**, 133 (1982).

[136] M. Miura *et al.* (Super-Kamiokande Collaboration), “Search for nucleon decay at Super-Kamiokande”, Nuclear and Particle Physics Proceedings **273-275**, 516 (2016).

[137] M. B. Smy on behalf of the Hyper-Kamiokande Collaboration, “Hyper-Kamiokande”, Phys. Sci. Forum **8**, 41 (2023).

[138] M. B. Smy *et al.* (DUNE Collaboration), “Prospects for beyond the standard model physics searches at the Deep Underground Neutrino Experiment”, Eur. Phys. J. C **81**, 322 (2021).

[139] B. Abi *et al.* (DUNE Collaboration), “Supernova neutrino burst detection with the Deep Underground Neutrino Experiment”, Eur. Phys. J. C **81**, 423 (2021).

[140] F. Capozzi, S. W. Li, G. Zhu, and J. F. Beacom, “DUNE as the next-generation solar neutrino experiment”, Phys. Rev. Lett. **123**, 131803 (2019).

[141] A. Avasthi *et al.*, “Low background kton-scale liquid argon time projection chambers”, arXiv:2203.08821v1 (2022).

[142] D. N. Schramm and J. W. Truran, “New physics from Supernova SN1987A”, Phys. Rept. **189**, 89 (1990).

[143] F. Vissani, “Comparative analysis of SN1987A antineutrino fluence”, J. Phys. G: Nucl. Part. Phys. **42**, 013001 (2015).

[144] F. Vissani and G. Pagliaroli, “Features of Kamiokande-II, IMB, and Baksan observations and their interpretation in a two-component model for the signal”, Astronomy Letters **35**, 1 (2009).

[145] X.-J. Xu, Z. Wang, and S. Chen, “Solar neutrino physics”, Progress in Particle and Nuclear Physics **131**, 104043 (2023).

[146] M. Altmann *et al.* (GNO Collaboration), “Complete results for five years of GNO solar neutrino observations”, Phys. Lett. B **616**, 174 (2005).

[147] K. Abe *et al.* (Super-Kamiokande Collaboration), “Solar neutrino results in Super-Kamiokande-IV”, Phys. Rev. D **94**, 052010 (2016).

[148] M. Dentler *et al.*, “Updated global analysis of neutrino oscillations in the presence of eV-scale sterile neutrinos”, JHEP **08**, 010 (2018).

[149] S. Gariazzo, C. Giunti, M. Laveder, and Y. F. Li, “Updated global 3+1 analysis of short-baseline neutrino oscillations”, JHEP **06**, 135 (2017).

[150] J. Alexander *et al.*, “Dark sectors 2016 workshop: community report”, arXiv:1608.08632 (2016).

[151] M. Battaglieri *et al.*, “Us cosmic visions: new ideas in dark matter 2017: community report”, arXiv:1707.04591 (2017).

[152] J. LoSecco *et al.*, “Limits on the production of neutral penetrating states in a beam dump”, Phys. Lett **102B**, 209 (1981).

[153] J. Berger, Y. Cui, and Y. Zhao, “Detecting boosted dark matter from the Sun with large volume neutrino detectors”, JCAP **1502**, 005 (2015).

[154] J. Huang and Y. Zhao, “Dark matter induced nucleon decay: model and signatures”, JHEP **02**, 077 (2014).

[155] K. Kong, G. Mohlabeng, and J.-C. Park, "Boosted dark matter signals uplifted with self-interaction", Phys. Lett. **B743**, 256 (2015).

[156] K. Agashe, Y. Cui, L. Necib, and J. Thaler, "(In)direct detection of boosted dark matter", JCAP **1410**, 062 (2014).

[157] D. Kim, K. Kong, J.-C. Park, and S. Shin, "Boosted dark matter quarrying at surface neutrino detectors", JHEP **08**, 155 (2018).

[158] M. H. Kalos and P. A. Whitlock, *Monte carlo methods* (WILEY-VCH Verlag GmbH, Weinheim, 2008).

[159] E. Snider and G. Petrillo, "LArSoft: toolkit for simulation, reconstruction and analysis of liquid argon TPC neutrino detectors", J. Phys.: Conf. Ser. **898**, 042057 (2017).

[160] B. Baller *et al.*, "Liquid Argon Time Projection Chamber research and development in the United States", JINST **9**, T05005 (2014).

[161] P. Abratenko *et al.*, "ICARUS at the Fermilab Short-Baseline Neutrino program: initial operation", Eur. Phys. J. C **83**, 467 (2023).

[162] C. Green *et al.*, "The art framework", J. Phys.: Conf. Ser **396**, 022020 (2012).

[163] B. Stroustrup, *The c++ programming language* (Addison-Wesley, Massachusetts, 1997).

[164] C. Andreopoulos *et al.*, "The GENIE neutrino monte carlo generator", Nucl. Instrum. Meth. Phys. Res., Sect. A **614**, 87 (2010).

[165] D. Heck *et al.*, "CORSIKA: a Monte Carlo code to simulate extensive air showers", Forschungszentrum Karlsruhe Report No. FZKA6019 (1998).

[166] V. A. Kudryavtsev, "Muon simulation codes MUSIC and MUSUN for underground physics", Computer Physics Communications **180**, 339 (2009).

[167] S. Agostinelli *et al.*, "Geant4 — a simulation toolkit", Nucl. Instrum. Meth. Phys. Res., Sect. A **506**, 250 (2003).

[168] R. Acciarri *et al.*, "The Pandora multi-algorithm approach to automated pattern recognition of cosmic-ray muon and neutrino events in the MicroBooNE detector", Eur. Phys. J. C **78**, 82 (2018).

[169] C. Hagman *et al.*, "Cosmic-ray shower library CRY", Tech. Rep. UCRL-TM-229453 (2012).

[170] V. A. Kudryavtsev, M. Richardson, J. Klinger, and T. K. Warburton, "Muon simulations for LBNE using MUSIC and MUSUN", LBNE Technical Note.

[171] P. Antonioli, C. Ghetti, E. V. Korolkova, V. A. Kudryavtsev, and G. Sartorelli, "A three-dimensional code for muon propagation through the rock: MUSIC", Astroparticle Physics **7**, 357 (1997).

[172] W. Shockley, "Currents to conductors induced by a moving point charge", Journal of Applied Physics **9**, 635 (1938).

[173] S. Ramo, "Currents induced by electron motion", Proc. Ire. **27**, 584 (1939).

[174] R. Veenhof, “Garfield, recent developments”, Nucl. Instrum. Meth. Phys. Res., Sect. A **419**, 726 (1998).

[175] T. K. Gaisser, *Cosmic rays and particle physics* (Cambridge University Press, Cambridge, 1991).

[176] M. Aglietta *et al.*, “Muon “depth-intensity” relation measured by the LVD underground experiment and cosmic-ray muon spectrum at sea level”, Physical Review D **58**, 092005 (1998).

[177] A. Tang, G. Horton-Smith, V. A. Kudryavtsev, and A. Tonazzo, “Muon simulations for Super-Kamiokande, KamLAND, and CHOOZ”, Phys. Rev. D **74**, 053007 (2006).

[178] M. Aglietta *et al.*, “Upper limit on the prompt muon flux derived from the LVD underground experiment”, Phys. Rev. D **60**, 112001 (1999).

[179] A. Dar, “Atmospheric neutrinos, astrophysical neutrons, and proton-decay experiments”, Phys. Rev. Lett **51**, 227 (1983).

[180] M. Aglietta *et al.*, “Muon “depth-intensity” relation measured by the LVD underground experiment and cosmic-ray muon spectrum at sea level”, Phys. Rev. D **58**, 092005 (1998).

[181] N. P. Ilina *et al.*, “The analysis of the PCR nucleon energy spectrum and charm production cross-section as observed in MSU muon experiment”, Proceedings of the 24th international cosmic ray conference, Rome, Italy **1**, 524 (1995).

[182] F. F. Khalchukov *et al.*, “The spectrum of cosmic ray muons obtained with 100-ton scintillation detector underground and the analysis of recent experimental results”, Proceedings of the 19th international cosmic ray conference, La Jolla, California **8**, 12 (1998).

[183] M. Ambrosio *et al.*, “Vertical muon intensity measured with MACRO at the Gran Sasso laboratory”, Phys. Rev. D **52**, 3793 (1995).

[184] J. A. Formaggio and C. Martoff, “Backgrounds to sensitive experiments underground”, Ann. Rev. Nucl. Part. Sci. **54**, 361 (2004).

[185] M. Tanabashi *et al.* (Particle Data Group), “Review of particle physics”, Phys. Rev. D **98**, 030001 ((2018) and 2019 update).

[186] C. Waltham *et al.*, “Through-going muons in the Sudbury neutrino observatory”, in *Proc. 27th Int. Cosmic Ray Conf.*, Hamburg, 991 (2001).

[187] M. Aglietta *et al.*, “Neutrino-induced and atmospheric single-muon fluxes measured over five decades of intensity by LVD at Gran Sasso Laboratory ”, Astropart. Phys. **3**, 311 (1995).

[188] Y. M. Andreev, V. I. Gurentzov, and I. M. Kogai, “Muon intensity from the Baksan underground scintillation telescope”, in *Proc. 20th Int. Cosmic Ray Conf.*, Moscow, **6**, 200 (1987).

[189] C. Berger *et al.*, “Experimental study of muon bundles observed in the Frejus detector”, Phys. Rev. D **40**, 2163 (1989).

[190] M. Crouch, “An improved world survey expression for cosmic ray vertical intensity vs. depth in standard rock”, in *Proc. 20th Int. Cosmic Ray Conf.*, Moscow, **6**, 165 (1987).

[191] R. L. Workman (Particle Data Group), “Review of particle physics”, Prog. Theor. Exp. Phys. **2022**, 083C84 (2022).

[192] V. A. Kudryavtsev, E. V. Korolkova, and N. J. C. Spooner, “Narrow muon bundles from muon pair production in rock”, Phys. Lett. B **471**, 251 (1999).

[193] B. Abi *et al.* (DUNE Collaboration), “Deep Underground Neutrino Experiment (DUNE), Far Detector Technical Design Report, Volume I: Introduction to DUNE”, arXiv: 2002.02967v2 (2020).

[194] M. Richardson, “Cosmic ray background estimations in large liquid argon detectors for proton decay via $p \to K^+\bar{\nu}$ and ν_e appearance from ν_μ beams”, PhD thesis (University of Sheffield, 2016).

[195] J. F. Ziegler, “Comments on ICRU report no. 49: stopping powers and ranges for protons and alpha particles”, Radiat. Res. **152**, 219 (1999).

[196] D.-M. Mei, C. Zhang, K. Thomas, and F. Gray, “Early results on radioactive background characterization for sanford laboratory and DUSEL experiments”, Astropart. Phys. **34**, 33 (2010).

[197] M. L. Cherry, M. Deakyne, K. Lande, C. K. Lee, and R. I. Steinberg, “Multiple muons in the Homestake underground detector”, Phys. Rev. D **27**, 1444 (1983).

[198] T. K. Warburton, “Simulations and data analysis for the 35 ton liquid argon detector as a prototype for the DUNE experiment”, PhD thesis (University of Sheffield, 2017).

[199] N. Agafonova *et al.*, “Measurement of the atmospheric muon charge ratio with the OPERA detector”, Eur. Phys. J. C **67**, 25 (2010).

[200] R. Miskimen, “Neutral pion decay”, Annu. Rev. Nucl. Part. Sci. **61**, 1 (2011).

[201] G. Zhu, S. W. Li, and J. F. Beacom, “Developing the MeV potential of DUNE: Detailed considerations of muon-induced spallation and other backgrounds”, Phys. Rev. C **99**, 055810 (2019).

[202] K. Nakamura *et al.* (Particle Data Group), “Review of particle physics”, J. Phys. G: Nucl. Part. Phys. **37**, 075021 (2010).

[203] E. A. Paschos and D. Schalla, “Coherent pion production by neutrinos”, Phys. Rev. D **80**, 033005 (2009).

[204] J. Matthews, “A Heitler model of extensive air showers”, Astroparticle Physics **22**, 387 (2005).

[205] R. Brun and F. Rademakers, “ROOT - An object oriented data analysis framework”, Nuclear Instruments and Meth. in Physics Research A **389**, 81 (1997).

[206] J. Stock, *cheat::BackTracker class reference*, https://internal.dunescience.org/doxygen/BackTracker_8cc_source.html.

[207] R. Acciarri *et al.* (ArgoNeut Collaboration), “A study of electron recombination using highly ionising particles in the ArgoNeuT Liquid Argon TPC”, JINST **8**, P08005 (2013).

[208] S. Amoruso *et al.* (The ICARUS Collaboration), “Measurement of the μ decay spectrum with the ICARUS liquid argon TPC”, Eur. Phys. J. C **33**, 233 (2004).

[209] P. V. Vavilov, “Ionisation losses of high-energy heavy particles”, Sov. Phys. JETP **5**, 749 (1957).

[210] Paticle Data Group. Atomic and nuclear properties of liquid argon, https://pdg.lbl.gov/2020/AtomicNuclearProperties/HTML/liquid_argon.html.

[211] Convoluted Landau and Gaussian fitting function, https://root.cern.ch/doc/master/langaus_8C_source.html.

Appendix A

Neutrinos

A.1 Neutrinos oscillation probability

The oscillation probability in Equation 2.58 can be written as

$$\begin{aligned}
P_{\nu_\alpha \to \nu_\beta}(L,E) =& \sum_{k,j} U_{\alpha k}^* U_{\beta k} U_{\alpha j} U_{\beta j}^* \ \exp\left(-i \frac{\Delta m_{kj}^2 L}{2E}\right) \\
=& \sum_{k=j} U_{\alpha k}^* U_{\beta k} U_{\alpha j} U_{\beta j}^* \ \exp\left(-i \frac{\Delta m_{kj}^2 L}{2E}\right) \\
& + \sum_{k \neq j} U_{\alpha k}^* U_{\beta k} U_{\alpha j} U_{\beta j}^* \ \exp\left(-i \frac{\Delta m_{kj}^2 L}{2E}\right) \\
=& \sum_{k} U_{\alpha k}^* U_{\beta k} U_{\alpha k} U_{\beta k}^* + \sum_{k \neq j} U_{\alpha k}^* U_{\beta k} U_{\alpha j} U_{\beta j}^* \ \exp\left(-i \frac{\Delta m_{kj}^2 L}{2E}\right)
\end{aligned} \tag{A.1}$$

The Euler's formula is given as

$$\begin{aligned}
e^{-iA} &= \cos A - i \sin A, \\
&= 1 - 2\sin^2(A/2) - i \sin A.
\end{aligned} \tag{A.2}$$

Using Equation A.2, Equation A.1 can be expressed as

$$\begin{aligned} P_{\nu_\alpha\to\nu_\beta}(L,E) =& \underbrace{\sum_k U^*_{\alpha k}U_{\beta k}U_{\alpha k}U^*_{\beta k}}_{P_1} + \underbrace{\sum_{k\neq j} U^*_{\alpha k}U_{\beta k}U_{\alpha j}U^*_{\beta j}}_{P_2} \\ & \underbrace{- 2\sum_{k\neq j} U^*_{\alpha k}U_{\beta k}U_{\alpha j}U^*_{\beta j}\ \sin^2\left(\frac{\Delta m^2_{kj}L}{4E}\right)}_{P_3} \\ & \underbrace{- i\sum_{k\neq j} U^*_{\alpha k}U_{\beta k}U_{\alpha j}U^*_{\beta j}\ \sin\left(\frac{\Delta m^2_{kj}L}{2E}\right)}_{P_4} \end{aligned} \tag{A.3}$$

Simplifying P_1 and P_2 terms together of Equation A.3

$$\begin{aligned} P_1 + P_2 &= \sum_k U^*_{\alpha k}U_{\beta k}U_{\alpha k}U^*_{\beta k} + \sum_{k\neq j} U^*_{\alpha k}U_{\beta k}U_{\alpha j}U^*_{\beta j} \\ &= \sum_{k,j} U^*_{\alpha k}U_{\beta k}U_{\alpha j}U^*_{\beta j} \\ &= \sum_k\sum_j U^*_{\alpha k}U_{\beta k}U_{\alpha j}U^*_{\beta j} \\ &= \sum_k \left(U^*_{\alpha k}U_{\beta k}\right)\sum_j \left(U_{\alpha j}U^*_{\beta j}\right) \\ &= \left|\sum_k U_{\alpha k}U^*_{\beta k}\right|^2 \end{aligned} \tag{A.4}$$

The unitary matrix can be written as

$$U = \begin{pmatrix} U_{e1} & U_{e2} & U_{e3} \\ U_{\mu 1} & U_{\mu 2} & U_{\mu 3} \\ U_{\tau 1} & U_{\tau 2} & U_{\tau 3} \end{pmatrix}, \quad U^\dagger = \begin{pmatrix} U^*_{e1} & U^*_{\mu 1} & U^*_{\tau 1} \\ U^*_{e2} & U^*_{\mu 2} & U^*_{\tau 2} \\ U^*_{e3} & U^*_{\mu 3} & U^*_{\tau 3} \end{pmatrix}. \tag{A.5}$$

$$UU^\dagger = \begin{pmatrix} \sum_k U_{ek}U^*_{ek} & \sum_k U_{ek}U^*_{\mu k} & \sum_k U_{ek}U^*_{\tau k} \\ \sum_k U_{\mu k}U^*_{ek} & \sum_k U_{\mu k}U^*_{\mu k} & \sum_k U_{\mu k}U^*_{\tau k} \\ \sum_k U_{\tau k}U^*_{ek} & \sum_k U_{\tau k}U^*_{\mu k} & \sum_k U_{\tau k}U^*_{\tau k} \end{pmatrix}. \tag{A.6}$$

Since unitary matrix satisfy the condition $UU^\dagger = U^\dagger U = I$, I is a 3 × 3 unity matrix;

$$UU^\dagger = \begin{pmatrix} \sum_k U_{ek}U^*_{ek} & \sum_k U_{ek}U^*_{\mu k} & \sum_k U_{ek}U^*_{\tau k} \\ \sum_k U_{\mu k}U^*_{ek} & \sum_k U_{\mu k}U^*_{\mu k} & \sum_k U_{\mu k}U^*_{\tau k} \\ \sum_k U_{\tau k}U^*_{ek} & \sum_k U_{\tau k}U^*_{\mu k} & \sum_k U_{\tau k}U^*_{\tau k} \end{pmatrix} = \begin{pmatrix} 1 & 0 & 0 \\ 0 & 1 & 0 \\ 0 & 0 & 1 \end{pmatrix} \tag{A.7}$$

Equating the matrix elements of Equation A.7, we get

$$\sum_k U_{\alpha k} U^*_{\beta k} = \begin{cases} 1, & \text{if } \alpha = \beta, \\ 0, & \text{if } \alpha \neq \beta. \end{cases} \tag{A.8}$$
$$= \delta_{\alpha\beta}.$$

where $\delta_{\alpha\beta}$ is a Kronecker delta function.
Similarly,

$$U^\dagger U = \begin{pmatrix} \sum_\alpha U^*_{\alpha 1} U_{\alpha 1} & \sum_\alpha U^*_{\alpha 1} U_{\alpha 2} & \sum_\alpha U^*_{\alpha 1} U_{\alpha 3} \\ \sum_\alpha U^*_{\alpha 2} U_{\alpha 1} & \sum_\alpha U^*_{\alpha 2} U_{\alpha 2} & \sum_\alpha U^*_{\alpha 2} U_{\alpha 3} \\ \sum_\alpha U^*_{\alpha 3} U_{\alpha 1} & \sum_\alpha U^*_{\alpha 3} U_{\alpha 2} & \sum_\alpha U^*_{\alpha 3} U_{\alpha 3} \end{pmatrix} = \begin{pmatrix} 1 & 0 & 0 \\ 0 & 1 & 0 \\ 0 & 0 & 1 \end{pmatrix} \tag{A.9}$$

Equating the matrix elements of Equation A.9, we get

$$\sum_\alpha U^*_{\alpha k} U_{\alpha j} = \begin{cases} 1, & \text{if } j = k, \\ 0, & \text{if } j \neq k. \end{cases} \tag{A.10}$$
$$= \delta_{jk}.$$

where δ_{jk} is a Kronecker delta function.

From Equation A.8 and Equation A.4

$$P_1 + P_2 = \delta_{\alpha\beta}. \tag{A.11}$$

Now, simplifying the term P_3 of Equation A.3:

$$\begin{aligned}
P_3 &= \sum_{k\neq j} U^*_{\alpha k}U_{\beta k}U_{\alpha j}U^*_{\beta j}\ \sin^2\left(\frac{\Delta m^2_{kj}L}{4E}\right)\\
&= \sum_{k>j} U^*_{\alpha k}U_{\beta k}U_{\alpha j}U^*_{\beta j}\ \sin^2\left(\frac{\Delta m^2_{kj}L}{4E}\right) + \sum_{k<j} U^*_{\alpha k}U_{\beta k}U_{\alpha j}U^*_{\beta j}\ \sin^2\left(\frac{\Delta m^2_{kj}L}{4E}\right)\\
&\text{(switching } k \text{ and } j \text{ indices of the second term without loss of generality),}\\
&= \sum_{k>j} U^*_{\alpha k}U_{\beta k}U_{\alpha j}U^*_{\beta j}\ \sin^2\left(\frac{\Delta m^2_{kj}L}{4E}\right) + \sum_{k>j} U^*_{\alpha j}U_{\beta j}U_{\alpha k}U^*_{\beta k}\ \sin^2\left(\frac{\Delta m^2_{kj}L}{4E}\right)\\
&\text{(since } \sin^2 x \text{ is an even function: } \sin^2(\Delta m^2_{kj}L/4E) = \sin^2(\Delta m^2_{jk}L/4E))\\
&= \sum_{k>j} \sin^2\left(\frac{\Delta m^2_{kj}L}{4E}\right)\left(U^*_{\alpha k}U_{\beta k}U_{\alpha j}U^*_{\beta j} + U^*_{\alpha j}U_{\beta j}U_{\alpha k}U^*_{\beta k}\right)\\
&= \sum_{k>j} \sin^2\left(\frac{\Delta m^2_{kj}L}{4E}\right)\left(U^*_{\alpha k}U_{\beta k}U_{\alpha j}U^*_{\beta j} + U_{\alpha k}U^*_{\beta k}U^*_{\alpha j}U_{\beta j}\right)\\
&= \sum_{k>j} \sin^2\left(\frac{\Delta m^2_{kj}L}{4E}\right)\left[U^*_{\alpha k}U_{\beta k}U_{\alpha j}U^*_{\beta j} + \left(U^*_{\alpha k}U_{\beta k}U_{\alpha j}U^*_{\beta j}\right)^*\right]\\
&\text{(using relation: } \mathcal{R}e(z) = (z+z^*)/2,\\
&\text{where z is a complex number and } \mathcal{R}e(z) \text{ is real part of z)}\\
&= 2\ \sum_{k>j} \mathcal{R}e(U^*_{\alpha k}U_{\beta k}U_{\alpha j}U^*_{\beta j})\ \sin^2\left(\frac{\Delta m^2_{kj}L}{4E}\right).
\end{aligned} \tag{A.12}$$

Now, simplifying the term P_4 of Equation A.3:

$$
\begin{aligned}
P_4 &= \sum_{k\neq j} U^*_{\alpha k}U_{\beta k}U_{\alpha j}U^*_{\beta j}\ \sin\left(\frac{\Delta m^2_{kj}L}{2E}\right) \\
&= \sum_{k>j} U^*_{\alpha k}U_{\beta k}U_{\alpha j}U^*_{\beta j}\ \sin\left(\frac{\Delta m^2_{kj}L}{2E}\right) + \sum_{k<j} U^*_{\alpha k}U_{\beta k}U_{\alpha j}U^*_{\beta j}\ \sin\left(\frac{\Delta m^2_{kj}L}{2E}\right) \\
&\text{(switching k and j indices of the second term without loss of generality),} \\
&= \sum_{k>j} U^*_{\alpha k}U_{\beta k}U_{\alpha j}U^*_{\beta j}\ \sin\left(\frac{\Delta m^2_{kj}L}{2E}\right) - \sum_{k>j} U^*_{\alpha j}U_{\beta j}U_{\alpha k}U^*_{\beta k}\ \sin\left(\frac{\Delta m^2_{kj}L}{2E}\right) \\
&\text{(since $\sin x$ is an odd function: } \sin(\Delta m^2_{kj}L/2E) = -\sin(\Delta m^2_{jk}L/2E)) \\
&= \sum_{k>j} \sin\left(\frac{\Delta m^2_{kj}L}{2E}\right)\left(U^*_{\alpha k}U_{\beta k}U_{\alpha j}U^*_{\beta j} - U^*_{\alpha j}U_{\beta j}U_{\alpha k}U^*_{\beta k}\right) \\
&= \sum_{k>j} \sin\left(\frac{\Delta m^2_{kj}L}{2E}\right)\left(U^*_{\alpha k}U_{\beta k}U_{\alpha j}U^*_{\beta j} - U_{\alpha k}U^*_{\beta k}U^*_{\alpha j}U_{\beta j}\right) \\
&= \sum_{k>j} \sin\left(\frac{\Delta m^2_{kj}L}{2E}\right)\left[U^*_{\alpha k}U_{\beta k}U_{\alpha j}U^*_{\beta j} - \left(U^*_{\alpha k}U_{\beta k}U_{\alpha j}U^*_{\beta j}\right)^*\right] \\
&\text{(using relation: $\mathcal{I}m(z) = (z - z^*)/2i$,} \\
&\text{where z is a complex number and $\mathcal{I}m(z)$ is imaginary part of z)} \\
&= 2i\ \sum_{k>j} \mathcal{I}m(U^*_{\alpha k}U_{\beta k}U_{\alpha j}U^*_{\beta j})\ \sin\left(\frac{\Delta m^2_{kj}L}{2E}\right).
\end{aligned}
\tag{A.13}
$$

From Equations A.11, A.12, and A.13, Equation A.3 can take the form

$$
\begin{aligned}
P_{\nu_\alpha\to\nu_\beta}(L,E) = \delta_{\alpha\beta} &- 2\times 2\sum_{k>j}\mathcal{R}e\left[U^*_{\alpha k}U_{\beta k}U_{\alpha j}U^*_{\beta j}\right]\sin^2\left(\frac{\Delta m^2_{kj}L}{4E}\right) \\
&- i\times 2i\sum_{k>j}\mathcal{I}m\left[U^*_{\alpha k}U_{\beta k}U_{\alpha j}U^*_{\beta j}\right]\sin\left(\frac{\Delta m^2_{kj}L}{2E}\right).
\end{aligned}
\tag{A.14}
$$

Hence, the final expression of neutrino oscillation probability to observe flavour ν_β from ν_α can be written as

$$
\begin{aligned}
P_{\nu_\alpha\to\nu_\beta}(L,E) = \delta_{\alpha\beta} &- 4\sum_{k>j}\mathcal{R}e\left[U^*_{\alpha k}U_{\beta k}U_{\alpha j}U^*_{\beta j}\right]\sin^2\left(\frac{\Delta m^2_{kj}L}{4E}\right) \\
&+ 2\sum_{k>j}\mathcal{I}m\left[U^*_{\alpha k}U_{\beta k}U_{\alpha j}U^*_{\beta j}\right]\sin\left(\frac{\Delta m^2_{kj}L}{2E}\right).
\end{aligned}
\tag{A.15}
$$